





PREMIO TESI DI DOTTORATO

– 57 –

PREMIO TESI DI DOTTORATO

Commissione giudicatrice, anno 2015

Vincenzo Varano, *presidente della Commissione*

Tito Arechchi, *Area scientifica*

Aldo Bompani, *Area Scienze Sociali*

Franco Cambi, *Area Umanistica*

Paolo Fellì, *Area Tecnologica*

Michele Arcangelo Feo, *Area Umanistica*

Roberto Genesio, *Area Tecnologica*

Mario Pio Marzocchi, *Area Scientifica*

Adolfo Pazzagli, *Area Biomedica*

Giuliano Pinto, *Area Umanistica*

Salvatore Ruggieri, *Area Biomedica*

Saulo Sirigatti, *Area Biomedica*

Fiorenzo Cesare Ugolini, *Area Tecnologica*

Graziella Vescovini, *Area Umanistica*

Niccolò Caselli

# **Imaging and engineering optical localized modes at the nanoscale**

Firenze University Press  
2016

Imaging and engineering optical localized modes at the nanoscale / Niccolò Caselli. – Firenze : Firenze University Press, 2016.

(Premio Tesi di Dottorato; 57)

<http://digital.casalini.it/9788864533513>

ISBN 978-88-6453-350-6 (print)

ISBN 978-88-6453-351-3 (online)

Front cover design: Alberto Pizarro Fernández, Pagina Maestra snc

Front cover photo: Niccolò Caselli, Federico La China

#### *Peer Review Process*

All publications are submitted to an external refereeing process under the responsibility of the FUP Editorial Board and the Scientific Committees of the individual series. The works published in the FUP catalogue are evaluated and approved by the Editorial Board of the publishing house. For a more detailed description of the refereeing process we refer to the official documents published on the website and in the online catalogue of the FUP ([www.fupress.com](http://www.fupress.com)).

#### *Firenze University Press Editorial Board*

G. Nigro (Co-ordinator), M.T. Bartoli, M. Boddi, R. Casalbuoni, C. Ciappei, R. Del Punta, A. Dolfi, V. Fargion, S. Ferrone, M. Garzaniti, P. Guarneri, A. Mariani, M. Marini, A. Novelli, M.C. Torricelli, M. Verga, A. Zorzi.

This work is licensed under a Creative Commons Attribution 4.0 International License  
(CC BY 4.0: <http://creativecommons.org/licenses/by/4.0/>)

**CC** 2016 Firenze University Press

Università degli Studi di Firenze

Firenze University Press

via Cittadella, 7, 50144 Firenze, Italy

[www.fupress.com](http://www.fupress.com)

*Printed in Italy*

# Contents

<b>Introduction</b>	<b>9</b>
<b>Chapter 1</b>	
<b>Optics at the nanoscale</b>	<b>13</b>
1.1 The diffraction limit	13
1.1.1 Evanescent waves	14
1.2 Modern microscopy	17
1.3 Scanning near-field optical microscopy	20
1.3.1 Probes design and fabrication	21
References	31
<b>Chapter 2</b>	
<b>Nanophotonics localized fields</b>	<b>37</b>
2.1 Photonic crystal nanoresonators	37
2.1.1 Photonic crystals	37
2.1.2 Photonic crystal nanocavity	41
2.1.3 Finite-difference time-domain calculations	43
2.2 Near-field probing	45
2.3 Disorder based nanocavities	49
References	55
<b>Chapter 3</b>	
<b>Deep sub-wavelength imaging</b>	<b>61</b>
3.1 Experimental setup	61
3.2 Test-bed sample: the D2 photonic nanocavity	63
3.2.1 Electric field intensity imaging	64
3.2.2 Magnetic field intensity imaging	66
3.3 Campanile tips for near-field probing	67
3.3.1 Mapping local charge recombination heterogeneity	68
3.3.2 Simultaneous imaging of electric and magnetic fields	70
References	84

Imaging and engineering optical localized modes at the nanoscale

<b>Chapter 4</b>	
<b>Phase sensitive Fano imaging</b>	<b>87</b>
4.1 Fano resonances	87
4.1.1 Fano resonances in photonic crystal cavities	89
4.2 Deep sub-wavelength Fano imaging	91
4.2.1 Resonant back-scattering	93
4.2.2 Resonant forward-scattering	97
References	110
<b>Chapter 5</b>	
<b>Photonic crystal molecules</b>	<b>113</b>
5.1 Coupled photonic nanocavities	113
5.1.1 Coupled modes theory	114
5.1.2 The D2 cavity-based photonic molecules	116
5.2 Post-fabrication control of evanescent coupling	117
5.2.1 Engineering the mode parity	118
5.2.2 Photoinduced non-thermal oxidation tuning	122
5.2.3 Antibonding ground state	125
5.2.4 Coupling strength control	126
5.3 Array of photonic molecules	129
References	146
<b>Chapter 6</b>	
<b>Engineering light confinement in disordered media</b>	<b>151</b>
6.1 Disorder driven light confinement	151
6.2 Engineering disordered photonic modes	154
References	161
<b>Conclusions</b>	<b>163</b>
<b>Appendix</b>	
<b>Coupling strength calculation in photonic molecule</b>	<b>165</b>

## **Introduction**

The work presented in this thesis concerns the optics research field that is commonly called micro or nano-photonics. The term “photonics” emerged at the end of last century to describe the fundamental study of light and its applications to technology, whose purpose is to accomplish functions traditionally undertaken by electronics, such as telecommunications, information processing, and so on. In fact, in the effort to further progress the high density transistor integration and thus the modern electronic system performances, scientists are now turning to photons instead of electrons as the information carriers in communication. Photons show several advantages. Light can carry a larger amount of information per second. In addition, at the single photon level, quantum information networks and quantum cryptography scheme can be pursued. Furthermore, photons are not as strongly interacting as electrons, thus reducing energy losses. However, in spite of the numerous advantages of photons, all optical integrated circuits have yet to be commercially available on large scale due to the difficulties in designing efficient optical components building blocks.

Nowadays, the suited objects to advance this research field are made up of photonic crystal devices, because of their versatility and ability to control the propagation of light at the nanoscale. Since the introduction of the photonic crystals, a great deal of groundbreaking phenomena concerning light-matter interaction at optical frequencies have been theoretically predicted and experimentally verified. They led to large technological developments, especially giving rise to innovative optoelectronic and photovoltaic applications. For instance, microscopic light manipulation is achievable through photonic crystals that exhibit finite energy band-gap for light. In particular, two-dimensional photonic crystal cavities fabricated on semiconductor slab are the state of the art devices to strongly localize electromagnetic (e.m.) fields in volumes below a cubic optical wavelength of light, thus acting as nano-resonators. In fact, they provide an efficient mechanism for controlling and inhibiting spontaneous light emission, or for reducing almost to zero the light group velocity. A noteworthy advantage of two-dimensional photonic crystal cavities is that they can be included in all-optical integrated circuits fabrication. The high quality factors enable these systems to reach the strong coupling regime between photonic localized modes and two level quantum emitters. However, the fundamental request to maximize these effects is the accurate positioning of the light source in the spot where the localized mode is maximum. Moreover, when systems of interacting resonators are conceived, a basic condition to be satisfied is the precise control on the overlap between adjacent elements to induce an effective coupling. The sub-wavelength imaging of the (e.m.) fields localized in

## Imaging and engineering optical localized modes at the nanoscale

optical nano-resonators is therefore of the utmost relevance in the road map to integrate photonic nano-resonators in chipset architectures. In order to achieve this goal we need to overcome the resolution limitations that are imposed by light diffraction to any standard microscope.

In Chapter (1) we review the more commonly methods employed to achieve a sub-wavelength spatial resolution. In particular, we describe the principle of operation of the scanning near-field optical microscope.

In Chapter (2) we describe the basic properties of light confinement in photonic crystal nanocavities and also in optical nano-resonators based on disordered arrangements of light scatterers, where multiple scattering regime gives rise to randomly placed nanocavities. In particular, we illustrate how near-field techniques can experimentally probe the e.m. optical fields localized at the nanoscale and how finite elements numerical calculations can simulate the behavior of light in such nano-resonators.

In Chapter (3), by exploiting the scanning near-field probe perturbation imaging technique, we report the sub-wavelength mapping of the electric or magnetic localized field component of light using dielectric tapered probes or aperture metal coated probes, respectively. The advent of artificial metamaterials operating at optical frequencies, in which the magnetic interaction with light can be as relevant as the electric response, makes it straightforward to simultaneously detect both the e.m. field components. We develop a plasmonic-based near-field probe to strongly enhance the collection efficiency and, more interestingly, to achieve an ultra-bright and sub-wavelength simultaneous detection of both the resonant electric and magnetic fields.

Photoluminescence based imaging methods, however, require optically active samples with the constrain of spectral and spatial matching between photonic mode and the light emitters, which may suffer from bleaching or blinking. Therefore, a pure optical method that can be applied on any kind of high quality factor nano-resonators to retrieve the confined modes distributions is actually missing. In order to achieve this goal we investigate the localized nanophotonic modes by developing a different approach. The experimental method, presented in Chapter (4), combines scanning near-field optical microscopy with resonant scattering spectroscopy, and it is called Fano-imaging. This technique largely extends the investigation of nanoscale localized light states, since it is applicable to nano-resonators based on any kind of material, even where light sources cannot be embedded. Moreover, resonant scattering experiments exhibit spectral Fano resonances, which correspond to the interference between light directly scattered from the sample and light scattered after being resonantly coupled to the localized mode. From the detailed analysis of Fano lineshapes it is possible to retrieve a deep sub-wavelength imaging of both the electric field intensity and the electric field spatial phase distribution, polarization resolved. Thus, we obtain unprecedented local information about the resonant light states.

In Chapter (5) we deeply investigate, both theoretically and experimentally, systems composed by coupled nano-resonators, called “photonic molecules”. In fact, light behavior in system based on multiple aligned photonic crystal nanocavities resembles the molecular interaction where the resulting normal modes exhibit energy splitting and spatial delocalization. This condition is achieved by an evanescent ph-

ton tunnelling. These structures represent a large research topic also for quantum optics. However, a fundamental requirement to create proper quantum-optics devices is the design and control of adjacent nanocavity modes at the target wavelengths, within an accuracy that is not experimentally obtainable due to the fabrication tolerances. The compensation of the fluctuations related to the structural disorder can lead to the control of the resonance wavelength of each resonator and of the tunnelling coefficient. In our analysis, we compare the interaction strength and the mode symmetry character of photonic molecules aligned along different lattice symmetry directions and composed by two or three photonic crystal nanocavities. Moreover, we theoretically evaluate the proper set of parameters to efficiently act on the coupling strength at the fabrication level or even with post-growing techniques. In particular, we develop a laser-assisted local oxidation of the dielectric environment in which the photonic cavities are fabricated. This oxidation induces a smooth and irreversible spectral shift of the resonant modes confined close to the laser spot. Therefore, the spatial selectivity of the post-fabrication technique is exploited not only to adjust the resonant wavelength of a given nano-resonator to a target value, but, more strikingly, to modify the coupling strength in photonic molecules. Finally, by comparing the case of two and three nano-resonators and next-nearest-neighbour coupling in array of photonic molecules.

The last part of the thesis deals with the engineering of light states localized in strongly scattering disordered media, as reported in Chapter (6). Light behavior in complex disordered systems attracts a lot of attention by fundamental physics as well as by technological applications involved in imaging through turbid media such as fog, clouds or living tissues. The occurrence of localized states in disordered media is a well-established phenomenon traced back to Anderson localization for electrons. However, the interaction between adjacent light sates driven by disorder has still to be completely understood. In Chapter (6) we demonstrate the possibility to engineer the confinement and the mutual interaction of modes in a two-dimensional disordered photonic structure. On one hand, the strong light confinement is achieved at the fabrication stage by an optimization of the design parameters. On the other hand, exploiting the local laser oxidation, we probe the interaction between overlapping localized modes, thereby paving the way for the creation of open transmission channels in strongly scattering media.



# Chapter 1

## Optics at the nanoscale

Until the second half of last century, the spatial resolution achievable by an optical microscope, even without any imperfections, was hampered to the diffraction limit. Only the development of new kinds of microscopes allowed for investigating object and light emitters down to a sub-wavelength scale. Here we report the basic principles of nanoscale optics. Firstly, by describing the limit imposed by light diffraction. Afterwards, by theoretically investigating and reviewing the methods largely employed to overcome this limitation and to achieve a sub-wavelength spatial resolution. We focus on detecting the optical near-field employing scanning microscopy, in particular we summarize the possible implementations and we introduce the most commonly used near-field probes.

### 1.1 The diffraction limit

The time when humans began to exploit the optical properties of materials to enlarge the vision of small or distant objects is traced back to centuries ago. As the scientific method was developed, both optics fundamental laws and technical achievements quickly enlarged the understanding of natural phenomena together with the instrument assisted eye perception. Likewise, the first prototype of an optical microscope (1610) is attributed to Galileo Galilei, however, only since the pioneering development of van Leeuwenhoek (1671) it was possible to observe red blood cells and bacteria gaining a few  $\mu\text{m}$  size resolution [1]. In the 1873 thanks to the advances of the theory of light waves Abbe, working at the Zeiss microscope factory, clarified that also an ideal microscope without any imperfections in the lenses or misalignments would not be able to overcome the physical resolution limit imposed by diffraction [2]. In particular, the Abbe's limit accounts for the smallest radial resolution ( $\Delta r_{//}$ ) obtainable in the image plane by an optical system that collects monochromatic light with vacuum-wavelength equal to  $\lambda$ :

$$\text{Min}[\Delta r_{//}] \approx \frac{0.61 \lambda}{n \sin \theta} \quad (1.1)$$

where  $n$  is the refractive index of the medium between the source and the microscope,  $\theta$  is the half-angle of the maximum light cone accepted by the lens, as reported in Fig. (1.1 a), and it is related to the numerical aperture of the optical system that is

defined as  $NA = n \sin\theta$ . The resolution of an optical microscope evaluated in Eq. (1.1) is defined as the shortest distance between two distinguishable points on a specimen that can still be observed as separate entities, following the Rayleigh criterion [3, 4]. In order to understand the basic imaging process let us consider the image formation of a point-like source (whose dimension are  $D \ll \lambda$ ), as schematically reported in Fig. (1.1 a). The incoming light is diffracted by the point-like specimen (S), as always happens when light encounters an obstacle, than it is once again diffracted by lens L, which mimics a generic microscopy objective. In the case of a finite size object, rays leaving with the same angle cross again exactly at the back focal plane  $\Sigma_F$ , and the finite object image appears in the conjugate plane  $\Sigma_I$  [5].

Abbe found by experimentation that a larger  $NA$  resulted in higher resolution, even though the apparent cone of incident light filled only a small portion of the lens. In fact, the entire size of L interacts with the diffracted light. Since  $NA$  can not be large enough to collect all the diffracted light ( $\theta < \pi/2$ ), the image recorded in  $\Sigma_I$  does not exactly correspond to the original object and it is blurred with the typical Airy disk intensity pattern shown in Fig. (1.1 b) [5]. The Airy disk is defined as the diffraction pattern created by a circular pupil of diameter  $D$ , uniformly illuminated. It consists on a central disk of angular radius  $1.22\lambda/D$ , surrounded by many alternatively dark and bright rings [6]. Therefore, in any finite optical system that detects e.m. radiation the image of a point-like light source is not a delta-like function but it is broadened as an Airy disk, which thus represents the point spread function. Abbe used the Airy disk properties to retrieve the net imaging resolution stated in Eq. (1.1), that is valid for every detector even with the highest collection efficiency. Moreover, any finite specimen can be schematized by a collection of point-like sources whose size is smaller than  $\lambda$ , consequently every time we use standard microscopy systems to perform images of small objects we inevitably loose information.

Although modern oil or solid immersion microscopes can achieve large equivalent  $NA$  up to 2.0 in the visible spectral range [7], Eq. (1.1) does not allow resolving an optical image with a sub-wavelength resolution ( $\Delta x \ll \lambda$ ), thus closely resembling and being related to the Heisenberg's uncertainty principle [8]. For instance, in the telecom window near-infrared spectral range the largest transparent  $NA$  is about 1.4 and gives a spatial resolution of  $\Delta x \approx 700$  nm.

### 1.1.1 Evanescent waves

As Maxwell equations were derived (1861), they entirely described the e.m. field behavior. But it took almost a century to discover a peculiar optical phenomenon that has put fundamental limits to any image reconstruction: this is the existence of e.m. evanescent waves in any diffraction process [9–11].

Evanescent e.m. waves are exact solutions of Maxwell wave-equations that do not propagate in space but exhibit an exponential decay of the amplitude. When total internal reflection occurs, they commonly describes light behavior in the low refractive index medium, as reported in Fig. (1.2 a). Evanescent waves do not deliver a net energy transfer. Only if frustrated total internal reflection takes place it is possible to

generate propagating waves in an high refractive index material close to the evanescent waves source (closely resembling the electrons tunnel effect), as shown in Fig. (1.2 b) [5]. Classical wave optics based on Huygens-Fresnel principle has a fundamental deficiency since it overlooks the role of evanescent waves in diffraction. In fact, the classical solution of diffraction problems are accurate in the radiation zone, but fails to reproduce what happens in close proximity to the light source.

In order to analyze the reason why, by collecting only propagating radiation with any kind of microscope (even an ideal one with  $\theta = \pi/2$ ), the image is always blurred, we exploit the argument based on the angular spectrum decomposition that is a noteworthy technique for describing optical fields in homogeneous media. Using this Fourier based characterization we can estimate the series expansion of an arbitrary field in terms of propagating and evanescent waves with variable amplitudes and directions. The description of the e.m. field radiated by a light source or scattered by an object, as shown in Fig. (1.3), evaluated by the angular spectrum representation in a arbitrary  $z = \text{const.}$  plane is [12]:

$$\mathbf{A}(\mathbf{r}, t) = \iint_{-\infty}^{\infty} \widehat{\mathbf{A}}(k_x, k_y, 0) \exp(ik_z z + ik_x x + ik_y y - i\omega t) dk_x dk_y \quad (1.2)$$

where  $\mathbf{A}(\mathbf{r}, t)$  represents either the electric ( $\mathbf{E}$ ) or the magnetic ( $\mathbf{H}$ ) field and  $\widehat{\mathbf{A}}(\mathbf{k})$  its Fourier transform; while  $\omega = 2\pi n c \lambda^{-1}$  is the angular frequency. Since the wavenumber is  $k = \sqrt{k_x^2 + k_y^2 + k_z^2}$ , the e.m. fields described by Eq. (1.2) have different behaviors in two complementary regimes in which the wavenumber component  $k_z$  is either real or imaginary.

$$k_x^2 + k_y^2 \leq \left(\frac{2\pi n}{\lambda}\right)^2 \Rightarrow k_z \in \mathbb{R} \quad (1.3)$$

$$k_x^2 + k_y^2 > \left(\frac{2\pi n}{\lambda}\right)^2 \Rightarrow k_z \in \mathbb{C} \quad (1.4)$$

Hence, for a purely dielectric medium with no losses, turns out that the factor  $\exp(ik_z z)$  is either an oscillatory or an exponentially decaying function if Eq. (1.3) or Eq. (1.4) respectively holds. Therefore, the angular spectrum is a superposition of both plane and evanescent waves. Remarkably, only if all the spatial frequencies  $(k_x, k_y)$  are collected it is possible to reconstruct without any distortions the field coming from the specimen by exploiting Eq. (1.2).

On the other hand, if the imaging system is sufficiently separated from the object, the contribution of the evanescent waves is negligible and only the low spatial frequencies, which satisfy Eq. (1.3), have to be considered. In other words, the image collected is a low pass filtered representation of the original field. By filtering out the high in plane spatial frequencies described by Eq. (1.4) we loose information about the object smallest details. In fact, dealing only with propagating waves the largest detectable in plane wavenumber  $k_{||} = 2\pi n \lambda^{-1} \sin\theta$ , where we consider also the practical limitation in collecting a given range of angles, as highlighted in Fig. (1.1 a).

Accordingly to the properties of conjugate variables of Fourier optics, which resembles the Heisenberg principle, the radial in plane uncertain  $\Delta r_{//} = \sqrt{(\Delta x)^2 + (\Delta y)^2}$  and the field finite angular spectrum  $\Delta k_{//}$  are related by:

$$\Delta k_{//}\Delta r_{//} \geq 1 \quad (1.5)$$

Hence, to achieve the minimum spatial uncertain the largest angular spectrum is needed, which corresponds to  $\Delta k_{//} = 2\pi NA\lambda^{-1}$ , giving for the ideal resolution:

$$\text{Min}[\Delta r_{//}] > \frac{\lambda}{2\pi NA} \quad (1.6)$$

Therefore, even if an objective may collect  $\theta = \pi/2$  it would not be able to interact with the evanescent waves and the specimen image would consequently still be incomplete. This limit is almost four times better with respect to Abbe's prediction of Eq. (1.1). In fact, Abbe required the paraxial approximation (small  $\theta$ ) and applied the arbitrary Rayleigh's criterion to the case of two parallel dipoles oriented perpendicular to the optical axis. Nevertheless, the two formulations must not be perceived as opposed but conveying the same straightforward result. Meaning that any standard microscope has a limited spatial resolution, which is about  $\Delta r_{//} \approx \lambda/2$ .

By performing and experiment in which also the evanescent waves are detected, an infinite bandwidth of spatial frequencies can, in principle, be achieved. But this kind of measurement requires to probe the e.m. fields in close proximity to the sample surface, where evanescent waves are not yet totally suppressed. From this analysis it is clear that two spatial regimes, which show very different light behaviors, are relevant for any imaging purpose:

Near-field	$r \ll \lambda$
Far-field	$\lambda < r$

where  $r$  is the distance between the specimen and the probe that collects the e.m. fields. The intermediate-field ( $r \sim \lambda$ ), also called "Fresnel-field", is the vaguely defined as the region in between the near-field and the far-field. In this region, near-field behavior ceases to be important and far-field effects become dominating.

The two extreme spatial regimes can be highlighted by studying the emission of a dipole, that is the smallest radiating e.m. unit source, which represents the first approximation of any antenna emission [13]. In the far-field the magnetic and the electric fields are, respectively:

$$\mathbf{B} = k^2(\mathbf{n} \wedge \mathbf{p}) \frac{\exp(i\mathbf{k} \cdot \mathbf{r})}{r} \quad (1.7)$$

$$\mathbf{E} = \mathbf{B} \wedge \mathbf{n} \quad (1.8)$$

where  $\mathbf{n} = (\mathbf{r}/r)$  is the unit vector of real space and the electric dipole moment is represented by  $\mathbf{p} = \int \mathbf{r} \rho(\mathbf{r}) d^3r$  with  $\rho(\mathbf{r})$  being the charges density. In the far-field region we find propagating spherical waves where both field radiation intensities

decrease as the square of distance. As in every propagating light wave, both fields described by Eq. (1.7) and Eq. (1.8) are strongly connected since each of them is generated by a variation of the other. Moreover, any absorption of the radiation does not feed back to the emitter. While in the near-field ( $kr \ll 1$ ) they become:

$$\mathbf{B} = ik(\mathbf{n} \wedge \mathbf{p})r^{-2} \quad (1.9)$$

$$\mathbf{E} = [3\mathbf{n}(\mathbf{n} \cdot \mathbf{p}) - \mathbf{p}]r^{-3} \quad (2.0)$$

Differently from the propagating regime, in the near-field region the electric and magnetic fields exist independently of each other, and one type of field can dominate the other. In particular, the magnetic induction is a factor  $kr$  smaller than the electric field. Moreover, the near-field components depend on the detailed properties of source. For instance, Eq. (1.10) coincides with the electrostatic dipole, and both decay very rapidly as a function of the distance. Consequently, in the since a finite emitter can be regarded as an ensemble of Hertzian dipoles, near-field components carry the information needed to determine the spatial distribution of any finite size emitter. In addiction, in the near-field region absorption of radiation does strongly affect the load on the emitter. For instance, the magnetic induction in a transformer can be seen as a simple model of near-field e.m. interaction.

In conclusion, it is straightforward that every time light is emitted or finds an obstacle and scatters there is a loss of information on propagating from the near-field region to the far-field. Optical techniques that allow near-field probing could improve the imaging hallmarks, reaching a sub-wavelength spatial resolution. However, the higher the spatial frequencies of an evanescent wave are, the faster the field decay along  $z$  will be. Therefore, unavoidable practical limitations always make the bandwidth finite.

## 1.2 Modern microscopy

Many fascinating and disruptive optical techniques have been proposed and developed through the last decades revolutionizing the field of optical microscopy by gaining a sub-wavelength spatial resolution. At first, we briefly review the most successful methods that exploit specific optical schemes by collecting only far-field radiation and afterwards we focus the attention on near-field detection that is the basic research topic discussed in this thesis.

Confocal microscopy was the first and simplest invention for increasing optical resolution and especially the signal-to-noise ratio [14]. It takes advantage of a spatial filtering performed by a pinhole placed in the conjugate plane of the specimen, so that light impinging the sample and light following the inverse path by passing through the pinhole have the same focus on the object plane as reported in Fig. (1.4 a). This geometry allows eliminating most of the out-of-focus light and prevents nearby scatterers from contributing to the detected signal. The confocal microscope must detect only light coming from one point at a time, therefore a scanning system is required for reconstructing two or three-dimensional images. The drawback is that the lateral resolution does not overcome the diffraction limit although in the vertical direction a

narrow depth of field is achieved with respect to standard microscopy [15]. Nevertheless, this non-invasive technique has gained popularity in biology, biophysics, semiconductor inspection and materials science, particularly for investigating thick specimens or buried samples [16].

On the other hand, the invention of pulsed laser radiation propelled the field of nonlinear optics enabling, for instance, the invention of multiphoton microscopy [17, 18]. With respect to confocal microscopy it offers the advantages of deeper penetration and less photodamage but has the disadvantage of requiring a non-linear medium and may damage the sample due to the high power laser excitation.

Recent advances in ultra-sensitive instrumentation have allowed for the detection, identification, and dynamic studies of single molecules in the condensed phase. This measurement capability provides a new set of tools to explore the frontiers in many scientific disciplines, such as chemistry, molecular biology, molecular medicine, and nanostructured materials. Optical detection of single molecules has been achieved by both frequency modulated absorption and laser-induced fluorescence. Since the latter exhibits lower background and higher signal-to-noise ratio, it is the more employed one [19, 20]. Highly fluorescent molecules have been synthesized that can be specifically attached to biological entities. This chemically specific labelling and the associated discrimination of different dyes based on their fluorescence emission allows scientists to visualize the interior of cells and study biochemical reactions in live environments.

Another noteworthy technique is the stimulated emission depletion (STED) microscopy, which provides super resolution by selectively deactivating fluorophores thus enhancing the imaging in a localized area [21, 22]. STED works by depleting specific regions of the sample while leaving a center focal spot active to emit fluorescence, leading to an improved resolution with respect to confocal microscopy as reported in Fig. (1.4 b). The focal area can be engineered by altering the properties of the pupil plane of the objective lens. In this context a sub diffraction method was also developed by using spatially structured illumination in a wide-field fluorescence microscope employing a series of different excitation light patterns [23].

Photoactivated localization microscopy (PALM) and stochastic optical reconstruction microscopy (STORM) have also proved to be super resolution microscopy techniques allowing to image specific proteins down to few nanometers and trajectories of single molecules [24–26]. They are both based on collecting under a fluorescent microscope a large number of images as a function of time, each containing just a few isolated stochastically activated fluorophores, resulting in a promising approach to distinguish neighboring molecules by separating their fluorescent emission in time. All these results recently gave to Betzig, Hell and Moerner the honour to be jointly awarded with the 2014 Nobel Prize in Chemistry [27].

A completely different approach was recently brought to the realm of device engineering by Pendry in his seminal work [28]. He proposed the realization of a “superlens” based on a metamaterial slab. Metamaterials are artificial material with both negative dielectric permittivity and negative magnetic permeability. As if the refrac-

tive index was negative, these engineered materials allows optical properties unavailable in naturally occurring substances, such as negative refraction, inverted Snell's law and Cherenkov radiation and optical cloaking [29–34]. The superlens is, in principle, able to gain a perfect resolution by retrieving all the information carried by evanescent waves, since in the transmission process they emerge from the metamaterial enhanced in amplitude after being resonantly coupled to surface plasmons, as shown in Fig. (1.4 c). Note that there is not any violation of energy conservation, since evanescent waves transport no energy, but nevertheless it is a surprising result confirmed by experiments that in the visible spectral range show a resolution down to  $\lambda/6$  [35, 36].

Instead of photons, by using electrons techniques to magnify objects down to the nanometer range have been developed by exploiting the shorter De Broglie wavelength of electrons, such as scanning electron microscope (SEM) or transmission electron microscope (TEM) [37, 38]. They involve an electron beam that generates a characteristic response from the sample surface (cathodoluminescence, back-scattered or secondary electrons) or is transmitted through an ultra-thin specimen, respectively.

Significant advances in instrumentation are pursued by the wide class of scanning probe microscopes, where a small probe tip is brought into intimate contact with the sample surface without damaging it. The presence of the specimen manifests itself as a tunnel current flowing between the tip and the sample in scanning tunneling microscopes (STM) or as a deflection in the tip-height during the scanning in atomic force microscopes (AFM) [39, 40]. Both techniques push the spatial resolution beyond the Nanoscale and retrieve the image of single atoms. The former case provides a topographic picture of the surface by keeping the tunnel current constant and monitoring displacements of the metal tip given by the voltages applied to piezoelectric drives. Unfortunately, electron microscopes have to be operated in vacuum, which limits their application in life sciences, and requires special sample preparation. The AFM is a higher sensitivity tool designed to investigate both conductors and insulators down to the atomic scale. The typical AFM setup reported in Fig. (1.5 a) shows that the cantilever deflection is measured using a laser spot reflected from the top surface of the cantilever into an array of photodiodes. With this microscope images are obtained by measuring the force on a sharp tip (insulating or not) created by the proximity to the surface such as van der Waals forces, capillary forces, chemical bonding, electrostatic forces, magnetic forces and so on. This force is kept small and at a constant level with a piezoelectric based feedback mechanism to adjust the tip-to-sample distance, so that when the tip is moved sideways it follows the surface contours as is highlighted by the trace B in Fig. (1.5 b). Although these scanning techniques achieve a deep sub-wavelength resolution in mapping any sample topography, they cannot investigate or detect the light behavior in the same media and consequently retrieve the noteworthy spectral and dynamic properties of the sample.

Therefore, all the described methods are complementary to those presented in this work, since, on one hand, PALM and STED are based on standard optical microscopy instrumentation and rely on fluorescent labeling of the sample, on the other hand, TEM and AFM provide a high-resolution topography but cannot probe the sample optical response.

### 1.3 Scanning near-field optical microscopy

If AFM shear-force probe microscopy is combined with optical detection huge advantages can be achieved in the characterization of light emitting nanostructures and fluorescent molecules. The most striking example is near-field scanning optical microscopy (SNOM), in which the apex of a tapered or pulled optical fiber acts like a AFM tip, thus providing both optical and topographical information of the sampling surface. This integrated microscope works in close proximity with the sample surface, thus being strongly interacting with optical near-field and evanescent waves. Sub-wavelength imaging based on SNOM was experimentally tested for the first time in the visible spectral range more than 30 years ago by Pohl et al. employing aperture probes [41]. The principle of SNOM imaging operation relies on the point-by-point investigation by raster-scanning the local probe over the sample surface and recording at every position the corresponding optical signature. The local probe acts as an optical antenna, converting localized e.m. fields into radiation, and vice versa. Therefore, SNOM detection gives ultra-sensitive optical measurement beyond the diffraction limit and provides light behavior at the nanoscale, together with the topographical capability of the AFM imaging. Although the morphological performance is not as good as in cantilever based AFM, SNOM proved to be the state of the art technique for investigating nanostructures such as quantum wells, quantum dots, nanoresonators or for single molecules since it combines the excellent spectroscopic and temporal selectivity of classical optical microscopy with the sub-wavelength spatial resolution [42–44].

The concept of near-field optical microscopy was originally proposed in by Synge 1928 in a prophetic article, where he proposed an apparatus similar to the actual SNOM implementations [45]. A sub-wavelength aperture in an opaque plate placed in close proximity to the sample surface creates an illumination spot not limited by diffraction. Scanning the source along the surface and recording the transmitted, or reflected, light produces an image with subwavelength resolution. In fact, the resolution of such an image should be limited only by the size of the aperture and not by diffraction, as was also pointed out years later by Bethe studying the diffraction by small holes [46]. Only after the invention of the STM an efficient positioning technology was available at the nanoscale. Therefore an optical microscope similar to Synge's proposal was realized, firstly in the microwave by Nicholls and Ash, then in the visible spectral range simultaneously by Pohl et al. and Lewis et al. due to the obviously different fabrications difficulties demonstrating a sub-wavelength imaging with a resolution of  $\lambda/60$  and  $\lambda/20$ , respectively [41, 47, 48]. The key innovation was the fabrication of a sub-wavelength optical aperture at the apex of a sharply pointed transparent (quartz) probe tip whose sidewalls were coated by metal. Such sharp aperture replaces the Synge's opaque screen for experimental purposes. In addition, a feedback loop was implemented based on proper piezoelectric quartz tuning forks (later replaced by piezoelectric bimorph bender element) maintaining the tip-sample distance constant (at few nanometers) while raster scanning the sample surface [49]. SNOM technique was systematically advanced and extended over the years to various configurations that provide a sharp confined photon flux in the near-field region, as

summarized in Fig. (1.6 a-d). Aperture probes are used in near-field illumination or detection, as reported in Fig. (1.6 a-b), respectively, or in the case of a sufficiently strong signal they can be even employed in illumination/collection geometry, Fig. (1.6 c). The last one is the best suited for improving the spatial resolution, since it provides an almost background free illumination. These configurations are suited of employing aperture or dielectric probe which, by exploiting the frustrated total internal reflection that occurs at the fiber end, allow the conversion of evanescent waves with high spatial frequencies to e.m. fields propagating through the optical fiber and finally measured by a conventional far-field detector.

In Fig. (1.6 d) SNOM setup is based on sharply pointed apertureless tip (a-SNOM) that locally enhances light scattering. Both illumination and collection are in the far-field, therefore a-SNOM requires a sophisticated method for filtering out the huge background. Moreover, in order to enhance light scattering apertureless probes are commonly fabricated on high refractive index material, such as silicon, that would drastically perturb strongly localized optical modes, which are the basic topic of the research presented in this thesis.

In combination with time-resolved excitation and detection schemes, near-field microscopy has the potential to give direct access to processes on ultra-short time and length scales. Near-field microscopy has therefore all the advantages of conventional spectroscopy with a high spatial resolution solely defined by the probe size.

### 1.3.1 Probes design and fabrication

The fundamental parameter of a SNOM setup is the near-field probe, as it defines the spatial resolution, the amount of detected signal and the induced perturbation on a given sample. In this section, we review the basic near-field probe designs, fabrication method and optical properties focusing on those that will be mentioned in the thesis concerning the experiments discussion.

In e.m. theory an antenna is a device used to create e.m. waves with a well-defined radiation pattern, or to receive e.m. waves from a remote source in order to extract some encoded information, by measuring changes in their intensity, or by exploiting the transmitted power [50]. So antennas main ability relies in establishing efficient coupling between the near-field and the far-field by enhancing and concentrating the incoming fields and simultaneously allowing to control the directional emission of light sources placed in the near-field zone [51, 52]. Moreover, optical antenna can enhance light absorption, leading to advantageously photodetection and to photovoltaics applications [53]. Although antenna theory has been developed for the radio-frequency and the microwave range it holds great promise for inspiring new concepts in the optical frequency range. Therefore, the local SNOM probe can be viewed acting as an optical antenna, converting the investigated near-field into propagating radiation and vice-versa (because of reciprocity), with a net energy transfer efficiency that defines the antenna throughput. Standard aperture probes need a trade-off between spatial resolution versus throughput, since the transmission through a metal screen with a sub-wavelength hole of radius  $a$  scales as  $(a/\lambda)^4$ , with the same wavelength dependence of the Rayleigh scattering [46, 54, 55].

Many different near-field probe designs have been conceived and have been tested in the last decades. They can be grouped in four categories: *i*) dielectric, i.e. transparent, probes that are also called uncoated tips, *ii*) metal coated aperture probes, *iii*) pointed probes (used in a-SNOM setup), *iv*) probes functionalized by placing a nano emitter or a plasmonic nanoantenna at the tip apex.

### Dielectric probes

Dielectric tips are the fundamental class of near-field optical probes since they represent the key components for the fabrication of more complex probes. Tapering of dielectric optical fibers can be done by chemical etching, or by local heating and subsequent pulling.

A well established method for fabricating smooth dielectric tapered probes is the tube etching method [56, 57]. We exploit this recipe to produce by ourselves the dielectric probes employed the SNOM experiments that will be described in the thesis. Glass tip formation occurs inside a cylindrical cavity formed by the polymercoating of an optical glass-core fiber which is not stripped away prior to etching in aqueous 48% hydrofluoric acid (*HF*). The two basic steps of the etching mechanism are reported in Fig. (1.7 a-b). In the first one, the acid largely corrodes the lateral side of the fiber core with respect to the central part since at the rim of the glass cylinder *HF* supply occurs out of a larger volume as compared to the central region. As soon as the preliminary taper is formed, step convection driven by concentrations gradients that are influenced by the etching process itself and the gravitational removal of the reaction products delivers *HF* to the upper cone region. After about 90 minutes of tube-etching the fiber is rinsed with ethanol and successively the jacket is removed without damaging the cone. The solution is covered by an organic overlayer (isooctane) to protect the fiber against acid vapor. Moreover, since the etching process takes places inside a hollow cylinder formed by the protective jacket, it is less sensitive to environmental influences such as vibrations or temperature drifts. The procedure gives tapered probes with large cone angles (about 30°) and small apex (less than 100 nm size), resulting in a strong decrease of the loss region with respect to pulled probes [58], and low sidewall surface roughness, since the meniscus formed by the acid along the fiber does not move during the etching. Dielectric tips with reproducible shapes and optical performance are formed in a high yield, as the one reported in the SEM image of Fig. (1.7 c). Since glass is almost transparent in the visible and near-infrared spectral range, these tapered dielectric probes show a high throughput (more than 50%), thus being suited for the high-contrast illumination-collection geometry.

However, the drawback is the low spatial resolution in the direct imaging. This feature can be simply explained if we consider how the fundamental mode of the optical fiber interacts with the tapered apex and it is focused in the near-field. The tapered, conical part of the probe can be represented as a series of glass disks with decreasing diameters and infinitesimal thicknesses. With each step part of the radiation is reflected, and the transmitted mode becomes less confined, since the field extends more and more into the surrounding medium (air) and exhibits increasing losses. By

reciprocity, it is clear that dielectric probes collect not only evanescent waves in the near-field by frustrated total internal reflection at the tip apex, but also a considerable amount of the propagating e.m. far-field injected through the upper part of the cone. Therefore, by collecting also large  $k_{\parallel}$ , high throughput but poor spatial resolution are expected for uncoated probes and the use of such a probe is not always convenient.

### Coated aperture probes

Tapered rather than pulled glass based tips, after metal coating in high vacuum evaporator by sputtering, can be modeled to result in small well-defined apertures at the apex, showing good homogeneity and negligible leakage of light along the cone [12]. Typically the metal is an aluminum or sometimes a gold layer of about 100 nm thickness, but the former is preferred for the smallest skin depth in the visible spectrum. The aperture is formed by metal shadowing evaporation (that is rotating the probe along the cone axis during the coating process) and it is typically between 100 nm and 200 nm diameter size for balancing high resolution and good throughput, see Fig. (1.8 a) [59, 60].

A more sophisticated fabrication technique allows for obtaining a well-defined flat circular aperture with controllable diameter size down to 20 nm, by milling the coating with a focused ion beam (FIB) [61]. FIB is the state of the art method to build high quality nanoscale structures; however, it is a rather expensive and inherently slow technique. Significantly less expensive and reproducible procedures have been put forward for the reliable fabrication of aperture probes as controlled electrolysis, aperture punching, selective resin coating or by integrating a waveguide into the AFM cantilever making the most of established silicon engineering techniques [62–65].

The lateral metal coating avoids the leakages in the outer space thus confining the e.m. fields at the aperture. In fact, by approaching the tapered tip apex light is progressively confined, but exceeding a transverse diameter size smaller than the wavelength of the modes propagating in the fiber, all the sustained modes are back reflected or absorbed and dissipated by the metal and cannot propagate any further. For this reason, the sub-wavelength aperture probes introduce a diameter-size dependent cut-off causing only evanescent waves to escape, as highlighted in Fig. (1.8 b) [12, 60]. Of course, this characteristic gives an experimental extremely small throughput with respect to dielectric probes (with a ratio of about  $10^{-5}$ ) but allows to obtain high spatial resolution since only the near-field is excited/detected [66].

### Apertureless probes

Also by using narrow pointed apertureless probes, made of metal or high refractive index dielectric such as silicon, it is possible to retrieve optical information during the scan by exploiting the strong field enhancement in the proximity of the antenna that for gold tips is predicted to be very large, up to 50 [67]. Of course, the only available configuration is collecting in the far-field the scattered light tip-sample system that carries information about the near-field interaction, as shown in Fig. (1.6 d). The

illumination can be provided by standard microscopes as well as by evanescent waves from total internal reflection [68]. The optical signal is measured by inducing a modulation in the tip oscillations and performing homodyne or heterodyne interferometric detection using lock-in techniques in order to demodulate the beat signal at higher harmonics of the tip vibration; therefore the far field part can be suppressed effectively to discriminate the small scattered signal from the tip apex against the diffraction limited background, leading to a few nanometers resolution in the infrared spectral range [69–71].

### Functionalized probes

In order to manipulate and confine optical radiation at subwavelength scales a key improvement has been developed by integrating single light sources or nanostructured devices on the apex of standard probes. In this way a further nanoantenna is created on top of the near-field probe and a tremendous advancement in terms of spatial resolution, throughput and sensitivity is achieved.

On one hand, the modification of the spontaneous emission rate of an emitter placed in a nano-optical resonator device (Purcell effect [72]) can be monitored by grafting the light source at the end of a scanning probe, see Fig. (1.9 a), and then performing fluorescence lifetime measurements as a function of position [73, 74]. However, the disadvantage is that single nano-emitters may suffer of bleaching and/or blinking [75, 76].

On the other hand, thanks to high reliable nano-fabrication procedures which in most of the cases exploit FIB or electron-beam lithography, metal-based nano-antennas milled at the apex of standard probes are fabricated in order to achieve outstanding spatial resolution and bright near-field probes, thus overcoming the throughput constrain imposed by the aperture dimension, by squeezing the near-field by means of localized plasmons coupling [77].

It is a well known principle of microwave engineering that the most efficient way to couple far-field radiation to a device of dimension much smaller than the light wavelength is to connect the device to an antenna [50]. If we follow the parallelism with antenna theory, in the optical regime we need to introduce metal materials losses, however such losses may be compensated by collective electron resonances, i.e. surface plasmons [78]. In fact, the recent enormous advance in nano-imaging techniques coincided with the introduction of concepts from plasmonics, such as surface plasmon polaritons (SPPs) confinement along metal-dielectric interfaces, into the design of nearfield probes [79, 80]. SPPs are waves that propagate along the surface of a conductor. By altering the structure of a metal surface the SPP interaction with light can be tailored on demand, offering the potential for developing new types of photonic devices, making optical antennas particularly efficient at selected frequencies and broadening the perspectives of near-field optics. With respect to metallic coated probes, plasmonic functionalized tips exhibit either a better spatial resolution (at constant throughput) or larger throughput (at constant resolution). Several high-performance near-field probe geometries, in which plasmonic nanoantennas are included,

have been engineered and optimized both experimentally and theoretically with respect to size, shape and material in order to efficiently transform light from the far-field to the near-field and the other way round, and for increasing the radiation efficiency of nano-optical emitters [81–83].

Although the design of optical antennas is likely to be inspired by radio-frequency or microwave regime working geometries, it can be expected that the presence of new physical phenomena will demand the exploration of new structures and material compositions. The first developed plasmonic geometry was the renowned bow-tie nanoantenna that is constituted of two metal triangles facing each, as shown in Fig. (1.9 b), and optimizes the impedance matching, thus delivering high throughput and local field enhancement [84–86]. The practical realization on top of a scanning probe is performed by FIB, creating a bow-tie nano-aperture at the apex of a coated probe [87]. Other realizations are, for instance, mini-tip on aperture, single metal nanoparticle, see Fig. (1.9 c), and diabolo (complementary to the bow-tie) antenna structures have been grown on the end faces of aperture-type near-field probes [88–92]. However, all the reported functionalized probes rely on resonant structures with a limited spectral bandwidth that impose the spectral matching between the field enhancement effect and wavelength operation of the investigated sample.

In Chapter (3) we will discuss SNOM experiments performed with a recently developed next generation plasmonic nanoantenna, called “Campanile tip”. This near-field probe milled by FIB on top of a gold coated tip shows a broadband operation and allows us for mapping with unprecedented spatial resolution the influence on carrier recombination in local trap states within individual solid state emitters (quantum wires) as well as the simultaneous electric and magnetic field distributions confined in nanoresonators.

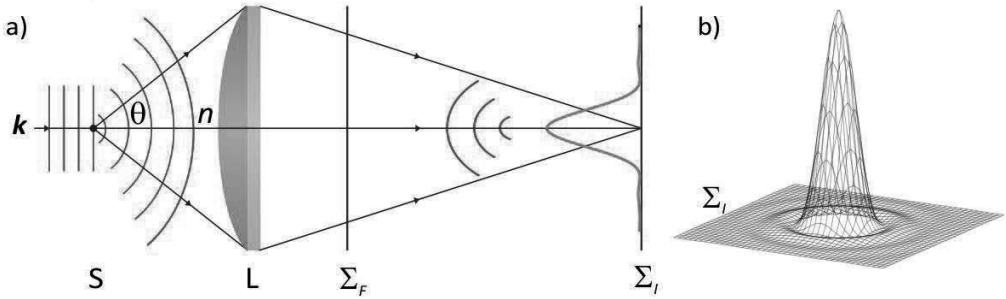


Figure 1.1: a) Schematics concerning the image formation on the plane  $\Sigma_I$  of a point-like object (S) illuminated by a monochromatic plane wave with wavevector  $\mathbf{k}$  performed by the optical system L (lens or objective).  $\theta$  is the half-angle of the maximum light cone accepted by L and  $\Sigma_F$  is the back focal plane. Red curves describe the behavior of radiation field wave front. The blue curve represents a one-dimensional profile cut of the Airy disk in  $\Sigma_I$ . b) Typical three-dimensional Airy disk intensity pattern representing the image of the point-like source in  $\Sigma_I$ .

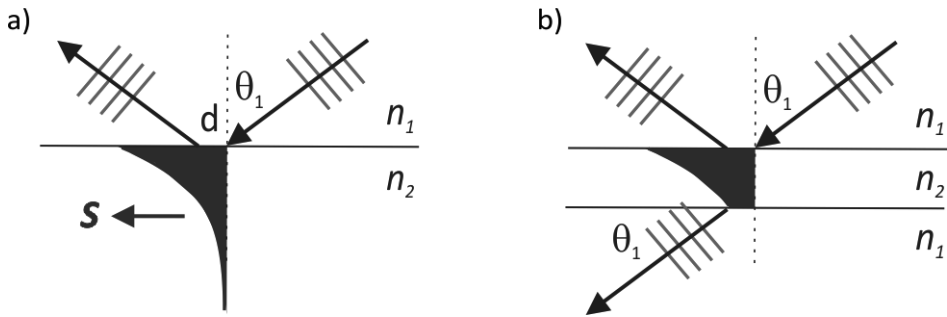


Figure 1.2: a) Total internal reflection at the interface between two media with  $n_2 < n_1$  if  $\theta_1 > \arctan(n_2/n_1)$ . The displacement  $d$  represents the Goos-Hänchen shift. The evanescent wave in  $n_2$  medium is schematically reported exhibiting a Poynting vector  $\mathbf{S}$  parallel to the interface. b) Frustrated total internal reflection occurs in a successive  $n_1$  medium placed in close proximity to  $n_2$  if the evanescent wave is not completely decayed.

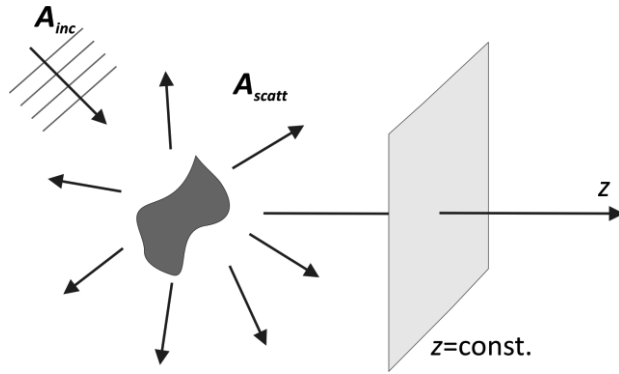


Figure 1.3: In the angular spectrum representation the e.m. fields are evaluated in a plane perpendicular to an arbitrarily chosen  $z$  axis. In this case we evaluate the total field  $\mathbf{A}_{inc} + \mathbf{A}_{scatt}$ .

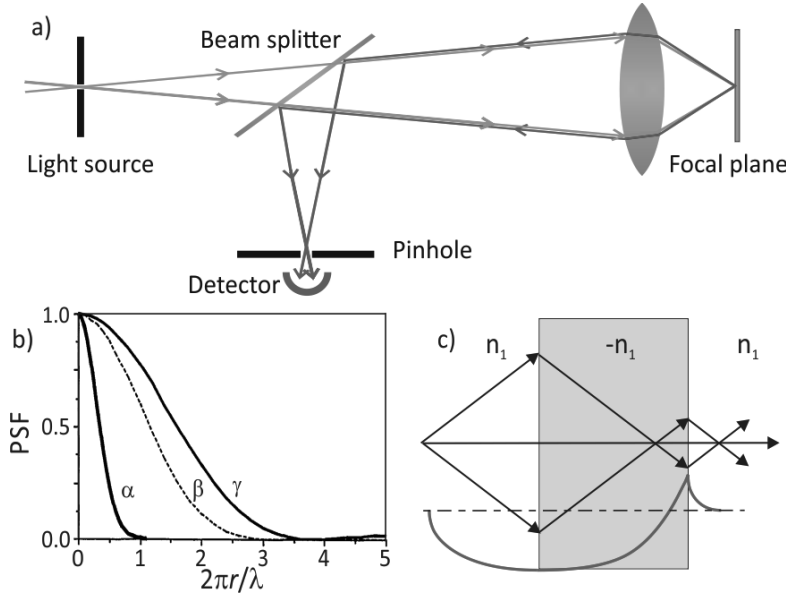


Figure 1.4: a) Principle of confocal microscopy: the pinhole in front of detector filters out the light that does not come from the focal spot. b) Comparison between normalized point spread function (PSF) of STED fluorescence microscope, confocal microscope and conventional scanning microscope reported by  $\alpha$ ,  $\beta$  and  $\gamma$  curves, respectively, as evaluated in [21]. c) Pendry's superlens principle of operation. Negative refraction occurs inside the negative refractive index media ( $-n_1$ ) leading to a double focusing inside and outside the slab. The red curve describes the evanescent wave decay in  $n_1$  and its amplification inside the superlens, so that in the image plane the initial evanescent wave amplitude is retrieved.

## Imaging and engineering optical localized modes at the nanoscale

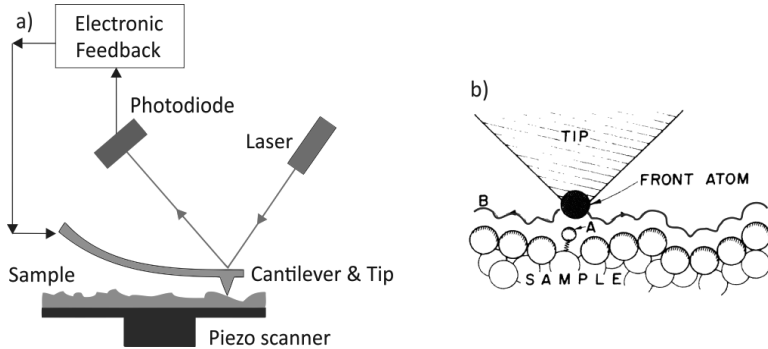


Figure 1.5: a) Principle of AFM microscopy: the tip attached to the cantilever scan the sample surface following the blue curve B reported in b), while the laser deflections are measured by a four-quadrant photodiode. The electronic feedback control assures a constant tip-sample distance. b) Zoom on the tip-sample gap that highlights the path scanned by the tip. Only the tip front atoms interact with the specimen [39].

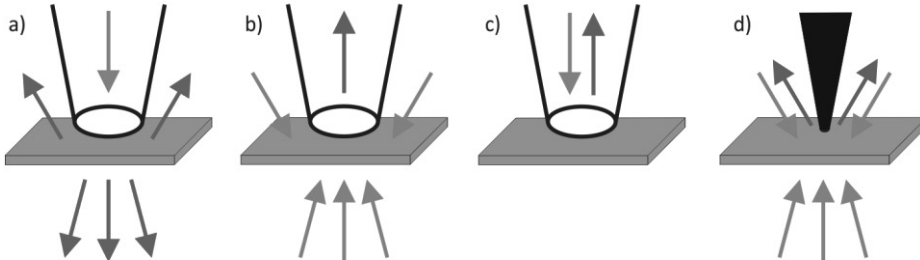


Figure 1.6: Schematics of the four more widespread SNOM configurations. a) Incoming light illuminates the sample in the near-field by means of an aperture probe and the scattered light is detected in far-field by standard microscopes. b) Complementary regime with respect of a): far-field illumination and near-field detection. c) Illumination/collection geometry in which both the near-field illumination and collection occur through the tip. d) Apertureless probe enhances the scattering in the near-field, whose information are analyzed by far-field detection.

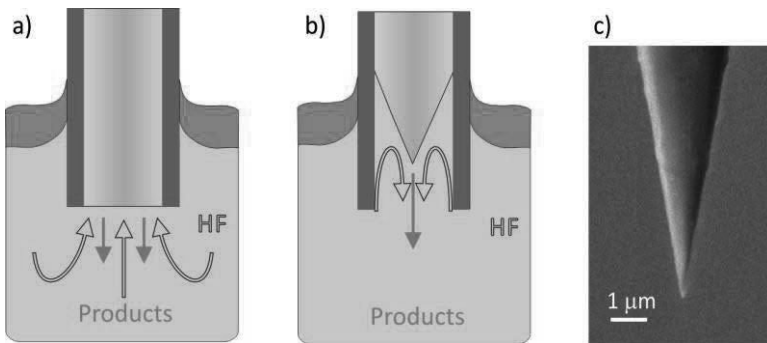


Figure 1.7: Dielectric tapered fiber etching process in aqueous hydrofluoric acid [56]. a) First etching step: diffusive motion of the *HF* solution. b) Second etching step: convective motion of the *HF* solution. c) SEM image of an etched dielectric tapered fiber.

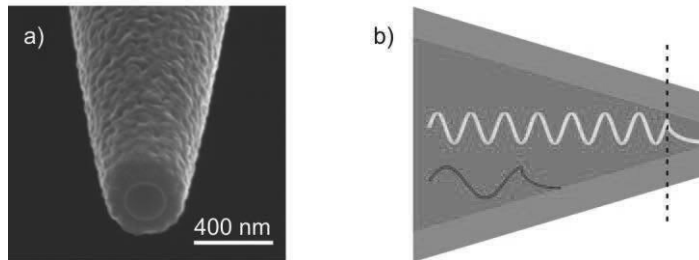


Figure 1.8: a) SEM image of an aluminum coated probe with a nominal aperture of 200 nm crated by shadowing evaporation, which is commercially available by the company LovaLite. b) Aperture probe lateral view schematics. It is highlighted the cutoff of the propagating modes when they approach the tip apex with an aperture size smaller than  $\lambda$  that allows only evanescent waves to escape.

Imaging and engineering optical localized modes at the nanoscale

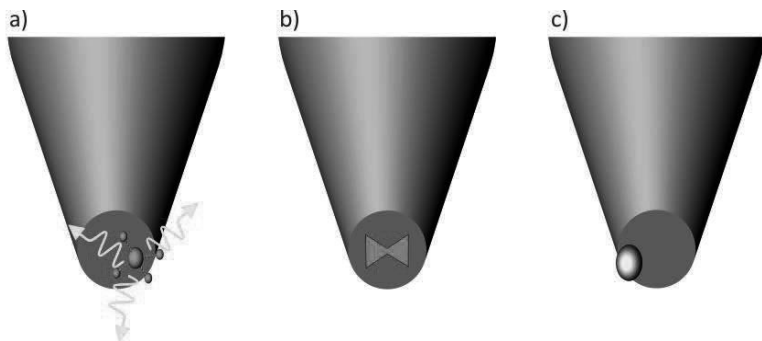


Figure 1.9: Schematics of functionalized near-field probes. a) Single molecule light source grafted at the end of the tip. b) Bow-tie aperture at the apex of a metal coated probe. c) Gold nanoparticle at the tip apex acts like a plasmonic nanoantenna.

## References

- [1] M. Born and E. Wolf. Principles of Optics. Oxford: Pergamon, 6th edn. (1970).
- [2] E. Abbe. “Beiträge zur Theorie des Mikroskops und der mikroskopischen Wahrnehmung” In: Archiv f. Miroskop. Anat. 9, 1 (1873), pp. 413–468.
- [3] F. Lord Rayleigh. “Investigations in optics, with special reference to the spectroscope” In: Philos. Mag. (fifth series) 8, 49 (1879), pp. 261–274.
- [4] F. Lord Rayleigh. “On the theory of optical images with special reference to the microscope” In: Philos. Mag. 5 (1896), pp. 167–195.
- [5] E. Hecht. Optics. Adelphi university international edition, 4th edn., (2001).
- [6] G. Airy. “On the diffraction of an object glass with circular aperture” In: Trans. Camb. Phil. Soc. 5 (1834), pp. 283–291.
- [7] Q. Wu, G. Feke, R. Grober, and L. Ghislain. “Realization of numerical aperture 2.0 using a gallium phosphide solid immersion lens” In: Appl. Phys. Lett. 75, 26 (1999), pp. 4064–4066.
- [8] E. Stelzer and S. Grill. “The uncertainty principle applied to estimate focal spot dimensions” In: Opt. Commun. 173 (2000), pp. 51–56.
- [9] G. Toraldo di Francia. “Alcuni fenomeni di diffrazione trattati mediante il principio dell’interferenza inversa” In: Ottica 7 (1942), p. 117.
- [10] G. Toraldo di Francia. “Le onde evanescenti nella diffrazione” In: Ottica 7 (1942), p. 197.
- [11] M. Schaffner and G. Toraldo di Francia. “Microonde evanescenti generate per diffrazione” In: Il Nuovo Cimento 6, 2 (1949), pp. 126–130.
- [12] B. H. L. Novotny. Principles of Nano-Optics. Cambridge University Pr., (2006).
- [13] J. Jackson. Classical Electrodynamics. New York, John Wiley and Sons, 3th edn., (1998).
- [14] M. Minsky. “Memoir on inventing the confocal scanning microscope” In: Scanning. 10, 4 (1988), pp. 128–138.
- [15] R. Webb. “Confocal optical microscopy” In: Rep. Prog. Phys. 59 (1996), pp. 427–471.
- [16] T. Wilson. Confocal Microscopy. London: Academic Press, (1990).
- [17] W. Denk and W.W. Strickler J.H. “Two-Photon Laser Scanning Fluorescence Microscopy” In: Scanning. 248, 4951 (1990), pp. 73–76.
- [18] W. Zipfel, R. Williams, and W. Webb. “Nonlinear magic: multiphoton microscopy in the biosciences” In: Nat. Biotechnol. 21 (2003), pp. 1369–1377.
- [19] W. Moerner and L. Kador. “Optical detection and spectroscopy of single molecules in a solid” In: Phys. Rev. Lett. 62, 21 (1989), pp. 2535–2538.
- [20] W. Moerner and M. Orrit. “Illuminating Single Molecules in Condensed Matter” In: Science 283, 5408 (1999), pp. 1670–1676.

## Imaging and engineering optical localized modes at the nanoscale

- [21] S. W. Hell and J. Wichmann. “Breaking the diffraction resolution limit by stimulated emission: stimulated-emission-depletion fluorescence microscopy” In: Opt. Lett. 19, 11 (1994), pp. 780–782.
- [22] K. Willig, S. Rizzoli, V. Westphal, R. Jahn, and S. Hell. “STED microscopy reveals that synaptotagmin remains clustered after synaptic vesicle exocytosis” In: Nature 440 (2006), pp. 935–939
- [23] M. Gustafsson. “Surpassing the lateral resolution limit by a factor of two using structured illumination microscopy” In: J. Microsc. 198, 2 (2000), pp. 82–87.
- [24] E. Betzig, G. Patterson, R. Sougrat, O. Lindwasser, S. Olenych, J. Bonifacino, M. Davidson, J. Lippincott-Schwartz, and H. Hess. “Imaging Intracellular Fluorescent Proteins at Nanometer Resolution” In: Science 313, 5793 (2006), pp. 1642–1645.
- [25] S. Manley, J. Gillette, G. Patterson, H. Shroff, H. Hess, E. Betzig, and J. Lipincott-Schwartz. “High-density mapping of single-molecule trajectories with photoactivated localization microscopy” In: Nat. Methods 5 (2008), pp. 155–157.
- [26] M. Rust, M. Bates, and X. Zhuang. “Sub-diffraction limit imaging by stochastic optical reconstruction microscopy (STORM)” In: Nat. Methods 3 (2006), pp. 793–796.
- [27] Nobelprize.org. The Nobel Prize in Chemistry 2014. url: [http://www.nobelprize.org/nobel\\_prizes/chemistry/laureates/2014/](http://www.nobelprize.org/nobel_prizes/chemistry/laureates/2014/) (visited on 10/15/2014).
- [28] J. Pendry. “Negative Refraction Makes a Perfect Lens” In: Phys. Rev. Lett. 85, 18 (2000), pp. 3966–3969.
- [29] V. Veselago. “The electrodynamics of substances with simultaneously negative values of  $\epsilon$  and  $\mu$ ” In: Soviet Phys. Uspekhi 10, 4 (1968), pp. 509–514.
- [30] R. Shelby, D. Smith, and S. Schultz. “Experimental Verification of a Negative Index of Refraction” In: Science 292, 5514 (2001), pp. 77–79.
- [31] J. Pendry, A. Holden, D. Robbins, and W. Stewa. “Magnetism from Conductors and Enhanced Nonlinear Phenomena” In: IEEE Trans. Microw. Theory Tech. 47, 11 (1999), pp. 2075–2084.
- [32] M. Notomi. “Theory of light propagation in strongly modulated photonic crystals: Refraction-like behavior in the vicinity of the photonic band gap” In: Phys. Rev. B 62, 16 (2000), pp. 10696–10705.
- [33] J. Pendry, D. Schurig, and D. Smith. “Controlling Electromagnetic Fields” In: Science 312, 5781 (2006), pp. 1780–1782.
- [34] T. Ergin, N. Stenger, P. Brenner, J. Pendry, and M. Wegener. “Three-Dimensional Invisibility Cloak at OpticalWavelengths” In: Science 328, 5976 (2010), pp. 337–339.
- [35] N. Fang, H. Lee, C. Sun, and X. Zhang. “Sub-Diffraction Limited Optical Imaging with a Silver Superlens” In: Science 308, 5721 (2005), pp. 534–537
- [36] Z. Liu, S. Durant, H. Lee, Y. Pikus, N. Fang, Y. Xiong, C. Sun, and X. Zhang. “Far-Field Optical Superlens” In: Nano Letters 7, 2 (2007), pp. 403–408.

- [37] J. Goldstein, D. Newbury, P. Echlin, D. Joy, C. Fiori, and E. Lifshin. Scanning electron microscopy and X-ray microanalysis. A text for biologists, materials scientists, and geologists. English. Plenum Publishing Corporation, 1981.
- [38] D. Williams and C. Carter. The Transmission Electron Microscope. English. Springer US, 1996.
- [39] G. Binnig, C. Quate, and C. Gerber. “Atomic Force Microscope” In: Phys. Rev. Lett. 56, 9 (1986), pp. 930–933.
- [40] G. Binnig, H. Rohrer, C. Gerber, and E. Weibel. “Surface Studies by Scanning Tunneling Microscopy” In: Phys. Rev. Lett. 49, 1 (1982), pp. 57–61.
- [41] D. Pohl, W. Denk, and M. Lanz. “Optical stethoscopy: Image recording with resolution  $\lambda/20$ ” In: Appl. Phys. Lett. 44 (1984), pp. 651–653.
- [42] E. Betzig and J. Trautman. “Near-Field Optics: Microscopy, Spectroscopy, and Surface Modification Beyond the Diffraction Limit” In: Science 257, 5067 (1992), pp. 189–195.
- [43] R. Grober, T. Harris, J. Trautman, E. Betzig, W. Wegscheider, L. Pfeiffer, and K. West. “Optical spectroscopy of a GaAs AlGaAs quantum wire structure using near-field scanning optical microscopy” In: Appl. Phys. Lett. 64, 11 (1994), pp. 1421–1423
- [44] E. Betzig and R. Chichester. “Single Molecules Observed by Near-Field Scanning Optical Microscopy” In: Science 262, 5138 (1993), pp. 1422–1425.
- [45] E. Synge. “A suggested method for extending microscopic resolution into the ultra-microscopic region” In: Philos. Mag. 6, 35 (1928), pp. 356–362.
- [46] H. Bethe. “Theory of Diffraction by Small Holes” In: Phys. Rev. 66, 7-8 (1944), pp. 163–182.
- [47] E. Ash and G. Nicholls. “Super-resolution Aperture Scanning Microscope” In: Nature 237 (1972), pp. 510 –512.
- [48] A. Lewis, M. Isaacson, A. Harootunian, and A. Murray. “Development of a 500Å spatial resolution light microscope: light is efficiently transmitted through  $\lambda/16$  diameter apertures” In: Ultramicroscopy 13, 3 (1972), pp. 227 –231.
- [49] K. Karrai and R. Grober. “Piezoelectric tip-sample distance control for near field optical microscopes” In: Appl. Phys. Lett. 66, 14 (1995), pp. 1842–1844.
- [50] B. C.A. Antenna Theory: Analysis and Design. New York: Wiley, 2nd edn., (1997).
- [51] K. Crozier, A. Sundaramurthy, G. Kino, and C. Quate. “Optical antennas: Resonators for local field enhancement” In: J. Appl. Phys. 94, 7 (2003), pp. 4632–4642.
- [52] T. Taminiau, F. Stefani, F. Segerink, and N. van Hulst. “Optical antennas direct single-molecule emission” In: Nat. Photon. 2 (2008), pp. 234–237.
- [53] L. Novotny and N. van Hulst. “Antennas for light” In: Nat. Photon. 5 (2011), pp. 83–89.
- [54] C. Bouwkamp. “Diffraction Theory” In: Rep. Prog. Phys. 17, 1 (1954), p. 35.
- [55] F. G. de Abajo. “Light transmission through a single cylindrical hole in a metallic film” In: Opt. Express 10, 25 (2002), pp. 1475–1484.

## Imaging and engineering optical localized modes at the nanoscale

- [56] R. Stöckle, C. Fokas, V. Deckert, R. Zenobi, B. Sick, B. Hecht, and U. Wild. “High-quality near-field optical probes by tube etching” In: *Appl. Phys. Lett.* 75, 2 (1999), pp. 160–162
- [57] P. Lambelet, A. Sayah, M. Pfeffer, C. Philipona, and F. Marquis-Weible. “Chemically etched fiber tips for near-field optical microscopy: a process for smoother tips” In: *Appl. Opt.* 37, 31 (1998), pp. 7289–7292
- [58] G. Valaskovic, M. Holton, and G. Morrison. “Parameter control, characterization, and optimization in the fabrication of optical fiber near-field probes” In: *Appl. Opt.* 34, 7 (1995), pp. 1215–1228.
- [59] F. Intonti. “Near-field optical spectroscopy of disorder in semiconductor nanostructures” PhD thesis. Germany: Humboldt University of Berlin, 2002, p. 50.
- [60] B. Hecht, U. Sick B.and Wild, V. Deckert, R. Zenobi, O. J. Martin, and D. Pohl. “Scanning near-field optical microscopy with aperture probes: Fundamentals and applications” In: *J. Chem. Phys.* 112, 18 (2000), pp. 7761–7774.
- [61] J. Veerman, A. Otter, L. Kuipers, and N. van Hulst. “High definition aperture probes for near-field optical microscopy fabricated by focused ion beam milling” In: *Appl. Phys. Lett.* 72, 24 (1998), pp. 3115–3117.
- [62] D. Haefliger and A. Stemmer. “Subwavelength-sized aperture fabrication in aluminum by a self-terminated corrosion process in the evanescent field” In: *Appl. Phys. Lett.* 80, 18 (2002), pp. 3397–3399.
- [63] T. Saiki and K. Matsuda. “Near-field optical fiber probe optimized for illuminationcollection hybrid mode operation” In: *Appl. Phys. Lett.* 74, 19 (1999), pp. 2773–2775.
- [64] S. Mononobe, M. Naya, T. Saiki, and M. Ohtsu. “Reproducible fabrication of a fiber probe with a nanometric protrusion for near-field optics” In: *Appl. Opt.* 36, 7 (1997), pp. 1496–1500.
- [65] R. Eckert, J. Freyland, H. Gersen, H. Heinzelmann, G. Schürmann, W. Noell, U. Staufer, and N. de Rooij. “Near-field fluorescence imaging with 32 nm resolution based on microfabricated cantilevered probes” In: *Appl. Phys. Lett.* 77, 23 (2000), pp. 3695–3697.
- [66] T. Saiki, S. Mononobe, M. Ohtsu, N. Saito, and J. Kusano. “Tailoring a hightransmission fiber probe for photon scanning tunneling microscope” In: *Appl. Phys. Lett.* 68, 19 (1996), pp. 2612–2614
- [67] Y. Martin, H. Hamann, and H. Wickramasinghe. “Strength of the electric field in apertureless near-field optical microscopy” In: *J. Appl. Phys.* 89, 10 (2001), pp. 5774–5778.
- [68] S. Patanè, P. Gucciardi, M. Labardi, and M. Allegrini. “Apertureless near-field optical microscopy” In: *Rivista del Nuovo Cimento* 27, 1 (2004), pp. 1–46.
- [69] B. Knoll, F. Keilmann, A. Kramer, and R. Guckenberger. “Contrast of microwave near-field microscopy” In: *Appl. Phys. Lett.* 70, 20 (1997), pp. 2667–2669.

- [70] J. Chen, M. Badioli, P. Alonso-Gonzalez, S. Thongrattanasiri, F. Huth, J. Osmond, M. Spasenovic, A. Centeno, A. Pesquera, P. Godignon, A. Z. Elorza, N. Cama, F. J. G. de Abajo, R. Hillenbrand, and F. Koppens. “Optical nanoimaging of gate-tunable graphene plasmons” In: *Nature* 487 (2012), pp. 77–81.
- [71] M. Schnell, A. García-Etxarri, A. Huber, K. Crozier, J. Aizpurua, and R. Hillenbrand. “Controlling the near-field oscillations of loaded plasmonic nanoantennas” In: *Nat. Photon.* 3 (2009), pp. 287–291.
- [72] E. Purcell. “Spontaneous emission probabilities at radio frequencies” In: *Phys. Rev.* 69 (1946), p. 681.
- [73] M. Frimmer, Y. Chen, and A. Koenderink. “Scanning Emitter Lifetime Imaging Microscopy for Spontaneous Emission Control” In: *Phys. Rev. Lett.* 107, 12 (2011), p. 123602.
- [74] V. Krachmalnicoff, D. Cao, A. Cazé, E. Castanié, R. Pierrat, N. Bardou, S. Collin, R. Carminati, and Y. D. Wilde. “Towards a full characterization of a plasmonic nanostructure with a fluorescent near-field probe” In: *Opt. Express* 21, 9 (2013), pp. 11536–11545.
- [75] M. Nirmal, B. Dabbousi, M. Bawendi, J. Macklin, J. Trautman, T. Harris, and L. Brus. “Fluorescence intermittency in single cadmium selenide nanocrystals” In: *Nature* 383 (1996), pp. 802–804.
- [76] W. van Sark, P. Frederix, A. Bol, H. Gerritsen, and A. Meijerink. “Blueing, Bleaching, and Blinking of Single CdSe/ZnS Quantum Dots” In: *ChemPhysChem* 3, 10 (2002), pp. 871–879.
- [77] P. Biagioni, J.-S. Huang, and B. Hecht. “Nanoantennas for visible and infrared radiation” In: *Rep. Prog. Phys.* 75, 2 (2012), p. 024402.
- [78] W. Barnes, A. Dereux, and T. Ebbesen. “Surface plasmon subwavelength optics” In: *Nature* 424 (2003), pp. 824–830.
- [79] A. Zayats, I. Smolyaninov, and A. Maradudin. “Nano-optics of surface plasmon polaritons” In: *Phys Rep.* 408, 3-7 (2005), pp. 131 –314.
- [80] J.-C. Weeber, J. Krenn, A. Dereux, B. Lamprecht, Y. Lacroute, and J. Goudonnet. “Near-field observation of surface plasmon polariton propagation on thin metal stripes” In: *Phys. Rev. B* 64, 4 (2001), p. 045411.
- [81] S. Kühn, U. Håkanson, L. Rogobete, and V. Sandoghdar. “Enhancement of Single-Molecule Fluorescence Using a Gold Nanoparticle as an Optical Nanoantenna” In: *Phys. Rev. Lett.* 97, 1 (2006), p. 017402.
- [82] L. Neumann, Y. Pang, A. Houyou, M. Juan, R. Gordon, and N. van Hulst. “Extraordinary Optical Transmission Brightens Near-Field Fiber Probe” In: *Nano Lett.* 11, 2 (2011), pp. 355–360.
- [83] J. Farahani, D. Pohl, H.-J. Eisler, and B. Hecht. “Single Quantum Dot Coupled to a Scanning Optical Antenna: A Tunable Superemitter” In: *Phys. Rev. Lett.* 95, 1 (2005), p. 017402.
- [84] R. Grober, R. Schoelkopf, and D. Prober. “Optical antenna: Towards a unity efficiency near-field optical probe” In: *Appl. Phys. Lett.* 70, 11 (1997), pp. 1354–1356.

## Imaging and engineering optical localized modes at the nanoscale

- [85] P. Schuck, D. Fromm, A. Sundaramurthy, G. Kino, and W. Moerner. “Improving the Mismatch between Light and Nanoscale Objects with Gold Bowtie Nanoantennas” In: *Phys. Rev. Lett.* 94, 1 (2005), p. 017402.
- [86] A. Kinkhabwala, Z. Yu, S. Fan, Y. Avlasevich, K. Müllen, and W. Moerner. “Large single-molecule fluorescence enhancements produced by a bowtie nanoantenna” In: *Nat. Photon.* 3 (2009), pp. 654–657.
- [87] M. Mivelle, I. Ibrahim, F. Baida, G. Burr, D. Nedeljkovic, D. Charraut, J.-Y. Rauch, R. Salut, and T. Grosjean. “Bowtie nano-aperture as interface between near-fields and a single-modefiber” In: *Opt. Express* 18, 15 (2010), pp. 15964–15974.
- [88] H. Frey, F. Keilmann, A. Kriele, and R. Guckenberger. “Enhancing the resolution of scanning near-field optical microscopy by a metal tip grown on an aperture probe” In: *Appl. Phys. Lett.* 81, 26 (2002), pp. 5030–5032.
- [89] T. Taminiua, R. Moerland, F. Segerink, L. Kuipers, and N. van Hulst. “ $\lambda/4$  Resonance of an Optical Monopole Antenna Probed by Single Molecule Fluorescence” In: *Nano Lett.* 7, 1 (2007), pp. 28–33.
- [90] T. van Zanten, M. Lopez-Bosque, and M. Garcia-Parajo. “Imaging Individual Proteins and Nanodomains on Intact Cell Membranes with a Probe-Based Optical Antenna” In: *Small* 6, 2 (2010), pp. 270–275.
- [91] T. Kalkbrenner, U. Håkanson, A. Schädle, S. Burger, C. Henkel, and V. Sandoghdar. “Optical Microscopy via Spectral Modifications of a Nanoantenna” In: *Phys. Rev. Lett.* 95, 20 (2005), p. 200801.
- [92] T. Grosjean, M. Mivelle, F. Baida, G. Burr, and U. Fischer. “Diabolo Nanoantenna for Enhancing and Confining the Magnetic Optical Field” In: *Nano Lett.* 11, 3 (2011), pp. 1009–1013.

## **Chapter 2**

### **Nanophotonics localized fields**

The nano-photonics research field has been quickly growing since the introduction of artificial photonic crystal media engineered at the nanoscale. In particular, photonic crystal cavities fabricated on semiconductor slab are the state of the art devices to strongly localize light fields in volumes comparable to  $(\lambda/n)^3$  acting as efficient nano-resonators. They provide an efficient mechanism for controlling and inhibiting spontaneous light emission, for reducing almost to zero the light group velocity and they can also be easily included in all-optical integrated circuits. Here, we describe the basic properties of photonic crystal nanocavities. In particular, how, on one hand, SNOM techniques can experimentally probe the e.m. optical fields localized at the nanoscale and, on the other hand, how finite elements numerical calculations can simulate the behavior of light in such nano-resonators. In addiction, we address also the description of optical nano-resonators based on disordered arrangements of light scatterers. In these systems the interference between all the possible photon random-walks, due to multiple scattering, gives rise to random spatially and spectrally placed finite quality factor nanocavities.

### **2.1 Photonic crystal nanoresonators**

#### **2.1.1 Photonic crystals**

Nowadays, the most widespread and versatile devices conceived to mold the flow of light at the nanoscale are represented by artificial photonic crystals, which were introduced to the scientific community in the 1987 [1, 2]; although a century before Lord Rayleigh already studied a simplified analogous structure [3]. Photonic crystals are low-loss dielectrics systems in which a periodic modulation of the refractive index, with a period comparable to  $\lambda$ , is present. Dielectric modulation can be created along one, two or even three spatial dimensions thus defining 1D, 2D or 3D photonic crystals, respectively. As the ions in solid state materials occupy defined lattice positions inducing an effective periodic potential to electron wavefunctions, the refractive index arrangement defines a lattice that gives the name to this engineered periodic crystal, in which the e.m. fields experience an effective periodic potential [4].

Due to the multiple scattering of light at the dielectric interfaces, interference phenomena deeply affect the the e.m. wave propagation inside photonic crystals. By engineering different periodic modulation geometry and also by altering the amplitude

of the refractive index contrast it is possible, for instance, to prevent light from propagating inside the photonic crystal in certain directions and with specified wavelength. Therefore, being fully back-reflected when it shine on the photonic crystal external surface [4]. Even though, the behavior of electrons in semiconductors is different with respect the light propagation in photonic crystals the analogy can include Bloch formalism since photonic band-gaps resemble the electrons energy band-gap in semiconductors [5]. If the lattice potential is strong enough the photonic energy gap can extend over all possible directions, resulting in a complete photonic band-gap, as it happens in semiconductors for electron energy between the valence and the conduction band [6–8].

Since fabricating photonic crystals in the optical spectral range requires a dielectric modulation of the order of  $(\lambda/n)$ , it is mandatory a huge technical effort, especially in three-dimensional geometries. Due to the enormous progress in lithographic techniques established over the past decades for engineering semiconductor systems, fabrication resolutions down to few nanometers size are today attainable, allowing the manufacturing of high quality and high refractive index contrast photonic crystals operating at optical frequencies [9].

In this context, it is not surprising that nature has beaten us to the draw, since 3D photonic crystals can be largely found. In fact, they are responsible for the structural color that, as opposed to colors resulting from absorption by chemical pigments, enables the bright and iridescent long-lasting colors owned, for instance, by a large variety of butterflies, peacocks, jellyfishes and other animals (profitably due to millions of years lasting evolution) as well as by some opals and berry fruits [10–13].

The description of light behavior in photonic crystals must involve the solution of Maxwell's equations in a periodic dielectric medium. The usual simplified hypothesis are the absence of e.m. sources, homogeneous and neutral linear dielectric media (with a magnetic permeability  $(\mu_r = 1)$  so that the dielectric constant  $(\epsilon = n^2)$  is a scalar, which depends only on the spatial coordinate. After factorizing the temporal evolution, it follows that the magnetic field has to satisfy the Master equation (in *c.g.s* units) [4]:

$$\left\{ \nabla \wedge \frac{1}{\epsilon(\mathbf{r})} \wedge \right\} \mathbf{H}(\mathbf{r}) = \left( \frac{\omega}{c} \right)^2 \mathbf{H}(\mathbf{r}) \quad (2.1)$$

while the corresponding electric field can be evaluated as  $\mathbf{E}(\mathbf{r}) = (i\omega/c) \wedge \mathbf{H}(\mathbf{r})$ . Solving Eq. (2.1) is equivalent to an eigenvalues problem for each field component, like the stationary Schrödinger equation. Therefore, if  $\epsilon(\mathbf{r})$  is perfectly periodic the solutions of Eq. (2.1) are characterized by a wavevector  $\mathbf{k}$  and a band index  $n$ :

$$\mathbf{H}(\mathbf{r}, t) = \mathbf{H}_{k,n}(\mathbf{r}) \exp(i\mathbf{k} \cdot \mathbf{r} - i\omega_{k,n}t) \quad (2.2)$$

where  $\mathbf{H}_{k,n}(\mathbf{r})$  has the same periodicity of the dielectric modulation  $\epsilon(\mathbf{r})$ . Eq. (2.2) does not differ for any translation in the  $k$ -space equal to an integer multiple of the reciprocal lattice wavevector.

A reliable fully-vectorial computational technique that allows to solve the Master equation in complex periodic structures is the plane wave expansion method (PWE).

By exploiting this method is can be easily calculated band structure (dispersion relation) of any specific photonic crystal geometries [14, 15]. The algorithm expands in terms of Fourier series along the reciprocal lattice vector the periodic Bloch functions that represent fields and dielectric permittivity. Of course, this Fourier expansion is truncated to a fixed number of terms, limiting the accuracy of the calculation. A notable example is the band diagram of a multilayer periodic in one dimension (1D photonic crystal) calculated by PWE, as reported in Fig. (2.1). The lower energy band is denominated dielectric-band since it represents modes whose electric field maxima mainly occur in the higher refractive index layer. On the other hand, the higher energy band is called air-band, since it describes modes showing electric field maxima in the lower refractive index layer (that is usually air). PWE predicts also the positions and the widths of photonic band-gaps.

The more convenient parameter to understand and quantify how photonic crystals mold the light behavior is the local optical density of e.m. states (LDOS) or  $\varrho(\mathbf{r})$ . This quantity, in analogy with solid-state physics, accounts for the number of available optical modes per unit of frequency and volume. Usually it is derived from the Green function of the e.m. system by taking the imaginary part of the trace of the Green dyadic summed over all the possible states [16]. Furthermore, it is a common strategy to discern between the electric and magnetic contribution and, especially when concerning light-matter interaction, to define partial LDOS for particular dipole directions. For instance, the electric LDOS average over all solid angle results:

$$\varrho(\mathbf{r}, \omega) = \sum_n \int_{1BZ} d\mathbf{k} \delta(\omega - \omega_{\mathbf{k},n}) |\mathbf{E}_{\mathbf{k},n}|^2 \quad (2.3)$$

Eq. (2.3) highlights the fact that electric (magnetic) LDOS is related to the intensity of the electric (magnetic) field associated to all the modes that exist at frequency  $\omega$ . Furthermore, it can be proved that LDOS is inversely proportional to the group velocity of light [5, 17]. In order to understand the differences in light propagation induced by the presence of a periodic dielectric modulation, we report the LDOS in vacuum:

$$\varrho_{vac}(\mathbf{r}, \omega) = \frac{\omega^2}{\pi^2 c^3} \quad (2.4)$$

that is homogeneous and isotropic. Otherwise, inside a photonic crystal the LDOS experiences a strong inhomogeneity. Remarkably, in correspondence of the photonic band-gap LDOS vanishes. Since the spontaneous emission rate of a light emitter, according to Fermi's golden rule, is proportional to the e.m. LDOS at the emitter's position, when the light source is located inside the photonic crystal and its energy emission lies in the photonic band-gap, the spontaneous emission can be fully suppressed. This was also the first Yablonovitch's idea, which led to the introduction of photonic crystals [1]. The LDOS is a crucial parameter in photonics because it is the only quantitative way to describe the continuous part of the spectrum of any system independently of the excitation mode. This means that the LDOS provides spectroscopic information that are intrinsically independent on the illumination mode.

Photonic crystals based devices have been a strong impact in a large variety of optical applications. Concerning optoelectronic, a noteworthy result is that in 1D photonic crystal Bragg reflection will occur and light with wavelength  $\lambda$  incident along the periodicity direction will be reflected back with nearly 100% efficiency if the layered media is a quarter-wave stack, that is the period of the medium formed by  $n_1$  and  $n_2$  is equal to  $(\lambda/2n_1 + \lambda/2n_2)$  [18]. So they are used in modern devices such as the highly efficient and selective dielectric mirrors, dielectric Fabry-Pérot filters, in distributed feedback lasers, low-loss waveguides and in photovoltaic applications [4, 19–23]. It is possible to engineer photonic crystals in order to control photons dispersion relation for achieving almost zero group velocity (“slow light” effect) to maximize radiation/matter interaction, leading also to novel thin-film solar cells [24, 25]; or for creating an environment where temporally narrow pulses can travel great distances without being extended or even being compressed, thus enhancing non-linear effects [26, 27]; or even for realizing optical metamaterials that exhibit a negative refractive index [28].

## 2D Photonic crystals on slab

Although fabrication breakthroughs in layer-by-layer deposition and in self assembly structures drastically improved the performances of 3D photonic crystals, there are still large difficulties in obtaining efficient, reproducible, cost-effective devices exhibiting a three-dimensional modulation at the nanoscale [29]. In order to overcome these limitations the well-established manufacturing techniques that employ semiconductor nanostructures has been emerged as a powerful tool to manipulate light in the three dimensions without the need to create 3D photonic crystals [30]. Fabricating 2D photonic crystals on a semiconductor slab suspended in air, with a thickness comparable to the in plane lattice constant, represents a smart strategy to solve the issue. In the out-of-plane direction, the slab structure provides an index guiding by total internal reflection, as in standard optical fibers. The amount of light that escapes from the 2D photonic crystal plane radiates outside the “light cone” ( $a/\lambda = ak_{\parallel}/2\pi n$ ). In Fig. (2.2 a) is reported the design of a 2D photonic crystal of air holes arranged on a hexagonal lattice with a filling fraction ( $f$ , defined as the ratio between the area occupied by voids and the area occupied by dielectric medium in the unit cell) equal to 35%. The relative PWE calculated energy band diagram is reported in Fig. (2.2 b) in the first Brillouin zone, where the high symmetry points of reciprocal space are  $\Gamma = (0, 0)$ ,  $M = (\pi/a, \sqrt{3}\pi/3a)$  and  $K = (4\pi/3a; 0)$ . It shows a photonic band-gap beneath the light line for the TE-like modes only, which exhibit a magnetic field mostly orthogonal to the slab plane. Actually, in a real slab only TE-like modes can be defined. While pure TE modes, with the magnetic field exactly orthogonal to the slab plane, exist only for pure 2D systems. In fact, the slab symmetry causes the modes to be purely transverse only in the mirror plane of the vertical direction, i.e. in the middle of the slab. In conclusion, the realization of 2D photonic crystal hybrid slab structures allows to discard the quest for a periodicity in three dimensions and for a complete band-gap, since it conveys all the advantages of photonic crystal into standard light-guiding devices.

A further advantage of 2D photonic crystals is that nanoscale fabrication can easily induce in them intentional and reproducible defects in the periodicity that can locally sustain strong light confinement. In the thesis we will deal only with 2D photonic crystal on slab based devices, in particular we will focus the attention on hexagonal lattice of air holes just like the one reported in Fig. (2.2).

### 2.1.2 Photonic crystal nanocavity

The e.m. fields, solutions of Maxwell's equations Eq. (2.1), with energies inside the band-gap do not propagate in the photonic crystal. Nevertheless they are present as oscillating evanescent waves (whose intensity decay exponentially with superimposed an oscillatory behavior) [31]. The scheme of permitted and prohibited modes can be altered by introducing a narrow bandwidth and spatially localized mode inside the photonic band-gap if the discrete translational symmetry, typical of photonic crystals, is broken by perturbing even a single site lattice, that corresponds to a defect in the periodic lattice. In fact, the LDOS becomes strongly modified in the close proximity of such defects and can be enhanced by many orders of magnitude. Consequently, the local symmetry breaking can trap light of a given  $\lambda$  and behaves just like an optical cavity, being surrounded by perfectly reflecting walls due to the photonic band-gap. The analysis of the LDOS in a photonic crystal modified by the presence of defects tighten the analogy with semiconductor physics, where the doping is a common technique able to introduce discrete energy modes inside the forbidden band-gap. In photonics, if the defect involves removal of dielectric then the localized mode in the cavity evolves from the dielectric-band (lower-energy) and can be made sweeping across the band-gap by adjusting the amount of dielectric removed. Similarly, if the defect involves an addition of extra dielectric material then the cavity mode drops down from the air-band (higher energy) [4]. Therefore, acting on the defect geometry and on the refractive index it is possible to tune the localized mode wavelength to a target level inside the band-gap. There have been developed many types of photonic nanoresonators, most of them rely on planar photonic crystal on slab and a complete review can be found in [32]. We will deal with photonic crystal nanocavities (PCN) formed by the removal of one or more air holes in a 2D photonic crystal slab analogous of the one reported in Fig. (2.2). The typical volume occupied by such cavity modes can be very small, of the order of  $V = (\lambda/n)^3$ , and the quality factor  $Q = \lambda/\Delta\lambda$  (where  $\Delta\lambda$  is the resonant mode linewidth) can become sufficiently large, up to  $10^6$  [33]. The most widespread type of PCN consists on the absence of three adjacent holes along the unit cell direction, denominated L3 cavity [34].

In order to achieve ultra-high  $Q$ , it has been proved that the PCN realization should confine light gently to be effective, meaning the defect must not be an abrupt hole removal or hole filling. For instance, by inducing a displacement on the air holes that surround the L3 cavity the out-of-plane leakages are minimized since the field inside the light cone is reduced [33]. Also by carefully shifting more holes by superimposing one or more additional periodic lattices to the photonic crystals, it is possible to control the angular out-of-plane emission pattern by making the band-diagram fold

in the Brillouin zone and enhancing the  $Q$  [35]. Recently, exploiting a genetic optimization of the positions of few nearby cavity holes, a quality factor of the conventional L3 nanocavity that exceeds  $10^6$  was experimentally measured [36].

The realization of ultra-high  $Q$  and small mode volume PCNs is of the utmost relevance for a large research field that studies the interaction between a quantum emitter and a single radiation-field mode, called solid-state cavity quantum electrodynamics (CQED) [37, 38]. Experiments on atom-like emitters embedded in cavities can be described by elementary models, but reveal intriguing subtleties about the interplay of coherent dynamics with external couplings.

In the noteworthy case of interaction between localized cavity fields and atom-like emitters, schematized as dipole light sources, we can discern two different regimes: the weak-coupling, characterized by an interaction that is lower than both the emitter and cavity mode decay rates, and the strong-coupling where the light/matter interaction is strong enough that the two initial states cannot be seen as separate entities [39, 40]. In the weak-coupling regime Purcell predicted that the spontaneous emission rate could be tailored by modifying the density of available photon modes (LDOS) of the bare cavity [41]. For an ideal electric dipole source, spectrally resonant and with the same polarization of the cavity mode, placed at the maximum of the localized electric field, the nanocavity figure of merit, which gives an estimation of the electric spontaneous emission enhancement with respect to the emission rate when the dipole is in vacuum, is defined as the Purcell factor:

$$F = \frac{3}{4\pi^2} \frac{Q}{V} \left( \frac{\lambda}{n} \right)^3 \quad (2.5)$$

where the electric mode volume is defined as:

$$V = \frac{\int \epsilon(\mathbf{r}) |\mathbf{E}_0(\mathbf{r})|^2 d\mathbf{r}}{\max[\epsilon(\mathbf{r}) |\mathbf{E}_0(\mathbf{r})|^2]} \quad (2.6)$$

with  $\mathbf{E}_0(\mathbf{r})$  representing the electric field of the resonant mode of the bare nanocavity. Therefore, the Purcell factor of Eq. (2.5) can be strongly enhanced in photonic crystal nanocavities by exploiting the deterministic fabrication techniques that allow for accurately positioning light emitters like quantum dots (QDs) in precise PCN positions [42–44]. The contribution of photonic crystal nanocavities triggers also the evolution of a variety of applications ranging from efficient light-emitting-diodes to ultra-fast and low-threshold lasers, including illumination, optical communication, solar energy and even quantum-information systems [45, 46].

On the other hand, if the emitter and the localized field are in the strong-coupling regime, coherent entangled states of quantum superposition exhibiting characteristic Rabi temporal oscillations and Rabi spectral splitting, even in the zero-detuning condition (which implies a perfect spectral matching between the bare resonant mode and the isolated emitter), has been predicted and experimentally observed [47, 48]. This feature extends the application range of CQED to fundamental physic concerning basic light/matter interaction. As an example, in the strong coupling regime nonlinear optics occurs even with only two photons, giving rise to the photon-blockade effect

[49]. In fact, the transmission or reflection from the cavity can be controlled by absorption of just a single photon, since it modifies the energy states distribution of the system and prevent a subsequent identical photon to interact with the system.

Self-assembled QDs are preferred candidates for the observation of these intriguing light/matter interactions since they can be easily embedded inside 2D photonic crystal cavity on slab by exploiting the well-established molecular beam epitaxy semiconductor growing technique [50, 51]. Moreover, they are space-fixed nanostructure with a stable atom-like emission spectrum that reaches few  $\mu\text{eV}$  linewidth at low temperatures [52]. Single QDs have been reported as reliable non-classical light sources, able to generate defined single photon states. It is therefore very useful for quantum information and quantum cryptography applications to include these kinds of emitters into photonic nanocavities, which allow an efficient information transfer between a solid-state qubit and a flying qubit, as the emitted photon coupled to the cavity mode [53].

It is evident that the development of integrated nano-optical resonators is a fundamental step in the route towards ultrahigh density all-optical integrated circuits as well as to all-integrated quantum photonic networks, since they are suited to stand for the building blocks of these systems such as optical switches and add-and-drop filters [54–57]. For instance, a single photon transistor in which one stored gate photon controls the resonator transmission of subsequently applied source photons has been recently demonstrated [58]. Photonic crystal fibers involves a linear defect line and are an established 2D photonic crystals device for fiber-optic communications, fiber lasers, nonlinear devices and high-power transmission [59]. Moreover, exploiting strong light-matter interaction between photons and excitons in solid state quantum wells confined in PCN, polariton quasi-particles have been observed [60]. Also AND/OR gate operation has been shown, thus validating the connectivity of multiple transistors in the microcavity plane and paving the way to the implementation of polariton integrated circuits. Recent activity in this area has pioneered powerful approaches to the study of quantum coherence and has fueled the growth of quantum information science.

In conclusion, and more importantly, the characterization of e.m. fields localized in photonic crystal nanocavities with a sub-wavelength spatial resolution is essential for proving the intimate proprieties of CQED effects and for efficiently coupling light emitters in photonic devices.

### 2.1.3 Finite-difference time-domain calculations

Accurate analytic evaluation of the e.m. LDOS in complex photonic structures such as PCNs it is a difficult task. Plane wave expansion calculation method, presented in Chapter (1), is not suited for estimating the spectral properties and the field distributions of the localized modes. A useful common numerical technique developed to address this quest is the finite-difference time-domain (FDTD) method [61, 62]. It is used for modeling full-vector e.m. waves evolution in arbitrary structures by finding approximate solutions to the associated time-dependent Maxwell's equations over time in any specific positions. FDTD algorithms involve both the discretization

of the wave equations, by using second-order central-difference approximations to the space and time partial derivatives of the fields, and the meshing of the dielectric environment by a dense discrete grid. Each cell of the grid has its own electric permittivity together with the electric and magnetic field defined both in the center and at the edges of the unit-cell faces, as reported in Fig. (2.3 a). The resulting finite-difference equations are solved in a leapfrog manner by applying the usual tangential field continuity condition at each cell interface. In particular, the value of a field vector component at any lattice point depends only on its previous value and on the previous value of the components of the other field vector at adjacent points. Therefore, the updated electric field in time is dependent on the stored electric field and on the spatial variation of the magnetic field, as highlighted by the simplified scheme reported in Fig. (2.3 a). The process is iterated for every field component until the desired transient or steady-state e.m. field is fully evolved. When the stability criteria are fulfilled, the FDTD algorithm provides a reliable computing scheme [61].

FDTD algorithms finally involve a Fourier-transform of the calculated time-varying fields to obtain the system spectral response. The electric and magnetic field spatial distributions at a given wavelength are therefore easily achieved, thus giving a direct estimation of both the electric and magnetic LDOS of the investigated structure.

Typically, in any FDTD calculation extraordinary care must be taken in designing the dielectric environment, the light sources properties (dipoles, plane waves or Gaussian beams with defined polarization, wavelength, bandwidth, intensity, position that have to be suited for exciting a given PCN eigenmode) as well as in defining the actual “detectors”, which represent the positions whose fields are stored permanently in the calculator memory as a function of time. Since it is a time-domain method, FDTD solutions can simultaneously cover a wide frequency range. Moreover, the direct benefit in representing the field vectors in every cell, is achieving LDOS distributions with a high spatial resolution. It is, in fact, defined by the dimensions of the single cell, whose lower limit is given by the maximum memory that can be allocated in the calculator. On the other hand, the spectral resolution is bounded to the number of time-steps for which the fields evolve, and then it is limited both by the calculator memory and by the overall calculation time.

Nevertheless, due to the time domain discretization, dispersive materials such as metals are difficult to handle with FDTD. A calculation procedure that overcomes this limitation performing approximate solution of partial differential equations is the finite element method (FEM) [63]. The approach is based on eliminating the time derivatives, thus investigating only steady state problems. It is a fast method to obtain the stationary spatially resolved field distributions at a fixed wavelength for modes at least partially localized in any resonators, since the result is equivalent to a very long FDTD calculation.

In conclusion, finite-element calculation methods represent the main theoretical predictions with whom compare the experimental data. Nowadays, many commercial finite-element are available. In this thesis the FDTD theoretical predictions concerning the LDOS of modes localized in PCNs will be calculated by means of Crystal Wave (by Photon Design), while the FEM calculations to estimate the local field enhancement in plasmonic functionalized near-field probes will be performed by Comsol.

As a remarkable example, in Fig. (2.4) we report a FDTD calculation performed by Crystal Wave on a modified L3 PCN where two lateral holes are gently shifted and reduced. In Fig. (2.4 b) is reported the top-view design of the PCN on slab as it is stored in the FDTD solver calculator with a cubic grid of 22 nm size. The detector of the near-field is placed 22 nm on top of the slab. The photonic crystal is designed to have a lattice constant of 308 nm,  $f = 35\%$  and a slab refractive index of  $n = 3.484$  (that is the same of GaAs for  $\lambda = 1.3 \mu\text{m}$ ). The single time step is fixed at 0.4756 fs and the overall time sampling in this case covers 131072 time steps. In the calculation design we embed e.m. dipole sources in the slab with different orientations and a spectral range that covers all the photonic band-gap, reported in Fig. (2.4 a). Following this approach we excite all the available photonic modes of the system, hence including the localized PCN modes but also the “leaky modes” (non-stationary states inside the photonic band-gap that are non completely inhibited contributing to the PCN leakages). Therefore, the spectrum averaged over the whole detector size of Fig. (2.4 b), represents the spatially integrated LDOS as a function of the wavelength, as reported in normalized arbitrary units in Fig. (2.4 a). The intensity is almost zero in a large spectral range, which corresponds to the photonic band-gap where the LDOS vanishes, while the narrow peaks indicate the allowed modes inside the band-gap. The contribution of leaky modes is negligible in this case and the electric LDOS is dominated by few very localized modes. Figures (2.4 c) reproduces the electric field intensity distribution calculated by FDTD at the peak spectral position that exhibits the higher intensity mode of the PCN ( $\lambda = 1285 \text{ nm}$ ). Such spatially resolved calculation can be directly identified with the electric LDOS at a given wavelength. From this map it is evident that the related experimental challenge concerns the probing of the nanoscale modulation of the electric LDOS localized in PCNs.

## 2.2 Near-field probing

In this section a state-of-the-art review of efficient and commonly employed methods to detect the light fields localized in photonic crystal nanocavities is provided. We also describe some typical near-field measurements performed with the SNOM setup exploited in the following Chapters, which describe experimental results.

Although several developments have improved the SNOM sensitivity, versatility and resolution, a complete understanding of tip-light-sample interactions, and specifically which components of the electromagnetic field are collected by SNOM probes, is still lacking. In fact, this issue depends on many subtle aspects such as the exact tip geometry, the orientation of electric and magnetic dipoles with which the probes can be approximated, the polarization of the investigated light, and more in general on the performed experimental configuration. By exploiting the reciprocity theorem, it is proved that SNOM and STM can be handled using the same formalism [64, 65]. It follows that a tip is able to detect high spatial frequencies if the tip itself creates high spatial frequencies when it is illuminated from the far field. More importantly, the detected field is given by an overlapping integral between the experimental field and

the response function of the probe, describing the spatial localization of the detection process, the polarization effects, and the spectral response [66–68].

In the experimental framework, nanostructures such as micro-disks, nanoparticles, nanoplasmonic resonators, and especially photonic crystal nanocavities represent successful platforms for investigating the nature of the signal detected by any SNOM probe, since they are able to localize e.m. fields in very small modal volumes [69]. It has been shown that, on one hand, the signal directly collected by dielectric tips or by metal coated circular aperture probes is the signature of the electric field intensity of the localized optical mode [70, 71]. On the other hand, aperture metal coated tips fabricated with a wavelength dependent specific metal thickness or with a split ring can directly probe a signal that is proportional to a specific spatial component of the magnetic field intensity of light [72–74]. Recently, unexpected results have been proved to overcome this dichotomy by showing that aluminum coated circular aperture probes directly detect a combination of all the in-plane electric and magnetic components, with relative weights that depend both on the probe geometry and on the probe-sample distance [75].

In order to improve the SNOM fidelity imaging of localized photonic modes and, at the same time, to circumvent the uncertainties related to the direct signal mapping, it has been demonstrated that an advantageous imaging technique relies on the tip-induced perturbation on the nanocavity environment. The strength of this method relies on the fact that, the presence of the probe itself is responsible of a spectral shift of the PCN localized modes, with respect to the unperturbed case, with a shift amplitude proportional to the mode e.m. field intensity [76–80]. As the presence of the tip above the cavity adiabatically changes the resonance wavelength without introducing significant additional scattering losses (assumptions confirmed by experimental observations), the relative wavelength shift ( $\delta\lambda/\lambda$ ) is defined by the overlap integral between the unperturbed ( $\mathbf{E}_0, \mathbf{H}_0$ ) and the effective ( $\mathbf{E}, \mathbf{H}$ ) fields inside the perturbation volume  $V_p$ , as exactly derived from Maxwell's equations [77, 81, 82]:

$$\frac{\delta\lambda}{\lambda} = \frac{\int_{V_p} [\mathbf{E}_0^*(\mathbf{r}) \cdot \overline{\alpha^e} \mathbf{E}_0(\mathbf{r}) + \mathbf{H}_0^*(\mathbf{r}) \cdot \overline{\alpha^m} \mathbf{H}_0(\mathbf{r})] d\mathbf{r}}{\int [\varepsilon(\mathbf{r}) |\mathbf{E}_0(\mathbf{r})|^2 + \mu(\mathbf{r}) |\mathbf{H}_0(\mathbf{r})|^2] d\mathbf{r}} \quad (2.7)$$

where the 3x3 matrix  $\overline{\alpha^e}$  and  $\overline{\alpha^m}$  in the coordinates basis ( $x, y, z$ ) are the electric and magnetic polarizability of the tip, respectively. The relation Eq. (2.7) predicts that the wavelength shift induced by a near-field tip is entirely set by the opto-geometric properties of the tip and the field distribution of the PCN mode. It also reveals that a tip exhibiting a dielectric polarizability perturbs only the electric field of the cavity while a tip with an effective magnetic polarizability interacts only with the magnetic field. Then, by mapping the spectral shift induced by a probe with an effective electric (magnetic) polarizability as a function of position it is possible to experimentally retrieve the electric (magnetic) LDOS confined in the nanocavity for every attainable wavelength.

To describe the light-probe interaction and the effective tip polarizability the sub-wavelength tip apex can be approximated with an electric ( $\mathbf{p}$ ) or magnetic ( $\mathbf{m}$ ) dipole induced by the external fields [83]:

$$\mathbf{p} = \bar{\alpha^e} \mathbf{E} \quad (2.8)$$

$$\mathbf{m} = \bar{\alpha^m} \mathbf{H} \quad (2.9)$$

Generally, in light-matter interaction the magnetic coupling is smaller than the electric coupling, in particular, at the macroscopic level the magnetic susceptibility of a material is generally about  $10^{-4}$  the electric susceptibility [84]. Hence, light-matter coupling is mainly governed by the electric interaction mediated by the electric polarizability. Therefore, for a tip apex composed by homogeneous media at optical wavelengths the only non-negligible matrix is  $\bar{\alpha^e}$ . However, it is important to stress that this behavior can change as a function of the probe geometry.

For a dielectric probe the apex can be approximated as a sub-wavelength dielectric sphere. Due to the symmetry only the diagonal terms of the electric polarizability are non-vanishing and since all directions are equivalent we find  $\alpha_{xx}^e = \alpha_{yy}^e = \alpha_{zz}^e$  meaning that an electric field oriented along a given axis cannot induce a dipole along a different one. Moreover, concerning the direct imaging only the induced dipoles that lie in the sample plane ( $xy$  plane) are coupled to the modes propagating in the fiber and therefore only TE-like modes can be directly detected, while the induced out-of-plane dipole does not emit radiation along  $z$ . Since the size of the dielectric tip apex can be very small, by investigating the perturbation effect induced by  $\alpha^e$  it is possible to retrieve the localized electric field distribution with an improved spatial resolution with respect to the direct signal detection that is affected by far-field radiation collected from lateral sidewalls.

In particular, the insertion of a dielectric (uncoated) near-field probe provides a local increase of the dielectric constant  $\delta\epsilon$  due to the tip positive effective electric polarizability. This induces a spectral red-shift (towards higher wavelengths) of the nanocavity resonances that is proportional to electric field intensity component, thus ensuring a sensitive imaging of the electric field intensity of the optical modes localized in PCNs [76, 78]. In the approximation of weakly perturbation ( $\delta\lambda/\lambda \ll 1$ ) induced by a pure dielectric nanometric object placed at distance  $z$  from the PCN surface, the resulting spectral shift of a given mode is proportional to the electric field intensity. It follows by specifying Eq. (2.7) in the case where the in plane coordinates  $\mathbf{r}_{//}$  are separated to the  $z$  axis and the unperturbed field  $\mathbf{E}_0(\mathbf{r}_{//})$  is assumed constant over the small tip cross section [76]:

$$\frac{\delta\lambda(\mathbf{r}_{//}, z)}{\lambda} = \frac{\alpha^e}{2V} \frac{|\mathbf{E}_0(\mathbf{r}_{//})|^2}{\max[\epsilon(\mathbf{r})|\mathbf{E}_0(\mathbf{r}_{//})|^2]} e^{-z/d} \quad (2.10)$$

where the modal volume  $V$  is defined by Eq. (2.6) and  $d$  represents the exponential decay length of the mode outside the slab in the  $z$  direction. The effective tip polarizability can be evaluated by assuming that only the very tip apex contributes to

the local dielectric perturbation, and that it can be approximated with a cylinder of volume  $\pi R_p^2 d$  and dielectric constant  $\epsilon_p$ , where  $R_p$  is the tip apex radius:

$$\alpha^e = 3 \frac{\epsilon_p - 1}{\epsilon_p + 2} \pi R_p^2 d \quad (2.11)$$

Therefore, Eq. (2.10) points out that the spectral shift has a straight correspondence with the unperturbed mode distribution while it is inversely proportional to the unperturbed mode volume. Being for a dielectric material  $\epsilon_p > 1$ , from Eq. (2.11) results that  $\alpha^e$  is positive and hence induces a spectral shift towards lower wavelengths. The dependence of  $V$  allows to intuitively explain the dielectric induced spectral shift towards higher wavelength, as a result of mode volume increase in the system composed by the PCN and the near-field tip, with respect to the PCN alone. In fact, the mode that is resonant to the tip-cavity system has an electric field intensity delocalized also in the dielectric tip apex and experiences a higher effective refractive index that induces the mode wavelength to be red-shifted [4]. Moreover, Eq. (2.10) accounts for the exponential decrease of the spectral shift amplitude as a function of the tip-slab separation. By performing an experiment in which the dielectric probe is raster scanned at constant height above the PCN surface, Eq. (2.10) points out that the unperturbed electric field intensity distribution can be retrieved by mapping the tip induced spectral shift as a function of position. This result was for the first time theoretically presented in ref. [76], as highlight in Fig. (2.5).

In contrast, metallic coated tips with a circular symmetric aperture act as diamagnetic systems, inducing a mode blue-shift, which is found to be proportional to the intensity of the magnetic field component that is orthogonal to the PCN surface (TE-like mode) [79, 80]. In fact, due to the metallic probe geometry the aperture coated probe exhibits a negative magnetic polarizability that induces a magnetic response to the e.m. modes. By approximating the coated probe apex with a metallic hollow cylinder, a time-varying magnetic field oriented along the cylinder axis induces a current flowing in the metal, due to the Faraday's law [80, 83]. This current, in turn, produces an induced magnetic field opposed to the total field inside the cylinder, hence letting the effective tip magnetic polarizability to be negative. In short, the probe geometry exhibits a non-vanishing magnetic dipole, given by Eq. (2.9), and its symmetry imposes that the non-diagonal terms of  $\alpha^m$  are vanishing, while  $\alpha_{xx}^m$  and  $\alpha_{yy}^m$  can be considered negligible with respect to  $\alpha_{zz}^m$  since the flux of the in-plane components of the magnetic field is negligible with respect to the flux of the out-of-plane component. The resulting perturbation of the PCN magnetic environment produces a sizeable blue-shift of the localized eigenmodes, which according to Eq. (2.7) accurately map the spatial distribution of the resonant magnetic field intensity oriented along  $z$ . For instance, the experiment described in ref. [79] shows that the spectral shift map performed with an Al-coated aperture probe on top of an L3 nanocavity and reported in Fig. (2.6 b), results in excellent agreement with the intensity of the magnetic field component orthogonal to the slab surface, shown in Fig. (2.6 c).

In a simple and intuitive picture, the coated probe apex can be seen as a local metal mirror on top of the sample surface that reduces the PCN effective mode vol-

ume, thus shifting the resonant modes towards lower wavelengths [85]. It is also important to note that a magnetic response of the constituent materials, namely glass and aluminum, is virtually absent and the effective magnetic response is only induced by the probe geometry.

## 2.3 Disorder based nanocavities

A small amount of disorder in a periodic photonic crystals would not destroy a photonic band-gap or localization light behavior. However, it would strongly change the properties of the localized modes, such as the resonant wavelength and the quality factor [86, 87]. Even in the limit of highly disordered dielectric structures light propagation can still be prevented and strong mode localization be achieved through the mechanism of Anderson localization [88–90].

Wave localization in random media occurs as a consequence of coherent constructive/destructive interference in multiple scattering and it plays a central role in the description of transport of quantum and classical waves. The physical mechanism behind localization, was introduced by Anderson in quantum electron transport [88]. The explanation is so general that the study of localization has not been restricted to electrons but light, sound waves, microwaves, and ultracold atoms have been considered in theoretical and experimental investigations. Photons exhibit the advantage that no inter-particle interaction is present at moderate intensity (neglecting non-linear mechanisms), thus making photonic systems more suitable for studying Anderson localization than electronic ones [91].

Disordered photonic systems are material in which the refractive index varies randomly in space. Different light mesoscopic regimes can be found as a function of the light wavelength ( $\lambda$ ), the sample size ( $L$ ), and the photon scattering mean free path ( $l_{tr}$ ), which quantifies the average distance travelled by the particle between successive scattering events), as highlighted in Fig. (2.7 a-c). Neglecting absorption, the single scattering regime describes the case where the photon has a high probability to perform up to one scattering event before leaving the sample, exhibiting  $l_{tr} \approx L$ , see Fig. (2.7 a). In general, the magnitude of the refractive index mismatch determines scattering strength. The ratio between  $\lambda$  and the scatterer size gives the angular dependence of the scattering as well as the scattering cross-section in Mie's theory [92, 93]. For example, if the scatterer size is much smaller than  $\lambda$ , the photon will be scattered nearly isotropically. On the other hand, if the size of the scatterer is comparable to  $\lambda$ , the photon will be mainly scattered in the forward direction. When a disordered sample is illuminated by a coherent light source, the outgoing scattered light projected into a screen gives rise to a complex bright-dark intensity pattern, which is called laser speckle pattern. The analysis of the speckle pattern has developed a powerful tool for the study of the dynamic behavior of particles suspensions or macromolecules [94].

In another limit, for  $\lambda \ll l_{tr} \ll L$ , the photon may scatter many times before leaving the disordered sample. This is the diffusion regime, which concerns a large variety of phenomena in opaque media, where multiple light scattering takes place, as reported in Fig. (2.7 b). Diffused photons undergo multiple scattering events and quickly loose the initial coherence before exiting the sample in a randomized direction. The

phase of the scattered waves after each scattering event is random, and thus one can model light propagation as a random-walk which leads to a multiple scattering process. But, the diffusive picture is not complete as some interference effects can survive the multiple scattering, as highlight by the two closed loop interference trajectories in Fig. (2.7 c). In fact, as the scatterers density increases and the condition (known as the modified Ioffe-Regel criterion [89])  $l_{tr} \leq \lambda$  holds, a transition from diffusion to localization occurs for light, driven by multiple elastic scattering interference. In this case the interference effects are so strong that light transport comes to a halt and the waves becomes trapped in randomly distributed modes inside the sample. This phenomenon is called Anderson localization regime. Light behaves as being trapped in an optical nanoresonator. Therefore, disordered structure can sustain optical modes localized at the nanoscale.

Of course, the main difficulty in the search for light localization relies on the realization of sufficiently strong scattering sample, in which the electric field can not even perform one oscillation before the wave is scattered for a second time. Considering a semiconductor slab analogous to the one of Fig. (2.2 a), in which photonic crystals are designed, it is possible to achieve strong light localization by randomly engineering the air holes pattern distribution, see Fig. (2.8 a), as reported in the intensity distribution obtained in ref. [95]. This is also shown in Fig. (2.8 b), which experimentally demonstrates the presence of cavity-like confined optical modes. The two-dimensional random nanotextured slab has been proved to be a fertile system to study the localization regime, which is interesting also for other kinds of particles, because of the universality of this phenomenon in every random media wave transport. Moreover, it accounts for necklace states occurrence and even for improving the absorption efficiency of thin film solar cells [95–98].

In Chapter (6) experimental near-field analysis of a random system on slab analogous to the schematics reported in Fig. (2.8 a) will be presented. In particular, the light confinement will be engineered as a function of the design structural parameters and as a function of the post-fabrication oxidation technique that locally modifies the dielectric environment.

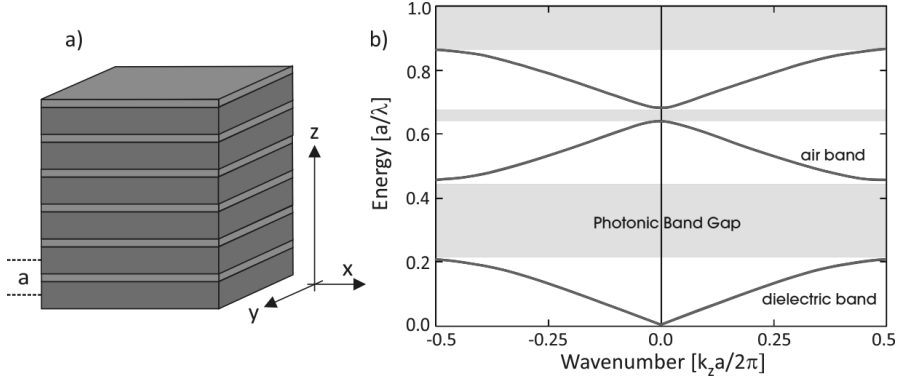


Figure 2.1: a) Schematics of the 1D photonic crystal along  $z$  direction with lattice constant  $a$ , for which the band diagram calculation reported in b) is performed. The details of the two media are:  $\epsilon_1 = 13$  and layer thickness  $0.2a$ ,  $\epsilon_2 = 1$  and layer thickness  $0.8a$ , respectively. b) Energy band diagram calculated by PWE in the first Brillouin zone for the infinite stack structure reported in a). In yellow are reported the photonic band gaps. The group velocity  $vg = d\omega/dk$  vanishes at the border of the Brillouin zone and also for  $k_z = 0$ , with the exception of the lower energy band.

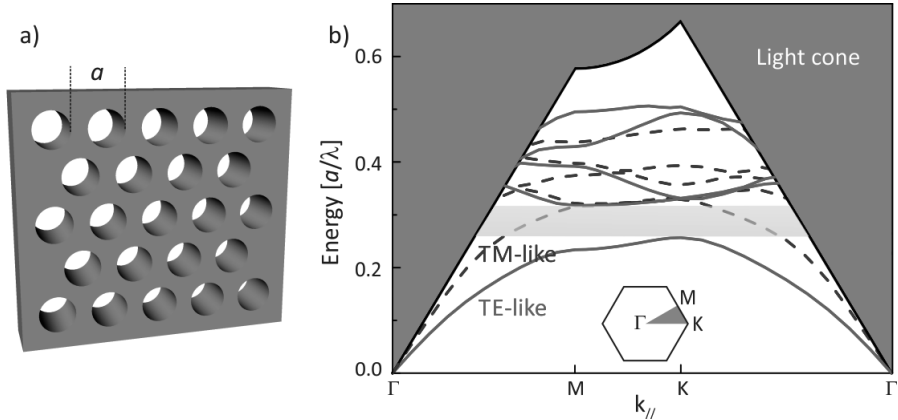


Figure 2.2: a) Schematics of the 2D photonic crystal of air holes arranged on a hexagonal lattice with lattice constant  $a$  and filling fraction  $f = 35\%$ , in a  $\epsilon = 12$  slab with thickness  $1.03a$ , whose band diagram calculated by PWE is reported in b). The Energy band diagram is reported as a function of the in plane wavevector in the first irreducible Brillouin zone (reported in the inset with the high symmetry points). Only the five lower energy band for the TE-like and TM-like modes are reported. The yellow stripe represents the photonic band-gap that occurs for the TE-like modes only. The blue regions correspond to modes above the light cone that are not confined in the slab.

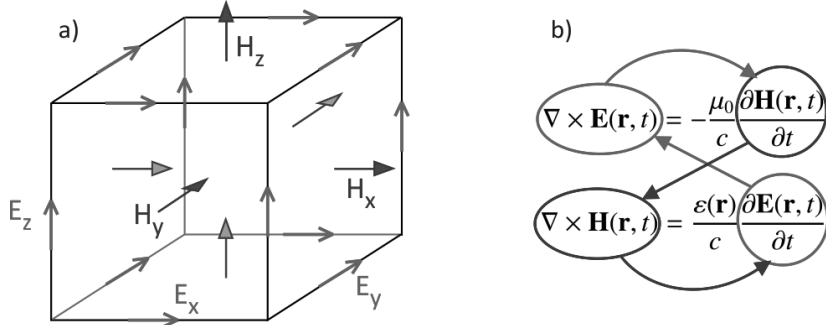


Figure 2.3: a) Representation of the unit-cell mesh used for FDTD calculations. It highlights the positions where local electric and magnetic field components are evaluated. b) Simplified scheme involved in the FDTD calculation loop to evaluate the e.m. fields by solving the approximated Maxwell's curl equations in which the derivatives become finite-differences.

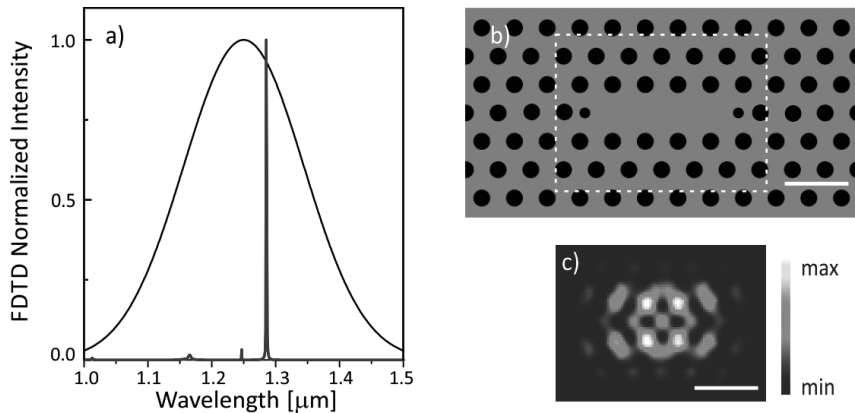


Figure 2.4: a) FDTD calculated normalized spectrum (blue line) of the modified L3 PCN on-slab reported in b) together the normalized emission of the electric dipoles placed inside the slab (black line). b) Top-view zoom of the 3D environment where the fields evolve according to the FDTD algorithm. The unit cell size of the discrete grid is 22 nm. Black holes represent air ( $n = 1$ ) and orange environment simulates GaAs ( $n = 3.484$ ). The white dashed rectangle highlights the edges of the FDTD detector. c) Electric field intensity distribution calculated at the wavelength of the most intense resonant mode ( $\lambda = 1285$  nm). The scale bar is 600 nm.

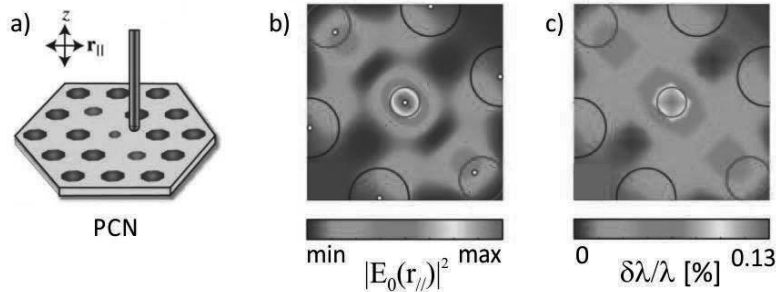


Figure 2.5: a) Schematic of the PCN exhibiting a resonance at  $\lambda = 1500$  nm, whose surface is raster scanned by cylindrical silicon tip with a diameter of 125 nm that is placed at 30 nm above the slab. b) Electric field intensity distribution of the unperturbed mode calculated by FDTD in a plane placed at 30 nm above the slab. The black circumferences outline the air pores. c) Calculated resonance frequency shift induced by the tip as a function of position by exploiting Eq. (2.10), Eq. (2.11) and FDTD calculations. Figures adapted from [76].

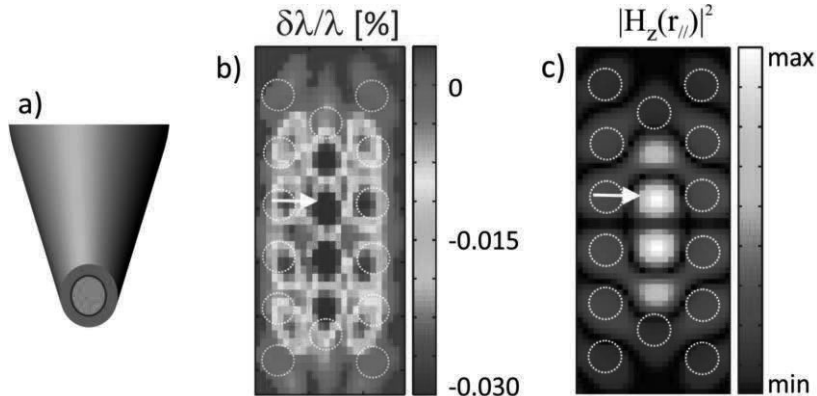


Figure 2.6: a) Schematics of the Al-coated aperture probe. b) Measured spectral shift as a function of position in a PCN exhibiting a resonant mode at  $\lambda = 1530$  nm. The white circles outline the air pores. c) FDTD calculation of the intensity of the magnetic field component orthogonal to the slab surface. Both maps are adapted from [79].

Imaging and engineering optical localized modes at the nanoscale

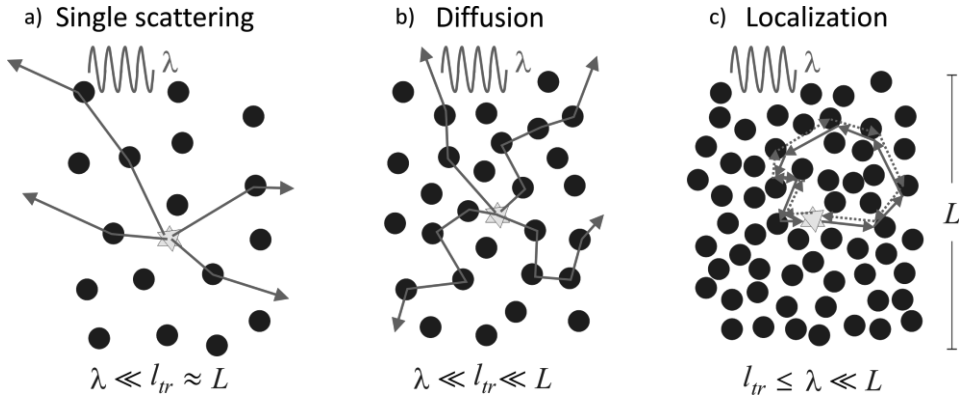


Figure 2.7: Schematics of the three main light regimes in a disordered structure made of randomly placed dielectric spheres, for increasing scatterers density. The yellow spot is the light source and the red arrows describe the light random-walk trajectories. a) Single scattering regime takes place if the scattering mean free path is of the order of the sample size. b) Diffusive regime is found when multiple scattering occurs along with the condition  $\lambda \ll l_{tr}$ . c) Light localization can take place if  $l_{tr} \leq \lambda$  due to strong interference. For instance, two trajectories propagating in opposite directions along a closed loop exhibit constructive interference and maximize the probability of localization.

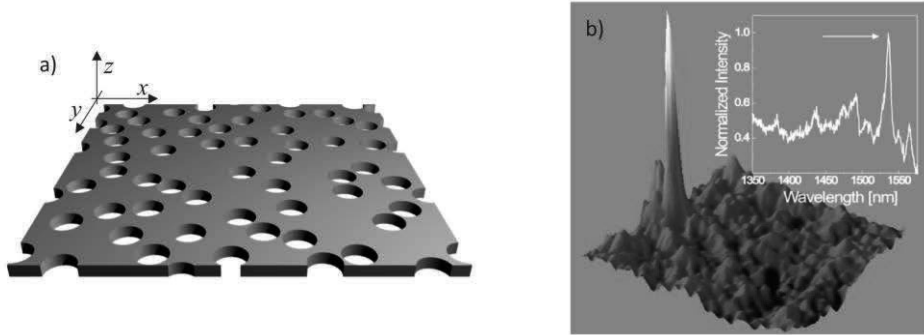


Figure 2.8: a) Schematics of the randomly nanostructured semiconductor slab. b) Experimental three-dimensional view of the near-field intensity distribution of a localized mode corresponding to the peak wavelength shown in the inset. Figure b) is adapted from [95].

## References

- [1] E. Yablonovitch. “Inhibited Spontaneous Emission in Solid-State Physics and Electronics” In: Phys. Rev. Lett. 58, 20 (20 1987), pp. 2059–2062.
- [2] S. John. “Strong localization of photons in certain disordered dielectric superlattices” In: Phys. Rev. Lett. 58, 23 (1987), pp. 2486–2489.
- [3] F. Lord Rayleigh. “On the maintenance of vibrations by forces of double frequency, and on the propagation of waves through a medium endowed with a periodic structure” In: Philos. Mag. 24, 147 (1887), pp. 145–159.
- [4] J. Joannopoulos, S. Johnson, J. Winn, and R. Meade. Photonic Crystals: Molding the Flow of Light. Princeton University Press, 2nd edn. (2008).
- [5] N. Ashcroft and N. Mermin. Solid State Physics. Harcourt Inc., Orlando, FL, USA, (1976).
- [6] E. Yablonovitch, T. Gmitter, and K. Leung. “Photonic band structure: The face-centered-cubic case employing nonspherical atoms” In: Phys. Rev. Lett. 67, 17 (1991), pp. 2295–2298.
- [7] A. Blanco, a. S. G. E. Chomski, M. Ibáñez, S. John, S. Leonard, C. Lopez, F. Meseguer, H. Miguez, J. Mondia, G. Ozin, O. Toader, and H. M. van Driel. “Large-scale synthesis of a silicon photonic crystal with a complete three-dimensional bandgap near 1.5 micrometres” In: Nature 405 (2000), pp. 437–440.
- [8] A. Moroz. “Three-Dimensional Complete Photonic-Band-gap Structures in the Visible” In: Phys. Rev. Lett. 83, 25 (1999), pp. 5274–5277.
- [9] M. Campbell, D. Sharp, M. Harrison, R. Denning, and A. Turberfield. “Fabrication of photonic crystals for the visible spectrum by holographic lithography” In: Nature 404 (2000), pp. 53–56.
- [10] P. Vukusic and J. Sambles. “Photonic structures in biology” In: Nature 424 (2003), pp. 852–855.
- [11] A. Parker. “515 million years of structural colour” In: J. Opt. 2, 6 (2000), R15–R28.
- [12] J. Zi, X. Yu, Y. Li, X. Hu, C. Xu, X. Wang, X. Liu, and R. Fu. “Coloration strategies in peacock feathers” In: Proc. Natl. Acad. Sci. USA 100, 22 (2003), pp. 12576–12578.
- [13] S. Vignolini, P. Rudall, A. Rowland, A. Reed, E. Moyroud, R. Faden, J. Baumberg, B. Glover, and U. Steiner. “Pointillist structural color in *Pollia* fruit” In: Proc. Natl. Acad. Sci. USA 109, 39 (2012), pp. 15712–15715.
- [14] S. Johnson and J. Joannopoulos. “Block-iterative frequency-domain methods for Maxwell’s equations in a planewave basis” In: Opt. Express 8, 3 (2001), pp. 173–190.
- [15] S. Shi, C. Chen, and D. Prather. “Plane-wave expansion method for calculating band structure of photonic crystal slabs with perfectly matched layers” In: J. Opt. Soc. Am. A 21, 9 (2004), pp. 1769–1775.
- [16] K. Joulain, R. Carminati, J.-P. Mulet, and J.-J. Greffet. “Definition and measurement of the local density of electromagnetic states close to an interface” In: Phys. Rev. B 68, 24 (2003), p. 245405.

## Imaging and engineering optical localized modes at the nanoscale

- [17] I. Nikolaev, W. Vos, and A. Koenderink. “Accurate calculation of the local density of optical states in inverse-opal photonic crystals” In: *J. Opt. Soc. Am. B* 26, 5 (2009), pp. 987–997.
- [18] M. Born and E. Wolf. *Principles of Optics*. Oxford: Pergamon, 6th edn. (1970).
- [19] E. Garmire. “Theory of quarter-wave-stack dielectric mirrors used in a thin Fabry- Perot filter” In: *Appl. Opt.* 42, 27 (2003), pp. 5442–5449.
- [20] M. Meier, A. Mekis, A. Dodabalapur, A. Timko, R. Slusher, J. Joannopoulos, and O. Nalamasu. “Laser action from two-dimensional distributed feedback in photonic crystals” In: *Appl. Phys. Lett.* 74, 1 (1999), pp. 7–9.
- [21] S. McNab, N. Moll, and Y. Vlasov. “Ultra-low loss photonic integrated circuit with membrane-type photonic crystal waveguides” In: *Opt. Express* 11, 22 (2003), pp. 2927–2939.
- [22] A. Mekis, J. Chen, I. Kurland, S. Fan, P. R. Villeneuve, and J. Joannopoulos. “High Transmission through Sharp Bends in Photonic Crystal Waveguides” In: *Phys. Rev. Lett.* 77, 18 (1996), pp. 3787–3790.
- [23] L. Zeng, P. Bermel, Y. Yi, B. Alamariu, K. Broderick, J. Liu, C. Hong, X. Duan, J. Joannopoulos, and L. Kimerling. “Demonstration of enhanced absorption in thin film Si solar cells with textured photonic crystal back reflector” In: *Appl. Phys. Lett.* 93, 22 (2008), p. 1105.
- [24] Y. Vlasov, M. O’Boyle, H. Hamann, and S. McNab. “Active control of slow light on a chip with photonic crystal waveguides” In: *Nature* 438 (2005), pp. 65–69.
- [25] D. Duché, L. Escoubas, J.-J. Simon, P. Torchio, W. Vervisch, and F. Flory. “Slow Bloch modes for enhancing the absorption of light in thin films for photovoltaic cells” In: *App. Phys. Lett.* 92, 19 (2008), p. 3310.
- [26] T. Krauss. “Slow light in photonic crystal waveguides” In: *J. Phys. D: Appl. Phys.* 40, 9 (2007), pp. 266–2670.
- [27] M. Soljacic, S. Johnson, S. Fan, M. Ibanescu, E. Ippen, and J. Joannopoulos. “Photonic-crystal slow-light enhancement of nonlinear phase sensitivity” In: *J. Opt. Soc. Am. B* 19, 9 (2002), pp. 2052–2059.
- [28] M. Notomi. “Theory of light propagation in strongly modulated photonic crystals: Refraction-like behavior in the vicinity of the photonic band gap” In: *Phys. Rev. B* 62, 16 (2000), pp. 10696–10705.
- [29] M. de Dood, B. Gralak, A. Polman, and J. Fleming. “Superstructure and finitesize effects in a Si photonic woodpile crystal” In: *Phys. Rev. B* 67, 3 (2003), p. 035322.
- [30] E. Chow, S. Lin, S. Johnson, P. Villeneuve, J. Joannopoulos, J. Wendt, G. Vawter, W. Zubrzycki, H. Hou, and A. Alleman. “Three-dimensional control of light in a two-dimensional photonic crystal slab” In: *Nature* 407 (2000), pp. 983–986.
- [31] P. Russell. “Optics of Floquet-Bloch waves in dielectric gratings” In: *Appl. Phys. B* 39, 4 (1986), pp. 231–246.
- [32] K. Vahala. “Optical microcavities” In: *Nature* 424 (2003), pp. 839–846.
- [33] Y. Akahane, T. Asano, B.-S. Song, and S. Noda. “High-Q photonic nanocavity in a two-dimensional photonic crystal” In: *Nature* 425 (2003), pp. 944–947.
- [34] A. Chalcraft, S. Lam, D. O’Brien, T. Krauss, M. Sahin, D. Szymanski, D. Sanvitto, R. Oulton, M. Skolnick, A. Fox, D. Whittaker, H.-Y. Liu, and M. Hopkinson. “Mode structure of the L3 photonic crystal cavity” In: *Appl. Phys. Lett.* 90, 24 (2007), p. 1117.

- [35] N.-V.-Q. Tran, S. Combrie, and A. De Rossi. “Directive emission from high-Q photonic crystal cavities through band folding” In: Phys. Rev. B 79, 4 (2009), p. 041101.
- [36] Y. Lai, S. Pirotta, G. Urbinati, D. Gerace, M. Minkov, V. Savona, A. Badolato, and M. Galli. “Genetically designed L3 photonic crystal nanocavities with measured quality factor exceeding one million” In: Appl. Phys. Lett. 104, 24 (2014), p. 1101.
- [37] S. Haroche and D. Kleppner. “Cavity quantum electrodynamics” In: Phys. Today 42 (1989), p. 24.
- [38] H. Mabuchi and A. C. Doherty. “Cavity Quantum Electrodynamics: Coherence in Context” In: Science 298, 5597 (2002), pp. 1372–1377.
- [39] S. Noda, M. Fujita, and T. Asano. “Spontaneous-emission control by photonic crystals and nanocavities” In: Nat. Photon. 1 (2007), pp. 449–458.
- [40] G. Khitrova, H. Gibbs, M. Kira, S. Koch, and A. Scherer. “Vacuum Rabi splitting in semiconductors” In: Nature Phys. 2 (2006), pp. 81–90.
- [41] E. Purcell. “Spontaneous emission probabilities at radio frequencies” In: Phys. Rev. 69 (1946), p. 681.
- [42] J.-M. Gerard and B. Gayral. “Strong Purcell Effect for InAs Quantum Boxes in Three-Dimensional Solid-State Microcavities” In: J. Light Tech. 17, 11 (1999), pp. 2089–2095.
- [43] D. Englund, D. Fattal, E. Waks, G. Solomon, B. Zhang, T. Nakaoka, Y. Arakawa, Y. Yamamoto, and J. Vuckovic. “Controlling the Spontaneous Emission Rate of Single Quantum Dots in a Two-Dimensional Photonic Crystal” In: Phys. Rev. Lett. 95, 1 (2005), p. 013904.
- [44] A. Badolato, K. Hennessy, M. Atatüre, J. Dreiser, E. Hu, P. Petroff, and A. Imamoglu. “Deterministic Coupling of Single Quantum Dots to Single Nanocavity Modes” In: Science 308, 5725 (2005), pp. 1158–1161.
- [45] H. Altug, D. Englund, and J. Vuckovic. “Ultrafast photonic crystal nanocavitylaser” In: Nature Phys. 2 (2006), pp. 484–488.
- [46] H.-G. Park, S.-H. Kim, S.-H. Kwon, Y.-G. Ju, J.-K. Yang, J.-H. Baek, S.-B. Kim, and Y.-H. Lee. “Electrically Driven Single-Cell Photonic Crystal Laser”. In: Science 305, 5689 (2004), pp. 1444–1447.
- [47] T. Yoshie, A. Scherer, J. Hendrickson, G. Khitrova, H. Gibbs, G. Rupper, C. Ell, O. Schekin, and D. Deppe. “Vacuum Rabi splitting with a single quantum dot in a photonic crystal nanocavity” In: Nature 432 (2004), pp. 200–203.
- [48] K. Hennessy, A. Badolato, M. Winger, D. Gerace, M. Atatüre, S. Gulde, S. Fält, E. Hu, and A. Imamoglu. “Quantum nature of a strongly coupled single quantum dot-cavity system” In: Nature 445 (2007), pp. 896–899.
- [49] A. Imamoglu, H. Schmidt, G. Woods, and M. Deutsch. “Strongly Interacting Photons in a Nonlinear Cavity” In: Phys. Rev. Lett. 79, 8 (1997), pp. 1467–1470.
- [50] C. Adelmann, J. Simon, G. Feuillet, N. Pelekanos, B. Daudin, and G. Fishman. “Self-assembled InGaN quantum dots grown by molecular-beam epitaxy”. In: Appl. Phys. Lett. 76, 12 (2000), pp. 1570–1572.
- [51] A. Kiraz, C. Reese, B. Gayral, L. Zhang, W. Schoenfeld, B. Gerardot, P. Petroff, E. Hu, and A. Imamoglu. “Cavity-quantum electrodynamics with quantum dots” In: J. Opt. B 5, 2 (2003), pp. 129–137.

- [52] C. Becher, A. Kiraz, P. Michler, A. Imamoglu, W. Schoenfeld, P. Petroff, L. Zhang, and E. Hu. “Nonclassical radiation from a single self-assembled InAs quantum dot” In: *Phys. Rev. B* 63, 12 (2001), p. 121312.
- [53] S. Carter, T. Sweeney, M. Kim, C. Kim, D. Solenov, S. Economou, T. Reinecke, L. Yang, A. Bracker, and D. Gammon. “Quantum control of a spin qubit coupled to a photonic crystal cavity” In: *Nat. photon.* 7 (2013), pp. 329–334.
- [54] K. Preston, B. Schmidt, and M. Lipson. “Polysilicon photonic resonators for large-scale 3D integration of optical networks” In: *Opt. Express* 15, 25 (2007), pp. 17283–17290.
- [55] B. Hausmann, I. Bulu, P. Deotare, M. McCutcheon, V. Venkataraman, M. Markham, D. Twitchen, and M. Loncar. “Integrated High-Quality Factor Optical Resonators in Diamond” In: *Nano Lett.* 13, 5 (2013), pp. 1898–1902.
- [56] G. Shambat, M. S. Mirotznik, G. Euliss, V. O. Smolski, E. G. Johnson, and R. A. Athale. “Photonic crystal filters for multi-band optical filtering on a monolithic substrate” In: *J. Nanophoton.* 3, 1 (2009), pp. 031506–031506–11.
- [57] H. Takano, B.-S. Song, T. Asano, and S. Noda. “Highly efficient multi-channel drop filter in a two-dimensional hetero photonic crystal” In: *Opt. Express* 14, 8 (2006), pp. 3491–3496.
- [58] W. Chen, K. Beck, R. Bücker, M. Gullans, M. Lukin, H. Tanji-Suzuki, and V. Vuletic. “All-Optical Switch and Transistor Gated by One Stored Photon” In: *Science* 341, 6147 (2013), pp. 768–770.
- [59] P. Russell. “Photonic Crystal Fibers”. In: *Science* 299, 5605 (2003), pp. 358–362.
- [60] D. Ballarini, M. D. Giorgi, a. H. E. Cancellieri, E. Giacobino, R. Cingolani, A. Bramati, G. Gigli, and D. Sanvitto. “All-optical polariton transistor” In: *Nat. Commun.* 4, 1778 (2013).
- [61] A. Taflove. “Review of the formulation and applications of the finite-difference time-domain method for numerical modeling of electromagnetic wave interactions with arbitrary structures” In: *Wave Motion* 10, 6 (1988), pp. 547–582.
- [62] K. Kunz and R. Luebers. *The finite differences time domain method*. CRC, Boca Raton, Fla., (1993).
- [63] J. Jian. *Finite element method in electromagnetics*. New York, NY: Wiley, (2002).
- [64] R. Carminati and J.-J. Sàenz. “Scattering Theory of Bardeen’s Formalism for Tunneling: New Approach to Near-Field Microscopy” In: *Phys. Rev. Lett.* 84, 22 (2000), pp. 5156–5159.
- [65] R. Carminati, M. Nieto-Vesperinas, and J.-J. Greffet. “Reciprocity of evanescent electromagnetic waves”. In: *J. Opt. Soc. Am. A* 15, 3 (1998), pp. 706–712
- [66] J.-J. Greffet and R. Carminati. “Image formation in near-field optics” In: *Progr. Surf. Sci.* 56, 3 (1997), pp. 133–237.
- [67] J. Porto, R. Carminati, and J.-J. Greffet. “Theory of electromagnetic field imaging and spectroscopy in scanning near-field optical microscopy” In: *J. Appl. Phys.* 88, 8 (2000), pp. 4845–4850.
- [68] A. Dereux, C. Girard, and J.-C. Weeber. “Theoretical principles of near-field optical microscopies and spectroscopies” In: *J. Chem. Phys.* 112, 18 (2000), pp. 7775–7789.

- [69] C. Girard. “Near fields in nanostructures” In: Rep. Prog. Phys. 68, 8 (2005), pp. 1883–1933.
- [70] J.-C. Weeber, E. Bourillot, A. Dereux, J.-P. Goudonnet, Y. Chen, and C. Girard. “Observation of Light Confinement Effects with a Near-Field Optical Microscope” In: Phys. Rev. Lett. 77, 27 (1996), pp. 5332–5335.
- [71] M. Burresi, R. Engelen, A. Opheij, D. van Oosten, D. Mori, T. Baba, and L. Kuipers. “Observation of Polarization Singularities at the Nanoscale” In: Phys. Rev. Lett. 102, 3 (2009), p. 033902.
- [72] E. Devaux, A. Dereux, E. Bourillot, J.-C. Weeber, Y. Lacroute, J.-P. Goudonnet, and C. Girard. “Local detection of the optical magnetic field in the near zone of dielectric samples” In: Phys. Rev. B 62, 15 (2000), pp. 10504–10514.
- [73] M. Burresi, D. van Oosten, T. Kampfrath, H. Schoenmaker, R. Heideman, A. Leinse, and L. Kuipers. “Probing the Magnetic Field of Light at Optical Frequencies”. In: Science 326, 5952 (2009), pp. 550–553.
- [74] D. Denkova, N. Verellen, A. Silhanek, V. Valev, P. Dorpe, and V. Moshchalkov. “Mapping Magnetic Near-Field Distributions of Plasmonic Nanoantennas” In: ACS Nano 7, 4 (2013), pp. 3168–3176.
- [75] B. le Feber, N. Rotenberg, D. Beggs, and L. Kuipers. “Simultaneous measurement of nanoscale electric and magnetic optical fields” In: Nature Photon. 8 (2014),
- [76] A. Koenderink, M. Kafesaki, B. Buchler, and V. Sandoghdar. “Controlling the Resonance of a Photonic Crystal Microcavity by a Near-Field Probe” In: Phys. Rev. Lett. 95, 15 (2005), p. 153904.
- [77] L. Lalouat, B. Cluzel, P. Velha, E. Picard, D. Peyrade, J. Hugonin, P. Lalanne, E. Hadji, and F. de Fornel. “Near-field interactions between a subwavelength tip and a small-volume photonic-crystal nanocavity” In: Phys. Rev. B 76, 4 (2007), p. 041102.
- [78] F. Intonti, S. Vignolini, F. Riboli, A. Vinattieri, D. Wiersma, M. Colocci, L. Balet, C. Monat, C. Zinoni, L. Li, R. Houtré, M. Francardi, A. Gerardino, A. Fiore, and M. Gurioli. “Spectral tuning and near-field imaging of photonic crystal microcavities” In: Phys. Rev. B 78, 4 (2008), p. 041401.
- [79] M. Burresi, T. Kampfrath, D. van Oosten, J. Prangsma, B. Song, S. Noda, and L. Kuipers. “Magnetic Light-Matter Interactions in a Photonic Crystal Nanocavity” In: Phys. Rev. Lett. 105, 12 (2010), p. 123901.
- [80] S. Vignolini, F. Intonti, F. Riboli, L. Balet, L. Li, M. Francardi, A. Gerardino, A. Fiore, D. Wiersma, and M. Gurioli. “Magnetic Imaging in Photonic Crystal Microcavities”. In: Phys. Rev. Lett. 105, 12 (2010), p. 123902.
- [81] R. A. Waldron. “Perturbation theory of resonant cavities”. In: Proc. Inst. Electr. Eng. 107, 12 (1960), pp. 272–274.
- [82] O. Klein, S. Donovan, M. Dressel, and G. Grüner. “Microwave cavity perturbation technique: Part I: Principles”. In: Int. J. Infrared Millim. Waves 14, 12 (1993), pp. 2423–2457.
- [83] M. Burresi. “Nanoscale investigation of light-matter interactions mediate by magnetic and electric coupling”. PhD thesis. The Netherlands: AMOLF Institute, Amsterdam, 2009, p. 31.
- [84] L. Landau and E. Lifshitz. Electrodynamics of continuous media. Wiley, (1984).

## Imaging and engineering optical localized modes at the nanoscale

- [85] T. Grosjean, A. El Eter, M. Mivelle, T.-P. Vo, A. Belkhir, C. Ecoff, D. Nedeljkovic, A. Rahmani, C. Seassal, S. Callard, and F. Baida. “Extraordinary blueshift of a photonic crystal nanocavity by reducing its mode volume with an opaque microtip” In: *Appl. Phys. Lett.* 101, 5 (2012), p. 1102.
- [86] S. Fan, P. Villeneuve, and J. Joannopoulos. “Theoretical investigation of fabrication related disorder on the properties of photonic crystals” In: *J. Appl. Phys.* 78, 3 (1995), pp. 1415–1418.
- [87] A. Rodriguez, M. Ibanescu, J. Joannopoulos, and S. Johnson. “Disorder-immune confinement of light in photonic-crystal cavities” In: *Opt. Lett.* 30, 23 (2005), pp. 3192–3194.
- [88] P. W. Anderson. “Absence of Diffusion in Certain Random Lattices”. In: *Phys. Rev.* 109, 5 (1958), pp. 1492–1505.
- [89] D. Wiersma, P. Bartolini, A. Lagendijk, and R. Righini. “Localization of light in a disordered medium” In: *Nature* 390 (1997), pp. 671–673.
- [90] S. John. “Electromagnetic Absorption in a Disordered Medium near a Photon Mobility Edge” In: *Phys. Rev. Lett.* 53, 22 (1984), pp. 2169–2172.
- [91] A. Lagendijk, B. van Tiggelen, and D. Wiersma. “Fifty years of Anderson localization” In: *Phys. Today* 62, 8 (2009), pp. 24–29.
- [92] G. Mie. “Beiträge zur Optik trüber Medien, speziell kolloidaler Metallösungen” In: *Annalen der Physik* 330, 3 (1908), pp. 377–445.
- [93] C. Lam, P. Leung, and K. Young. “Explicit asymptotic formulas for the positions, widths, and strengths of resonances in Mie scattering”. In: *J. Opt. Soc. Am. B* 9, 9 (1992), pp. 1585–1592.
- [94] R. Pecora. “Dynamic Light Scattering Measurement of Nanometer Particles in Liquids” In: *J. Nanopart. Res.* 2, 2 (2000), pp. 123–131.
- [95] F. Riboli, P. Barthelemy, S. Vignolini, F. Intonti, A. D. Rossi, S. Combrie, and D. Wiersma. “Anderson localization of near-visible light in two dimensions”. In: *Opt. Lett.* 36, 2 (2011), pp. 127–129.
- [96] J. Bertolotti, S. Gottardo, D. Wiersma, M. Ghulinyan, and L. Pavesi. “Optical Necklace States in Anderson Localized 1D Systems” In: *Phys. Rev. Lett.* 94, 11 (2005), p. 113903.
- [97] K. Vynck, M. Burresi, F. Riboli, and D. Wiersma. “Photon management in two-dimensional disordered media” In: *Nat. Mater.* 11 (2012), pp. 1017–1022.
- [98] L. Sapienza, H. Thyrrstrup, S. Stobbe, P. Garcia, S. Smolka, and P. Lodahl. “Cavity Quantum Electrodynamics with Anderson-Localized Modes” In: *Science* 327, v (2010), pp. 1352–1355.

## Chapter 3

### Deep sub-wavelength imaging

Photonic and plasmonic devices rely on the nanoscale control of the spatial and energy distributions of the local density of optical states in dielectric and metallic environments. The tremendous progresses in designing and tailoring the electric LDOS of nano-resonators demand for a deep sub-wavelength imaging tool able to access the optical mode features, triggering the development of different nanoscale imaging techniques. By exploiting the near-field probe perturbation imaging technique, on one hand, SNOM equipped with dielectric tapered probes provides a sub-wavelength electric LDOS detection; on the other hand, SNOM equipped with aperture metal coated probes provides the localized magnetic field component of light. The advent of artificial metamaterials operating at optical frequencies, in which the magnetic interaction with light can be as relevant as the electric response, makes it straightforward to simultaneously detect both field components. Here, we develop a plasmonic near-field probe to strongly enhance the collection efficiency from light-emitters and, more interestingly, to achieve a simultaneous electric and magnetic fields deep subwavelength detection.

### 3.1 Experimental setup

The scanning near-field optical microscope we used is a room-temperature commercial apparatus (TwinSNOM by Omicron), that is assembled on an Zeiss microscope conveniently modified to house the tip holder together with the scanning stages. The standard optical microscope is used for correctly positioning the probe on the sample surface but also to measure the far-field emission. The sample is mounted on piezoelectric stages (P-500 by Physik Instrumente) that enable a nominal spatial accuracy along  $x$ ,  $y$  and  $z$  directions (where the  $xy$  plane is parallel to the sample surface) equal to (1, 1, 0.1) nm in the range (100, 100, 10)  $\mu\text{m}$ . The scanning speed is kept sufficiently low to prevent artefacts caused by the limited photo detector response time. As we have discussed in Chapter (1), in order to achieve a sub-wavelength imaging resolution two requirements have to be fulfilled: *i)* the probe has to be placed in the near-field of the sample; *ii)* the probe must have a sufficiently high throughput.

In the experimental setup the optical fiber terminating in the sharp-tip is glued on an insulating module equipped with a piezoelectric bimorph, as reported in Fig. (3.1 a-b) following the scheme developed in [1]. Bimorph is made of two plates of piezoelectric material with opposite polarization vectors as shown in Fig. (3.1 c). If a voltage

is applied to bimorph electrodes, one of the plates will extend and the other will be compressed, resulting in a bend of the whole element. In order to control the probe-sample distance the excitation piezoelectric, layer 2 in Fig. (3.1 b), induces a small lateral tip oscillation parallel to the sample surface, with a frequency resonant to the system own mechanical frequency (about 60 KHz). While the detection piezoelectric, layer 1 in Fig. (3.1 b), measures the effective tip oscillation signal with amplitude and phase, in analogy with the tuning fork mechanism reported in [2]. As the probe approaches the surface, due to probe-sample interacting shear forces that are effective only at few nanometers distances, the detected amplitude decreases and the relative phase between excitation and detection signals changes. In order to keep constant this phase difference, an electronic feedback drives the sample stage along z, thus ensuring a constant probe-sample distance throughout the whole scan. Finally, by reporting the signal that controls the z piezo as a function of position, we are able to map the surface topography resembling the AFM detection. Furthermore, condition *i*) is satisfied since by a proper calibration of the measured phase difference we can fix the tip-sample distance in a range between 5 nm and 20 nm, which corresponds to the near-field regime, if working with visible or infrared light. On the other hand, condition *ii*) requires a detailed characterization of the apex of the near-field probe. This SNOM setup allows to employ different probes as well as different configurations, such as illumination-collection or near-field collection with far-field illumination. Moreover, many laser sources are available in the visible and near-infrared spectral range in order to perform photoluminescence (PL) of optically active samples or resonant scattering measurements in samples in which light sources are not present.

The schematic of the typical experimental setup performed to detect the PL signal that is coupled to the localized PCN modes, thus allowing us to address the optical properties of the nanocavities, is reported in Fig. (3.2). The SNOM is used in illumination-collection geometry. The PL of the QDs is excited by a laser coupled into a given near-field probe. In the excitation path laser collimated light transmitted through an optical Faraday isolator (F), to prevent back-reflection that alters the laser stability, then through a simple telescope (T) formed by two lens, with  $f_2/f_1 < 1$  to reduce the beam spot size. Before being coupled to the optical fiber that ends with the near-field probe, it passes through a dichroic mirror (DM) that with high efficiency (up to 90%) selectively transmits visible light (up to 1.0  $\mu\text{m}$ ) and reflects infrared light. The laser power emission is possibly adjusted by neutral density filters and the optical fiber used is a single mode fiber operating at 1300 nm. The PL is collected by the same probe, reflected by the dichroic hot mirror, dispersed by a spectrometer (SP, with a 30 cm focal length equipped with a 600 lines/mm grating that exhibits 1.0  $\mu\text{m}$  blaze). Finally, it is detected by a liquid nitrogen-cooled InGaAs array detector (DTC, equipped with an array of 1024 photodiodes, each with a 25  $\mu\text{m} \times 500 \mu\text{m}$  size). The overall spectral resolution is 0.11 nm, as obtained from the FWHM of the experimental spectral response to a delta-like CW laser emitting at  $\lambda = 1300 \text{ nm}$ . At every tip position a PL spectrum is collected, thus obtaining a hyperspectral image of the PCN.

### 3.2 Test-bed sample: the D2 photonic nanocavity

The investigated 2D photonic crystal, together with the inserted nanocavity, is realized on a air-suspended membrane of Gallium Arsenide (GaAs) and it is composed by hexagonal lattice of air holes with  $f = 35\%$  that has been presented in Chapter (2) [3, 4]. The fabrication process involves four steps schematically reported in Fig. (3.3 a). In the middle of the 320 nm thick membrane three layers of high-density ( $10^{11} \text{ cm}^{-2}$ ) Indium Arsenide (InAs) QDs are grown by molecular beam epitaxy, by exploiting the Stranski-Krastanov self-assembly technique [5]. The membrane is grown on top of a 1.5  $\mu\text{m}$  thick  $\text{Al}_{0.7}\text{Ga}_{0.3}\text{As}$  sacrificial layer by patterning a 150 nm thick  $\text{SiO}_2$  mask with a 100 kV electron beam lithography and subsequent  $\text{CHF}_3$  plasma etching. Then, the negative of the mask is transfer on the GaAs layer by  $\text{SiCl}_4/\text{O}_2/\text{Ar}$  reactive ion etching. The suspended membrane is finally released by a selective etching of the sacrificial layer in a Hydrofluoric acid (HF) solution. To obtain PL emission we illuminate the sample by the SNOM probe with a laser that ensures sufficient light energy to excite the QDs exciton recombination, in particular a  $\lambda = 780 \text{ nm}$  cw diode laser or a  $\lambda = 514 \text{ nm}$  cw Argon laser are available. At room-temperature the PL of the large ensemble of quantum dots acts as a broadband internal light source that covers the spectral region in which the PCN modes are present (1200 nm and 1350 nm). The near-field PL spectrum averaged on a membrane region outside the photonic crystal (where the QDs emission is not reduced by the photonic band-gap) is reported in Fig. (3.3 b) and shows two broad peaks corresponding to the single QDs ground state and first excited state, respectively. When the photonic crystal structure is superimposed to the QDs layers, only the allowed narrow are clearly observed since a large amount of QDs emission is inhibited. The investigated photonic nanocavity is formed by removing 4 adjacent holes from the crystal lattice in diamond-like geometry, as highlighted by the SEM image of Fig. (3.4 a). This kind of PCN is called D2 nanocavity and has already been widely studied [6–10]. Due to the peculiar geometry, the local defect lowers the symmetry of the two-dimensional lattice and the PCN belongs to the  $C_{2v}$  spatial symmetry point group and each PCN localized mode is attributed to one of the group irreducible representations [11–13]. Therefore, the D2 cavity supports non-degenerate resonant modes that exhibit different TE-like polarization with defined spatial symmetries in the localized e.m. field distribution [7, 8].

The typical SNOM PL spectrum averaged over the entire PCN and collected by a dielectric probe is reported in Fig. (3.4 b). It shows two narrow and spectrally separated peaks with  $Q = 3000$  corresponding to non-degenerate resonant modes. It has been shown that the lower energy mode (M1) has a linear polarization along  $x$  while the first excited energy mode (M2) shows elliptical polarization with the dominant contribution parallel to  $y$  axis [7]. Different structure, where the photonic crystal lattice constant varies in the range  $0.22 < a/\lambda < 0.29$  but with the same filling fraction, are realized in order to overcame the unavoidable fabrication induced disorder in the photonic crystal, which can largely shift the PCN resonant modes. These scaled structures show the same optical properties apart from different resonant wavelengths, and we choose to investigate the one with the best wavelength matching between the QDs

emission and the PCN modes. Moreover, the same PCN is replicated several times to verify the fabrication reproducibility.

### 3.2.1 Electric field intensity imaging

By performing SNOM measurements it is a straightforward result to achieve the intensity map of every resonant mode on the sample surface. In Fig. (3.6 a-b) are plotted the experimental intensity distributions for the M1 and M2 mode, respectively, centered on the D2 nanocavity and evaluated by reporting as a function of position (i.e. for each spectrum collected) the intensity corresponding to the maximum wavelength of each mode. In particular, the M1 mode is found to be elongated along the  $y$  axis with three circular equally spaced high intensity regions, while M2 shows two lateral crescent shapes distributed along  $x$  direction and a dark central region. Eventually, both intensity distributions have even parity along both axes. The choice of plotting the maximum wavelength maximizes the map intensity contrast.

As explained in Chapter (2) a sophisticated method to improve the SNOM spatial resolution and mode fidelity imaging, without performing further measurements, relies in the study of the tip-induced perturbation imaging and the accurate analysis of the localized modes spectral shift ( $\delta\lambda$ ) as a function of position. In the case of dielectric near-field probes this spectral shift corresponds to the electric field intensity, i.e. the electric LDOS, as stated in Eq. (2.10). The principle underlying the spectral shift evaluation is briefly explained in Fig. (3.5). In Fig. (3.6 c-d) are shown, for both resonant modes, the spectral shift amplitude maps evaluated by performing a Lorentzian function fit of each spectrum in the peak wavelength range and then by extrapolating the spectral shift as a function of position following the method reported in Fig. (3.5). Hence, the blue regions of Fig. (3.6 c-d) represent a wavelength difference equal to zero.

The high fidelity with which the spectral shift maps reproduce the electric LDOS of the nanocavity localized modes is demonstrated by the very good agreement with the three-dimensional FDTD calculated electric LDOS reported in Fig. (3.6 e-f) for both M1 and M2 with unit-cell edge length equal to 10 nm and a spectral resolution of 0.03 nm. The spectral shift distributions clearly show more and smaller details with respect to the intensity maps. In the case of M1, Fig. (3.6 c), are present five intensity lobes along  $y$  that exhibit the maximum spectral shift in correspondence of four symmetric hot-spots. In order to evaluate the SNOM imaging spatial resolution we compare the normalized vertical profiles centered on the experimental and theoretical maps of the mode M1, as reported in Fig. (3.7). In particular, in Fig. (3.7 b) on one hand, the raw PL intensity data do not reproduce every spatial oscillation of the electric field intensity as calculated through FDTD, resulting in a spatial resolution insufficient to detect all the relevant mode features. On the other hand, the spectral shift profile nicely shows the same modulation of the theoretical profile. However, to figure out the actual experimental spatial resolution it is not correct to evaluate the smallest spatial feature of the map. The reason is that the investigated PCN localized modes do not show delta-like spatial features, but the smallest map lobe calculated by FDTD is of the order of 100 nm. Therefore, to estimate the spatial resolution we compare the

experimental spectral shift profile to the profile obtained from the convolution between the calculate LDOS map and two-dimensional Gaussian point-spread functions, characterized by different full widths at half maximum (FWHM). In Fig. (3.7 c) are reported the experimental data and the theoretical profile obtained by a convolution with a Gaussian function of 70 nm FWHM, that minimizes the  $\chi^2$  distribution resulting to a reduced- $\chi^2$  of 1.1. Furthermore, it is important to notice that since the resonant wavelength are extrapolated from Lorentzian fits, the resulting uncertain is lower than the experimental spectral resolution and it is directly provided by the fitting algorithm for each spectrum, as reported in the error bars of Fig. (3.7 c). Therefore, the SNOM PL, combined with the tip-induced spectral shift analysis, allows us to obtain high fidelity electric LDOS mode imaging with an ultra-subwavelength spatial resolution of 70 nm, comparable to the so far best result obtained on PCNs [14].

By the way, the reported spectral shift measurements are in principle analogues to the result obtained in ref. [6] but with an improved spatial resolution, down to  $\lambda/19$  where  $\lambda$  is the vacuum wavelength of the localized mode. Moreover, the reported near-field PL experiments are performed at sufficiently low power laser excitation (60  $\mu$ W) to avoid the presence of a spectral red-shift induced by local high-power laser heating, that may be superimposed or even comparable to the tip-induced spectral shift [9].

The dielectric tip induced perturbation is referred to as “gentle” perturbation meaning that an observable spectral shift is achievable without a large degradation of the cavity  $Q$  factor, thus preserving the resonant mode features such as the electric field spatial distribution. This assumption is confirmed by far-field confocal experiments where the SNOM probe in Fig. (3.2) is replaced by a standard 50X objective and a single mode optical fiber acts as a pinhole, that gives the estimation of the actual unperturbed nanocavity  $Q$  [8, 15]. In particular, for the same nanocavity investigated in Fig. (3.4) the bare PCN possesses  $Q = 3100$  and the dielectric probe locally induces a  $Q$  decrease that ranges in between 5% (when the tip is positioned on the mode tail) and 20% (for tip positioned on the mode electric field maximum) with respect to the unperturbed value.

As in any real experiment, the reported SNOM perturbation imaging technique has also some limitations. To address the issue of reproducibility the same measurements are repeated several times also with different dielectric tips. We find that not every probe gives the same result and a selection of good tips is needed. Only about 25% of the total number of dielectric probes that we fabricate by tube chemical etching gives reproducible results to map the electric LDOS by inducing a gentle and detectable spectral shift. Concerning the imaging performed by a given tip, we obtain similar spectral shift maps and analogue values of maximum spectral shift independently on the investigated nanocavity. However, every near-field probe tends to be damaged by the use, exhibiting a lifetime of the order of a couple of weeks of continuous work. Moreover, since the spectral shift is inversely proportional to the unperturbed resonant mode volume, the perturbation imaging technique could be efficiently applied to any optical nanoresonator in which the perturbing volume is not negligible with respect to the localized cavity mode volume, as stated in [16]. For instance, in the case of M1 mode in the D2 nanocavity we find by accurate FDTD calculation (by employing many large detectors parallel to the slab plane at different

height both inside and outside the slab) and exploiting Eq. (2.6) a mode volume  $V = 0.033 \mu\text{m}^3$ , which is comparable to the L3 nanocavities mode volume [17]. In addition, we are able to give an estimation of the effective tip apex size that is responsible of the dielectric perturbation, approximated with a glass sphere of radius  $R_P$  and 1.5 refractive index. We use Eq. (2.10) and Eq. (2.11) to link the measured maximum spectral shift to FDTD parameters such as the nanocavity mode volume and the out of slab electric field intensity decay rate ( $d=40 \text{ nm}$ , calculated employing multiple field detectors outside the slab). Then, we obtain the tip effective electric polarizability a  $\alpha^e = 1.1 \cdot 10^{-21} \text{ m}^3 \epsilon_0$  and the radius size  $R_P = 100 \text{ nm}$ . This vale of  $R_P$  is comparable to the estimation evaluated by SEM image of the tip. Therefore, the assumption of a tiny but non negligible perturbation is correct, since the perturbing volume  $V_P = \pi R_P^2 d$  is about 30% of the mode volume  $V$ . Finally, it is worth stressing that the estimation of the experimental electric LDOS imaging spatial resolution, 70 nm reported in Fig. (3.7 c), is in agreement (being of the same order of magnitude) with the estimation of the effective tip apex radius that induces the observed spectral shift.

### 3.2.2 Magnetic field intensity imaging

The capability of the SNOM imaging can be enlarged towards the detection of the magnetic component of light localized in a PCN if the dielectric probe is replaced with a metal (aluminum) coated aperture probe. In fact, as discussed in Chapter (2), the aperture probe placed on top of a nanocavity acts as a conductive ring in which the PCN localized magnetic field induces an opposed magnetic dipole, see Fig. (3.8 a-b). The perturbation effect induces a resonant mode blue-shift (towards lower wavelengths) that is proportional to the intensity of the magnetic field component orthogonal to the PCN plane ( $H_z^2$ ), as stated in Eq. (2.7). The magnetic intensity can be retrieved with a sub-wavelength spatial resolution by performing the PL measurements and spectral shift analysis employing metal coated tips. Therefore, we have the capability to image a quantity that in general interacts very weakly with ordinary matter. The first reported observations has been performed simultaneously in ref.s [10, 18]. The former work, investigating a L3 nanocavity, found an effective negative magnetic polarizability for the aperture tip, equal to  $\alpha_{zz}^m = 12 \cdot 10^{-21} \text{ m}^3 / \mu_0$ . The main results of ref. [10] are reported in Fig. (3.8 c-h), since they concern both M1 and M2 modes of the D2 nanocavity. The collected PL intensity maps, Fig. (3.8 c-d), reproduce the basic features of the localized electric field intensity for both modes, with a 100 nm spatial resolution limited by the probe aperture size. However, normalizing for the incident laser power used in experiments with dielectric probes, a huge decrease of the collected signal, down to  $10^{-5}$ , is found. This requires time-consuming measurements with coated probes. In addiction, by reconstructing the spectral shift amplitude maps, Fig. (3.8 e-f), are obtained the images of  $H_z^2$  for both modes in agreement with the FDTD calculations reported in Fig. (3.8 g-h) and, with a sub-wavelength spatial resolution. However, it is clear that the experimental spectral blue-shift maps are affected by strong noise. This behavior is due to the fact that in the regions of maximum blue-shift the PL signal is minimum. In fact, for a spatially confined

mode the magnetic field has a local maximum (proportional to the spectral shift amplitude) in the positions where the electric field (proportional to the signal intensity) is minimum and vice-versa.

In conclusion, the perturbation imaging allows, to map the PCN localized electric field intensity, by employing dielectric near-field probes, and also to retrieve the intensity of the localized magnetic field component that is orthogonal to the photonic slab, by using metal coated aperture probes.

### 3.3 Campanile tips for near-field probing

Given the electric and the magnetic field imaging, it is tempting to combine the two spectrally opposite dielectric and metallic perturbations by employing a probe featuring both an electric and a magnetic effective polarizability. A promising approach can be found in near-field probes functionalized with plasmonic based nanoantenna, as described in Chapter (1). In fact, by designing an advanced metal-dielectric structure on top of a dielectric tip we will show how it is possible to induce a simultaneous electric and magnetic interaction that are comparable in strength. Moreover, this plasmonic probe can be easily employed in the SNOM illumination /collection configuration, since it allows for an efficient far-field to near-field bidirectional coupling over a wide spectral range with an outstanding sub-wavelength spatial resolution.

The geometry of the presented plasmonic SNOM probe consists of a square-based three-dimensional tapered structure terminating in a metal-insulator-metal (MIM) nanogap, which resembles the shape of a campanile bell tower, hereafter referred to as “campanile tip”. The campanile tip design is reported in Fig. (3.9 a). This structure merges high e.m. field enhancement and confinement at the nanoscale with a broadband operation, since it exploits adiabatic plasmonic compression [19–22]. The fabrication process is performed at the apex of a glass-core optical fiber (single mode for  $\lambda = 633$  nm, with core diameter size equal to  $2.5 \mu\text{m}$ ) tapered by the tube etching technique described in Chapter (1). Using a Gallium focused ion beam (FIB) milling (Zeiss Crossbeam 1540), the campanile geometry is carved into the etched glass fiber tip. Using shadow evaporation, 50 nm thick Au layer is evaporated on two opposing sides of the campanile structure. Typically, the resolution of the angle resolved evaporation is not sufficient to create a well-defined gap between the two triangular plates at the tip apex. Hence, a gap is subsequently cut by FIB at the tip apex, resulting in a 40-50 nm wide and 30 nm long gap. The SEM images of the campanile tip apex that exhibits a clear nanogap formation are reported in Fig. (3.9 b-c). Of course, the fabrication resolution can be even increased by using a Helium FIB. The campanile tip geometry allows strong electric field enhancement confined at the nanogap, as shown by the finite element calculation performed by COMSOL Multiphysics 4.2 software reported in Fig. (3.10). The calculation are evaluated at  $\lambda = 666$  nm for a nanogap size of 10 nm. The other design parameters are reported in the caption of Fig. (3.9), and the frequency dependent relative permittivity of gold is taken from Palik’s handbook [23] while the refractive index of the  $\text{SiO}_2$  layer is set as  $n = 1.5$ . The electric field enhancement distribution inside the campanile tip, that is the ratio of the electric field

strength,  $|E|^2$ , in the nanogap and the incoming field strength,  $|E_0|^2$ , is reported in Fig. (3.10 a-b). It shows that the probe provides efficient coupling between far-field and near-field. In fact, the fundamental mode in an MIM structure, polarized along the direction perpendicular to the metal surface ( $y$ ), is supported without any cutoff frequency, no matter how thin the insulating layer [20]. The plasmonic mode in the campanile is confined to the gap region, which thus defines the improved spatial resolution with respect to conventional metal coated aperture probes. The field enhancement is plotted in Fig. (3.10 c) for an aperture size of 10 nm. Typically, in conventional aperture probe, a 30-100 nm thick metallic cladding is employed to confine light inside the fiber and funnel it to the nanoscale aperture, as described in Fig. (1.8 b). However, this metal coating implies boundary conditions for the e.m. wave travelling inside the fiber leading to a mode cutoff, including the SPP mode, before reaching the aperture. The strong field confinement in the campanile tip is due to the smooth reduction of the radius of the metal tapered waveguide that produces an adiabatic transformation of the SPPs. Phase and group velocity of the SPPs tend to zero while approaching the tip, and at the same time the SPPs e.m. fields are largely enhanced, thus producing a nano-focusing effect. Moreover, the high throughput is effective over a broad spectral range, as highlighted in Fig. (3.10 d). The operating bandwidth is limited only by metal absorption at short wavelengths and extends into the infra-red region. The calculations of Fig. (3.10 d) also point out that the electric field enhancement is larger than the one of a bow-tie antenna with same-sized gap. Here, we evaluate only the electric enhancement, which corresponds to the tip ability to detect a signal in PL measurements, since we are interested in the campanile tip throughput. While the tip induced perturbation effect will be afterwards analyzed. Another advantage of the campanile tip relies on the highly confined field in the gap region and results in almost background free acquisition. By operating with the experimental setup presented in Fig. (3.2), the PL signal collected back through the antenna gap is affected by the background arising from the edge-scattered light, which is found to be far below the noise threshold.

### 3.3.1 Mapping local charge recombination heterogeneity

In order to demonstrate the notable performances of the plasmonic nanoantenna, we employ campanile tips with 40 nm gap for mapping the inhomogeneous radiative recombination in individual InP quantum-wires. These nanostructures are chosen because of the intense and linearly polarized PL emission in the near-infrared and the potential application as light-harvesting nanostructures, due to the 1.4 eV bandgap and low surface recombination rates [24, 25].

The indium phosphide nano-wires are prepared by chemical vapor deposition using trimethylindium and tertbutylphosphine as In and P sources, respectively. The nanowires are grown at 415 C for 10 minutes and under a flow of H<sub>2</sub>, on a Si [111] substrate with a 2 nm thick gold film acting as catalyst for the nano-wire formation. The process gives 1-5 m long and 30-100 nm thick nanowires. TEM analysis shows that the wires have a zinc-blend structure and grow in the [111] direction with cylindrical shapes with clean, often atomically flat, cleaved ends. The nano-wires are then

dried and transferred to 100 nm thick SiO<sub>2</sub> support with alignment marks to allow us to investigate the same wire with multiple techniques. A SEM image of one of the examined wires is reported in Fig. (3.11 e).

The single nano-wire PL is collected by campanile tips employing the experimental setup of Fig. (3.2) with a He-Ne laser excitation, with a 50/50 beam splitter for replacing the dichroic mirror, with a 695 nm long pass filter in front of the spectrometer and a Si-based CCD camera for detection at wavelength around 850 nm, with a spectral resolution of 0.10 nm. The light polarization is controlled during the propagation along the optical fiber by using mechanical compensator based on a Babinet-Soleil compensator, that permits to apply a controlled pressure and rotation to the fiber. Therefore, acting on the compensator, by maximizing the PL signal of the nano-wire, the excitation light is forced to be polarized along  $y$  when it approaches the campanile tip. At each pixel during the scan a spectrum is recorded, thus hyperspectral imaging is obtained as shown in Fig. (3.11 a-c). In Fig. (3.11 d and e) the same InP quantum-wire is investigated by a confocal setup, with a 100x and 0.7 NA objective, to highlight a comparison with the results obtained by campanile tip.

In Fig. (3.11 c) normalized spectra acquired along the wire length by campanile tip are reported. They show evident local spectral variations. In particular, the hot spots of the intensity map in Fig. (3.11 a) shows spectra with a blue-shift emission of the band-edge, as well as stronger contributions from trap-related spectral components above the bandgap that broadens the spectra considerably. In fact, the emission peak at 839 nm (1.47 eV) corresponds to the expected 100-meV blue-shift relative to bulk InP wire, independent on quantum confinement [26].

In contrast, confocal intensity map of the same wire evaluated at the same wavelength, reported in Fig. (3.11 d), displays two maxima but without any spectral variation along the wire, see Fig. (3.11 f). It was previously observed that strong PL enhancements and spectral blue-shifts result from passivated InP nano-wire surfaces [26]. This was attributed to Coulombic interactions between excitons and positively charged trap states on the wire surfaces, that influence the optoelectronic properties of nanocrystals and nano-wires [27]. The exciton diffusion length in these materials is hundreds of nanometers, and therefore individual trap states within the diffusion volume should strongly influence the local absorption energy and charge recombination rate.

We believe that the heterogeneity observed along the wires, Fig. (3.11 a), on length scales well below the exciton diffusion length, are direct maps of trap-state modifications of the local exciton properties. The observed hot spots are probably due to an increase of trap-state densities (and changes in the native oxide layer) at the wire ends. Their spectral characteristics are consistent with a trap-induced Stark shift, predicted to be about 60 to 70 nm above the band-edge for positive trap states [26, 27]. The absence of spectral variations in the confocal measurements is attributed to the low spatial resolution obtainable in the far-field, especially in the  $z$  direction that force to probe the entire wire thickness. Then surface-specific effects are obscured by the bulk behaviour. A different experimental approach based on cathodoluminescence could achieve a comparable spatial resolution. However, the large number of incident electrons fill the trap states and do not detect any spatial variation in emission from InP nano-wires [28].

In order to test the imaging reproducibility, we investigated a second quantum-wire, whose SEM image is reported in Fig. (3.12 a), by a different campanile tip. The PL intensity distribution evaluated at every wavelength in the peak emission shows the same heterogeneity of the previous Fig. (3.11 a). The campanile tip provides an optical resolution much higher than the confocal approach, as can be seen in Fig. (3.12 d) by comparing the intensity profile along the line orthogonal to the wire length acquired by campanile tip, by confocal setup and by SEM topography, highlighted by the red lines in Fig. (3.12 a, b and c) respectively. A line scan along the wire length, reported in Fig. (3.12 e), reveals a spatial resolution of 40 nm approximately equal to the nanogap size, whereas the topographic line scan is almost flat and shows negligible variations. Here, the spatial resolution is evaluated as the spatial difference between 90% to 10% of the PL signal in the measured sharpest variation, since, differently from PCNs, we cannot model or calculate the emission properties of the investigated quantum-wires.

In conclusion, we prove that campanile-style far-field to near-field transformers provide a pathway for understanding energy conversion processes at critical length scales, yielding insights into the role of local trap states in radiative charge recombination in InP nano-wires. More generally, our study demonstrates the impact of the campanile geometry on a wide range of nano-optical measurements, because it can virtually be implemented in many imaging and spectroscopy methods, including Raman and infrared/Fourier transform, as well as white-light nano-ellipsometry/interferometric mapping of dielectric functions. We expect that the large bandwidth enhancement makes them ideal for ultrafast pump-probe and nonlinear experiments down to molecular length scale [29, 30]. They also could be used for ultrasensitive medical detection, photo-catalysis and quantum-optics investigations, as plasmonic optomechanics and circuitry elements. Finally, concerning the measurements presented in this section, seven campanile tips on different optical fibers were produced. We tested all of them and they gave reproducible results.

### 3.3.2 Simultaneous imaging of electric and magnetic fields

In order to demonstrate that campanile tips are able to simultaneously image both the electric and the magnetic field intensity of light localized in optical nanoresonators, we perform PL measurements on the D2 photonic crystal nanocavity presented in Fig. (3.4). We employ the experimental setup of Fig. (3.2). As reported in the schematics of Fig. (3.13 a), the measurements are performed exciting the QDs embedded inside the sample with the cw diode laser (780 nm) and a power of 120  $\mu\text{W}$  delivered to the near-field probe. The typical SNOM spectrum acquired in this configuration in the middle of the PCN with lattice constant  $a = 311 \text{ nm}$  is shown in Fig. (3.13 b), in the spectral range of M1 and M2 modes. It highlights a high signal/noise ratio, signature of an excellent tip throughput with respect to standard coated aperture probes. In fact, if we compare the signal detected in Fig. (3.4 b) with the one reported in Fig. (3.13 b) on the same PCN, we find only one order of magnitude reduction in the throughput achieved by campanile tips with respect to dielectric tapered probes.

The high throughput is unfolded by the strong electric field enhancement confined at the nanogap, together with a magnetic field enhancement inside the tip in close proximity to the apex. These results are shown by the FEM calculation, evaluated at  $\lambda = 1.3\mu\text{m}$  for a 40 nm nanogap, reported in Fig. (3.13 c-d), respectively, in close analogy with the behavior reported in Fig. (3.10 b), which is evaluated at smaller wavelength and for a smaller nanogap. Moreover, we demonstrate that the high tip throughput is effective in a broad spectral range as highlighted in Fig. (3.13 e). Concerning the induced perturbation on the PCN, the metal-insulator-metal (MIM) apex of the campanile tip can be modelled by two metal dipole nanoantennas spaced by 40 nm of dielectric material. Mimicking this kind of system by an equivalent RLC circuit is a widely used approach [31]. It is well-known that RLC circuits show an effective electric interaction associated with the capacity C together with an effective magnetic interaction that is driven by the inductance L. In fact, the electric polarizability describes dielectric probes as effective capacitors, while the diamagnetic response allows schematizing metallic coated aperture tips as inductances. The interaction of the campanile tip apex with AC electromagnetic fields can be mimicked by an equivalent RLC circuit. This analogy helps us to understand the simultaneous presence of both electric and magnetic polarizability. In particular, in the campanile tip the inductance is driven by a combination of electric and displacement currents flowing at the MIM apex structure. Moreover, around the resonant wavelength the electric and magnetic energies stored in the circuit are of the same order of magnitude [32]. The key point we exploit is that, while the induced electric dipole is parallel to the external electric field, the L response is diamagnetic, meaning that the associated magnetic dipole is antiparallel to the inducing magnetic field. This has strong effects on the tip perturbation of the nanocavity mode wavelengths, since the electric induced shift is expected to be toward red spectral regions, while the magnetic perturbation induces a blue-shift. Therefore, the role of the campanile tip is twofold. On one hand, it combines the dielectric perturbation effect with the perturbation induced by a metal coated tip, resulting in a concomitant electric and magnetic polarizability. On the other hand, the electromagnetic field enhancement accounts for PL spectra with a signal/noise ratio that allows monitoring with high accuracy the spectral position of the resonant mode maximum. We evaluate the PCN localized modes spectral shift that is related to the electric and/or magnetic field component of light, depending on the effective electric and/or magnetic interaction.

By exploiting the perturbation approach, we experimentally succeed, during the same scan, in extracting high quality maps of the electric and the magnetic field intensities of the localized modes with a sub-wavelength spatial resolution. This allows us to overcome the long-standing problem, discussed in Sec. (2.2), that is related to the critical interpretation of the signal directly collected by SNOM probes. This issue normally requires an accurate model of the experimental configuration and comparison of the collected signal with the calculated spatial distribution of the electric and magnetic fields, thus differentiating our work with respect to ref. [33].

We find that the peak wavelength of each mode is strongly dependent on the tip position on the sample surface. The effect is highlighted for M1 in Fig. (3.14 a-b), which report the schematic of the sample where three different spots (A, B and C) are indicated, together with the normalized PL spectra collected at these positions by the

campanile tip, respectively. The PL spectrum recorded at position A, where M1 mode has maximum electric field as stated in Fig. (3.6 e), shows a red-shift with respect to the spectrum detected outside the PCN (position C, where the intensity of the mode M1 is quite negligible). At the same time the PL peak observed when the tip is positioned in B is blue-shifted with respect to the spectrum detected in C. In fact, in B the cavity resonant magnetic field intensity has a local maximum, as highlighted by the dominant out-of-plane intensity component calculated in Fig. (3.8 g). Since the tip perturbation can be considered negligible a few microns outside the nanocavity, the observed red and blue spectral shift demonstrates the simultaneous electric and magnetic susceptibility of the campanile near-field probe. In order to establish the precise resonant wavelength of both modes, Lorentzian fits of each spectrum are performed. To highlight the variation of the shift, we report in a two-dimensional map the wavelength difference between the peak wavelength at every position and the peak wavelength outside the PCN. The results are shown in Fig. (3.14 c-d), and correspond to the spectral shift maps of the M1 and M2 modes, respectively. Notably, a significant modulation of the spectral shift is observed in both maps. Of course, a useful characteristic of the investigated PCN in discriminating the tip induced shift of both modes is that they are more spectrally separated than the maximum observed spectral shift. The experimental ratio between the magnetic and electric response of the campanile tip can be evaluated as the ratio  $\beta$  between the maximum blue-shift and the maximum red-shift. For both modes it is found to be of the order of 0.5 and in particular:

$$\beta(M1) = |-0.28 \text{ nm}| / 0.60 \text{ nm} = 0.47 \quad (3.1)$$

$$\beta(M2) = |-0.18 \text{ nm}| / 0.33 \text{ nm} = 0.55 \quad (3.2)$$

which demonstrate a well-balanced dielectric and diamagnetic response of the campanile probe. This characteristic gives simultaneous access, in a single measurement, to both fields with similar sensitivity, which is intriguing if one considers that the diamagnetic response of normally occurring materials in the optical spectral range is usually many orders of magnitude smaller than the dielectric response [34].

The experimental data show that the campanile probe has a concomitant positive electric and negative magnetic polarizability, as initially supposed. The different sign of the dielectric and diamagnetic response, together with the fact that for any standing wave the nodes of the electric field correspond to the maxima of the magnetic field and vice-versa, allow us to discriminate with high fidelity between the two field components. In principle, similar properties could also apply to other plasmonic nanoantennas. The use of a campanile probe has a double benefit, as it enhances the near field coupling and also makes the magnetic and electric perturbation interaction of comparable magnitude.

To corroborate this interpretation we perform FDTD calculations of the field distributions of the localized photonic modes. The maps associated to M1 and M2 are reported in Fig. (3.15 a-b) for the electric field intensity (red color scale) and in Fig. (3.15 c-d) for the magnetic field intensity in negative units (blue color scale), respectively. In order to compare the numerical calculations and the experimental data reported in Fig. (3.14 c-d), the experimental parameters  $\beta$  between the magnetic and the electric response of the campanile tip evaluated in Eq. (3.1) and Eq. (3.2) are used

to reproduce the expected spectral shift map. In particular, we construct a linear combination of the FDTD calculated electric and magnetic normalized intensities, assuming a negligible electric field at the magnetic field maxima and conversely, by using a simple relation formula deduced from Eq. (2.7):

$$\frac{\delta\lambda}{\lambda} \propto \frac{|\mathbf{E}_0(\mathbf{r})|^2}{|\mathbf{E}_0(\mathbf{r})|_{max}^2} + \beta \frac{|\mathbf{H}_0(\mathbf{r})|^2}{|\mathbf{H}_0(\mathbf{r})|_{max}^2} \quad (3.3)$$

The maps calculated with  $\beta(M1) = 0.47$  and  $\beta(M2) = 0.55$  for the modes M1 and M2 are reported in Fig. (3.15 e-f), respectively, and closely match the experimentally measured field patterns of Fig. (3.14 c-d) in all the relevant details.

The experimental spatial resolution of the perturbation imaging method obtained with the campanile tip is estimated by analyzing the map along one-dimensional profile cut. For instance, in Fig. (3.16 a-b) are shown the M2 experimental spectral shift map and the FDTD calculation using Eq. (3.3), respectively, where the central horizontal dashed lines represent the two spatial profiles to be compared. The nanogap size at the apex of the campanile probe is a priori expected to give a spatial resolution of 40 nm. This assumption is examined by comparing the spectral shift data profile and the theoretical profiles obtained by the convolution between the FDTD map of Fig. (3.16 b) and two-dimensional Gaussian point spread functions, characterized by different FWHM and whose intensities are normalized to the experimental spectral shift amplitude range. The profile obtained with a Gaussian point spread function of 40 nm FWHM nicely reproduces the measured values within the experimental uncertainties, by minimizing the  $\chi^2$  distribution. In Fig. (3.16 c) we report the spectral shift data profile along with the FDTD results convoluted with Gaussian functions of 40 nm and 80 nm FWHM. The former convolution better reproduces the experimental data. Therefore, the spatial resolution achieved by the campanile probe imaging technique reaches the expected 40 nm limit (down to  $\lambda/30$ ), determining a huge improvement with respect to standard dielectric or metal coated probes.

There are many advantages with respect to direct near-field signal collection imaging performed with standard coated tip. First of all, the technique is sensitive not only to the in-plane e.m. fields, thus neglecting the dominant contribution to the magnetic component of the TE-like mode, but it can access the total intensity of both fields, which correspond to the electric and magnetic LDOS of the localized modes. Secondly, the mode perturbation induced by the tip polarizabilities is directly proportional to the LDOS and does not require a detailed model of the near-field probe signal collection. This not only means a high fidelity imaging but also that after calibrating the mode shift on a well characterized sample it is possible to obtain a quantitative measurement of the electric and magnetic LDOS for any nanoresonators.

Finally, and importantly for many applications, the campanile tip has an enhanced throughput, which leads to the possibility of investigating also weak resonances and even individual quantum emitters. For instance in the reported measurements the collected PL signal with campanile tip is three orders of magnitude higher than the PL collected in nominally identical experiments performed with Al-coated aperture probes with a nominal aperture of 200 nm, normalized at the same excitation power and integration time. The excellent agreement between the experimental data and the

near-field numerical calculations clearly indicates that the campanile probe induced-perturbation imaging is able to catch the details of the electric and the magnetic intensity distributions of optical modes, with an ultra sub-wavelength spatial resolution.

Combined access to the near-field electric and magnetic components of optical modes, could improve innovative devices based on the interplay between the electric and the magnetic optical response, such as nano-metamaterials at optical frequencies. These nanoscale architectures, where the magnetic interaction with light can be as relevant as the electric response, exhibit unprecedented light behaviors, such as negative or zero refractive index, optical cloaking and superluminal phenomena [35, 36]. Furthermore, they are promising both for fundamental science and for cutting edge technologies, triggering the quest for novel sensing applications and field-enhancement effects at the nanoscale [37, 38]. One possible actual implementation could be coupling light nano-emitters (like molecules or quantum dots) to metamaterial or nanoresonator for tailoring the spontaneous emission rate through electric and/or magnetic dipoles interaction (electric or magnetic Purcell effect [39, 40]), by exploiting the knowledge of electric and magnetic local density of states with a unprecedented spatial resolution.

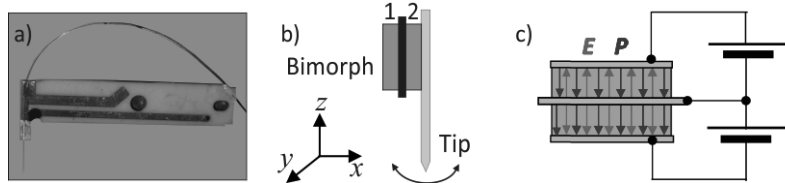


Figure 3.1: a) Image of the optical fiber that ends with the SNOM tip. The fiber is glued to the module that possesses piezoelectric controller whose electric contacts are clearly visible. b) Lateral view of the module schematics to highlight the bimorph piezoelectric (orange) whose detection and the excitation components are labelled as 1 and 2, respectively. Black arrows show the tip controlled oscillation plane. c) Schematics of the piezoelectric bimorph operation, where ***E*** and ***P*** represent the electric field and polarization, respectively.

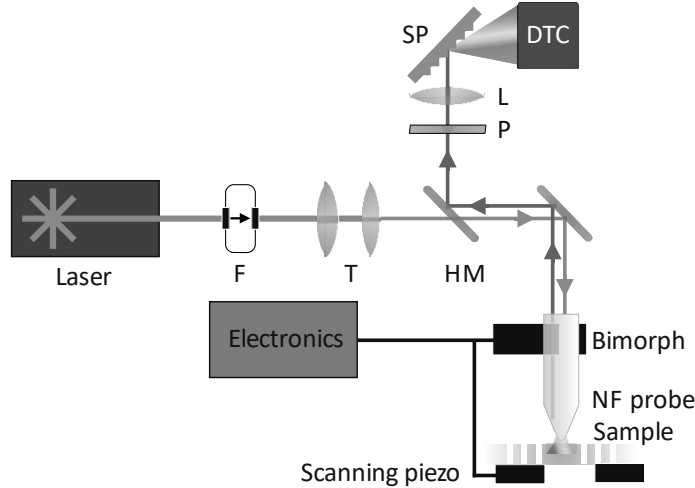


Figure 3.2: Schematics of the illumination-collection SNOM setup able to detect the photoluminescence signal emitted in the localized PCN modes. F corresponds to a Faraday optical isolator, T is a telescope formed by two lens, HM an hot dichroic mirror, P a long-wavelength pass filter, L a lens that focuses the PL signal to a spectrometer (SP) and DTC a detector composed by an array of InGaAs photodiodes. The piezoelectric bimorph and scanning system are both driven by the same electronic central unit.

Imaging and engineering optical localized modes at the nanoscale

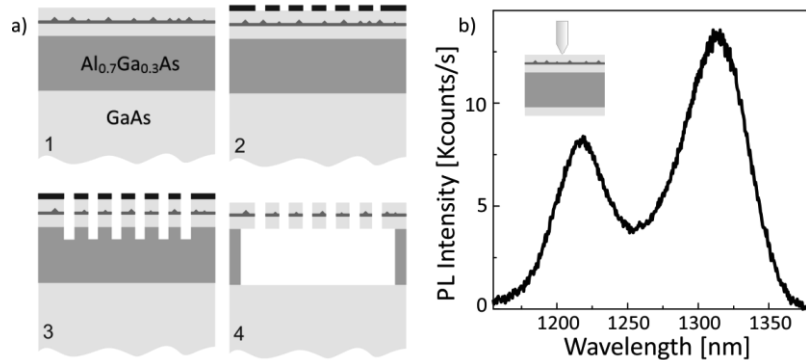


Figure 3.3: a) Four subsequent fabrication steps (1-4) performed to create the GaAs (light-gray) photonic crystal slab with InAs QDs embedded (red layer). The dark-gray region represents the Al<sub>0.7</sub>Ga<sub>0.3</sub>As sacrificial layer and the black layer is the SiO<sub>2</sub> mask. b) Typical spectrum of the quantum dots PL detected by SNOM equipped with dielectric probe in a region outside the photonic crystal, as highlighted by the inset. The excitation light is provided by the  $\lambda = 780$  nm cw diode laser with 60  $\mu$ W power delivered to the probe.

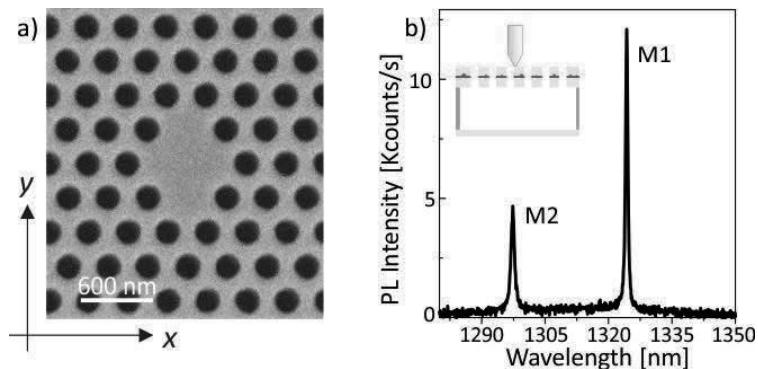


Figure 3.4: a) SEM image of the investigated D2 PCN with lattice constant  $a = 331$  nm. b) Typical spectrum averaged over the D2 cavity detected by SNOM dielectric probe as highlighted by the inset. The excitation light is provided by the  $\lambda = 780$  nm cw diode laser with 60  $\mu$ W power delivered to the probe. Both resonant modes M1 and M2 exhibit clear PL peaks.

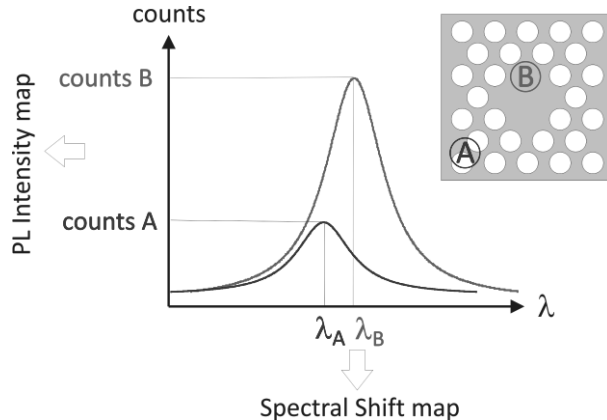


Figure 3.5: Schematic explanation of the spectral shift evaluation technique. Two spectra, blue and red lines, are reported as a function of the wavelength and correspond to the signal collected by the SNOM dielectric tip in position A and B on the D2 nanocavity, respectively. The spectrum acquired inside the PCN (position B) has higher counts and a higher wavelength peak position with respect to the spectrum collected outside the cavity. By analyzing the number of counts collected as a function of tip position, we retrieve the intensity map of the mode. On the other hand, by reporting the peak wavelength as a function of tip position we obtain the spectral shift map.

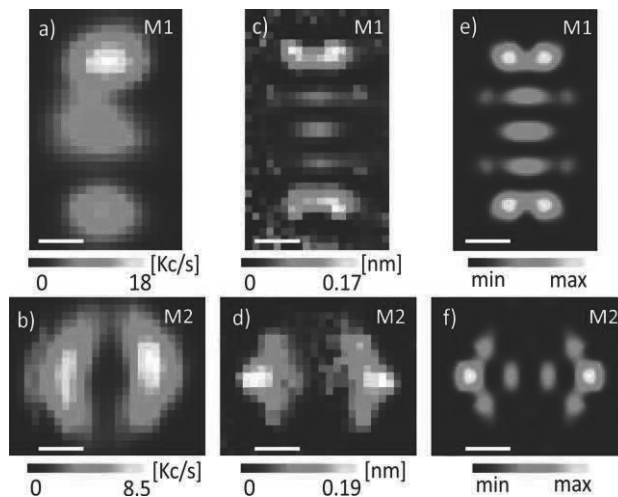


Figure 3.6: a)-b) Map of the intensity collected in the  $xy$  plane few nanometers above the slab at M1 and M2 peak wavelength, respectively. c)-d) Map of the induced spectral shift amplitude for M1 and M2, respectively. e)-f) FDTD electric field intensity distribution calculated at M1 and M2 unperturbed resonant wavelength, respectively. The scale bar in all the maps is 300 nm.

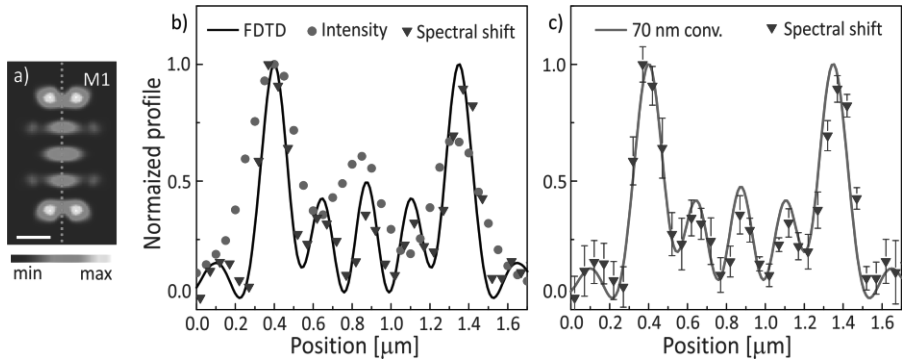


Figure 3.7: a) Map of the electric LDOS intensity calculated by FDTD at M1 resonant wavelength. The dotted orange line highlights the position where the profiles reported in b) and c) are considered, both in the experimental and in the theoretical map. b) Comparison between the normalized vertical profiles of M1 obtained by the FDTD calculation (black line), by the PL intensity (red dots) and by the spectral shift analysis (blue triangles), respectively. c) Comparison between the normalized vertical profiles of M1 obtained by a convolution of the FDTD map with 70 nm FWHM two-dimensional Gaussian point-spread function (red line) and the experimental spectral shift profile (blue triangles), where the error bars are provided by the Lorentzian fit.

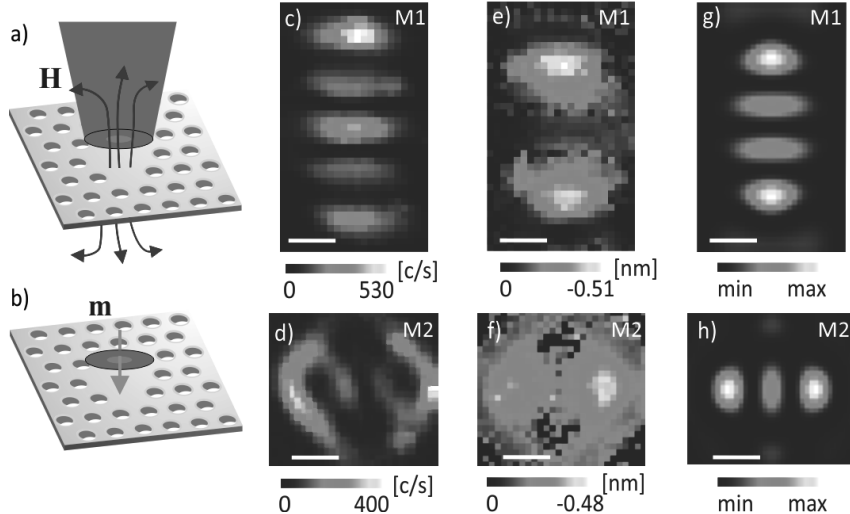


Figure 3.8: a) Schematics of the metal coated probe interaction with the magnetic field of light (blue arrows) localized in the PCN. b) The near-field probe is represented as a conducting ring that generates a magnetic dipole (green arrow) opposite to the out-of-plane magnetic field. c)-d) Map of the intensity collected in the  $xy$  plane few nanometers above the slab for the M1 and M2 peak wavelength, respectively. e)-f) Map

of the induced spectral shift amplitude towards lower wavelength for M1 and M2, respectively. The excitation light is provided by the  $\lambda = 780$  nm cw diode laser with 2.0 mW power delivered to the probe. g)-h) FDTD intensity distribution of the magnetic field out-of-plane component calculated for M1 and M2, respectively. The scale bars in all the maps are 300 nm. Adapted from [10].

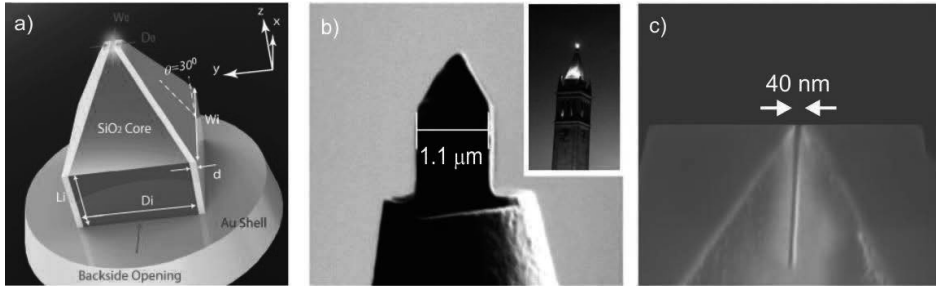


Figure 3.9: a) Schematics of the campanile tip geometry composed of a gold tapered metal-insulator-metal waveguide fabricated at the end of a tapered glass fiber with the identification of the characteristic parameters:  $d=50$  nm,  $\theta=30^\circ$ ,  $W_0=20$  nm,  $L_i=200$  nm,  $W_i=200$  nm,  $D_0=10$  nm,  $D_i=200$  nm. b)-c) SEM images of the campanile tip with a 40 nm nanogap, which resembles the shape of a bell tower, as shown in the photo of the Berkeley campanile reported in the inset of b).

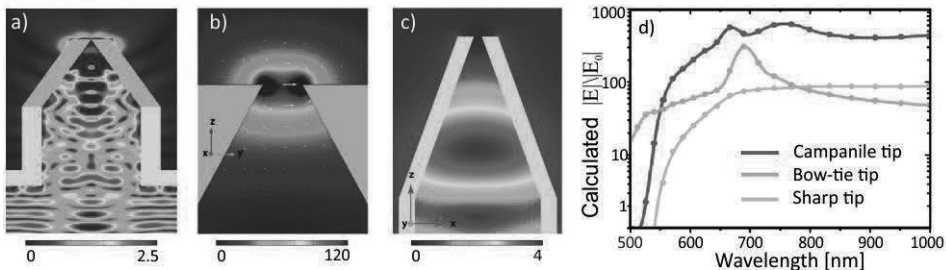


Figure 3.10: a) Finite element method calculation of the electric field enhancement distribution at the campanile tip apex for a nanogap size of 10 nm and  $\lambda = 666$  nm. The mode propagating in the fiber is excited by a plane wave linearly polarized along  $y$ . b) Same result of a), but restricted to the nanogap region and in a saturated color-scale contrast to show the nearly background-free enhancement at the tip apex. c) Electric field enhancement distribution at the apex of a conventional gold coated probe for an aperture size of 10 nm. d) FEM electric field enhancement calculation as a function of the incident wavelength for a campanile tip with a 2 nm gap (red curve) that extends over larger bandwidth than does the response of a bow-tie antenna (blue curve) with the same gap or a sharp gold tip with a 20 nm size aperture (gray curve).

## Imaging and engineering optical localized modes at the nanoscale

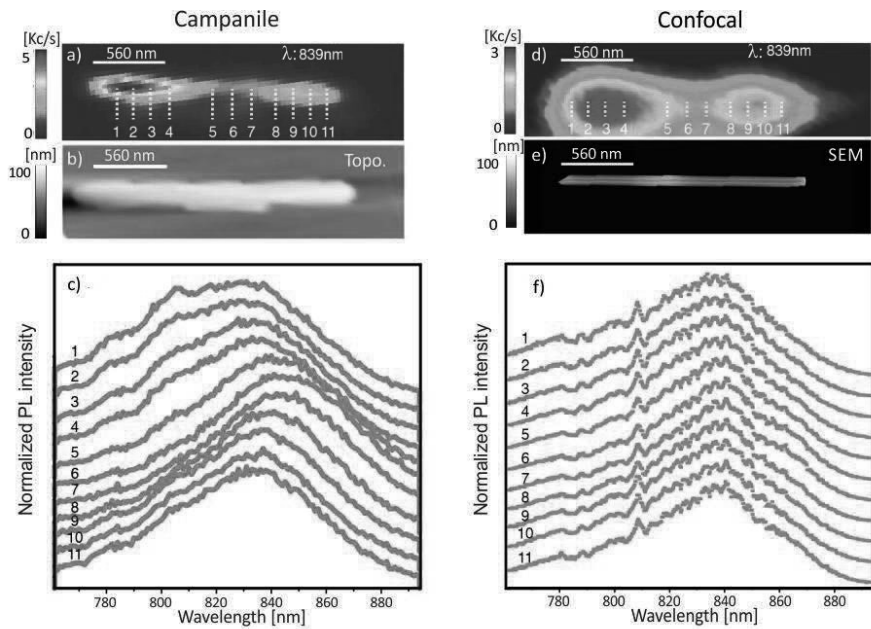


Figure 3.11: a)-c) SNOM PL measurements performed by campanile tip on a InP quantum-wire, using He-Ne cw laser emitting at  $\lambda = 633\text{ nm}$  and employing an excitation power of  $100\text{ }\mu\text{W}$  inside the tip. a) PL intensity distribution evaluated at  $\lambda = 839\text{ nm}$ ; b) topography image; c) waterfall plot of normalized spectra acquired at positions 1 to 11 reported in a) shows strong local spectral variations. d) and f) PL measurements performed on the same quantum-wire by a confocal setup. d) and f) are the confocal analogous of a) and c), respectively. e) SEM image of the wire.

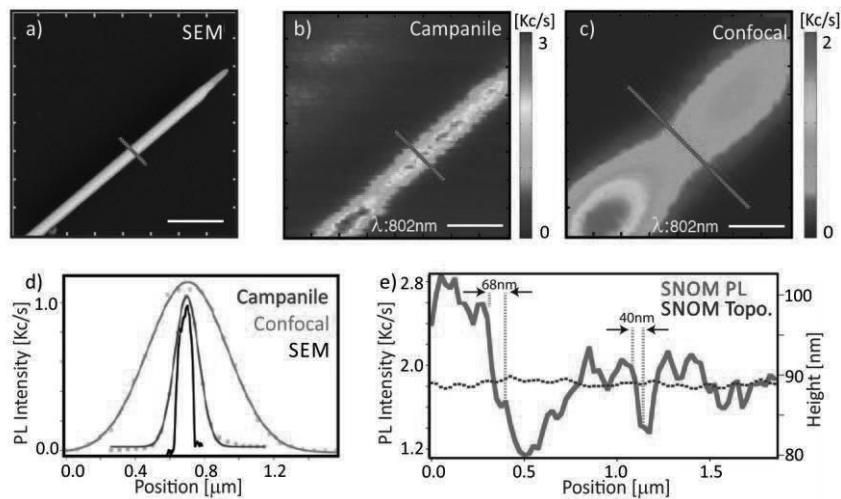


Figure 3.12: a) SEM image of a different quantum wire with respect to Fig. (3.11). b)-c) PL intensity distribution evaluated at  $\lambda = 802$  nm by campanile probe and by confocal setup, respectively. d) Comparison between intensity acquired in a)-c) along the central profile orthogonal to the wire length (red lines). e) Intensity profile (red curve) and topography profile (dotted curve) collected by SNOM along the wire length reveal a spatial resolution of about 40 nm.

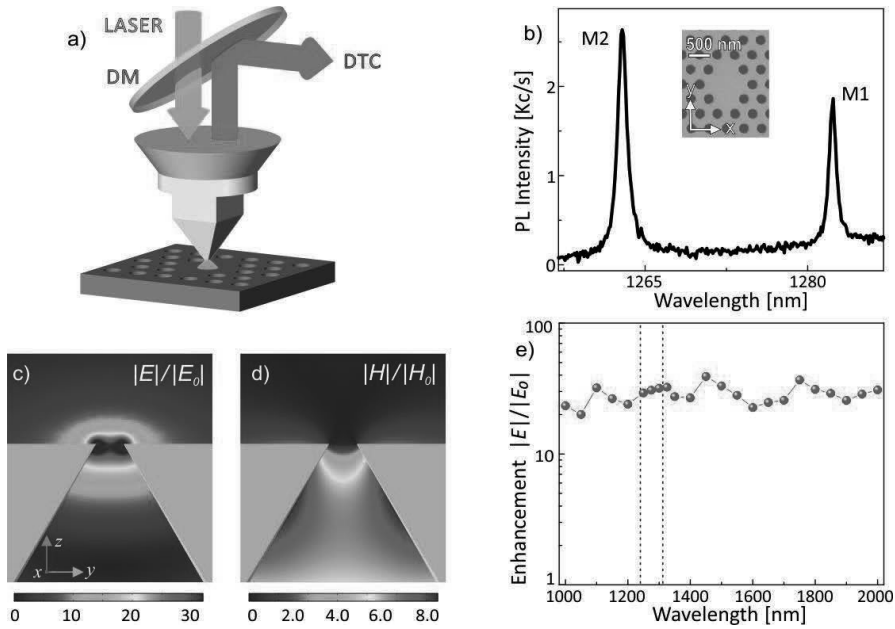


Figure 3.13: a) Three-dimensional schematics of the experimental setup. The excitation light is provided by the cw diode laser (780 nm) with  $120 \mu\text{W}$  power. DM is the dichroic mirror and DTC represents the detection unit. b) Typical PL spectrum collected by the campanile tip in the middle of the PCN with lattice constant  $a = 311$  nm reported in the inset. c)-d) FEM calculations of the electric and magnetic field enhancement distribution, respectively, at the campanile tip apex for a nanogap size of 40 nm and  $\lambda = 1.3 \mu\text{m}$ . The mode propagating in the fiber is excited by a plane wave with electric field linearly polarized along  $y$ , it follows that the electric (magnetic) field at the tip apex is mainly  $y$  ( $x$ ) polarized. e) FEM electric field enhancement calculated over the near-infrared spectral range for a campanile tip with a 40 nm gap. The dashed vertical lines highlight the experimental spectral region.

Imaging and engineering optical localized modes at the nanoscale

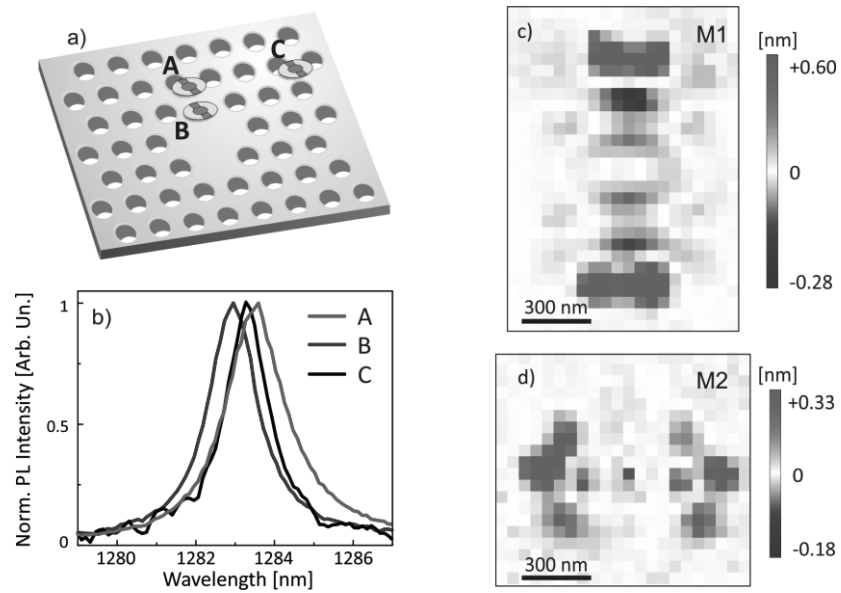


Figure 3.14: a) Schematic of the investigated PCN where the three yellow-blue rings A, B and C represent the positions where the spectra reported in b) are collected by the campanile tip. b) Normalized PL signal of the M1 mode collected in the three positions reported in a). In the same scan the evidence of both a red (A) and a blue (B) tip induced spectral shift, with respect to the peak detected outside the cavity (C), is clear. c)-d) Experimental spectral shift amplitude distributions for the M1 and M2 mode, respectively. They are obtained reporting the maximum peak wavelength, evaluated by a Lorentzian fit, as a function of the tip position. The white color, for each map, corresponds to the smaller-perturbed wavelength detected in the position about 1  $\mu\text{m}$  away from the center of the PCN.

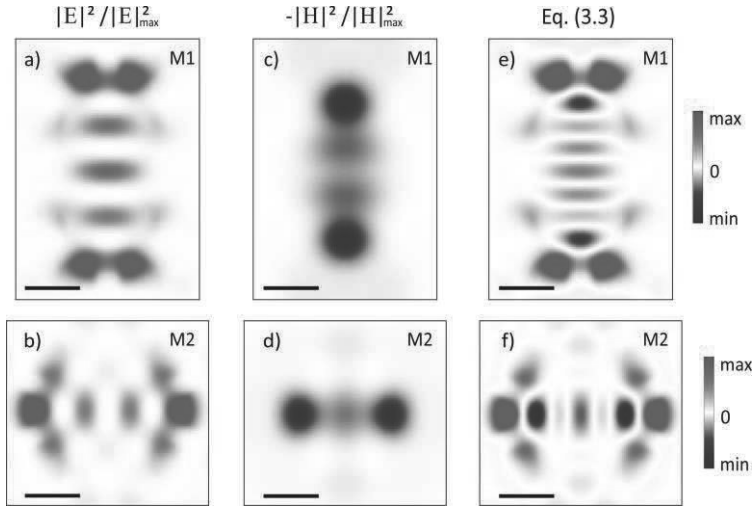


Figure 3.15: Finite-Difference Time-Domain calculations. a)-b) ( $\mathbf{E}^2$ ) distribution normalized to the maximum for M1 and M2 mode, respectively. c)-d) ( $-\mathbf{H}^2$ ) distribution normalized to the maximum for M1 and M2 mode, respectively. e)- f) Distributions evaluated using Eq. (3.3) with  $\beta(M1) = 0.47$  and  $\beta(M2) = 0.55$ , respectively. These maps nicely reproduce the experimental spectral shift maps reported in Fig. (3.14 c-d). The spatial scale bar is 300 nm in every map.

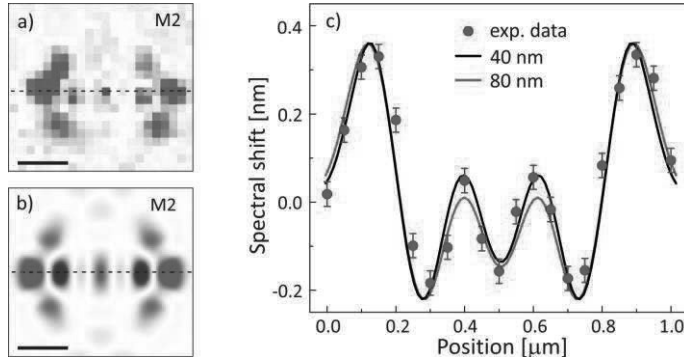


Figure 3.16: Spatial resolution of the campanile tip perturbation imaging method. a)-b) Comparison between the spectral shift data and the FDTD calculation using Eq. (3.3) with  $\beta(M2) = 0.55$ . The horizontal dashed lines indicate where the spatial profiles reported in c) are evaluated. The scale bars are 300 nm. c) Spectral shift data (red dots) collected, as a function of position, along the dashed line in a), and compared to the theoretical profiles obtained by the convolution between the FDTD map of b) and two-dimensional Gaussian point spread functions, characterized by FWHM of 40 nm (black curve) and 80 nm (green curve), whose intensities are normalized to the experimental spectral shift amplitude range. The error bars are provided by the Lorentzian fit.

## References

- [1] G. Shang, C. Wang, J. Wu, C. Bai, and F. Lei. “Shear force scanning near-field optical microscope based on a piezoelectric bimorph cantilever” In: Rev. Sci. Instrum. 72, 5 (2001), pp. 2344–2349.
- [2] K. Karrai and R. Grober. “Piezoelectric tip-sample distance control for near field optical microscopes” In: Appl. Phys. Lett. 66, 14 (1995), pp. 1842–1844.
- [3] M. Francardi, L. Balet, A. Gerardino, C. Monat, C. Zinoni, L. Li, B. Alloing, N. Le Thomas, R. Houdre, and A. Fiore. “Quantum dot crystal nanocavities at 1300 nm for telecom-wavelength single-photon sources”. In: Phys. Status Solidi C 3 (2006), pp. 3693–3696.
- [4] M. Francardi, L. Balet, A. Gerardino, N. Chauvin, D. Bitault, L. Li, B. Alloing, and A. Fiore. “Enhanced spontaneous emission in a photonic-crystal lightemitting diode” In: Appl. Phys. Lett. 93, 14 (2008), p. 3102.
- [5] B. Daudin, F. Widmann, G. Feuillet, Y. Samson, M. Arlery, and J. Rouvière. “Stranski-Krastanov growth mode during the molecular beam epitaxy of highly strained GaN” In: Phys. Rev. B 56, 12 (12 1997), R7069–R7072.
- [6] F. Intonti, S. Vignolini, F. Riboli, A. Vinattieri, D. Wiersma, M. Colocci, L. Balet, C. Monat, C. Zinoni, L. Li, R. Houdré, M. Francardi, A. Gerardino, A. Fiore, and M. Gurioli. “Spectral tuning and near-field imaging of photonic crystal microcavities” In: Phys. Rev. B 78, 4 (2008), p. 041401.
- [7] S. Vignolini, F. Intonti, F. Riboli, D. Wiersma, L. Balet, L. Li, M. Francardi, A. Gerardino, A. Fiore, and M. Gurioli. “Polarization-sensitive near-field investigation of photonic crystal microcavities” In: Appl. Phys. Lett. 94, 16 (2009), p. 3102.
- [8] F. Intonti, F. Riboli, N. Caselli, M. Abbarchi, S. Vignolini, D. Wiersma, A. Vinattieri, D. Gerace, L. Balet, L. Li, M. Francardi, A. Gerardino, A. Fiore, and M. Gurioli. “Young’s Type Interference for Probing the Mode Symmetry in Photonic Structures” In: Phys. Rev. Lett. 106, 14 (2011), p. 143901.
- [9] S. Vignolini, F. Intonti, L. Balet, M. Zani, F. Riboli, A. Vinattieri, D. Wiersma, M. Colocci, L. Li, M. Francardi, A. Gerardino, A. Fiore, and M. Gurioli. “Nonlinear optical tuning of photonic crystal microcavities by near-field probe” In: Appl. Phys. Lett. 93, 2 (2008), p. 3124.
- [10] S. Vignolini, F. Intonti, F. Riboli, L. Balet, L. Li, M. Francardi, A. Gerardino, A. Fiore, D. Wiersma, and M. Gurioli. “Magnetic Imaging in Photonic Crystal Microcavities” In: Phys. Rev. Lett. 105, 12 (2010), p. 123902.
- [11] K. Sakoda. Optical properties of photonic crystals. Springer-Verlag Berlin Heidelberg, (2001).
- [12] O. Painter, J. Vuckovic, and A. Scherer. “Defect modes of a two-dimensional photonic crystal in an optically thin dielectric slab” In: J. Opt. Soc. Am. B 16, 2 (1999), pp. 275–285.
- [13] B. Gallinet, J. Kupec, B. Witzigmann, and M.-A. Dupertuis. “Analysis of photonic crystal defect modes by maximal symmetrization and reduction” In: J. Opt. Soc. Am. B 27, 7 (2010), pp. 1364–1380.

- [14] R. Sapienza, T. Coenen, J. Renger, M. Kuttge, N. van Hulst, and A. Polman. “Deep-subwavelength imaging of the modal dispersion of light” In: *Nat. Mater.* 11 (2012), pp. 781–787.
- [15] F. Intonti, N. Caselli, S. Vignolini, F. Riboli, S. Kumar, A. Rastelli, O. Schmidt, M. Francardi, A. Gerardino, L. Balet, L. Li, A. Fiore, and M. Gurioli. “Mode tuning of photonic crystal nanocavities by photoinduced non-thermal oxidation” In: *Appl. Phys. Lett.* 100, 3 (2012), p. 3116.
- [16] A. Koenderink, M. Kafesaki, B. Buchler, and V. Sandoghdar. “Controlling the Resonance of a Photonic Crystal Microcavity by a Near-Field Probe” In: *Phys. Rev. Lett.* 95, 15 (2005), p. 153904.
- [17] S. Nakayama, S. Ishida, S. Iwamoto, and Y. Arakawa. “Effect of cavity mode volume on photoluminescence from silicon photonic crystal nanocavities” In: *Appl. Phys. Lett.* 98, 17 (2011), p. 1102.
- [18] M. Burresi, T. Kampfrath, D. van Oosten, J. Prangsma, B. Song, S. Noda, and L. Kuipers. “Magnetic Light-Matter Interactions in a Photonic Crystal Nanocavity” In: *Phys. Rev. Lett.* 105, 12 (2010), p. 123901.
- [19] M. Staffaroni, J. Conway, S. Vedantam, J. Tang, and E. Yablonovitch. “Circuit analysis in metal-optics” In: *Photonics Nanostructures Fundam. Appl.* 10, 1 (2012), pp. 166–176.
- [20] M. Stockman. “Nanofocusing of Optical Energy in Tapered Plasmonic Waveguides” In: *Phys. Rev. Lett.* 93, 13 (2004), p. 137404.
- [21] F. De Angelis, G. Das, P. Candeloro, M. Patrini, M. Galli, A. Bek, M. Lazzarino, I. Maksymov, C. Liberale, L. Andreani, and E. Di Fabrizio. “Nanoscale chemical mapping using three-dimensional adiabatic compression of surface plasmon polaritons” In: *Nat. Nanotechnol.* 5 (2010), pp. 67–72.
- [22] A. Giugni, B. Torre, A. Toma, M. Francardi, M. Malerba, A. Alabastri, R. Proietti-Zaccaria, M. Stockman, and E. Di Fabrizio. “Hot-electron nanoscopy using adiabatic compression of surface plasmons” In: *Nat. Nanotechnol.* 8 (2013), pp. 845–852.
- [23] E. Palik. *Handbook of Optical Constants of Solids*. Academic Press, San Diego, CA, (1997).
- [24] J. Wang, M. Gudiksen, X. Duan, Y. Cui, and C. Lieber. “Highly Polarized Photoluminescence and Photodetection from Single Indium Phosphide Nanowires” In: *Science* 293, 5534 (2001), pp. 1455–1457.
- [25] K. Cho, D. Ruebusch, M. Lee, J. Moon, A. Ford, R. Kapadia, K. Takei, O. Ergen, and A. Javey. “Molecular monolayers for conformal, nanoscale doping of InP nano-pillar photovoltaics”. In: *Appl. Phys. Lett.* 98, 20 (2011), p. 3101.
- [26] L. van Vugt, S. Veen, E. Bakkers, A. Roest, and D. Vanmaekelbergh. “Increase of the Photoluminescence Intensity of InP Nanowires by Photoassisted Surface Passivation” In: *J. Am. Chem. Soc.* 127, 35 (2005), pp. 12357–12362.
- [27] A. Franceschetti and A. Zunger. “Optical transitions in charged CdSe quantum dots” In: *Phys. Rev. B* 62, 24 (2000), R16287–R16290.
- [28] N. Yamamoto, S. Bhunia, and Y. Watanabe. “Polarized cathodoluminescence study of InP nanowires by transmission electron microscopy” In: *Appl. Phys. Lett.* 88, 15 (2006), p. 3106.

Imaging and engineering optical localized modes at the nanoscale

- [29] M. Balistreri, H. Gersen, J. Korterik, L. Kuipers, and N. van Hulst. “Tracking Femtosecond Laser Pulses in Space and Time” In: *Science* 294, 5544 (2001), pp. 1080–1082.
- [30] M. Seo, J. Kyoung, H. Park, S. Koo, H.-S. Kim, H. Bernien, B. Kim, J. Choe, Y. Ahn, H.-T. Kim, N. Park, Q.-H. Park, K. Ahn, and D.-S. Kim. “Active Terahertz Nanoantennas Based on VO<sub>2</sub> Phase Transition” In: *Nano Lett.* 10, 6 (2010), pp. 2064–2068.
- [31] N. Engheta, A. Salandrino, and A. Alù. “Circuit Elements at Optical Frequencies: Nanoinductors, Nanocapacitors, and Nanoresistors” In: *Phys. Rev. Lett.* 95, 9 (2005), p. 095504.
- [32] B. Abasahl, C. Santschi, and O. J. Martin. “Quantitative Extraction of Equivalent Lumped Circuit Elements for Complex Plasmonic Nanostructures” In: *ACS Photonics* 1, 5 (2014), pp. 403–407.
- [33] B. le Feber, N. Rotenberg, D. Beggs, and L. Kuipers. “Simultaneous measurement of nanoscale electric and magnetic optical fields” In: *Nature Photon.* 8 (2014), pp. 43–46.
- [34] L. Landau and E. Lifshitz. *Electrodynamics of continuous media*. Wiley, (1984).
- [35] C. Soukoulis and M. Wegener. “Past achievements and future challenges in the development of three-dimensional photonic metamaterials” In: *Nat. Photon.* 5, 9 (2011), pp. 523–530.
- [36] N. Liu, T. Weiss, M. Mesch, L. Langguth, U. Eigenthaler, M. Hirscher, C. Sönnichsen, and H. Giessen. “Planar Metamaterial Analogue of Electromagnetically Induced Transparency for Plasmonic Sensing” In: *Nano Letters* 10, 4 (2010), pp. 1103–1107.
- [37] S. Burgos, R. de Waele, A. Polman, and H. Atwater. “A single-layer wideangle negative-index metamaterial at visible frequencies” In: *Nat. Mater.* 9 (2010), pp. 407–412.
- [38] H. Atwater and A. Polman. “Plasmonics for improved photovoltaic devices” In: *Nat. Mater.* 9 (2010), pp. 205–213.
- [39] Z. Jacob, I. Smolyaninov, and E. Narimanov. “Broadband Purcell effect: Radiative decay engineering with metamaterials” In: *Appl. Phys. Lett.* 100, 18 (2012), p. 1105.
- [40] A. Slobozhanyuk, A. Poddubny, A. Krasnok, and P. Belov. “Magnetic Purcell factor in wire metamaterials”. In: *Appl. Phys. Lett.* 104, 16 (2014), p. 1105.

## Chapter 4

### Phase sensitive Fano imaging

Photoluminescence based imaging methods require optically active samples with constrain of spectral and spatial matching between the photonic mode and the light sources, which may suffer of bleaching or blinking. Therefore, a pure optical method that can be applied on any kind of high  $Q$  nano-resonators to retrieve the confined mode distribution is actually missing. Here, for the first time, a resonant scattering setup is implemented on a scanning near-field optical microscope.

This scheme allows us to perform hyperspectral imaging of the light states localized in optical nano-resonators, independently on the material they are made of. This novel imaging technique deeply exploits the nature of Fano resonances, which emerge from the interference between a resonant and a non-resonant signal. Actually, the detailed analysis of the Fano spectral lineshapes not only allows us to retrieve the electric-LDOS of nanoscale modes, but also provides unprecedented insight into the confined electric field phase spatial modulation. In fact, Fano imaging intrinsically includes a near-field integrated interferometer for a direct phase retrieval of any investigated polarization components. Hence, Fano imaging constitutes a substantial advance for mapping localized optical states. In particular, we prove that it stimulates a deep sub-wavelength imaging of both the electric LDOS and the electric field phase of the modes localized in photonic crystal nanocavities.

#### 4.1 Fano resonances

In this section we present a brief review of the previously developed resonant scattering experiments on PCNs and the theory that accounts for the observed asymmetric spectral resonances, that significantly differ from the symmetric well-known Lorentzian shape of a conventional resonance.

The beginning of the story traces back in 1935, when unexpected experimental evidences of strong asymmetric profiles in absorption spectra were observed in Rydberg atoms by Beutler [1]. In the same year U. Fano, Fig. (4.1), working with E. Fermi proposed the theoretical explanation that predicts the shape of the observed spectral lines, based on a superposition principle from quantum mechanics calculation [2]. According to Fano: “*The Beutler spectra showed unusual intensity profiles which struck me as reflecting interference between alternative mechanisms of excitation*”

*tion*”. The interpretation provided by Fano is based on the interference between a discrete excited state of an atom and states described by a continuum energy band, if the continuum bandwidth covers the energy of the discrete state.

In 1961 he published a much more elaborated theoretical work, today considered his masterpiece, where are presented and analyzed peculiar shapes of the inelastic scattering spectra of electrons on He atoms [3]. The phenomenon described by Fano turned out to be universal, because the manifestation of interference effect does not depend on the peculiar system considered and it was called “Fano resonance”. Therefore, it is not surprising that, over the years, Fano resonances have been observed across many different branches of physics, including nuclear, atomic, molecular and condensed matter [4–11]. Recently, also a classical analogy of two coupled oscillators has been proposed [12].

Fano resonance takes place when a narrow band of virtually any origin (corresponding to a discrete atomic level) is superimposed on a spectrally flat background spectrum (corresponding to a continuous band of atomic states). In particular, they arises when a particle may reach the same final state via two different scattering pathways, as highlight in Fig. (4.2 a): (*i*) scattering mediated by the interaction with a discrete energy state, where the field phase changes by  $\pi$  as a function of the wavelength (resonant path), or (*ii*) through direct scattering with a continuum of energy states where the field phase and amplitude are nearly constant (non-resonant path). Therefore, the analysis of Fano resonances provides fundamental information on the geometric configuration or internal potential of the system.

Fano derived a simple expression for the cross section of an e.m. transition described by a given quantum operator (for instance the absorption of a photon) from an initial bound state (we shall consider the ground state) to a final continuum state owing the same energy of an excited discrete level, and that can be reached through the pathways (*i*) and (*ii*) [3]:

$$\sigma = \frac{(\varepsilon+q)^2}{1+\varepsilon^2} \quad (4.1)$$

where the reduced energy  $\varepsilon = 2(E - E_0)/\Gamma$  is a function of the particle energy  $E$ , the energy and the linewidth of the discrete state  $E_0$  and  $\Gamma$ , respectively, while the phenomenological shape-parameter  $q$  is introduced by Fano so that  $\pi q^2/2$  represents the ratio between the transition probability to the mixed state (discrete state modified by the interference with the continuum) and to the unperturbed continuum states in an energy bandwidth  $\Gamma$  [3].

Eq. (4.1) nicely reproduces the asymmetric observed lineshapes, as schematically reported in Fig. (4.2 b). Moreover, in order to highlight the basic properties of the Fano relationship, in Fig. (4.3) are plotted various lineshapes as a function of the reduced energy for different values of the parameter  $q$ . The shape parameter governs the lineshape asymmetry. In fact, as reported in Fig. (4.3 a), the case of  $q = 0$  describes a symmetrical dip, which corresponds to the case where the non-resonant scattering path (*ii*) is the dominating contribution. When  $q = 1$  the continuum and discrete transitions are of the same strength, resulting in a perfectly odd-profile with respect

to the energy axis. For increasing  $q$  the lineshape is mainly determined by the transition through the discrete state and, in the limit  $q \rightarrow +\infty$ , it approaches the standard Lorentzian profile of a Breit-Wigner resonance. For any  $q \neq 0$  the Fano profile shows the maximum amplitude value at energy  $E_0 + \Gamma/(2q)$  and the minimum at  $E_0 - q\Gamma/2$ . The resonant energy of the discrete level may lie somewhere between the maximum and the minimum of the asymmetric profile, and the parameter  $q$  defines the relative deviation. For  $q \rightarrow +\infty$ , the resonant energy coincides with the lineshape maximum, while in the case of  $q = 0$  it coincides with the minimum. Notably, for  $q = 1$  it is located exactly at half the distance between the minimum and maximum. The effect of the shape parameter sign inversion is evaluated in Fig. (4.3 b), where two profiles calculated with opposite  $q$  values are reported, showing that for a negative shape parameters the lineshape undergoes a reflection with respect to the vertical axis. Furthermore, every lineshape shows an energy for which the amplitude vanishes, implying that for that energy destructive interference occurs. The basic properties that distinguishes Fano resonance from conventional resonances, in which an external excitation at a proper energy enhances the system response, is therefore the presence of a possible destructive interference that manifest itself as an antiresonance, that means  $\sigma = 0$  for a particular energy. In Fano resonances the character of the interference changes rapidly as a function of the energy, giving rise to asymmetric lineshapes.

#### 4.1.1 Fano resonances in photonic crystal cavities

In optics, Fano resonances have been widely observed especially in plasmonic based nanostructures, metamaterials and photonic crystals; large reviews can be found in [11, 13]. Since we will focus on the Fano lineshape variations in scattering near-field measurements performed on PCNs, it is important to introduce previous experiments and theoretical works that deal with Fano resonance in photonic nanocavities. In fact, it has already been demonstrated that the  $q$  parameter can be tuned. For instance, the absorption spectra of a single quantum dot vary from a symmetrical profile to an asymmetrical one with increasing laser power, indicating an enhancement of the continuum transition [14]. Even reflectance spectra on single quantum-well structure performed at low temperature show periodic Fano lineshape variation, from dispersive-like to absorptive-like and inverse absorptive-like, as a function of the barrier thickness layer [15]. This behavior is due to the interference between the reflected waves from the sample surface and from the quantum-well, and their analysis carries information about both the absorption coefficient and the exciton transition.

A wealth class of studies concerning Fano resonances have been performed on photonic crystals nanocavity platform. In a disordered photonic crystal Fano resonance may occurs via the interaction of the narrow Bragg band with the extra scattering induced by disorder [16, 17]. In photonic crystals slab structures, a three-dimensional frequency and time-domain theoretical analysis proved the presence of spectral sharp asymmetric lineshapes superimposed upon a smooth background [18]. The sharp features come from the guided resonances confined in the slab that can be coupled to radiation modes, while the slowly-varying background corresponds to Fabry-Pérot spectral oscillations of a uniform slab (without holes). The Fano lineshapes

emerges as the interference between a non-resonant pathway, which corresponds to the direct transmission or reflection, and a resonant pathway, in which the remaining portion of the incident light interacts with the exponential decaying amplitudes of the slab guided resonances. Notably, the resulting spectral sharp profiles show different shapes and symmetry, depending on the relative spectral position (phase shift) between the guided mode and the background.

For analytically investigating the Fano resonances in optical cavities a temporal coupled-mode theory has been developed [20]. This theory models the spectral response in term of the transmission and reflection coefficients of the medium together with the resonant energy and the quality factor of a localized mode. It has been applied to the interesting case of an optical system, consisting of a waveguide side coupled to a single-mode cavity, that offers potential applications in optical modulations and switching [19, 21]. In particular, concerning ref. [19], as reported in Fig. (4.4), they studied a system consisting of a square based photonic crystal of high-index dielectric rods, in which a line defect forms the waveguide that is coupled to a point defect nanocavity and in the middle near the nanocavity presents two small dielectric cylinders separated by  $l$ , to provide partial reflection for waveguide modes. The FDTD calculations of Fig. (4.4 a-c) prove how the presence of partially reflecting elements induces the spectral lineshape evaluated at the output of the waveguide to be asymmetric, with a fast frequency switch from zero to maximum output intensity. Differently, by removing the two rods inside the waveguide the spectrum is found to be an inverted Lorentzian dip. However, both the lineshapes reported in Fig. (4.4 c) can be described by Eq. (4.1), ad discussed in Fig. (4.3 a). In fact, at the waveguide output we find the interference between the field directly transmitted through the line defect and the field resonant to the cavity mode, that is trapped inside the cavity for a characteristic time (inversely proportional to cavity  $Q$ ) and then after a delay is coupled back to the waveguide mode. The role of the reflecting elements lies only in introducing a given retard, that is a phase shift, between the two pathways, and then changing the shape of the output spectrum. The coupled-mode theory calculations, reported in Fig. (4.4 d-g), faithfully reproduce the FDTD results and clearly show that, by arbitrary varying the phase shift between the cavity mode and the background, the output spectrum shape drastically changes. Therefore, the method allows to catch the fundamental behavior of Fano resonances.

Profound insight in high- $Q$  PCNs has been pursued by resonant scattering far-field experiments which display Fano-like resonances [22–25]. These alternative techniques exploit the light resonant scattering using a large bandwidth laser or a tunable laser able to span the spectral range of the investigated nanocavity illuminated by standard microscope objective. In this geometry Fano resonances arise from the interference of (*i*) light resonantly coupled to the cavity mode and then released in free space, and (*ii*) light directly diffused by the surface of the photonic crystal pattern, through a continuum of extended states, that is not coupled to the cavity mode. However, it is difficult to observe the cavity spectrum directly, because only a small fraction of the incident light couples to the PCN owing to poor mode matching between the gaussian probe beam and the cavity mode. For this reason, the signal is monitored in crossed-polarization detection scheme, thus eliminating the huge direct reflection signal and allowing the detection of the scattering amplitude. In particular, if the PCN

mode is expected to be linearly polarized along a given in-plane axis, in order to maximize the detection of the resonant mode over the background, the incoming light is set to be linearly polarized at  $45^\circ$  with respect to the resonant mode axis. Then, a second linear polarizer, whose axis is orthogonal to the polarization of the impinging light, filters the backward scattered light. This configuration, combined with the cross-polarization detection, suppresses the non-resonant contribution, as desired, while reducing the resonant contribution only by a factor of 2. It turns out that the two contributions are almost balanced and the Fano lineshapes can be nicely observed. The obtained Fano spectral lineshape intensity  $F(E)$  are commonly reproduced by the following relationship derived from Eq. (4.1) [23]:

$$F(E) = A_0 + F_0 \frac{[q+2(E-E_0)/\Gamma]^2}{1+[2(E-E_0)/\Gamma]^2} \quad (4.2)$$

where  $A_0$  and  $F_0$  are amplitude factors. The former corresponds the minimum intensity ( $F_{min} = A_0$ ); the latter to is related to the amplitude of the Fano lineshape, defined as the difference between the maximum and the minimum intensity, that corresponds to  $F_{max} - F_{min} = F_0(1 + q^2)$ .

By fitting the experimental data with Eq. (4.2) a characterization of the cavity mode in non-optically active samples is then achieved, concerning both the resonant wavelength ( $E_0$ ) and the quality factor ( $Q = E_0/\Gamma$ ). But a resonant scattering technique that, by means of Fano resonances detection in the near-field, would map the localized field distribution with a sub-wavelength resolution, is actually missing. In ref. [23] are also found clear lineshape variations, from strongly asymmetric profiles to symmetric Lorentzians, as the impinging beam waist is increased over the whole cavity area. This demonstrates an enhancement of the scattering in the continuum pathway and a decrease of the asymmetry parameter  $q$ .

Moreover, Eq. (4.2) can be understood more in details. In fact, considering energies far away from the cavity resonance,  $|E/E_0| \gg 1$ , the amplitude  $F$  tends to the value  $B = (A_0 + F_0)$ , which has to be equal to the background scattering signal non-resonant the cavity mode. Therefore, Eq. (4.2) can be written as [25]:

$$F(E) = B + F_0 \left\{ \frac{[q+2(E-E_0)/\Gamma]^2}{1+[2(E-E_0)/\Gamma]^2} - 1 \right\} \quad (4.3)$$

Notably, Eq. (4.3) remains invariant under the transformations ( $q' = -1/q$ ;  $F'_0 = -F_0 q^2$ ). Hence, two  $F_0$  with opposite signs give the same lineshape, and without any loss of generality is commonly considered that  $F_0 > 0$  [25].

## 4.2 Deep sub-wavelength Fano imaging

The resonant scattering technique overcomes the drawback of the most common experimental approaches to achieve PCN mode imaging characterization. They mainly rely on either internal light sources (PL experiments), or on evanescent cou-

pling between the investigated PCN and an optical waveguide [26, 27]. The first approach, which is applicable only to the small class of optically active media, such as the PCNs analyzed in Chapter (3), cannot be extended to silicon, glass or metal based materials. It also requires a spectral and spatial matching between the light source and the photonic modes. Moreover, it is limited by pump-induced losses of the active medium and to the presence of efficient light emitters, which may lower the cavity quality factor. Although the second approach is well suited for optically passive PCN, it requires the fabrication of an additional coupling waveguide, which complicate the experimental geometry and also may induce a loading effect on the PCN modes that can result drastically perturbed.

An alternative approach, based on cathodoluminescence, provides a deep sub-wavelength (about  $\lambda/20$ ) imaging of a two-dimensional  $\text{Si}_3\text{N}_4$  based PCN in a broad spectral range [28]. However, this technique is limited to the collection of the electric LDOS in dielectric regions and it is prevalently sensitive to the out-of-plane electric field component, which is the less important one in two-dimensional photonic crystal nanocavity on slab.

Pure photonic investigation techniques are potentially more powerful due to the covering of a broad spectral range, the possibility to address the distributions of localized modes also in air regions or in metal devices, the absence of detection polarization constraints and, in combination with heterodyne detection in an external interferometer, the possibility of phase retrieval as they preserve coherence [29, 30]. This approach relies on near-field surface enhanced light scattering performed with apertureless probes (a-SNOM), and have recently been applied to various contexts [29, 30]. The great sensitivity of the method is largely due to the use of high refractive index material (metal or silicon) probes in order to enhance the scattering. But, in the case of optical micro and nano resonators (such as ring resonators, microdisk cavities, PCNs) investigation, the a-SNOM probe would perturb too much the local dielectric environment, with respect to glass tapered probes, thus deteriorating the high quality factor and also detuning/mixing modes localized in coupled PCNs or in random cavities [31, 32]. Moreover this technique, like cathodoluminescence, suffers from being mainly sensitive to the out-of-plane component of the electric LDOS, and it is not suited for TE-like localized modes.

Therefore, it is clear that pure optical imaging techniques based on resonant scattering, that can be applied on high  $Q$  resonators in order to retrieve the intensity and the phase of the confined electric field, is highly desirable. In order to meet this crucial need for nanophotonics, we modify the scanning near-field optical microscopy setup presented in Fig. (3.2) to perform resonant scattering spectroscopy that, equipped with dielectric tapered probes, enables the hyperspectral imaging of the electric LDOS with outstanding spatial resolution, also for non optically active samples. We investigate the D2 photonic crystal nanocavity, exploiting a detailed spectral analysis of the observed Fano resonances. In addition, we use aperture aluminum coated probes and campanile tips to prove that the method intrinsically includes a near-field integrated interferometer for phase retrieval without the need of external heterodyne detection, thus revealing the sub-wavelength spatial modulation of both the intensity and the phase of the localized electric fields.

### 4.2.1 Resonant back-scattering

The schematics of the SNOM setup in the illumination/collection geometry equipped with a dielectric probe to perform resonant back-scattering (RBS) measurements is shown in Fig. (4.5 a). In particular, to cover the interesting spectral range in a single scan only we use a pulsed supercontinuum (SC) laser (Leukos-STM with pulse temporal width of 1 ns, repetition rate of 5 KHz), whose emission at the output of a photonic crystal fiber is reported in Fig. (4.5 b). Light coming from the laser is filtered by a long-wavelength pass filter (LP) that allows only  $\lambda > 1.2 \mu\text{m}$  to be transmitted, and it is linearly polarized by the transmission through a polarizing beam splitter cube (PBS), whose extinction ratio is  $2 \cdot 10^4$ . Then it is coupled to the dielectric near-field probe to illuminate the sample in the near-field. We convey inside the near-field probe an almost constant power spectral density of about  $5 \mu\text{W}$  per 10 nm.

Crossed polarization detection is performed to overcome the huge reflection signal, which has the same polarization of the incident light. In fact, only balancing the resonant and the diffused signals we are able to observe clear Fano lineshapes. The implementation of SNOM-RBS therefore requires the polarization control in both input and detection channel paths, which share the near-field probe. Therefore, a Babinet- Soleil compensator, reported in Fig. (4.5 c-d), is mounted on the optical fiber in order to control the light polarization at the end of the tip by twisting and squeezing the fiber. This provides a linear polarization, with an extinction ratio of 120 in the  $(1320 \pm 20)$  nm wavelength range, for the light incident on the sample with the electric field oriented at  $45^\circ$  with respect to the  $x$  axis of the photonic crystal. The polarization control is performed by collecting the light transmitted through the sample by a  $50\times 0.4 \text{ NA}$  objective (Ob.) and by measuring with a photodiode detector (PD, Femto-Watt series by New Focus), in a 40 nm spectral band, the ratio between the light polarized as the light impinging the sample, and the light orthogonally polarized with respect to the incoming beam. Moreover, we test that the investigated sample is not a birefringent material by measuring the polarization maintaining properties of linearly polarized light at 1300 nm. In fact, the incoming collimated free-standing laser light shows the same polarization degree after the transmission through the sample. The backward scattered light collected by the probe is filtered in crossed polarization configuration by the polarizing beam-splitter cube, and spectrally analyzed by the same detection scheme employed in PL measurements, see Fig. (3.2), with typical integration time of 100 ms, leading to a spectral resolution of 0.11 nm, that in photon energy units corresponds to 0.08 meV. Spectra are collected at every tip position on the sample surface. A typical raw RBS spectrum collected in the middle of D2 nanocavity with lattice constant 321 nm, is reported in Fig. (4.6 a). The spectrum displays two asymmetric resonances corresponding to the two lower energy modes (M1 and M2) superimposed to a large wavelength dependent background, whose intensity is generally comparable to the maximum observed amplitude (i.e. difference in counts between the maximum and minimum of a single sharp resonance). This background consists only in a non-resonant scattering signal that can be experimentally addressed by the averaged signal detected in a region located about  $4 \mu\text{m}$  away from the center of the cavity, where the photonic crystal is periodic and the PCN localized modes are no more detectable, as shown in Fig. (4.6 b). Of course, in order to observe clear Fano

lineshapes the resonant and non-resonant scattering signals must be almost balanced. This is the scope of the cross-polarization setup where the non-resonant contribution, which is mainly polarized as the incoming beam and larger than resonant channel, is strongly suppressed. Nevertheless, after the cross-polarization procedure, a non resonant contribution is still left and it is used to produce interference with the resonant channel. This remaining non-resonant contribution is polarized as the resonant mode, therefore for mode M1 is linearly polarized along the  $x$  axis of the PCN.

In order to directly observe the spectral region where the negative or positive interference between the two scattering signals occurs, the background has to be subtracted, as we reported in Fig. (4.6 c). In the resulting spectrum both resonances show a dispersive-like lineshape, fingerprint of the Fano resonance, and each mode includes both positive and negative values, evidence of a constructive and destructive interference, respectively. When the background-subtracted spectrum is averaged over adjacent positions during the SNOM scan, we achieve high signal/noise ratio lineshapes, see Fig. (4.6 d). Only after the background subtraction of each acquired spectrum we perform the Fano function fit of both modes intensity, as a function of the photon energy, by employing Eq. (4.2). The experimental data are well reproduced by the Fano formula, as shown in Fig. (4.7 a-b), and an accurate evaluation of the relevant parameters is pursued.

The power of the near-field microscope, configured for resonant scattering spectroscopy, fully emerges when optical imaging is achieved. By mapping, as a function of position, the parameters deriving from the Fano lineshape analysis, it is possible to retrieve the electric-LDOS imaging of both localized modes. In order to map the RBS amplitude for M1 and M2 we plot in Fig. (4.8 b and e), respectively, the value  $F_0(1 + q^2)$  provided by the fit, that corresponds to the difference in counts between the maximum and the minimum of each Fano lineshape. These maps reproduce the main features of the electric LDOS at the energy of the resonant modes obtained by finite difference time domain (FDTD) calculations reported in Fig. (4.8 d and g), respectively. However, they show a limited spatial resolution (about 250 nm) due to the fact that the amplitude map is directly proportional to the light collected by the dielectric uncoated near-field probe, whose resolution is bound to the few hundred nanometers large collecting area.

An improved spatial resolution is achievable from the same set of data making the best use of the tip local perturbation on the PCN dielectric environment. The slight perturbation induced by the near-field tip gently shifts the resonant modes towards lower energies proportionally to the strength of the local unperturbed electric field intensity, as demonstrated in Chapter (3) [26, 34]. This phenomenon is underlined by the two normalized intensity spectra reported in Fig. (4.8 a). The energy spectrum reported with black dots shows the largest tip perturbation and it is collected in the proximity of the maximum of the M1 intensity, corresponding to the red circle in Fig. (4.8 c). On the other hand, if the tip is located in the green circle position in Fig. (4.8 c), the PCN experiences the slightest disturbance resulting in a higher energy resonance, as highlighted by the spectrum reported with the triangles in Fig. (4.8 a).

Figures (4.8 c and f) show the spatial distributions of the tip induced spectral shift for M1 and M2, respectively, as obtained by reporting the fitting parameter ( $E_0 - E_{0\ min}$ ) as a function of position for each mode. The results are in excellent

agreement with the FDTD based electric LDOS calculations, shown in Fig. (4.8 d and g). Since the smallest LDOS spatial feature is about 100 nm, in order to estimate the spatial resolution of the Fano imaging technique, we compare the experimental M1 spectral shift map to the FDTD map convoluted with two-dimensional Gaussian point spread functions, characterized by different FWHM. In Fig. (4.9 a-b) are reported vertical and horizontal profiles, as highlighted in Fig. (4.8 d), of the experimental spectral shift data compared to theoretical profiles obtained by convolution with Gaussian of FWHM equal to 50 nm, 70 nm and 100 nm. The function with 70 nm FWHM minimizes the  $\chi^2$  distribution. Therefore, the combination of SNOM and RBS spectroscopy allows us to obtain high fidelity electric LDOS mode imaging with an ultra sub-wavelength spatial resolution of 70 nm, down to  $\lambda/19$ , comparable to the PL technique presented in Chapter (3) and to the so far best result obtained on PCNs [28].

Overall, the spatial resolution achieved, as well as the spectral shift amplitude obtained through Fano fits for both resonant modes are comparable to the spatial resolution and amplitude evaluated by Lorentzian fits of PL spectra measured with similar dielectric probes on equivalent D2 nanocavities. This feature confirms that the dielectric perturbation technique does not depend on the employed imaging method but it is a property of the cavity-probe system only. It is straightforward to notice that, although the investigated PCN has light source embedded (InAs quantum dots), in resonant scattering experiments we do not excite the QDs, since the illumination is performed with wavelengths greater than 1.2  $\mu\text{m}$  and at very low power. In fact, outside the photonic crystal, where only QDs are present in the slab, we do not collect any signal resembling the QDs emission, see Fig. (3.3 b).

The presented Fano imaging can be potentially applied to any nano-photonic and nanoplasmonic optical resonator that exhibits sharp spectral resonances, by confining light, for example, in silicon based materials as well as glass, polymer or metallic materials. By mapping the Fano lineshapes as a function of position in the near-field of the D2 nanocavity not only spectral shift and amplitude variations are evident. In fact, if for sake of simplicity we focus on the behavior of the M1 mode, which is known to possess a linear polarization component parallel to the  $x$  axis of the PCN, we find strong lineshape modifications during a single large scan over the PCN, as reported in the two spectra of Fig. (4.10 a). The Fano lineshape collected in position A exhibits positive signal with respect to the background, while the spectrum detected in B has almost exclusively negative values, as if the interference abruptly reverses from constructive to destructive when moving from point A to point B.

Moreover, in resonant scattering SNOM experiments a clear signature of the localized modes is detectable over a larger area with respect to PL measurements, until 3  $\mu\text{m}$  away from the cavity center, and also in the regions where LDOS is negligible. But this is not the only advantage, since the Fano lineshape analysis allows for mapping resonance amplitude, spectral shift, quality factor (as in PL measurements) and also, more strikingly, shape modification, which is a unique property of the resonant scattering technique. The idea is that the additional information contained in Fano shape modifications as a function of position allows to retrieve the spatial phase modulation of the localized modes. In fact, we already discussed that the shape of the Fano

resonance is given by the interference between non-resonant light diffused with a constant phase over the whole PCN and resonant signal, which has a defined phase spatial dependence. In our imaging setup, by employing a coherent light source and looking at the changes of the Fano lineshape as a function of position, we should get an equivalent integrated interferometer to locally probe the relative phase distribution of the PCN localized modes.

In order to obtain a distribution of the lineshape modifications it is a straightforward result to map the RBS intensity distribution at the energy of the most intense M1 peak, as reported in Fig. (4.10 b), which maximizes the counts difference. From this map the M1 distribution is recognizable in its main features and lineshapes inversions, as the one reported in Fig. (4.10 a), only occur between the blue and red regions of Fig. (4.10 b). But these regions are 3  $\mu\text{m}$  apart and do not correspond to adjacent intensity lobes. So, they do not correspond to the actual mode phase distribution behavior, as it is predicted by FDTD calculation of the real part of the M1 electric field  $x$  component evaluated in a plane placed at 22 nm from the slab surface, reported in Fig. (4.10 d). But if the intensity distribution is evaluated at an energy that maximizes the color contrast between regions with opposite intensity sign, we obtain a nice agreement with the calculated real part of the electric field  $x$  polarized evaluated at 200 nm height and shown in Fig. (4.10 e). The dielectric tapered probe collects light also from the lateral sidewall at longer distance from the PCN than the probe apex. This mixing of near-field and intermediate-field detection fairly gives a probe effective collection placed at about 200 nm distance from the sample surface, causing a depression of the obtained spatial resolution [24].

For an accurate sub-wavelength phase-sensitive imaging of the electric field component of light localized in the PCN a probe able to collect only the near-field contribution is therefore recommended. However, the RBS setup does not allow the use of Al-coated probes because of the extremely low throughput. On the other hand, the campanile near-field tips presented in Sec. (3.3), by exploiting the surface plasmon assisted enhancement, show high throughout and can be employed in the illumination/collection geometry. In Fig. (4.11 a) are reported three RBS background-subtracted spectra collected by campanile tip on different positions corresponding to adjacent electric LDOS lobes of the mode M1. A clear lineshape variation is present between positions C and D, while a similar spectrum of C is recovered in position E. In order to highlight these lineshape modifications as a function of tip position the intensity map evaluated at  $E = 931.28$  meV is reported in Fig. (4.11 b). It shows a reversal of the interference condition between adjacent LDOS modes, that is in good agreement with the electric field phase variations reported in Fig. (4.10 d). Therefore, the local changes of the Fano lineshape give direct access to the spatial modulation of the localized mode phase by means of an integrated interferometer related to the nature of the Fano resonances. It must be stressed that here we are not interested to the actual lineshape, (that can be a peak, a dip or a dispersive-like curve), but only care about the lineshape inversions in different positions, since the peculiar Fano lineshape depends also on the daily setup alignment that modifies the non-resonant signal and on the electric LDOS intensity. We estimate the spatial resolution of the phase sensitive Fano imaging by fitting the experimental data obtained by a vertical profile cut

of Fig. (4.11 b) with the error function, which comes out by convolving the experimental Gaussian point spread function and the supposed step-like variation of the phase modulation. We obtain the best fit using a Gaussian point spread function with FWHM equal to 85 nm, that corresponds to a deep sub-wavelength spatial resolution. The observed spatial resolution reduction is likely due to the prolonged use across many scan experiments, that induces the opening of the metallic nanogap.

For completeness, by fitting every spectrum acquired with the campanile tip with Eq. (4.2), in Fig. (4.11 d and e) are also reported the spectral shift map and the Fano lineshape amplitude map. These images fairly well reproduce the M1 behavior when the PCN is observed and perturbed by the campanile tip, as discussed in Sec. (3.3.2). In fact, the simultaneous blue and red spectral shift are present in the regions of maximum magnetic and electric field intensity, respectively, with a strength comparable to that observed in Fig. (3.14 d).

### 4.2.2 Resonant forward-scattering

In order to ensure a homogeneous excitation of the whole PCN with fixed relative phase of the incoming field between adjacent points we also implement a near-field collection setup in transmission geometry, whose schematics is reported in Fig. (4.12 a). This SNOM setup allows us to detect resonant forward scattering (RFS) of light from the investigated nanocavity. The linearly polarized light of the supercontinuum laser (transmitted through a Glan-Thompson polarizing prism, with extinction ratio of about  $3 \cdot 10^3$ , and oriented at  $45^\circ$  with respect to the PCN  $x$  axis) illuminates the sample from the far-field by means of a 50x objective ( $NA = 0.4$ ) that ensures an excitation spot diameter of about  $2 \mu\text{m}$ . The forward scattered light collected by an Al-coated aperture near-field probe (produced by LovaLite) is then filtered in crossed-polarization configuration and analyzed by the same polarizing beam-splitter and detection scheme of the RBS setup. By means of the Babinet-Soleil compensator tool the crossed-polarization condition is checked (providing a linear polarization response of the system fiber plus tip with an extinction ratio of 120) by minimizing the signal transmitted by PBS and detected by PD when the incoming light shines outside the photonic crystal on the bulk GaAs.

Figures (4.12 b) shows three RFS background-subtracted spectra spectra collected by the Al-coated aperture tip in three different cavity positions, corresponding the J, K and L defined in the inset of Fig. (4.12 a) and lie into adjacent M1 intensity lobes. All the reported spectra show both positive and negative values, depending on the interference condition between the resonant and non-resonant scattering channels. In particular, the spectra collected in J and L positions show a constructive interference for lower energies, while for higher energies the interference becomes destructive. On the contrary, the spectrum collected in K has an opposite lineshape, and this inversion is a clear indication that the resonant mode in K is characterized by a  $\pi$  phase variation with respect to J and L regions. Furthermore, the recovery of the J lineshape in the L position, points out that the photonic mode has the same phase in these regions.

In order to confirm the ability to retrieve the mode phase modulation through Fano lineshape changes, we perform three-dimensional FDTD calculations, as reported in

Fig. (4.13 a). A linearly  $x$ -polarized plane wave impinges the bare nanocavity and the forward signal is collected by three detectors placed 10 nm above the sample surface at the positions indicated by  $\alpha$ ,  $\beta$  and  $\gamma$ . Figure (4.13 b) shows that the spectra calculated in  $\alpha$  and  $\gamma$  are characterized by a similar lineshape, which differs only because the electric LDOS has distinct values in the two positions (i.e. the ratio between resonant and non-resonant scattering is slightly changed). The spectrum collected by the detector in  $\beta$  shows a lineshape inversion along the energy axis with respect to the other two calculated spectra, without any effective change of the resonant energy:  $E_0(\alpha) = E_0(\gamma) = 946.639$  meV,  $E_0(\beta) = 946.636$  meV. The three investigated positions are shown in the near-field calculation of the real part of the electric field of M1  $x$  component, reported in Fig. (4.13 c), to highlight that the localized field phase is reversed by  $\pi$  with respect to  $\alpha$  and  $\gamma$  positions. These calculations provide the interference reversal evidence as a function of position.

By reporting the RFS intensity map at a proper energy, as shown in Fig. (4.13 d), we can image the lineshape modifications also in resonant forward scattering. The spatial intensity sign alternation along the vertical direction nicely agrees with the phase modulation of the calculated electric field of Fig. (4.13 c). The good fidelity with which the map of RFS intensity reproduces the theoretical phase alternation map, proves the actual phase modulation imaging of the localized mode. As was done in the case of the campanile tip, we estimate the spatial resolution of the phase sensitive Fano imaging performed in RFS by a coated probe, by fitting the vertical profile of the experimental data in Fig. (4.13 d) with the error-function. Data and fitted curve are reported in Fig. (4.13 e), showing a mapping the phase modulations with a spatial resolution of 110 nm, as given by the FWHM of the Gaussian point spread function. The obtained resolution is limited by the probe aperture, which is nominally about 200 nm. Therefore, we also demonstrate that the phase modulation retrieval is independent on the tip nature and therefore the possibly tip induced phase distortions do not dramatically alter the phase imaging. In fact, with the Campanile probe in RBS configuration we obtain qualitatively analogue spatial lineshape inversions, with respect to Al-coated probes, which result in a similar intensity map, even if the spatial resolution are different. Finally, to address the issue of reproducibility the same measurement are repeated more times, giving the same results for every probe but, demonstrating that a selection of good tips is needed, both dielectric and metallic ones. In particular, concerning the electric LDOS imaging performed by a selected tip, we obtain every time a similar spectral shift map and analogue value of maximum spectral shift, independently on the alignment or on the investigated nanocavity. Concerning the phase modulation imaging by the Fano lineshape analysis, every selected probe is able to collect the resonant scattering signal and to show clear Fano lineshapes. Although the same Fano lineshape is not detected again in the same position on the PCN, if the setup is re-aligned or if the near-field probe is replaced, the same mode lineshape inversions occur between the same spatial intensity lobes, thus giving equivalent phase imaging results. We believe that spurious reflections may play a role in changing the amplitude and phase of the non-resonant scattering and that the method limitations are related to the pre-selection of good tips and to the aging of the tip after several measurements.

So far, we investigated the linearly polarized M1 mode. For this mode, to equilibrate the detection of resonant and non-resonant contributions, we took advantage of the crossed-polarization technique obtaining well resolved Fano resonance spectra. On the other hand, addressing the phase modulation imaging of the PCN excited mode M2 requires a more challenging experiment, since M2 shows an elliptical polarization, where both  $x$  and  $y$  polarization components are present (with the  $y$  component larger than the  $x$  one) [35]. Obviously, the phase distributions of the two perpendicular components are quite different, as reported in the FDTD near-field calculations of Fig. (4.14 d and h), and we must develop an experimental method to separate them.

Whenever the polarization of a given mode is unknown the cross-polarization detection apparatus can not be used. We then apply some modification to the RFS setup illuminating the sample alternatively with  $x$  or  $y$  linearly polarized light to retrieve separately the  $x$  and the  $y$  M2 phase spatial distributions. For each independent polarization we succeed in balancing the cavity resonant contribution and the transmitted light not coupled to the cavity, by exploiting the small size aperture of the Al-coated probe and eliminating the cross-polarization setup. In fact, differently from dielectric probes, metalized probes collect signal only from the small aperture placed few nanometers on top of the sample, spatially filtering out very efficiently the non-resonant component, thus increasing the ratio between the resonant and the non-resonant channels in detection. This polarization sensitive apparatus cannot be implemented in RBS, since releasing the crossed-polarization scheme by using dielectric probes leads to a huge background signal, which hides the resonant channel. On the other hand, by using metal coated probes it is not possible to collect any signal because of the very low tip throughput. The spectra reported in Fig. (4.14 a and e) show that the signal to noise ratio is still quite high and it allows us to image the phase modulation distribution of M2 in both polarization components by mapping the mode intensity, as shown in Fig. (4.14 c and g), respectively. The image fidelity of the experimental phase modulation is higher for the stronger polarization component (parallel to  $y$  axis) with respect to orthogonal polarization component (parallel to  $x$  axis), as inferred by the comparison between the experimental intensity maps in Fig. (4.14 c and g) and the real part of the  $x$  and  $y$  component of the electric field calculated by FDTD, shown in Fig. (4.14 d and h), respectively. Moreover, it is important to stress that the described experimental configuration for Fano phase modulation imaging does not need any pre-knowledge of the localized mode polarization.

In conclusion, we achieve an ultra-subwavelength Fano imaging of the electric LDOS and of the phase modulation of localized modes in a two-dimensional PCN by using a pure optical effect that bridges together resonant light scattering and near-field spectroscopy. This method has the considerable advantage of being applicable to resonators based on any kind of material and in a wide spectral range. In addition, for the first time, we directly probe the relative phase modulation of the localized mode without the use of an external interferometer, by exploiting the interferential nature of the Fano resonances. Near-field Fano imaging opens up new strategies to investigate with a deep-subwavelength spatial resolution the electric LDOS and the phase distribution of modes localized in a wealth class of nanophotonic and nanoplasmonic resonators, also based on materials without optical emission, and it can image different polarization components.



Figure 4.1: Prof. U. Fano (1912-2001), Italian theoretical physicist pioneer in developing the theory of resonant configurations interaction to describe asymmetric spectral lineshapes.

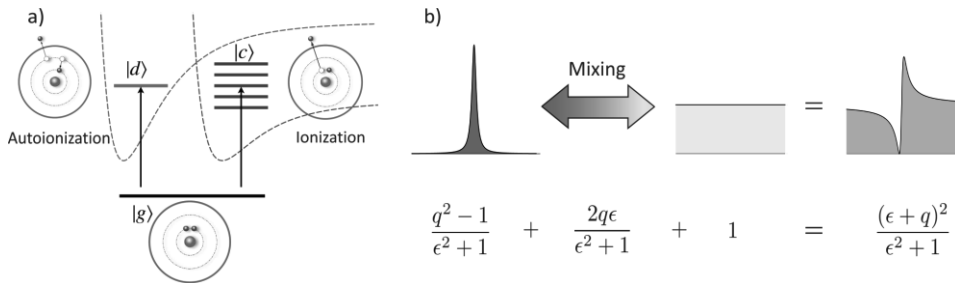


Figure 4.2: a) Fano resonance as a quantum interference between (i) autoionization of two excited electrons followed by the Auger effect and (ii) direct ionization of a deep inner-shell electron. The two pathways are represented as transitions from the atomic ground state  $|g\rangle$  either to a discrete excited autoionizing state  $|d\rangle$  or to a continuum of states  $|c\rangle$ , where the discrete energy of  $|d\rangle$  lies in the continuous range of values of  $|c\rangle$ . Dashed lines indicate double excitations and ionization potentials. b) Illustration of the Fano formula of Eq. (4.1) as a superposition of the Lorentzian line shape of the discrete level with a flat continuous background. Figures adapted from [11].

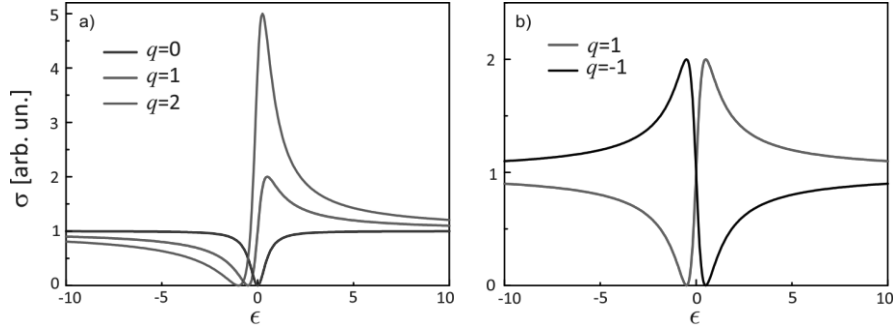


Figure 4.3: a) Fano lineshape as a function of the reduced energy calculated from Eq. (4.1) in arbitrary units for different values of the shape parameter:  $q = 0$  blue curve,  $q = 1$  red curve,  $q = 2$  green curve. b) Fano lineshapes with opposite values: of  $q = 1$  red curve,  $q = -1$  black curve

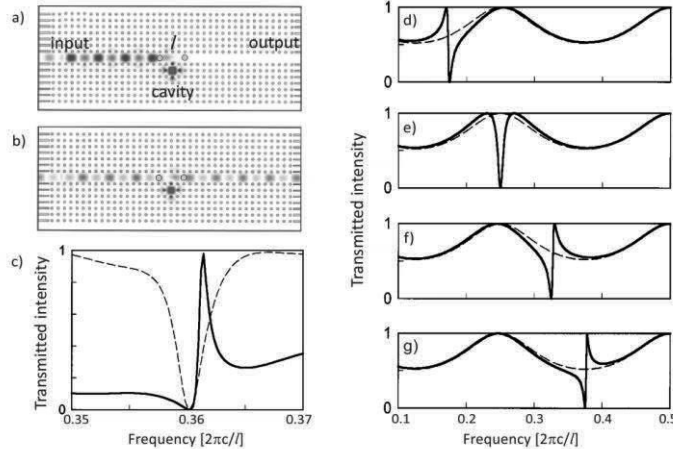


Figure 4.4: The system studied in [19] consists of a square lattice of dielectric rods with a line defect, in which two small cylinders separated by  $l$ , highlighted by yellow dots, are introduced to provide partial reflection. A nanocavity is side-coupled to the waveguide. a)-b) FDTD calculated electric field steady state distributions relative to the frequency of minimum and maximum output amplitude of the solid-line spectrum reported in c), respectively. c) Spectrum obtained by Fourier transforming the fields as a function of time, calculated at the output of the waveguide with (solid line) and without (dashed line) the two rods. d)-g) Transmission spectra calculated by coupled-mode theory (solid lines) for increasing cavity resonant frequency. The dashed lines

## Imaging and engineering optical localized modes at the nanoscale

represent the transmission spectrum through the two reflecting elements without the presence of the cavity. Figures adapted from [19].

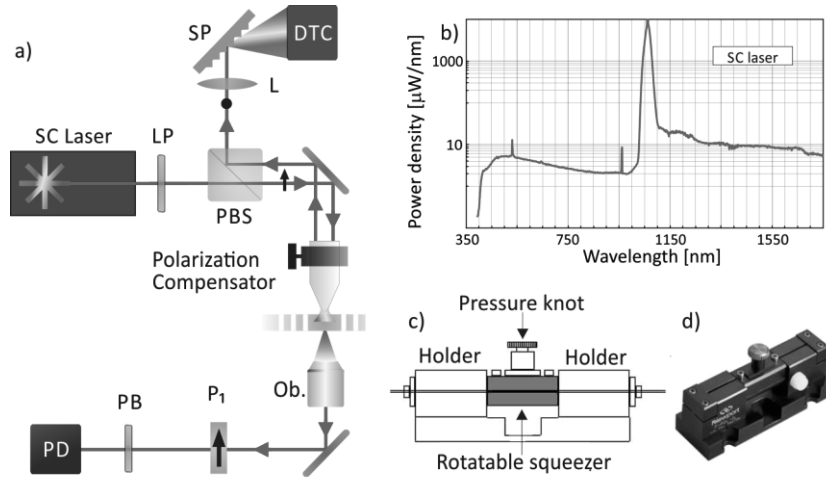


Figure 4.5: a) Schematics of the experimental SNOM setup employed in illumination/collection geometry, with dielectric probes for resonant back-scattering experiments. The part of the setup below the sample measures the degree of polarization after the near-field probe, controlled by means of the Babinet-Soleil compensator, whose schematics and image are reported in c)-d), respectively. SC is the supercontinuum laser source, whose spectral emission is reported in b) [33]. LP is a long-wavelength pass filter. P1 is a linear polarizer. PBS is a polarizing beam splitter cube. Ob. is a 50x, 0.4 NA objective. PB is a narrow band pass filter. PD is a photodiode light detector, L a lens that focuses the signal to the entrance slit of the spectrometer (SP) and to the detector (DTC) composed by an array of InGaAs photodiodes. The black arrow in the incoming light beam and the black dot in the collected light beam highlight the cross-polarization between the two branches. The electronic central unit and the piezoelectric movements are not shown, but are the same of Fig. (3.2).

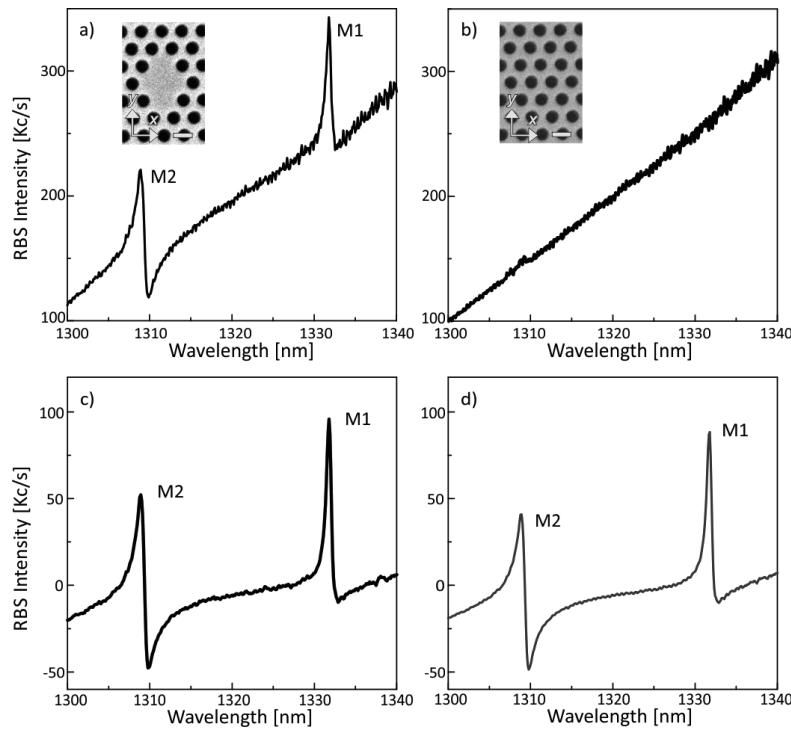


Figure 4.6: a) RBS raw spectra collected by dielectric probe in the middle of the D2 nanocavity with lattice constant 321 nm whose SEM image is reported in the inset with a scale bar of 300 nm. b) Background spectrum collected about 4  $\mu\text{m}$  away from the center of the cavity, as highlighted in the inset. c) Spectrum obtained by subtracting the background b) from the raw data a). d) Background subtracted spectrum averaged over 6 adjacent positions at the center of the cavity during the SNOM scan.

## Imaging and engineering optical localized modes at the nanoscale

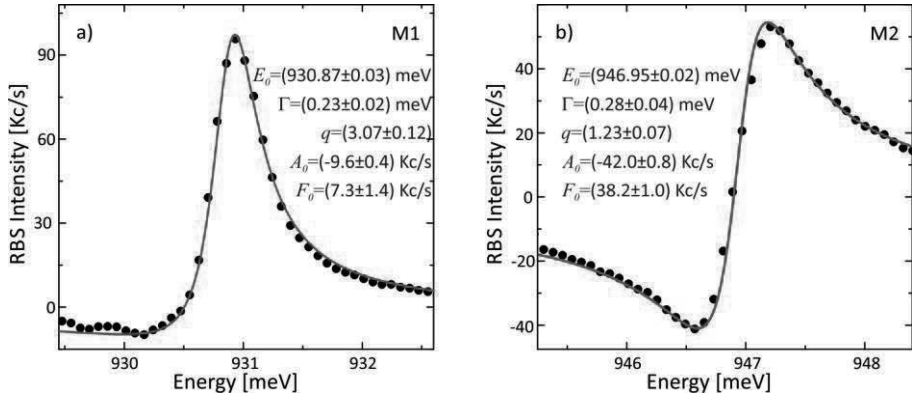


Figure 4.7: a) RBS spectrum of M1 acquired during a SNOM scan and background subtracted, is reported as a function of the photon energy (black dots) and fitted by the Fano formula of Eq. (4.2) (red curve). b) Experimental RBS of M2 acquired during a SNOM scan and background subtracted, is reported as a function of the photon energy (black dots) along with the Fano fitted lineshape (red curve). The calculated parameters and relative uncertain are shown in both insets.

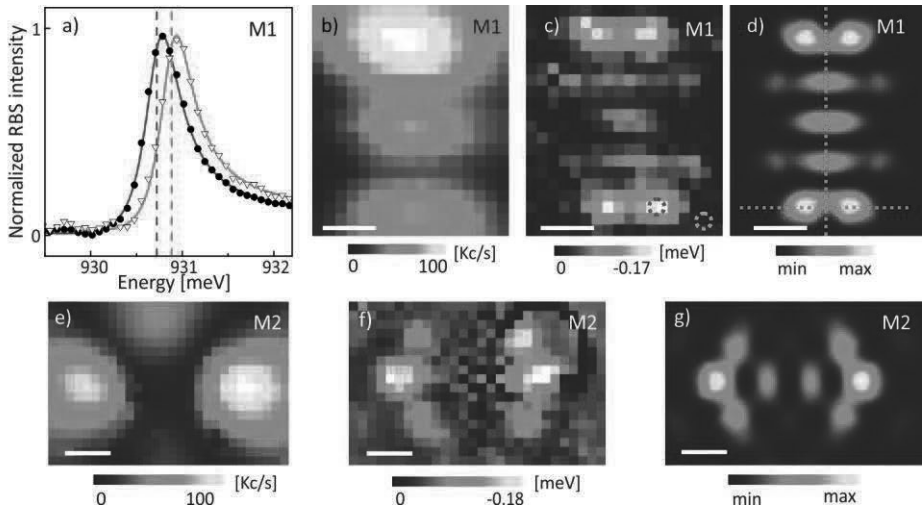


Figure 4.8: a) Dots and triangles represent normalized RBS spectra of the mode M1 collected at two different positions, corresponding to red and green circles in c). Both curves are reproduced by Eq. (4.2), which gives the red and the green normalized profiles with resonant energies  $E_0 = 930.72$  meV and  $E_0 = 930.88$  meV, highlighted by red green vertical dashed lines, respectively. b) Fano amplitude distribution, evaluated as  $F_0(1 + q^2)$  for the M1 mode. c) Tip induced spectral shift of M1. d) Electric-LDOS calculated by FDTD at the M1 peak energy. The dotted orange lines in d) indicate the positions where the profiles reported in Fig. (4.9) are considered. e) Fano amplitude distribution of the M2 mode. f) Tip induced spectral shift of M2. g) Electric-LDOS calculated by FDTD at the M2 peak energy. The scale bar is 250 nm.

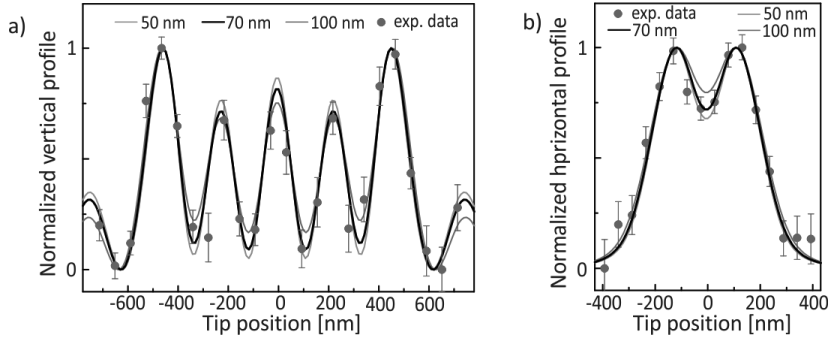


Figure 4.9: a) Comparison between the vertical profiles obtained from the normalized map of the spectral shift experimental data (red dots) of Fig. (4.8 c) and the ones obtained from the normalized convolution of the calculated electric-LDOS intensity map of Fig. (4.8 d) with two-dimensional Gaussian point spread functions of FWHM equal to 50 nm, 70 nm and 100 nm. The error bars are provided by the Fano function fit of each spectrum acquired. b) Same as a) for the horizontal profile of Fig. (4.8 c and d).

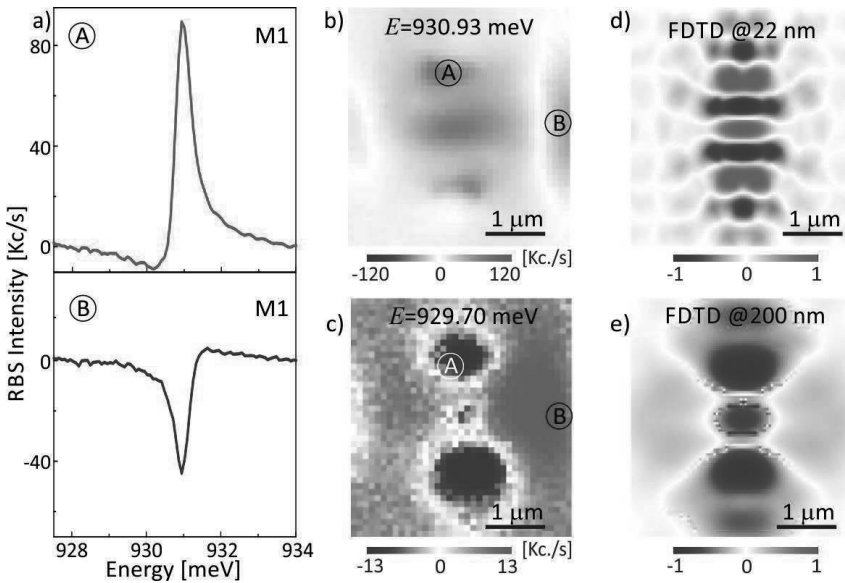


Figure 4.10: a) RBS background-subtracted spectra of the mode M1 collected in two different points, labeled A and B in b) and c). b) RBS intensity distribution evaluated

at the peak maximum energy of the M1 Fano resonance,  $E = 930.93$  meV. Withe color corresponds to zero intensity. c) RBS intensity distribution evaluated at the  $E = 929.70$  meV to maximize the color contrast between regions with opposite intensity sign. d) Real part of the  $x$  component of the electric field calculated by FDTD on a detector placed at 22 nm from the slab surface, evaluated at the energy of M1 and normalized in  $[-1; +1]$ . e) FDTD calculation of the real part of the  $x$  electric field, as in d), but in the case of a detector placed at 200 nm distance from the cavity.

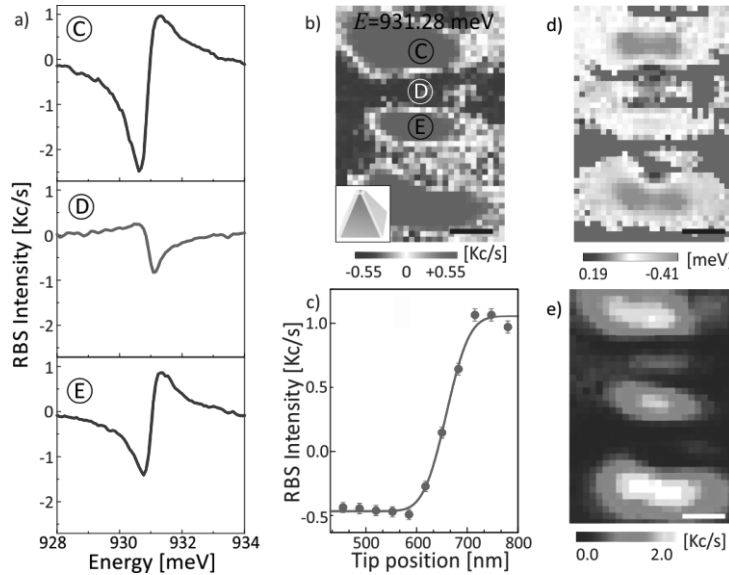


Figure 4.11: a) RBS background-subtracted spectra collected by the campanile tip on three different positions (C, D, and E) shown in the intensity map b), which is evaluated at  $E = 931.28$  meV. All the spectra recorded in the red (blue) regions have line-shapes similar to the C (D) spectrum. In the inset is reported the schematics of the campanile tip. c) Intensity data acquired along the central vertical profile between adjacent lobes in b). The error bars are provided as the square root of the intensity counts and the red curve is the error-function which best reproduces the experimental data. d)-e) Spectral shift map and amplitude map, evaluated as  $F_0(1 + q^2)$ , for the same SNOM measurement shown in b). The scale bar is 250 nm.

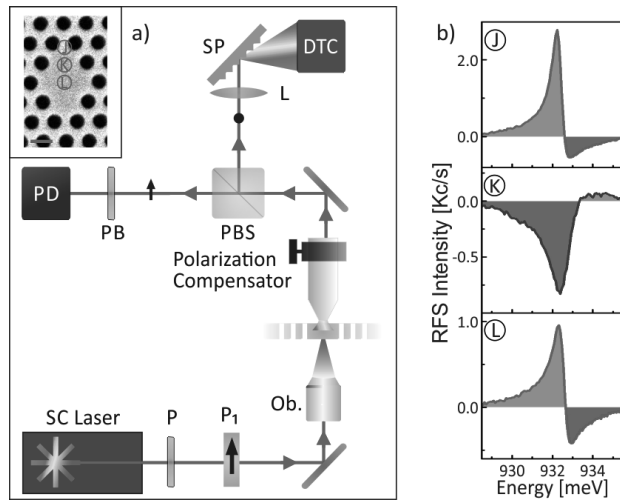


Figure 4.12: a) Schematics of the experimental SNOM setup in transmission geometry and equipped with coated probes or campanile tips for resonant forward-scattering experiments. All the optics and the instruments employed here are also present in the illumination/collection setup of Fig. (4.5 a) for RBS measurements. SC laser light linearly polarized illuminates the sample from the far-field by the objective (Ob.); the forward-scattering signal is analyzed in cross-polarization scheme and acquired by the spectroscopy detection apparatus. SEM image of the investigated nanocavity is reported in the inset along with the positions (J, K, L) where the background-subtracted spectra in b) are detected by aperture coated probe.

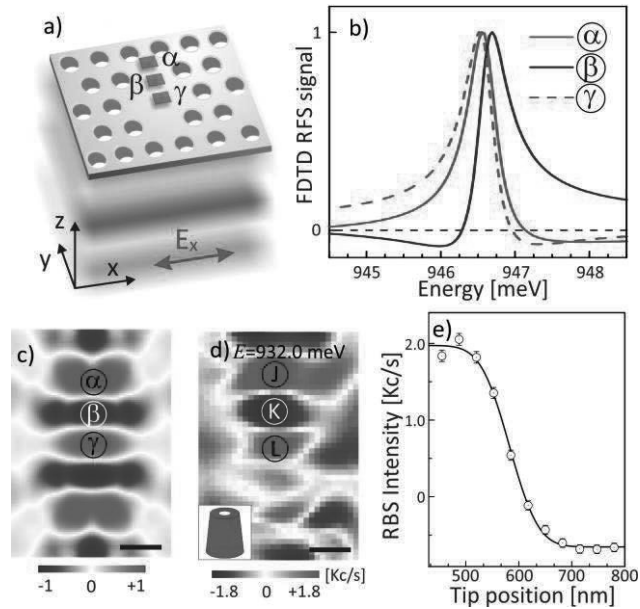


Figure 4.13: a) Schematic of the FDTD calculations modelling the RFS imaging. The PCN is excited from the bottom by a linearly polarized plane wave and three detectors (green squares), centered on the lobes indicated by  $\alpha$ ,  $\beta$  and  $\gamma$  in c), are placed 10 nm above the sample surface. b) Calculated RFS spectra collected by the three detectors in a); every spectrum is background subtracted and divided by its own maximum value. c) Real part of the  $x$  component of the M1 electric field calculated by FDTD 10 nm above the sample surface. d) Spatial distribution of the RFS intensity evaluated at 932.0 meV. J, K and L correspond to the position highlighted in Fig. (4.12 a). The inset represents the schematic of the coated probe. e) Intensity data acquired along the central vertical profile between adjacent lobes in d). The error bars are provided as the square root of the intensity counts and the red curve is the error-function that best reproduces the experimental data. The scale bar is 250 nm.

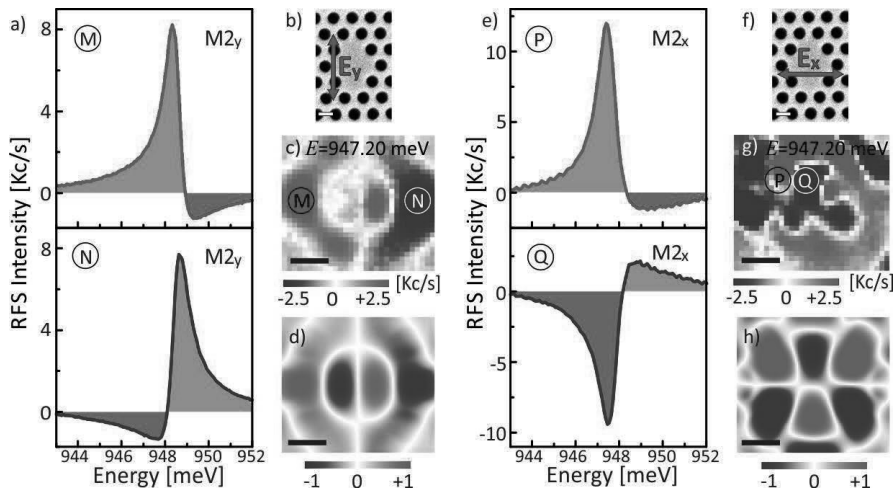


Figure 4.14: a) RFS spectra background-subtracted of the excited mode M2 collected by the Al-coated probe in the positions M and N reported in c). As highlighted by the schematic in b) the incoming light has a linear polarization along the  $y$  axis, and in the detection path no cross-polarization scheme is mounted. c) Spatial distribution of the experimental intensity of the M2  $y$ -component evaluated at 947.2 meV. d) Real part of the electric field relative to the M2  $y$ -component calculated by FDTD and normalized between  $[-1; +1]$ . e) RFS spectra background-subtracted of M2 collected by the Al-coated probe in the positions P and Q reported in g) for the case of  $x$ -polarized incoming light, as reported in f). g) Experimental spatial distribution of the  $x$ -component intensity evaluated at 947.2 meV. h) Real part of the electric field relative to the M2  $x$ -component calculated by FDTD and normalized between  $[-1; +1]$ . The scale bar in all the maps is 250 nm.

## References

- [1] H. Beutler. “Über absorptionsserien von argon, krypton und xenon zu termen zwischen den beiden ionisierungsgrenzen  ${}^2P_{3/2}^0$  und  ${}^2P_{1/2}^0$ ” In: Z. Phys. A 93 (1935), pp. 177–196.
- [2] U. Fano. “Sullo spettro di assorbimento dei gas nobili presso il limite dello spettro d’arco” In: Il Nuovo Cimento 12, 3 (1935), pp. 154–161.
- [3] U. Fano. “Effects of Configuration Interaction on Intensities and Phase Shifts” In: Phys. Rev. 124, 6 (1961), pp. 1866–1878.
- [4] H. Feshbach. “Unified theory of nuclear reactions” In: Ann. Phys. 5, 4 (1958), pp. 357–390.
- [5] H. Feshbach. “Unified theory of nuclear reactions II” In: Ann. Phys. 19, 2 (1962), pp. 287–313.
- [6] B. Lounis and C. Cohen-Tannoudji. “Coherent population trapping and Fano profiles” In: J. Phys. II France 2 (1992), pp. 579–592.
- [7] J. Faist, F. Capasso, C. Sirtori, K. West, and L. Pfeiffer. “Controlling the sign of quantum interference by tunnelling from quantum wells” In: Nature 390 (1997), pp. 589–591.
- [8] W. Johnson, K. Cheng, K.-N. Huang, and M. Le Dourneuf. “Analysis of Beutler-Fano autoionizing resonances in the rare-gas atoms using the relativistic multichannel quantum-defect theory” In: Phys. Rev. A 22, 3 (1980), pp. 989–997.
- [9] F. Cerdeira, T. Fjeldly, and M. Cardona. “Effect of Free Carriers on Zone-Center Vibrational Modes in Heavily Doped p-type Si. II. Optical Modes” In: Phys. Rev. B 8, 10 (1973), pp. 4734–4745.
- [10] M. Limonov, A. Rykov, S. Tajima, and A. Yamanaka. “Raman Scattering Study on Fully Oxygenated  $\text{YBa}_2\text{Cu}_3\text{O}_7$  Single Crystals:  $x - y$  Anisotropy in the Superconductivity Induced Effects”. In: Phys. Rev. Lett. 80, 4 (1998), pp. 825–828.
- [11] A. Miroshnichenko, S. Flach, and Y. Kivshar. “Fano resonances in nanoscale structures” In: Rev. Mod. Phys. 82, 3 (2010), pp. 2257–2298.
- [12] S. Yong, M. Arkady, and S. Chang. “Classical analogy of Fano resonances” In: Phys. Scr. 74, 2 (2006), p. 259.
- [13] B. Luk'yanchuk, N. Zheludev, S. Maier, N. Halas, P. Nordlander, H. Giessen, and C. Chong. “The Fano resonance in plasmonic nanostructures and metamaerials” In: Nat. Mater. 9 (2010), pp. 707–715.
- [14] M. Kroner, A. Govorov, S. Remi, B. Biedermann, S. Seidl, A. Badolato, P. Petrone, W. Zhang, R. Barbour, B. Gerardot, R. Warburton, and K. Karrai. “The nonlinear Fano effect” In: Nature 451 (2008), pp. 311–314.
- [15] X. Zheng, D. Heiman, B. Lax, and F. Chambers. “Reflectance line shapes from  $\text{GaAs}/\text{Ga}_{1-x}\text{Al}_x\text{As}$  quantum well structures” In: Appl. Phys. Lett. 52, 4 (1988), pp. 287–289.
- [16] M. Rybin, A. Khanikaev, M. Inoue, A. Samusev, M. Steel, G. Yushin, and M. Limonov. “Bragg scattering induces Fano resonance in photonic crystals” In: Phot. Nano. Fund. Appl. 8, 2 (2010), pp. 86–93.

- [17] A. Poddubny, M. Rybin, M. Limonov, and Y. Kivshar. “Fano interference governs wave transport in disordered systems” In: *Nat. Commun.* 3 (2012), p. 914.
- [18] S. Fan and J. Joannopoulos. “Analysis of guided resonances in photonic crystal slabs” In: *Phys. Rev. B* 65, 23 (2002), p. 235112.
- [19] S. Fan. “Sharp asymmetric line shapes in side-coupled waveguide-cavity systems” In: *Appl. Phys. Lett.* 80, 6 (2002), pp. 908–910.
- [20] S. Fan, W. Suh, and J. Joannopoulos. “Temporal coupled-mode theory for the Fano resonance in optical resonators” In: *J. Opt. Soc. Am. A* 20, 3 (2003), pp. 569–572.
- [21] Y. Yu, M. Heuck, H. Hu, W. Xue, C. Peucheret, Y. Chen, L. Oxenlowe, K. Yvind, and J. Mork. “Fano resonance control in a photonic crystal structure and its application to ultrafast switching” In: *Appl. Phys. Lett.* 105, 6 (2014), p. 11117.
- [22] M. McCutcheon, G. Rieger, I. Cheung, J. Young, D. Dalacu, S. Frédéric, P. Poole, G. Aers, and R. Williams. “Resonant scattering and second-harmonic spectroscopy of planar photonic crystal microcavities” In: *Appl. Phys. Lett.* 87, 22 (2005), p. 1110.
- [23] M. Galli, S. Portalupi, M. Belotti, L. Andreani, L. O’Faolain, and T. Krauss. “Light scattering and Fano resonances in high-Q photonic crystal nanocavities” In: *Appl. Phys. Lett.* 94, 7 (2009), p. 1101.
- [24] D. Englund, A. Faraon, I. Fushman, N. Stoltz, P. Pettrff, and J. Vuckovic. “Controlling cavity reflectivity with a single quantum dot” In: *Nature* 450 (2007), pp. 857–861.
- [25] S. Haddadi, L. Le-Gratiet, I. Sagnes, F. Raineri, A. Bazin, K. Bencheikh, J. Levenson, and A. Yacomotti. “High quality beaming and efficient free-space coupling in L3 photonic crystal active nanocavities” In: *Opt. Express* 20, 17 (2012), pp. 18876–18886.
- [26] F. Intonti, S. Vignolini, F. Riboli, A. Vinattieri, D. Wiersma, M. Colocci, L. Balet, C. Monat, C. Zinoni, L. Li, R. Houdré, M. Francardi, A. Gerardino, A. Fiore, and M. Gurioli. “Spectral tuning and near-field imaging of photonic crystal microcavities” In: *Phys. Rev. B* 78, 4 (2008), p. 041401.
- [27] M. Burresi, T. Kampfrath, D. van Oosten, J. Prangsma, B. Song, S. Noda, and L. Kuipers. “Magnetic Light-Matter Interactions in a Photonic Crystal Nanocavity” In: *Phys. Rev. Lett.* 105, 12 (2010), p. 123901.
- [28] R. Sapienza, T. Coenen, J. Renger, M. Kuttge, N. van Hulst, and A. Polman. “Deep-subwavelength imaging of the modal dispersion of light” In: *Nat. Mater.* 11 (2012), pp. 781–787.
- [29] J. Chen, M. Badioli, P. Alonso-Gonzalez, S. Thongrattanasiri, F. Huth, J. Osmond, M. Spasenovic, A. Centeno, A. Pesquera, P. Godignon, A. Z. Elorza, N. Camara, F. J. G. de Abajo, R. Hillenbrand, and F. Koppens. “Optical nanoimaging of gate-tunable graphene plasmons” In: *Nature* 487 (2012), pp. 77–81.
- [30] M. Schnell, A. García-Etxarri, A. Huber, K. Crozier, J. Aizpurua, and R. Hillenbrand. “Controlling the near-field oscillations of loaded plasmonic nanoantennas” In: *Nat. Photon.* 3 (2009), pp. 287–291.

## Imaging and engineering optical localized modes at the nanoscale

- [31] N. Caselli, F. Intonti, C. Bianchi, F. Riboli, S. Vignolini, L. Balet, L. Li, M. Francardi, A. Gerardino, A. Fiore, and M. Gurioli. “Post-fabrication control of evanescent tunnelling in photonic crystal molecules” In: *Appl. Phys. Lett.* 101, 21 (2012), p. 1108.
- [32] F. Riboli, N. Caselli, S. Vignolini, F. Intonti, K. Vynck, P. Barthelemy, A. Gerardino, L. Balet, L. Li, A. Fiore, M. Gurioli, and D. Wiersma. “Engineering of light confinement in strongly scattering disordered media” In: *Nat. Mater.* 13 (2014), pp. 720–725.
- [33] LEUKOS. Leukos STM spectral emission datasheet. url: <http://www.leukos-systems.com/spip.php?article147> (visited on 12/18/2014).
- [34] A. Koenderink, M. Kafesaki, B. Buchler, and V. Sandoghdar. “Controlling the Resonance of a Photonic Crystal Microcavity by a Near-Field Probe” In: *Phys. Rev. Lett.* 95, 15 (2005), p. 153904.
- [35] S. Vignolini, F. Intonti, F. Riboli, D. Wiersma, L. Balet, L. Li, M. Francardi, A. Gerardino, A. Fiore, and M. Gurioli. “Polarization-sensitive near-field investigation of photonic crystal microcavities” In: *Appl. Phys. Lett.* 94, 16 (2009), p. 3102.

## **Chapter 5**

### **Photonic crystal molecules**

The coupling between adjacent optical nano-resonators is a topic of vast attraction both for fundamental physics and for high density photonic integrated circuits applications. Interacting photonic nanocavities emerge as analogous of the basic interatomic coupling that gives rise to real molecules, described by wave-functions with defined symmetry character. They are called photonic molecules. The high spatial resolution imaging of the photonic molecules resonant modes it is a primary task to be achieved. Here we describe the basic principles of the interaction between coupled resonators and we study, both experimentally and theoretically, the light behavior in a photonic molecule formed by two and three interacting photonic crystal nanocavities aligned along different symmetry axes. We notably find that the photonic molecule ground state can be either bonding or antibonding and that the effective mode interaction cannot be limited to the nearest-neighbour. Moreover, we develop a post-fabrication method to tune the PCN localized modes by inducing a laser assisted nano-oxidation that produces a large blue-shift of the modes. This technique is also exploited to engineer the coupling strength in photonic crystal molecules and to prove the symmetry character inversion between the molecule ground state and the first excited state.

#### **5.1 Coupled photonic nanocavities**

Dielectric point defects in photonic crystals can generate localized light states in the photonic band gap, similarly to the case of electronic states in the band gap of semiconductor materials, as we discussed in Sec. (2.1.2) [1]. The light states localized in photonic crystal nanocavities play a relevant role in the development of light emitters and optical waveguides [2]. Extending the analogy between photonic modes resonant in single PCNs and electrons described by quantum mechanics in atomic-like states, coupled PCNs are also denominated photonic crystal molecules, due to an effective interaction between close nano-resonators [3–5]. Light behavior in systems based on aligned PCNs resembles the molecular interaction where the resulting normal modes exhibit energy splitting. This condition is achieved by an evanescent photon tunneling between each single PCN, whenever the resonant wavelength matching and the electric LDOS spatial overlap between them are fulfilled. Photonic molecules have been implemented on the basis of any kind of optical nanoresonator, ranging from the case of nominally identical micropillars, microdisks or dielectric spheres that

sustain whispering gallery modes, to the case of coupled identical or even non-identical PCNs, which lead to the formation of homo-atomic or hetero-atomic photonic crystal molecules, respectively [3, 6–10]. In the simplest and remarkable case of only two coupled PCNs, following quantum mechanics denominations, the diatomic molecular state that is symmetric in the exchange of the two atomic orbitals is named bonding (B) state and it corresponds to the ground state in the case of attractive (negative) coupling. While the antisymmetric molecular state is denominated antibonding (A) and it is associated to the ground state only if the coupling is positive. Interestingly, the molecular-like modes exhibit different radiation patterns, thus engineering the coupling strength is proposed as an alternative method to tailor the angular distribution properties of the resonant modes. Electromagnetically induced transparency like effects can occur in coupled optical resonators due to the coherent interference, as well as slow-light phenomena [11–13]. In quantum-information application it has been proved that a photonic molecule can enhance the spontaneous emission rate of an embedded single quantum dot, which emits a single pair of entangled photons, by ensuring a deterministic coupling of the molecule normal modes to the biexciton and exciton energy transitions, thus improving the source of entangled photons [14]. Photonic molecules would also represent the basis for developing two-qubit gates in integrated structures [15]. Also the possibility of using strongly coupled photonic molecules to efficiently increase the mutual interaction between atomic-like light emitters (quantum dots), even at large distance, has been theoretically addressed [16].

In a given resonator the strong coupling regime between a single emitter excitation and the cavity mode gives rise to a dressed-photon state (polariton). This behavior induces non-linear optics phenomena at extremely low light intensities, such as photon blockade and photon induced tunneling [17]. Within this framework, a fascinating implementation has lead to the proposal of an optical analogue of the Josephson interferometer consisting of two coherently driven linear optical cavities connected through a central cavity with a single-photon non linearity [18]. The big advantage of the system composed by interacting resonators relies in the accessibility to local properties such as the possibility to measure the output of a single cavity. Recently, complex architectures formed by large ensemble of strongly interacting dressed-photonic molecules have been proposed to address quantum many-body aspects of quantum gases, as the Mott insulator to superfluid transition, resembling the case of ultracold atoms in optical lattices [19, 20]. In order to create proper quantum optics devices a fundamental requirement is the design and control of adjacent nanocavity modes at the target wavelengths, within an accuracy which is not directly obtainable due to the fabrication tolerances. The compensation of the fluctuations related to the structural disorder and more generally the control of the resonance wavelength of each resonator within the array and also of the tunneling coefficient between adjacent nanocavities is of the utmost relevance in the roadmap toward quantum photonic devices.

### 5.1.1 Coupled modes theory

The analytical expression of the coupled PCNs mode features can be modeled by considering a system of two oscillators of resonant energy  $\hbar\omega_1$  and  $\hbar\omega_2$ , respectively,

whose interaction is mediated by a potential  $g$  that defines the coupling strength. The problem can be solved by calculating the eigenvalues and eigenvectors of the matrix:

$$H = \begin{pmatrix} \hbar\omega_1 & g \\ g & \hbar\omega_2 \end{pmatrix} \quad (5.1)$$

whose eigenvalues solutions, considering also the damping (where the resonant mode losses are  $\gamma_1$  and  $\gamma_2$  for the single oscillators and  $\Gamma$  for the supermodes), are given by:

$$\hbar\Omega_{\pm} + i\Gamma_{\pm} = \frac{1}{2} [\hbar\omega_1 + \hbar\omega_2 - i(\gamma_1 + \gamma_2) \pm \sqrt{|\hbar\omega_1 - \hbar\omega_2 - i(\gamma_1 - \gamma_2)|^2 + 4g^2}] \quad (5.2)$$

where  $\Omega_-$  and  $\Omega_+$  represent the molecular-like ground state and excited energy state, respectively. While the corresponding eigenvectors on the basis of the single oscillators are:

$$\Psi_- = \begin{pmatrix} \frac{\hbar\omega_1 - \hbar\omega_2 - \sqrt{(\hbar\omega_1 - \hbar\omega_2)^2 + 4g^2}}{2g} \\ 1 \end{pmatrix} \quad (5.3)$$

$$\Psi_+ = \begin{pmatrix} \frac{\hbar\omega_1 - \hbar\omega_2 + \sqrt{(\hbar\omega_1 - \hbar\omega_2)^2 + 4g^2}}{2g} \\ 1 \end{pmatrix} \quad (5.4)$$

where  $\Psi_-$  and  $\Psi_+$  are the molecular states relative to  $\Omega_-$  and  $\Omega_+$ , respectively. In the limit of negligible detuning, that is  $|\Delta| = |\hbar\omega_1 - \hbar\omega_2| \ll g$ , the lower energy molecular state,  $\Psi_-$ , can be either an even state  $(1; 1)$  if  $g < 0$ , or an odd state  $(-1; 1)$  if  $g > 0$ . While  $\Psi_+$  has always an opposite parity with respect to the  $\Psi_-$  state.

Moreover, if we consider  $g < 0$ , as happens for attractive potentials, and a negligible detuning, the molecular states result:

$$\Psi_- = \frac{1}{\sqrt{2}} (\varphi_1 + \varphi_2) \quad (5.5)$$

$$\Psi_+ = \frac{1}{\sqrt{2}} (\varphi_1 - \varphi_2) \quad (5.6)$$

where  $\varphi_1$  and  $\varphi_2$  are the wave-function of the two isolated oscillators, respectively. In particular, the molecular ground state eigenfunction (5.5) is given by a linear symmetric combination of the atomic-like states, which is called bonding state in analogy with real molecules behavior. While the eigenfunction (5.6) highlights that the excited state is formed by an antisymmetric combination, giving rise to the antibonding state. However, if the effective coupling strength is positive, an inversion between the molecular modes eigenfunctions of (5.5) and (5.6) occurs. In fact, the ground state acquires an antibonding character and the excited state becomes bonding.

In photonics the role of the wave-function is accomplished by the e.m. fields while the effective potential is related to the dielectric environment [1]. Since the e.m. fields are vectors, we need to separate them in each polarization component in order to get a fruitful comparison with the scalar theory that we presented. For instance, for a given

localized mode the symmetry character can be defined only for one single field polarization component and this information cannot be retrieved by means of PL measurements, independently on the spatial resolution, since they allow only electric and magnetic field intensities detection. In order to probe the symmetry character of the coupled modes a revisited Young's double slit experiment in the far-field has been tested with photonic molecules [21, 22]. The experimental results can be compared with accurate numerical calculations of the field, exhibiting both amplitude and phase information. Moreover, resonant scattering phase-sensitive measurements on photonic molecules are still lacking and they will be implemented in the future, employing the Fano-imaging setup proposed in Sec. (4.2.2).

The expression of the coupling strength in photonic molecules can be derived from the tight binding theory, in the approximation of effective electric interaction, see also the Appendix [23, 24]:

$$g = \frac{2\pi\hbar c}{\lambda} \frac{\int \Delta\epsilon(\mathbf{r}) \mathbf{E}_0(\mathbf{r}) \cdot \mathbf{E}_0(\mathbf{r}+\mathbf{D}) d\mathbf{r}}{\int [\mu_0 |\mathbf{H}_0(\mathbf{r})|^2 + \epsilon(\mathbf{r}) |\mathbf{E}_0(\mathbf{r})|^2] d\mathbf{r}} \quad (5.7)$$

where  $\mathbf{E}_0$  and  $\mathbf{H}_0$  are the electric and magnetic fields of the single PCN;  $\mathbf{D}$  describes the spatial separation between adjacent cavities;  $\Delta\epsilon$  is the difference between the dielectric constant of the coupled system and the dielectric constant of the single resonator. The relation (5.7) highlights how the photon tunneling is governed by the electric LDOS spatial overlap between neighboring resonators. It depends on both the system geometry and on the dielectric permittivity values.

### 5.1.2 The D2 cavity-based photonic molecules

Starting from the D2 photonic crystal nanocavity, considered as the atomic-like building block of complex coupled systems, two kinds of photonic molecules have been realized and investigated [6]. The one in which two D2 cavities are aligned along the M photonic crystal axis, and the other where the nano-resonators are aligned along the K symmetry direction, reported in the insets of Fig. (5.1 a) and Fig. (5.2 a), respectively. In the spectrum of M-aligned molecule, shown in Fig. (5.1 a), are present two pairs of peaks, P1-P2 exhibiting a large splitting and P3-P4 with a small spectral separation, comparable to the mode linewidth. All of them are roughly in the same spectral region of the M1 and M2 modes of the single D2 cavity. By analyzing Eq. (5.2), neglecting the losses, we find that the molecular mode splitting ( $\Omega_+ - \Omega_-$ ) reduces to  $\sqrt{\Delta^2 + 4g^2}$ . Then, the splitting between molecular modes is proportional to the coupling strength but it is also affected by detuning. Therefore, the presence of a double peak in the spectrum is not enough to state the presence of an effective coupling. More insight is pursued by the electric field intensity distribution analysis, performed by mapping for each mode the wavelength spectral shift induced by the SNOM dielectric probe, as reported in Fig. (5.1 b-e). P1 and P2 intensity distributions covers the whole molecule. In both maps is clearly recognizable the superposition of M1 mode intensity distribution on the two PCNs that constitute the molecule. Therefore, the combined spectral and spatial information makes clear that P1 and P2 are

molecular-like modes resulting from a strong coupling between the M1 modes of the single M-aligned PCNs. For the investigated sample, also the maps concerning P3 and P4 are delocalized on the entire molecule and are formed by a superposition of the M2 modes of the single PCNs, as reported in Fig. (5.1 d-e). Thus they result as molecular-like modes, whose spectral separation is ascribed to a small but effective coupling. The behavior of the M-aligned molecule is predicted by Eq. (5.7). In fact, a large overlap between the isolated PCN modes leads to a strong coupling, as happens for M1 that is elongated parallel to the M-axis resulting in P1 and P2 molecular-like modes. While a small overlap results in a reduced coupling that can be in competition with the disorder induced detuning, as it happens for the single cavity mode M2, which is elongated parallel to the K-axis and gives rise to P3 and P4 molecular modes.

Conversely, K-aligned molecule exhibits the opposite behavior with respect to the M-aligned molecule. In fact, due to the spatial properties of M1 and M2, the coupling between P1-P2 is smaller with respect to the interaction between P3-P4. In the investigated sample, whose spectrum is reported in Fig. (5.2 a), P1 and P2 modes show a small splitting. But the evidence of a negligible coupling, with respect to disorder induced detuning, is found only after the analysis of the electric field intensity maps of Fig. (5.2 b-c). Where it is clear that both P1 and P2 modes are localized only on one PCN and, therefore, instead of molecular modes they have to be considered as atomic-like modes. On the other hand, the widely spectrally separated modes P3 and P4 experience a strong coupling characterized by spatial distributions delocalized on the whole system, see Fig. (5.2 d-e). Therefore, in the investigated molecule the splitting between P1 and P2 modes has to be mainly ascribed to disorder induced detuning ( $g < \Delta$ ), while the splitting between P3 and P4 modes is largely attributed to an effective interaction ( $g > \Delta$ ).

The straightforward result of the angular emission pattern analysis, performed in the far-field for each polarization, is the symmetry character probing of the strongly coupled modes in both M-aligned and K-aligned D2-based photonic molecules [21]. In particular, the M-alignment is found to sustain a bonding ground state (P1), consequently exhibiting  $g < 0$ . On the other hand, in the K-alignment the molecule lower energy state symmetry character cannot be retrieved since the P1-P2 weak coupling can be deeply affected by the detuning between the two PCNs and, therefore, P1 can result in an atomic-like state, as reported in Fig. (5.2 b).

## 5.2 Post-fabrication control of evanescent coupling

Quite remarkably, in Sec. (5.1.2) it is shown that in photonic molecules the sign of the interatomic-like coupling is not uniquely defined and so is the parity of the modes. It is also proved, by the analysis of the far-field emission, that it is possible to change the character of a given molecular mode from even to odd, depending on the lattice direction along which the two PCN are aligned [21, 25]. Naturally emerges the question if in photonic molecules a fine tuning of the coupling strength expressed by Eq. (5.7) is achievable both at the design stage and with post-fabrication techniques, changing from positive to negative values, thus leading to an antibonding ground state. Firstly, we exploit accurate numerical FDTD-based calculations to neglect the

unavoidable fabrication induced disorder that leads to a significant detuning between the two PCNs. Such analysis allows us to demonstrate the possibility to tune the ground state of a given photonic molecule from a bonding to an antibonding character, by operating a local modification of the dielectric environment in between the two coupled nano-cavities. This also leads to possible implementation of a fine control of the photon tunnelling in coupled systems. Secondly, as a proof of principle, we experimentally probe the antibonding ground state nature along with the coupling strength induced variation of the K-aligned molecule. In order to achieve this goal we develop a local post-fabrication technique based on laser assisted non-thermal nano-oxidation [26].

### 5.2.1 Engineering the mode parity

For the numerical characterization of the resonant modes in photonic crystal molecules we employ the three-dimensional FDTD solver package presented in Sec. (2.1.3). We consider a 320 nm-thick semiconductor membrane with a refractive index  $n = 3.484$ , the same of GaAs material, but we could have chosen Si or  $\text{Si}_3\text{N}_4$  as well. The photonic structure is a two dimensional hexagonal lattice of holes ( $n = 1$ ) with lattice constant of  $a = 308$  nm, the pores have a diameter size  $d = 193.2$  nm, leading to a 35% filling fraction. Since the unit-cell by whom the dielectric matrix is discretized has size ( $x = a/28, y = \sqrt{3}a/28$ ) matched with the hexagonal lattice, every computed hole is exactly equal to the others and no detuning effect are present. The near-field detector is placed parallel to the PCN surface at a distance of 22 nm and covers the whole molecule.

The simulated photonic molecule is formed by two D2 nanocavities aligned along the K axis, since this configuration allows a small but sizable coupling between the M1 modes of the single PCN, resulting in the P1, P2 modes. In fact, the calculated spectrum of the nominal structure without detuning, reported in Fig. (5.3 a), shows a double peak structure with an energy splitting of the order of 1 meV. Neglecting the losses in Eq. (5.2), the molecular mode splitting  $\hbar\Omega_+ - \hbar\Omega_-$  reduces to  $2g$  for  $\Delta = 0$ , thus the splitting between P1 and P2 in FDTD spectrum gives a direct estimation of the coupling strength absolute value. Also the FDTD calculated electric field spatial distributions, reported in Fig. (5.3 b-d), are in agreement with the existence of a small but effective coupling, since both modes are delocalized over the molecule. The modes arising from M1 of the single PCN are linearly polarized along the cavity alignment direction, thus facilitating the numerical analysis since only one polarization component has to be investigated. Since M1 exhibits an even electric field distribution along both  $x$  and  $y$  axes, as reported in Fig. (4.10 c), the analysis of the maps in Fig. (5.3 b-c) points out that P1 mode has an antibonding character showing an odd spatial distribution with respect to the alignment axis inversion. While P2 mode is a bonding molecular mode with an even spatial distribution along  $x$ . Therefore, as highlighted by the electric field distribution of Fig. (5.3 b) and differently from real molecules, the K-coupling supports an antibonding ground state. An important outcome of the antibonding mode character is that the far-field emission is exactly zero along  $k_x = 0$  and in particular at normal direction, as shown in Fig. (5.3 c). This is a consequence

of destructive interference between the two out of phase coupled single PCNs [21]. For similar reasons, the bonding mode P1 has a strong emission along the normal direction, due to the constructive interference of the two in phase PCNs along  $k_x = 0$ , as reported in Fig. (5.3 c-e). Therefore, an inversion in the mode parity and symmetry can determine a large variation in the angular distribution of the photonic molecule modes.

As it is pointed out in Eq. (5.7) the character (B or A) of the ground state depends on the overlap integral between the two atomic-like modes weighted over  $\Delta\epsilon$ . In particular the interference of the two single cavity fields can result either in a positive or in a negative  $g$ , which induces the molecular ground state to be A or B, respectively. In fact, the single PCN localized mode  $\mathbf{E}_0$  exponentially decays moving away from the cavity with typical oscillation between positive and negative values superimposed. Therefore, the constructive interference between the two  $\mathbf{E}_0$  localized fields can provide  $g > 0$  and the antibonding ground state character.

It was also experimentally observed, for both the investigated polarization, that the K-aligned molecule sustains an antibonding lower energy state (P3) arising from the strong coupling between the M2 mode of the single D2 cavity, that give rise to P3 and P4 modes [21]. Analogous behavior can be also found in other kinds of nanocavity based photonic molecule [16, 22, 25, 27]. On the contrary, investigating the overall K-aligned molecule ground state (P1) is a difficult task. Since P1 and P2 modes are weakly coupled, a post-fabrication technique, able to compensate the disorder induced detuning, is required before measuring the coupled mode symmetry character.

Nevertheless, finding an antibonding lower energy molecular state is a counterintuitive result with respect to the standard expectation on the basis of the quantum mechanical analogy, for instance with standard coupled quantum wells. However, an antibonding ground state has been recently observed in coupled InAs quantum dots, where the heavy-hole light-hole mixing and the spin-orbit interaction causes this counterintuitive reversal for particular values of the barrier thickness [28]. An alternative description of the physics involved in photonic molecules, can be derived by recalling that the eigenstates of an arbitrary photonic system has to satisfy the variational principle, related to the minimization of the energy functional  $U$  [1]:

$$U = \frac{\int |\nabla \wedge \mathbf{E}(\mathbf{r})|^2 \cdot d\mathbf{r}}{\int \epsilon(\mathbf{r}) |\mathbf{E}(\mathbf{r})|^2 \cdot d\mathbf{r}} \quad (5.8)$$

The ways to minimize Eq. (5.8) are two: *(i)* by reducing the number of mode nodes and *(ii)* by increasing the field concentration in the high-dielectric regions. As in quantum mechanics, bonding states always satisfy the condition *(i)* and this is the reason why the ground states usually have bonding character. However, while the wave-function in atoms decays exponentially with distance from the nucleus, the localized electric field in a PCN shows an exponentially damped oscillation with distance from the local dielectric defect. The overlap between the oscillating evanescent electric field of the two single PCN modes produces constructive or destructive interference. Obviously, in the case of constructive (destructive) interference, the electric field is enhanced (reduced), and this decreases (increases)  $U$ . Therefore, the presence

of an antibonding ground states in photonics is associated with constructive interference in the defect region for the odd state, which may enhance the electric field concentration in the high-dielectric regions.

An open question is whether it would be possible to control both the photonic coupling strength value and sign by local modifications of the structure design. This adjustment has to be symmetric with respect to the molecule geometry, otherwise it induce a sort of detuning between the two single cavities. The region of strong overlap between the single molecular modes  $\mathbf{E}_0(\mathbf{r})$  and  $\mathbf{E}_0(\mathbf{r} + \mathbf{D})$  can be evaluated by mapping the value:

$$|\mathbf{E}_B(\mathbf{r})|^2 - |\mathbf{E}_A(\mathbf{r})|^2 \quad (5.9)$$

which for the considered K-coupled photonic molecule is reported in Fig. (5.4 a). The overlap is distributed on the whole system, but the maximum value is close to the four pores around the central hole between the two cavities. Then we reduce the diameter size of five central holes of the molecule, highlighted in Fig. (5.4 b), imposing a symmetric perturbation. Although such perturbation affects a region where  $\Delta\epsilon = 0$ , the coupling strength given by Eq. (5.7) is modified by a variation of the single cavity resonant mode  $\mathbf{E}_0$  equally for both PCNs, as assured by the symmetric dielectric alteration. This perturbation leads to a marked tuning of both molecular modes but with different strength. The peak energy values of the B and A modes are reported in Fig. (5.4 c) as a function of the modified holes diameter size  $d$ . Starting from the nominal  $d$  (193.2 nm), which corresponds to an A ground state with 1.0 meV energy splitting, we see that the diameter size reduction produces a continuous decreasing of the photonic coupling, directly evaluated from the mode splitting. For  $d = 183.2$  nm the molecular spectrum shows a single peak, meaning that the photonic coupling is decreased below the mode broadening. This leads to a degeneracy of the two molecular modes that is purely accidental, since the  $C_{2v}$  symmetry of the K-coupled D2 photonic cavities cannot support degenerate modes accordingly to the group theory [29]. With a further reduction of  $d$  the ground state changes into a bonding character, as a consequence of the change of the photonic coupling sign. For  $d = 173.2$  nm the mode splitting is 1.1 meV, almost equal to the nominal design, but with modes exhibiting a reversed parity. Therefore, a smooth transition of the lower energy state from bonding to antibonding can be achieved.

A more intuitive picture of the physics underlying the data reported in Fig. (5.4 c) can be obtained by considering the dielectric perturbation induced tuning in the basis of the molecular modes. In fact, decreasing  $d$  means adding dielectric material, accordingly with the observed red shift of both modes. In addition, the perturbation being very local, the mode shift is larger the higher is the mode electric field intensity at the dielectric modification position. Therefore, the presented local perturbation results in a more pronounced red-shift of the B mode with respect to the A mode.

Further information about the photonic molecular modes parity transition is obtained by analyzing the mode quality factors as a function of  $d$ , as shown in Fig. (5.4 d), where the mode broadening of both P1 and P2 modes are reported as a function of  $d$ . It is well known that the formation of the molecular modes with opposite parity also tailors the diffraction losses [30]. For the nominal structure with identical

holes the lower energy broadening is 0.38 meV, while a smaller broadening (0.22 meV) is found for P2, in agreement with the far-field patterns of Fig. (5.3 c and e), which show that P1 has larger diffractive losses. These values are almost constant when reducing  $d$  from the parity inversion, then they reach an intermediate value when the coupling vanishes and finally they are exchanged after the transition. In other words, we find that the  $Q$  of the A and B modes are almost unaltered. Moreover, the A mode is always broader than the B one, in contrast to the intuitive findings for coupled L3 cavities, associated to the strong (weak) emission of the B (A) mode in the vertical direction [30]. However, the discrepancy is only apparent, since always the broader mode has larger diffractive losses in the light cone. The different behavior is simply due to the differences in the angular patterns of the single modes, as L3 cavity is compared to the D2 cavity. Therefore, the broadening exchange between P1 and P2 is a consequence of the parity transition achieved with the manipulation of five central pores.

The counterintuitive change of the photonic molecule ground state from a bonding to an antibonding orbital character is also confirmed by performing numerical guided mode expansion method calculations [31]. In Fig. (5.5 a-b) are reported the resonant energy of both bonding and antibonding modes in M-aligned and K-aligned photonic molecules, respectively, as a function of the cavity-to-cavity distance. For these calculations, we use a supercell dimensions of up to  $16a \times 7w_0$  for the K-alignment (where  $w_0 = \sqrt{3}a$ ), and  $10a \times 13w_0$  for the case of M-alignment. The photonic molecules discussed so far are reported in the insets of Fig. (5.5 a-b) and correspond to a center-to-center distance equal to  $3\sqrt{3}a$  and  $3a$  for the M-aligned and K-aligned photonic molecules, respectively. Figure (5.5 a) shows that the ground state for the M coupled molecule, for increasing center-to-center distances, is always bonding and that the modes energy splitting decreases monotonically, as expected for standard coupled systems. On the contrary, in the case of K-aligned molecules the ground state symmetry does not follow a trivial behavior, as results from Fig. (5.5 b). In fact, the lower energy mode has either an even or an odd character as a function of the cavity separation. Furthermore, the small energy mode splitting shows little variations for center-to-center distance greater than  $3a$ . These results agree with experimental data and FDTD calculations thus confirming the subtle nature of the photonic coupling, driven by a complex interference between localized light states.

It could be interesting to explore whether also a post-fabrication tuning method would be able to control the molecular mode parity, thus it could be used to realize optical switches exploiting the inversion of the peculiar far-field patterns of the A and B modes. In order to propose experimental methods to achieve a post-fabrication coupling control, we consider a gentle modification of the refractive index within a circular central region of the photonic molecule with a diameter of the order of 0.8  $\mu\text{m}$ . To address the problem, a controlled reduction of the effective refractive index could be experimentally obtained either by a local photo-induced oxidation of the semiconductor slab that will be presented in Sec. (5.2.2); or dynamically by injecting free carriers, for instance with a fs pulsed laser [32–34].

We theoretically implement such techniques in the case of the modified photonic molecule with the five central hole diameter sizes reduced to 173.2 nm. Since starting from such geometry we can obtain the opposite ground state character transition to

the one reported in Fig. (5.4 c). The results are reported in Fig. (5.6), where the schematics of the modified photonic molecule are drawn as left panels and the corresponding calculated spectra are reported in the right panels. Starting from the nominal refractive index equal to 3.484, we reduce the refractive index of the circular central part of the underlying slab at 3.416. The corresponding calculated spectrum shows a single peak only, denoting a very small (if any) photonic coupling. Eventually, for a refractive index of 3.348, we find that the P1 character is changed into antibonding and that the splitting reaches 1.2 meV.

In summary, it is possible to tune a photonic molecule mode from the bonding to the antibonding character and vice versa. The control can be experimentally achieved by combining a careful design of the central region between the two PCNs or by post-fabrication techniques such as local laser-assisted oxidation or dynamic free-carriers injection exploiting fs pulsed laser, for instance. These properties would open the road to possible applications in quantum optical information processing, including the optical switch of the far-field pattern of quantum emitters.

### 5.2.2 Photoinduced non-thermal oxidation tuning

Concerning most of the PCNs applications in optoelectronic and quantum optics, a fundamental requisite relies on the design and control of the localized modes at the target wavelengths, within an accuracy which is not directly obtainable due to the unavoidable fabrication tolerances [35–37]. Different post-fabrication processing methods, able to tune the nanocavity modes for compensating the fabrication imperfections, have been demonstrated in the last few years, such as tip and thermal induced tuning, wet chemical digital etching, atomic layer deposition, AFM induced nano-oxidation, liquid nano-infiltration, and nano-electromechanical tuning induced by controlling the applied voltage to PCN based devices [32, 38–43, 25]. The combination of these techniques allows large and fine tuning of the resonant mode, with respect to the mode linewidth, and enables both a reversible or irreversible mode spectral shift towards lower or higher wavelength.

Recently, a very simple method based on the thermal oxidation by laser irradiation in air atmosphere has been realized in GaAs and Si structures [33, 44]. This method has the great advantage of being local without needing extra materials and processing tools. However, it requires a large thermal budget which can produce undesired annealing and modification of the underlying semiconductor layers. In order to overcome this drawback, we implement a method to achieve photo-induced fine-tuning of PCN resonant modes with very low thermal budget. It is based on light induced oxidation in air atmosphere which produces a local reduction of the GaAs membrane effective thickness and at the same time an enlargement of the holes diameter effective size resulting in a large and smooth blue-shift of the nanocavity modes.

The experimental setup employed to analyze the photo-induced oxidation is a confocal apparatus where a 50X microscope objective ( $NA = 0.7$ ) replaces the near-field probe in Fig. (3.2). The sample is excited either with light from a diode laser (780 nm) or by an Ar ion laser (514 nm), and the emitted PL signal is coupled to a

single-mode optical fibre of 6  $\mu\text{m}$  core diameter, acting as a confocal pinhole connected to a spectrometer with a 300 lines/mm grating that provides a spectral resolution of 0.5 nm. Finally, the sample is mounted on a  $xy$  stage so that it can be scanned in respect to the objective, allowing the collection of two-dimensional PL maps. Therefore, both the nanocavity mode observation and the laser-driven nano-oxidation are performed in the far-field to validate a proof-of-principle that can be extended, as we will show, to SNOM configuration for improving the induced oxidation resolution. The spatial resolution obtained by the confocal setup is evaluated performing a PL intensity map of the fundamental PCN mode M1 at low excitation power ( $P = 0.1 \text{ mW}$ ) with the  $\lambda = 514 \text{ nm}$  laser, where heating can be neglected, as reported in Fig. (5.7 a). The laser spot FWHM size results 1.1  $\mu\text{m}$  thus defining the spatial resolution. The local temperature of the samples under laser exposure is directly measured by using the PCN modes as a local thermometer and taking advantage of the thermal red-shift of the resonant modes that, around room temperature, has been calibrated for the M1 mode of the D2 nanocavity to be 0.12 nm/K [45].

By increasing the laser density power illuminating and collecting PL signal in the center of the PCN we observe a sizeable red-shift, as reported in Fig. (5.7 b) for 780 nm laser excitation. To get more insight into the temperature induced distribution the thermal induced spectral shift map and the average radial profile are evaluated in Fig. (5.7 cd), respectively. The map shows that the thermal gradient extends over a 2  $\mu\text{m}$  region, that is slightly larger than the excitation spot and allows us to retrieve the temperature distribution. However, during laser exposure, the PCN modes may shift due to oxidation, optical Kerr effect, free carrier injection, and heating. Oxidation leads to an irreversible blue-shift which is negligible for the experimental time exposure (100 ms) corresponding to the integration time of the spectra acquired in Fig. (5.7). Optical Kerr effect occurs at much higher excitation power, due to the small non-linearity of GaAs [46]. The tuning due to free carrier injection gives a blue-shift estimated to be of the order of 1 nm for the data reported in Fig. (5.7 c) by using the parameter given in ref. [34]. Heating gives a red-shift of the modes and, therefore, in the reported experimental condition proves to be the dominant effect. Still the correction for the blue-shift (of the order of 20% of the experimental red shift) due to free carrier injection has to be accounted for an accurate estimation of the sample temperature. The experimental spectral shift of M1 at the center of the spot in Fig. (5.7 c) is 4.7 nm, corresponding (including the estimated blue-shift for carrier injection) to a temperature rise as low as  $\Delta T < 47^\circ\text{C}$ . The temperature increase is large enough to be carefully measured but extremely low for thermal effects such as annealing or thermal oxidation to be activated. Data for green light from the Ar laser are very similar: at the maximum power used ( $P = 0.7 \text{ mW}$ ), we observe a temperature increase as  $\Delta T = 22^\circ\text{C}$ .

In order to verify that our data reflect the real temperature of the sample, we use FEM calculations to estimate the laser heating for the realistic structure in the experimental conditions. The temperature profile during laser irradiation is calculated by solving the heat conduction equation, taking into account the temperature-dependent thermal conductivity of bulk GaAs and the power lost due to reflection at the top surface of the membrane. We note that the actual thermal conductivity in the PCN

region may be lower than the bulk values due to phonon scattering at the etched interfaces. Heat losses due to convection and conduction in air are neglected. Multiple reflections inside the membrane are also not considered; for green light, the absorption in a single pass through the membrane is more than 90%, and therefore, the approximation is valid.

The spatial temperature gradient calculated by FEM at the top surface of the PCN at a laser power  $P = 0.7$  mW and  $\lambda = 516$  nm (because of the availability of the parameters required for the calculation) is reported in Fig. (5.8 a-b). It nicely agrees with the experimental data, giving a thermal distribution extending over 2  $\mu\text{m}$ . In particular, the temperature reaches the maximum value ( $\Delta T = 16$  °C) at the center of the laser spot and drops while moving away from it; thus, experimental data and theoretical simulations nicely fit together. On the other hand, in the case of infrared light assuming an excitation power of 2.7 mW and  $\lambda = 780$  nm, the FEM calculation gives a maximum heating equal to 21 °C. This value is underestimated because the membrane absorption in a single pass is only 38% of the incoming power and, therefore, neglecting the multiple reflection is likely to be incorrect. Nevertheless, the reliability of the temperature estimation and especially the very low thermal budget used in the experimental condition are supported by FEM calculations.

Despite the very low thermal budget of the exposure condition, we observe that a non-reversible modification of both the resonant mode wavelength and the PCN dielectric environment occurs after laser illumination of about half an hour under high excitation power, that is,  $P = 2.7$  mW for  $\lambda = 780$  nm and  $P = 0.7$  mW for  $\lambda = 514$  nm. In fact, when reducing the laser power and after waiting for the cooling of the sample, the PCN modes undergo sizeable blue-shift. The mode shift can be controlled either by varying the laser power or by iterating laser exposure steps. Figure (5.9 a) displays PL spectra acquired at low power (0.1 mW) after different exposure times with high power (0.7 mW) green Ar laser, showing a large blue-shift of both resonances without remarkable  $Q$  or intensity variations. To highlight the time dependence for both excitation lasers, the resonant wavelength variations of M1 are given as a function the square root of the time in Fig. (5.9 b). Although the 780 nm excitation induces a larger temperature rise, the comparison clearly indicates that the rate of blue-shift is much larger when the high power exposures are performed with  $\lambda = 514$  nm light, thus denoting a relevant wavelength dependence on the effect. The time evolution of the irreversible effect is a key aspect to assess its origin. Clearly, from the spectra of Fig. (5.9 a), it is evident that the blue-shift is not linear with the laser exposure time. But, as denoted in Fig. (5.9 b), it is linear with the square root of the time, thus indicating a fingerprint of a diffusive process [44]. Therefore, we attribute the progressive mode shift with irradiation time to a non-thermal oxidation of the GaAs membrane. The oxidation acts by reducing the membrane effective thickness and/or by increasing the effective photonic crystal pores diameters. In both cases, the effect on the PCN mode is a shift toward smaller wavelengths. In order to demonstrate that the blue-shift depends on the presence of oxygen in the environment of the sample during laser irradiation, we perform the same confocal experiment in a controlled nitrogen atmosphere. In this case, the blue-shift of the resonant modes is missing, indicating that oxygen is requisite for observing the PCN modes spectral shift.

It is well known that the local GaAs oxidation produces oxide protrusions due to the larger molar volume of the oxide with respect to the GaAs. A topography image of the D2 cavity, collected by a dielectric SNOM probe acting as shear-force sensor, after a laser exposure corresponding to an overall shift of 13 nm of the photonic modes is shown in Fig. (5.10 a). The presence of an oxide protrusion in a spatial region corresponding to the laser spot is clearly observed and the central horizontal line profile is displayed in Fig. (5.10 b) to depict the height of the oxidized area. A value of about 20 nm height is found with respect to the non oxidized region. This data could in principle be used to estimate the structural changes of the membrane. From the ratio of the molar volume of stoichiometric oxide, found in ref. [47], for the investigated D2 nanocavity we expect a reduction of the membrane thickness of the order of 10 nm on the top interface, and this could be used for calculating the mode shift.

The final point of our oxidation analysis is to address the physical mechanisms for explaining the laser assisted non-thermal oxidation of the GaAs. Effects on the GaAs surface after light illuminations have already been reported when the energy of the incident radiation is larger than the GaAs band gap [48]. This indicates that a carrier generation at the crystal surface is essential to observe the enhanced oxidation effect. Thus, the photo-generated electron-holes pairs can catalytically enhance the breaking of the substrate bonds and the dissociation of the adsorbate molecules [49]. The experimental evidence that the reaction rate per incident photon is strongly dependent on photon energy has been already observed and related to the interaction of hot electrons with O<sub>2</sub> via resonant tunneling [50]. Therefore, the catalytic effect of electron-hole pairs photo-generated at the surface of PCNs produces a large and fine controlled tuning of the resonances without drastically increasing the sample temperature. The laser assisted oxidation of the sample determines a local modification of the nanocavity dielectric environment, reducing the effective membrane thickness and increasing the effective photonic pores diameter. Furthermore, due to photo-enhanced reactivity of GaAs surface, green light laser is much more efficient in inducing the oxidation with respect to light wavelengths closer to the semiconductor band gap energy.

Finally and remarkably, post-growth local control of the photonic modes with a low thermal budget that avoids annealing and/or damage of the embedded light sources, such as quantum wells or quantum dots, can be exploited also for changing on demand the coupling strength between emitters and optical modes or between interacting optical modes in systems consisting on coupled PCNs.

### 5.2.3 Antibonding ground state

We also take advantage of the laser-assisted oxidation to directly measure the character of the weak coupled modes in K-aligned photonic molecule, thus experimentally demonstrating the existence of a photonic molecule antibonding ground state. This configuration, as theoretically predicted in Sec. (5.2.1) in the zero detuning case, provides an antisymmetric lower energy state. First of all, we need to compensate the fabrication induced disorder, which can be relevant in weak coupled modes. Therefore, we act on the detuning without significantly modify the coupling strength.

Since the oxidation produces a blue-shift of the photonic modes, we expose the laser beam on the PCN in which the ground state molecular mode (P1) is initially more confined. The resolved confocal PL is used to image with low spatial resolution both coupled modes, thus roughly monitoring the spatial distributions. As reported in the inset of Fig. (5.11 a), we expose the right-side of a K-aligned photonic molecules at steps of the order of half an hour with Ar at power of 1 mW. As a function of the oxidation induced detuning the mode splitting (of 1.2 nm) undergoes an anticrossing behavior, see Fig. (5.11 a). The initial splitting is of the order of 2.1 nm and reaches a minimum value of 1.2 nm after 150 minutes of laser exposure. When the condition of minimum  $\Omega$  is satisfied, a far-field angular emission pattern of both coupled modes is performed by means of modified confocal experimental setup developed in ref. [21]. This procedure allow us to retrieve constructive (destructive) interference, fingerprint of the bonding (antibonding) character. In particular, in the experimental far-field patterns of Fig. (5.11 b and d) we observe for the lower energy mode (P1) a destructive interference along the wavevector axis perpendicular to the alignment direction, while for the higher energy mode (P2) a vanishing signal is found along the same wavevector axis. These results are in agreement with the numerical FDTD calculations of the angular pattern distributions for both modes, reported in Fig. (5.11 c and e). This is a further signature of the antibonding ground state in K-aligned photonic crystal molecule.

### 5.2.4 Coupling strength control

The post-fabrication control of evanescent tunnelling in a D2 based photonic crystal molecules K-aligned is demonstrated through the combination of local and selective tuning techniques, such as infiltration of water, micro-evaporation, and laser induced non thermal oxidation [26, 42]. The value of the photonic coupling is directly measured by the molecular mode splitting at the anticrossing point. In fact, we are able to either increase or decrease the detuning ( $\Delta$ ) and the photonic coupling ( $g$ ), independently, by inducing a local asymmetric or symmetric perturbation with respect to the molecule environment, respectively. From Eq. (5.2), neglecting the losses, the mode splitting ( $\Omega$ ) between the molecular modes results:

$$\Omega = 4g^2 + \Delta^2 \quad (5.10)$$

The coupling strength described by Eq. (5.7) depends on the overlap between the single atomic-like modes localized in each resonator. Being directly proportional to (5.9), it is therefore sensitive to the fabrication-induced disorder present in the central region of the molecule. This would limit the possibility of developing extended array of identically coupled photonic molecules, unless a post-fabrication control of  $g$  is implemented. In order to engineer  $g$  parameter, we make the most of the non-thermal laser assisted oxidation presented in Sec. (5.2.2), by illuminating the sample with Ar laser (514 nm,  $P = 2.5$  mW) coupled to a SNOM dielectric probe, that guarantees a high degree of localization [51]. The laser high-power exposure is performed by keeping the tip in the middle of the photonic molecule in order to achieve a symmetric

oxidation that prevents mode detuning. After each laser exposition step the PL signal of photonic molecule is investigated by performing SNOM scan employing low excitation Ar laser power (0.1 mW). The topography detected by means of SNOM measurements allows us to precisely induce the local laser exposure in the center of the photonic molecule. In addition, we choose a photonic molecule with a very small splitting between P1 and P2, indicating that the disorder induced detuning is quite small. Furthermore, to assure a negligible detuning between the two PCNs we focus on the separation between the strongly coupled modes P3 and P4. The main effect of the laser exposure is to blueshift all the photonic modes, as shown for the case of P3 mode reported in Fig. (5.12 a) as a function of exposure time. More interestingly, we observe that  $\Omega$  undergoes a large and monotonic reduction from  $(14.7 \pm 0.2)$  nm to  $(10.2 \pm 0.2)$  nm, as shown in Fig. (5.12 b). Since P3 and P4 arise from the strong coupling regime, the observed splitting reduction is mainly attributed to an effective mode interaction variation rather than to an induced detuning. This assumption is confirmed also by the overlap map between the two strongly coupled modes P3-P4 reported in Fig. (5.12 e) and calculated from the difference between the FDTD calculated electric LDOS of P3 and P4 shown in Fig. (5.12 c-d), respectively. Therefore, the experimental  $\Omega$  reduction demonstrates that the laser induced oxidation is a powerful tool for adjusting the photonic tunneling rate; in this particular case for decreasing  $g$  about 30% of its initial value.

The laser induced oxidation of GaAs, due to the smaller index of refraction of the oxide, is equivalent to an effective reduction of the GaAs material that provides a blueshift of all the resonant modes. Therefore, as pointed out in Sec. (5.2.2), this process could imply a reduction of the effective slab thickness and/or an enlargement of the effective pore sizes. In order to understand the physical origin of the observed  $g$  reduction, we perform three-dimensional FDTD calculations either by reducing the slab thickness or by enlarging the diameter size of the eleven central pores of the K-aligned photonic molecule, as reported in Fig. (5.13 a-d). In both cases, all the photonic modes experience a blue-shift, as shown for the notable case of P3 in Fig. (5.13 a and c). However, a difference emerges in investigating the mode splitting reported in Fig. (5.13 b and d). On one hand, the slab reduction is almost ineffective in changing  $\Omega$ , on the other hand a reduction of the calculated  $\Omega$  comparable with the experimental data is obtained when enlarging the central eleven pore diameter sizes. A decrease of  $(4.5 \pm 0.4)$  nm, which matches the experimental value, is found. On the contrary, the only enlargement of the pore diameter sizes cannot explain the P3 mode experimental large blue-shift of  $(28.0 \pm 0.1)$  nm. So, we need to take into account also the slab thickness reduction, whose main effect, however, is only to blue-shift the resonant modes. Therefore, the laser induced oxidation is effective in decreasing the photon coupling as a consequence of the filling fraction reduction in between the two adjacent PCNs. Moreover, we also expect that the refractive index increase in the middle of the photonic molecule would result in increasing the coupling strength  $g$ .

In order to confirm this prediction, FDTD calculations are implemented assuming that the central pores of the molecule are completely filled by a medium with  $n = 1.33$  (the same refractive index of water). We perform different simulations by infiltrating 1, 5, and 11 central pores of the K-aligned molecule, respectively. The more the holes are infiltrated, the more the resonant modes are red-shifted, as highlighted

for P3 in Fig. (5.14 a). The calculated  $\Omega$  is reported as a function of the number of infiltrated pores in Fig. (5.14 b), exhibiting almost the same value in all the three cases. Therefore,  $g$  can be increased by local infiltration, but the main contribution is given by filling the single central pore, as highlighted by Fig. (5.12 e).

We therefore perform a micro-infiltration experiment with a diluted solution of water and rhodamine, which helps in removing air bubbles inside the pipette (as can be seen by optical inspection). Heuristically, we observed that this solution strongly improves in filling efficiently the photonic pores. Micro-infiltration experiments are more difficult to control since the observed increase of  $\Omega$  can also be produced by a nonsymmetric infiltration, with consequent increase of  $\Delta$ . So, we need to directly measure  $g$  in an anticrossing experiment, by acting on  $\Delta$  in order to reach the zero-detuning condition. Only in this condition, from Eq. (5.10),  $\Omega = 2g$  holds, and thus a direct measure of the coupling strength is obtainable. For this purpose, we implement a detailed experimental procedure schematized in Fig. (5.14 c) and employing the confocal PL oxidation-detection setup, since we do not require sub-wavelength resolution for the oxidation process. After each infiltration process, or laser exposure step, the PL signal of photonic molecule is investigated by performing a scan with low power excitation Ar laser (0.1 mW). In the first step (1) we infiltrate the pores in the external region adjacent to the right-side PCN. Then with the confocal setup we expose the infiltrated region with the Ar laser at 2.5 mW, forcing the water evaporation and inducing local photo-oxidation. This allows to measure the anticrossing curve and thus to extract the initial  $g$  value. In the second step (2) we perform an infiltration in the central region of the photonic molecule in order to change  $g$ . At the final step (3), we induce a second non-symmetric oxidation on the left side of the photonic molecule in order to determine by a second anticrossing curve the final value of  $g$ . Experimentally, the first infiltration step is implemented on the right side of the photonic molecule because the higher-energy weak-coupled mode P2 is initially found to be localized on the right cavity, as retrieved by low-power confocal PL spatial distribution (not shown here). After the right-side infiltration, the weak-coupled mode localized on the right cavity becomes red-shifted by 4 nm, while the left cavity one remains almost unchanged, confirming that the micro-infiltration is local and selective.

Reporting the mode splitting between P3 and P4 ( $\Omega$ ) as a function of the laser exposure time in Fig. (5.14 d) we find an increase of  $\Omega$  after the right side micro-infiltration that has to be ascribed to the induced detuning. Then, we force the water evaporation and at the same time induce oxidation by illuminating the infiltrated right-side region (1). By doing this, we still act on a single PCN therefore on  $\Delta$ . As a function of the exposure time during step (1) we observe in the blue dots of Fig. (5.14 d) an initial reduction of  $\Omega$ . Then, once the detuning is perfectly compensated,  $\Omega$  starts to increase, thus providing an anticrossing behavior. We can precisely extract the value of the coupling strength by measuring the minimum  $\Omega$ , for an exposure time of about 130 min, that results in  $g = (6.6 \pm 0.1)$  nm.

Now, in such a configuration, we infiltrate the central region of the molecule performing step (2) in Fig. (5.14 c) in order to increase the coupling strength. After the central infiltration  $\Omega$  increases from 14.1 nm to 17.4 nm, see the comparison between the last blue dot and the first black dot in Fig. (5.14 d). However, such enlargement cannot be simply ascribed to a coupling increase, since the infiltration could be not

perfectly symmetric. Therefore,  $g$  value after the infiltration (2) is determined by means of a second anticrossing curve obtained through an oxidation of the left-side region of the photonic molecule, see step (3) in Fig. (5.14 c). The results are reported by the black dots in Fig. (5.14 d), where the oxidation time is kept the same as measured by the beginning of the three steps. The experimental minimum splitting after the central pores infiltration gives  $g = (8.5 \pm 0.1)$  nm, with an increase of 28% with respect to the value measured before the central dielectric modification. The values of the photonic coupling, both before and after the infiltration (2) are in good agreement with the FDTD calculations reported in Fig. (5.14 d).

The presented combination of post-fabrication methods allows us to control with excellent accuracy the coupling strength in photonic molecules. The deterministic control of the photon evanescent tunneling rate can be extended to any photonic crystal molecule geometry, thus making possible the realization of array of photonic cavities with on demand tunneling rate between each pair of coupled resonators. Finally, this peculiar engineering of photonic crystal molecules would open the road to possible progress in the exploitation of coherent interference between coupled optical resonators both for quantum information processing and optical communication.

### 5.3 Array of photonic molecules

Photonic molecules permit the coupling of the identical modes of the bare cavities giving rise to spatially delocalized and spectrally separated modes. Nowadays, the nanotechnology research interest is deeply focused on devices, which are formed by an arrangement of nano-resonators in a long array, either one-dimensional or two-dimensional, since these systems represent a very promising platform for manipulating and controlling the light propagation and the modal dispersion at the nanoscale [52, 53].

Photonic molecules formed by an array of nominally identical cavities, like coupled resonator optical waveguide (CROW), exhibit spatially delocalized optical modes and spectral minibands, which describe the light “hopping” between adjacent resonators [23, 54]. The CROW systems are therefore highly promising elements for building large scale photonic integrated circuits and exploit “slow-light” behavior. However, despite the large interest in the field, very little is known on the role of different neighboring interaction between PCNs array molecules.

Here, we approach the photonic molecule of three coupled PCNs in two configuration geometries, leading to different behaviors in terms of mode splitting and spatial distribution, as the inter-cavity alignment changes. We demonstrate by near field optics that the photonic hopping between PCNs can be driven by the interplay between the nearest-neighbour and the next-nearest-neighbour interactions. When the nearest-neighbour coupling coefficient is the dominant term, the photonic molecular modes behave very similarly to quantum system, such as coupled quantum wells, concerning the mode envelope distributions [55]. On the contrary, by designing a photonic molecule where the role of the next-nearest-neighbour coupling is not negligible, we obtain a non-intuitive picture for the mode splitting and spatial distributions.

For sake of simplicity, in the following analysis we focus only on the coupling between the lower energy mode of each single D2 nanocavity (M1). The theoretical investigation of the differences between M-alignment and K-alignment is performed by two-dimensional plane wave expansion calculations, by modelling an infinite array of D2 PCNs, whose schematics are reported in the insets of Fig. (5.15 a-b), respectively. We obtain the energy band diagram projected along the wavevector component parallel to the coupling axis, within the first Brillouin zone of the photonic crystal for both the array alignments, as reported in Fig. (5.15 a-b). The finite width of both dispersion curves demonstrates the effective photonic hopping between the nanocavities. The expected interaction difference between the two kinds of alignments is confirmed by modal dispersion analysis, which shows clear minibands for both configurations but with different trends. For the M-alignment, a monotonic and large increase of the energy of the photonic guided mode as a function of  $k_y$  (wavevector component parallel to the coupling axis) is found, as reported in Fig. (5.15 a). This pattern corresponds to a photonic guided mode with positive group velocity. On the contrary, for the alignment along the K-axis a small and non-monotonic variation of the array photonic guided mode energy is found, as reported in Fig. (5.15 b). This is a signature of anomalous light propagation that shows a group velocity sign change, from negative to positive, along the modal dispersion. In the tight binding picture for a photonic waveguide consisting of identical coupled resonators, it is possible to estimate the amplitude of each neighbour coupling term for both array alignments. In fact, the mode interaction in CROW is the optical analogue of the tight-binding limit in condensed-matter physics, in which the overlap of atomic wave functions is large enough that corrections to the picture of isolated atoms are required, yet, at the same time, it is not large enough to render the atomic description completely irrelevant [56]. Therefore, the calculated minibands can be well reproduced by [24]:

$$\hbar\omega(k) = \hbar\omega_0 - \sum_{m=1}^{\infty} J_m \cos(mkD) \quad (5.11)$$

where  $k$  represents the wavevector component considered,  $\hbar\omega_0$  is the energy of the isolated single cavity,  $D$  is the spatial separation between adjacent resonators and the parameters  $J_m$  are the nearest-neighbour ( $m = 1$ ), the next-nearest-neighbour ( $m = 2$ ) and successive neighbouring coupling terms. Therefore,  $J_1$  corresponds to the nearest-neighbour interaction defined as  $g$  in Sec. (5.1) and Sec. (5.2). Each coupling term is expressed by the generalization of (5.7) [24]:

$$J_m = \hbar\omega_0 \frac{\int \Delta\varepsilon(\mathbf{r}) \mathbf{E}_0(\mathbf{r}) \cdot \mathbf{E}_0(\mathbf{r}+m\mathbf{D}) d\mathbf{r}}{\int [\mu_0 |\mathbf{H}_0(\mathbf{r})|^2 + \varepsilon(\mathbf{r}) |\mathbf{E}_0(\mathbf{r})|^2] d\mathbf{r}} \quad (5.12)$$

where  $\mathbf{D}$  is represented by  $3\sqrt{3}a\hat{y}$  for the M-alignment and by  $3a\hat{x}$  for the K-alignment. By fitting the calculated energy dispersion with Eq. (5.11), where only the first three  $J_m$  terms are considered, we find the coupling coefficient values reported in Table (5.1). In the M-alignment the modal dispersion of the miniband is governed by the coupling between adjacent PCNs ( $J_1/a = -12.8$  meV), while the amplitudes of the higher order contributions  $J_2$  and  $J_3$  are negligible. The case of K-aligned molecule is quite different. The values of  $J_1$  and  $J_2$  are of the same order of magnitude

( $J_1/a = 1.16$  meV,  $J_2/a = 1.55$  meV), while  $J_3$  is negligible. Therefore, in the K-aligned molecule the approximation of nearest-neighbour interaction fails and in any finite array a complex mode splitting and non-intuitive delocalization of the resonant fields is expected. Moreover, looking at the  $J_m$  signs, both the coupling terms in K-alignment show the opposite sign with respect to  $J_1$  of the M-aligned array. This sign inversion is in agreement with the behavior of the two coupled PCNs molecule discussed in Sec. (5.1.2). Therefore, the negative (positive) coupling strength gives rise to a bonding (antibonding) ground state in M-coupled (K-coupled) arrays of any length.

In order to validate the properties extracted from the array modal dispersion analysis, we experimentally investigate the photonic molecule array composed by three D2 nanocavities aligned either along the M or the K-axis. The SEM image of an M-aligned array with  $a = 311$  nm is reported in the inset of Fig. (5.16 a). The typical near-field PL spectrum, spatially averaged over the array, is reported in Fig. (5.16 a) and it shows three peaks almost equally spaced by 10 nm, hereafter denominated  $Tn$  ( $n = 1,2,3$  for decreasing wavelength), in agreement with the theoretical FDTD calculations shown in Fig. (5.16 c). The spectral offset between experiment and theory has to be ascribed to the fabrication-induced disorder (not considered in the simulations) and to the slab refractive index, which is evaluated as GaAs refractive index at the wavelength of interest neglecting any possible oxidation or dispersion of the material. The summary of  $Tn$  peak positions, evaluated by fitting the spectrum with a three Lorentzian peaks function, is reported in Fig. (5.16 b) for different samples, which possess nominal identical design and so differ only for the fabrication induced disorder. A spread of the order of few nm in the peak positions is clear, but the separations between T1-T2 and T2-T3 remain almost constant for every sample. This means that disorder has a limited impact on the mode coupling, since for the M-alignment the interaction strength is larger than the detuning.

The case of the K-aligned array molecule is more complex. A corresponding typical SEM image is reported in the inset of Fig. (5.16 d). The summary of the  $Tn$  peak positions for nominally identical samples are shown in Fig. (5.16 e). The overall resulting splitting between T1-T3 is much smaller with respect to the M-alignment, denoting a weaker mode coupling. We observe a large variation of the peak splitting as shown in Fig. (5.16 e) indicating that the disorder induces a mode detuning, which can be comparable with the mode coupling. The structure where the role of disorder is less pronounced is likely the array#1, whose PL spectrum is reported in Fig. (5.16 d). It shows an almost degeneration of T1 and T2 modes. In fact, we find that array#1 corresponds to a system of almost identical cavities, as inferred by the comparison between the experimental splittings of Fig. (5.16 d) and the FDTD calculated ones, reported in Fig. (5.16 f), relative to  $\Delta = 0$  configuration.

In order to understand the physics underlying the mode splitting of the two kinds of array we develop a minimal analytic model of three coupled resonators. The behavior of the M-aligned array can be reproduced by considering only the nearest-neighbour negative coupling  $-|g_M|$ . Assuming three identical resonators with energy  $\hbar\omega_0$ , thus neglecting  $\Delta$ , the coupled system mode energies and distributions are found by solving the eigenvalue problem of the M-matrix given by:

$$M = \begin{pmatrix} \hbar\omega_0 & -|g_M| & 0 \\ -|g_M| & \hbar\omega_0 & -|g_M| \\ 0 & -|g_M| & \hbar\omega_0 \end{pmatrix} \quad (5.13)$$

whose solutions are the eigenvalues  $E_n$  and the eigenvectors  $c_n$ :

$$E_1 = \hbar\omega_0 - \sqrt{2}|g_M| \quad c_1 = (1, \sqrt{2}, 1) \quad (5.14)$$

$$E_2 = \hbar\omega_0 \quad c_2 = (-1, 0, 1) \quad (5.15)$$

$$E_3 = \hbar\omega_0 + \sqrt{2}|g_M| \quad c_3 = (1, -\sqrt{2}, 1) \quad (5.16)$$

where the three components of  $c_n$  describe the envelope mode amplitude on the basis composed by the three single adjacent resonators. The energy splitting between the first and the last resonant mode ( $2\sqrt{2}|g_M|$ ) is  $\sqrt{2}$  times larger than the mode splitting of a system composed of only two coupled resonators. This prediction is in good agreement with the comparison between the average splitting of 20 nm between T1-T3 found in the investigated M-coupled array and the 13 nm observed in the two PCNs M-aligned photonic molecule, with an identical coupling region [6]. In addition, the FDTD calculated splitting between T1-T3 together with the analytic splitting expression from (5.14 and 5.16), allows us to retrieve the coupling strength,  $|g_M| = 5.6$  meV for a three-dimensional system. This result is almost a factor of two smaller than  $J_1$ . Such discrepancy can be explained by total suppression in two-dimensional calculations of the out-of-plane losses that enhance the field confinement strength, thus increasing the overlap integral of Eq. (5.12). The near-field spatial distribution of the array modes is addressed by imaging the PL intensity detected by the SNOM setup reported in Fig. (3.2). The comparison between the PL intensity map of the M-aligned array#2 and the electric field intensity map calculated by FDTD for the same structure is reported in Fig. (5.17) for every  $Tn$  modes. It is clear that T1 and T3 modes are mainly localized in the central PCN, thus corresponding to the  $c_1$  and  $c_3$  states, see (5.14 and 5.16). While the T2 mode is almost completely localized in the external PCNs, as expected for the  $c_2$  state, see (5.15). Finally, we observe that, since the experimental average mode splitting is of the order of 10 nm (corresponding to 7.3 meV), the role of disorder induced detuning is negligible in the investigated M-aligned arrays.

Concerning the K-aligned geometry a quite different behavior is observed. In this configuration the next-nearest-neighbour interaction plays a crucial role, as stated from the calculations of the two-dimensional infinite K-coupled array being, for which  $J_2/J_1 = 1.34$ , as reported in Table (5.1). The photonic molecule denoted as K-aligned array#1, is the structure where the disorder induced detuning is mostly negligible, as inferred by the comparison between the experimental and the FDTD calculated spectrum of Fig. (5.16 d and f), respectively. PL SNOM measurements are exploited to probe the mode intensity distributions, as reported in Fig. (5.18). In particular, the higher quality factor mode (T3) exhibits an intensity distribution mainly delocalized over the two external PCNs. This distribution is in agreement with the calculated FDTD electric field intensity map, as highlight by the comparison between

Fig. (5.18 e and f). Concurrently, the T1 and the T2 experimental mode distributions, whose peak wavelength is evaluated by a three Lorentzian functions fit of the entire spectrum, are delocalized over both central and left side PCNs, as reported in Fig. (5.18 a and c), respectively. The same results are retrieved by the FDTD calculated electric field intensity maps relative to the T1 and the T2 modes shown in Fig. (5.18 b and d). With the exception that T1 and T2 modes are exchanged with respect to the experimental case. This behavior can be driven by a little disorder induced detuning (even much smaller than the coupling strength), that slightly shifts T1 with respect to T2 or vice-versa, nevertheless resulting in a very small splitting.

In order to confirm this description of the K-aligned molecule, we employ the model of three coupled resonators including also the contribution of the next-nearest-neighbour coupling  $d_k = |d_k|$  besides the nearest-neighbour term  $g_k = |g_k|$ , which have to be positive. The resonant energies and distributions are found by solving the eigenvalue problem of the K-matrix given by:

$$K = \begin{pmatrix} \hbar\omega_0 - \Delta_l & g_k & d_k \\ g_k & \hbar\omega_0 - \Delta_c & g_k \\ d_k & g_k & \hbar\omega_0 \end{pmatrix} \quad (5.17)$$

where we also consider the possible mode detuning  $\Delta_l$  and  $\Delta_c$  relative to one lateral resonator and to the central resonator, respectively. Pushing further the analysis we are able to estimate the nearest and next-nearest neighbour coupling strength by firstly solving the eigenvalues problem for the K-matrix (5.17), when the condition  $\Delta_l = 0 = \Delta_c$  holds. Subsequently, by calculating the mode splittings of the FDTD spectrum reported in Fig. (5.16 f), which corresponds to 0.35 nm and 2.94 nm splitting between T1-T2 and T1-T3, respectively. We therefore find that these wavelength splittings are exactly reproduced by the analytic model in the condition  $g_k = 0.69$  meV,  $d_k = 0.88$  meV. The obtained values, like the ones for the M-coupling, are still two times smaller with respect to the two-dimensional estimation, but exhibit a ratio equal to 1.28 that is quite similar to the ratio  $J_2/J_1$ . The corresponding eigenvalues, evaluated in wavelength units as  $\lambda_n = \hbar c E_n^{-1}$ , and eigenvectors are:

$$\lambda_1 = 1306.26 \text{ nm} \quad c_1 = (-0.71, 0, 0.71) \quad (5.18)$$

$$\lambda_2 = 1305.92 \text{ nm} \quad c_2 = (0.38, -0.84, 0.38) \quad (5.19)$$

$$\lambda_3 = 1302.98 \text{ nm} \quad c_3 = (0.59, 0.54, 0.59) \quad (5.20)$$

While the peak positions can be reproduced quite accurately, the discrepancy between  $c_3$  and both the experimental and FDTD calculated spatial distributions reported in Fig. (5.18 e and f), likely suggests that the predictions of the analytic model are seminal but not fully correct, since the real system is more complex than three coupled oscillators. In any real device the dielectric disorder is an unavoidable drawback. A systematic analysis of the role of mode detuning is therefore needed and it could represent an outlook for nanophotonic devices to engineer the photon hopping between adjacent resonators in high density optical circuits. For this purpose, and in order to deeply study the role of detuning in both array configurations, we exploit the

noteworthy eigenvalues prediction coming from the analytic model of M-matrix and K-matrix in presence of both  $\Delta_l$  and  $\Delta_c$ .

In Fig. (5.19 a-d) we report the  $\lambda_n$  in wavelength units as a function of central detuning and as a function of lateral detuning, respectively. In the calculations we use the parameters:  $\hbar\omega_0 = 953.7$  meV ( $\lambda_0 = 1300$  nm),  $g_M = 5.6$  meV and  $d_M = 0$  meV in order to model the M-coupled array, see Fig. (5.19 a-b), and  $g_k = 0.69$  meV and  $d_k = 0.88$  meV in order to model the K-coupled array, see Fig. (5.19 c-d). The results for the M-aligned array show, as reported in Fig. (5.19 a), that  $\lambda_2$  remains constant and equal to  $\lambda_0$  as a function of the central detuning. While only the

lower energy and higher energy states shift, exhibiting a minimum  $\lambda_1 - \lambda_3$  splitting for  $\Delta_c = 0$ , fingerprint of an anticrossing behaviour. In fact,  $\lambda_2$  is not dependent from central detuning since the corresponding eigenvector  $c_2$  is given by (5.15). Therefore, the envelope of this state vanishes in the middle cavity and any local modification in the central molecule region does not affect the state energy or distribution. On the other hand, as reported in Fig. (5.19 b) with the same coupling terms of Fig. (5.19 a), all the eigenvalues change with  $\Delta_l$ . In this case the minimum  $\lambda_1 - \lambda_3$  splitting is still at zero detuning, while both  $\lambda_1 - \lambda_2$  and  $\lambda_2 - \lambda_3$  exhibit minimum separation for  $\Delta_l \neq 0$ . By analyzing the model (5.17) that reproduces the K-coupled array interaction we find that, differently from the two coupled cavities system, the minimum splitting condition between every pair of resonant states as a function of detuning occurs in  $\Delta_l \neq 0$  and  $\Delta_c \neq 0$ . In Fig. (5.19 c) is highlight the accidental degeneracy between  $\lambda_1$  and  $\lambda_2$  driven by a finite central detuning. Moreover, for  $\Delta_c$  lower than the one that corresponds to the accidental degeneracy  $\lambda_2$  is not affected by the perturbation and its envelope distribution vanishes in the central cavity, while for increasing  $\Delta_c$  these properties are gained by  $\lambda_1$ .

This inversion between the two lower energy modes as a function of  $\Delta_c$  can thus explain the inverted intensity distributions observed between the experimental and the calculated P1 and P2 modes, reported in Fig. (5.18 a-d). The trend evaluated in Fig. (5.19 d) as a function of lateral detuning is similar to the one reported in Fig. (5.19 c), with the exception that no accidental degeneracy is observed and an anticrossing behavior between  $\lambda_1$  and  $\lambda_2$  occurs. All these results highlight the quite complex detuning dependence of the relative mode splittings.

In conclusion, we show that different PCNs array configuration geometries lead to different results in terms of mode splitting and spatial distribution. When both the nearest and next-nearest-neighbour coupling terms are relevant, a non-intuitive picture describes the resonant modes, in addition the photon hopping between adjacent nanoresonators is strongly affected. These findings could open the way to exploit exotic configurations of coupled PCNs to tailor the mode spatial distribution or the group velocity in CROW of any length by engineering the dielectric properties of adjacent resonators in high-density optical circuits.

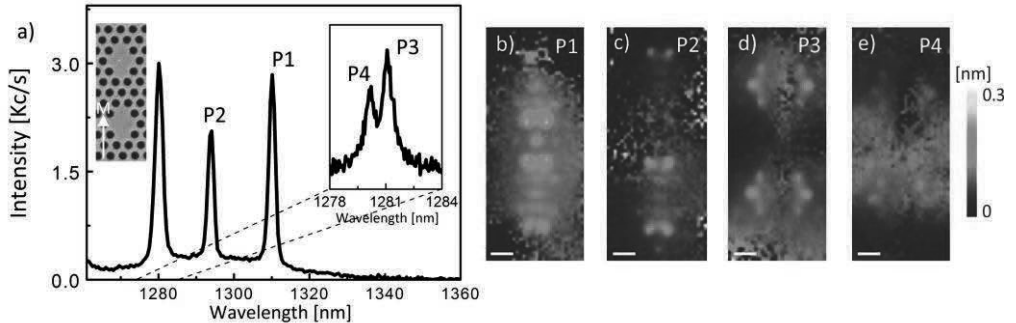


Figure 5.1: SNOM measurements on M-aligned photonic molecule with  $a = 311$  nm, performed by SNOM PL with dielectric tip. Figures adapted from [6]. a) Average spectrum of the molecule highlighted in the inset with the direction of the M-axis. b) Spectral shift maps of P1, P2, P3 and P4, respectively. The scale bar is 300 nm.

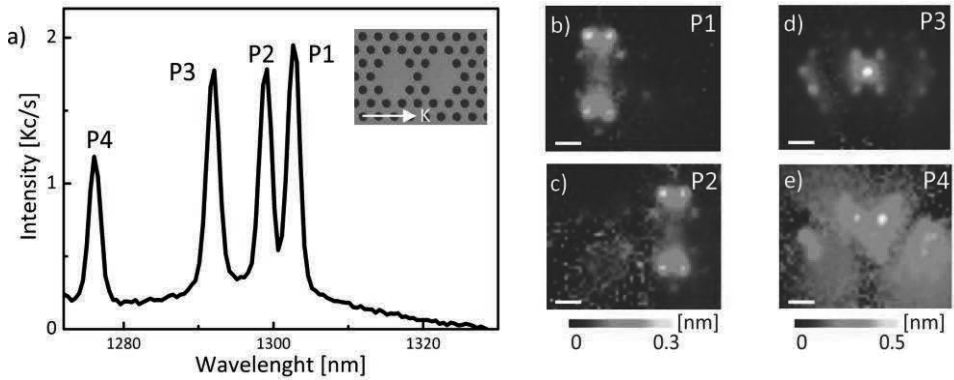


Figure 5.2: SNOM PL measurements on K-aligned photonic molecule with  $a = 311$  nm, performed with a dielectric tip. Figures adapted from [6]. a) Average spectrum of the molecule highlighted in the inset with the direction of the K-axis. b) Spectral shift maps of P1, P2, P3 and P4, respectively. The scale bar is 300 nm.

## Imaging and engineering optical localized modes at the nanoscale

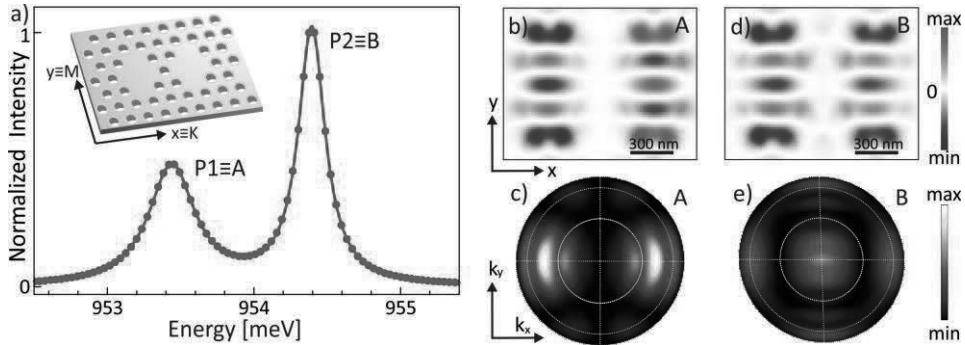


Figure 5.3: FDTD calculations of the K-coupled photonic molecule without detuning. a) Normalized spectrum averaged over the molecule reported in the inset. The P1 (lower energy) and P2 (higher energy) peaks correspond to the antibonding (A) and bonding (B) state, respectively. b)-c) Spatial distribution of the real part of the electric field and angular distribution in the wavevector space, relative to the antibonding mode (P1), respectively. d)-e) Spatial distribution of the real part of the electric field and angular distribution in the wavevector space, relative to the bonding mode (P2), respectively. The white circles in d) and e) indicate the aperture angles of 30° and 60°.

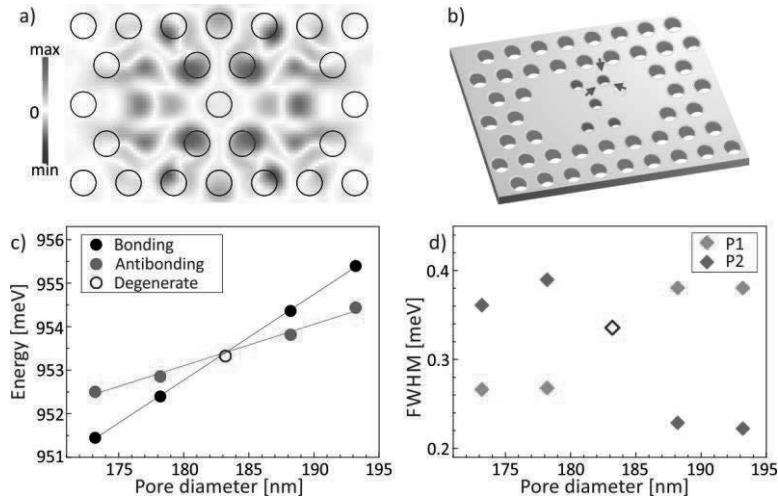


Figure 5.4: a) Map of the quantity (5.9) evaluated by FDTD. b) Scheme of the K-molecule where the size of the five central pores (red) is reduced for tuning the coupling strength. c) Calculated peak position of the B and A modes as a function of the diameter size of the five central pores highlighted in b). The blue circle corresponds to degenerate condition. d) Calculated spectral broadening of the ground state (P1) and the excited state (P2) as a function of the diameter size of the five central pores.

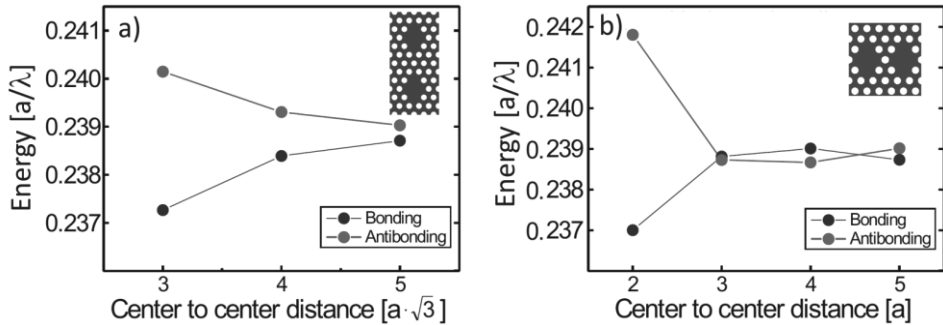


Figure 5.5: a)-b) Resonant energy of both bonding and antibonding modes in M-aligned and K-aligned photonic molecules, respectively, as a function of center-to-center separation (in units of the hole-to-hole distance). The calculations are performed by the guided-mode-expansion method [31]. In the insets are reported the design of the photonic molecule exhibiting a center-to-center separation of  $3\sqrt{3}a$  and  $3a$  for the M-aligned and K-aligned photonic molecules, respectively.

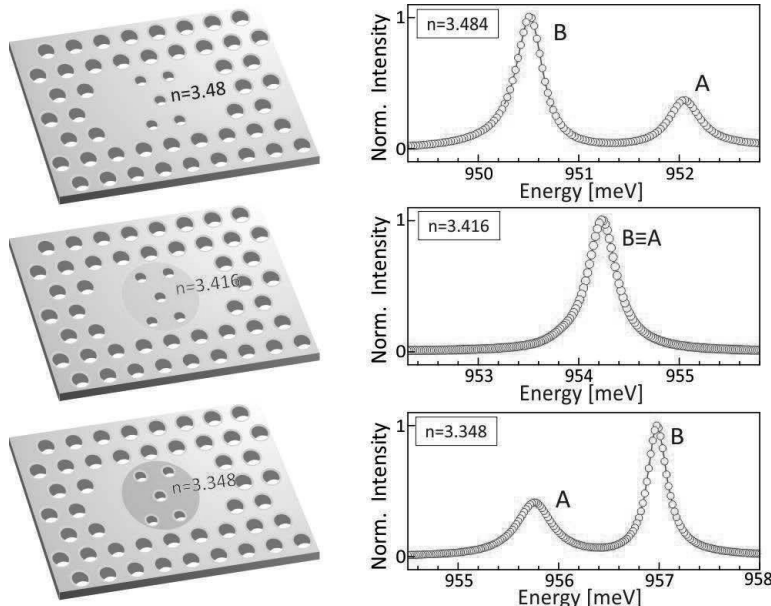


Figure 5.6: Left panel: schematics of the K-coupled molecule with five central pores diameter size reduced to 173.2 nm. First row, nominal sample with  $n = 3.484$ ; second row, reduction to  $n = 3.416$  in the central circular region (pale yellow circle); third row, reduction to  $n = 3.348$  in the central circular region (yellow circle). Right panel: FDTD spectra relative to the structure in the left panel. The bonding or antibonding character is highlighted.

Imaging and engineering optical localized modes at the nanoscale

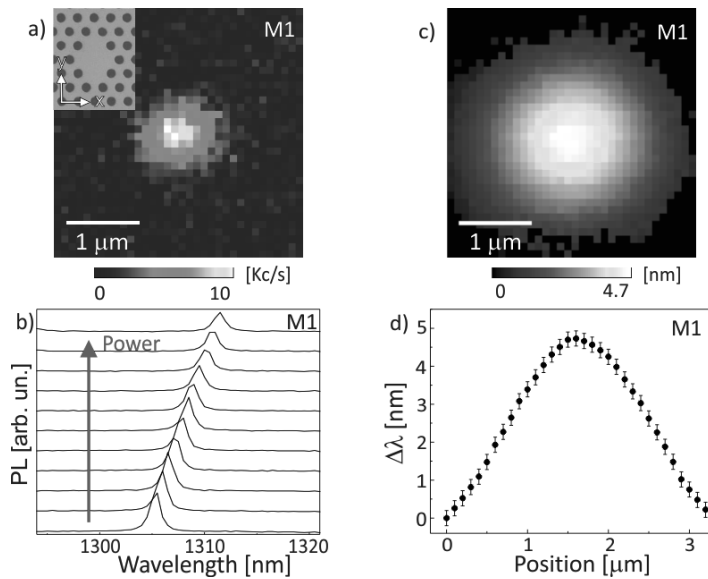


Figure 5.7: a) PL intensity map of the mode M1 of the PCN with  $a = 311$  nm reported in the inset, obtained at low excitation power ( $P = 0.1$  mW) with the 514 nm laser. b) M1 spectra acquired for increasing power excitation of the diode laser (780 nm) from 0.25 mW to 2.7 mW. c) Map of the M1 mode spectral shift measured with high excitation density ( $P = 2.7$  mW) provided by the 780 nm laser. d) Spatial profile of the thermal induced spectral shift evaluated from the average line cut in c).

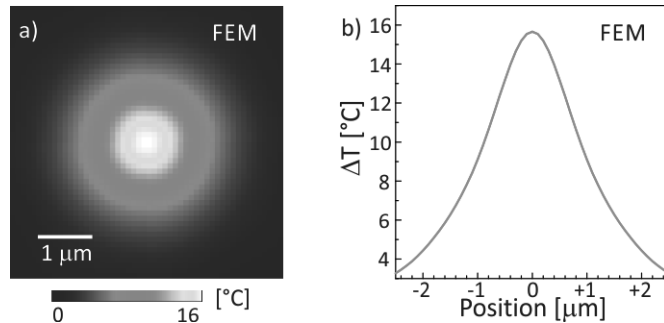


Figure 5.8: a) Spatial distribution of the temperature gradient calculated by FEM on the top surface of a D2 nanocavity with slab thickness 320 nm, employing laser irradiation at 516 nm with a power of 0.7 mW. b) Radial spatial profile extracted from a).

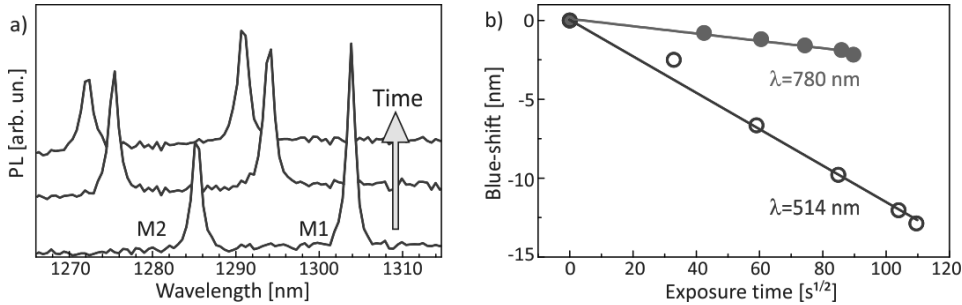


Figure 5.9: a) PL spectra of the investigated D2 nanocavity acquired at low Ar laser power (0.1 mW) after three subsequent exposures to high Ar laser power (0.7 mW). Starting from the bottom, the second and the third spectra are collected after 120 minutes and 200 minutes of high power laser exposition with respect to the first spectrum. b) M1 mode wavelength blue-shift plotted as a function of the square root of high power exposition time both for Ar and diode lasers.

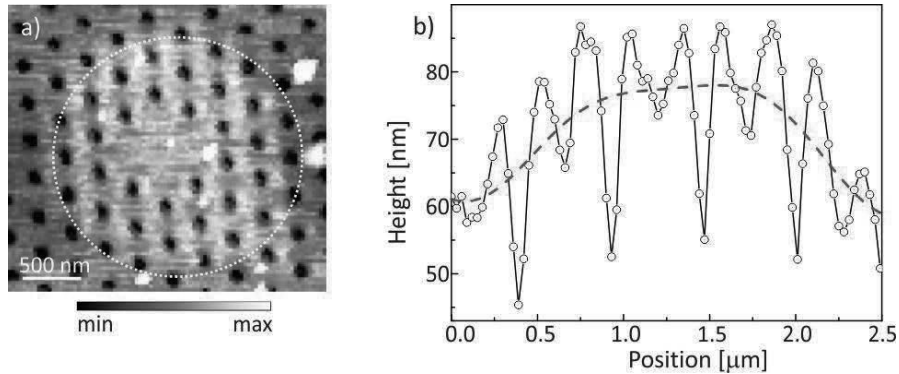


Figure 5.10: a) Topography of the PCN after a laser exposure corresponding to an overall shift of 13 nm for the M1 mode. The map is collected by a dielectric probe that acts as shear-force sensor. A protrusion is observed inside the dotted circle due to the laser local oxidation. b) Line profile of a) (black circles) for evaluating the height of the oxidized region, being approximately 20 nm. The red dashed line is a guide to the eyes obtained through a FFT low pass filtering.

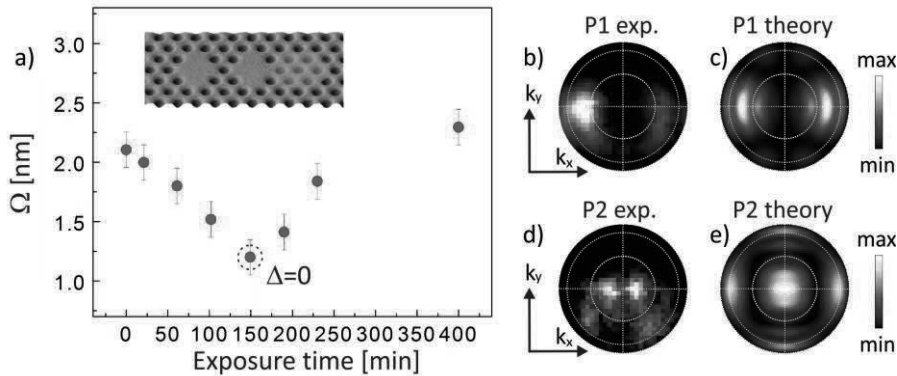


Figure 5.11: a) Splitting ( $\Omega$ ) between the weakly coupled modes P1 and P2 in K-aligned photonic molecules, as a function of the Ar laser exposure time. The local oxidation is performed by means of confocal setup illuminating with 1.0 mW on the right side of the molecule, as shown in the inset, since the ground state mode (P1) is initially localized on the right-side PCN. b)-c) Experimental far-field angular distribution and FDTD calculation, respectively, of the ground state molecular mode (P1) in the condition  $\Delta = 0$ . d)-e) Experimental far-field angular distribution and FDTD calculation, respectively, of the excited state molecular mode (P2) in the condition  $\Delta = 0$ . The white circles in b)-e) indicate the aperture angles of 30° and 60°.

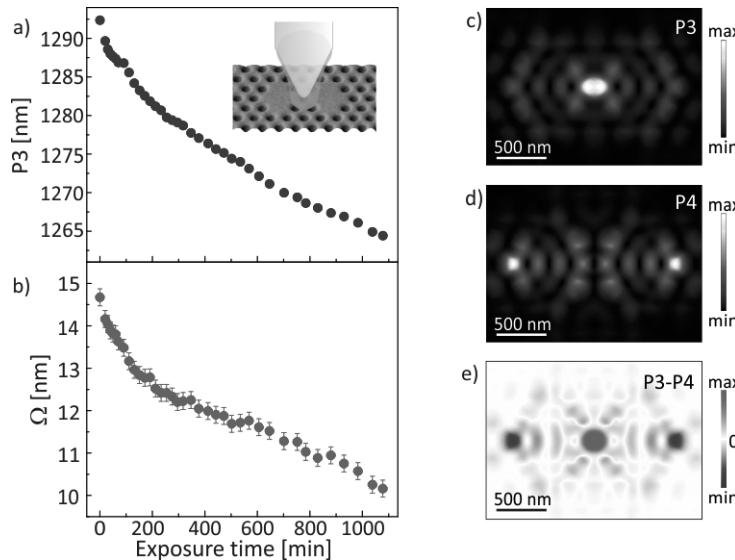


Figure 5.12: a)-b) Experimental P3 mode wavelength and splitting  $\Omega$  between P3 and P4, respectively, as a function of the Ar laser exposure time on K-aligned photonic molecule. The schematics of the exposition is reported in the inset of a). c)-d) Electric LDOS calculated by FDTD at the peak wavelength of P3 and P4, respectively. e) Difference between the maps in c) and d) to highlight the P3-P4 superposition regions.

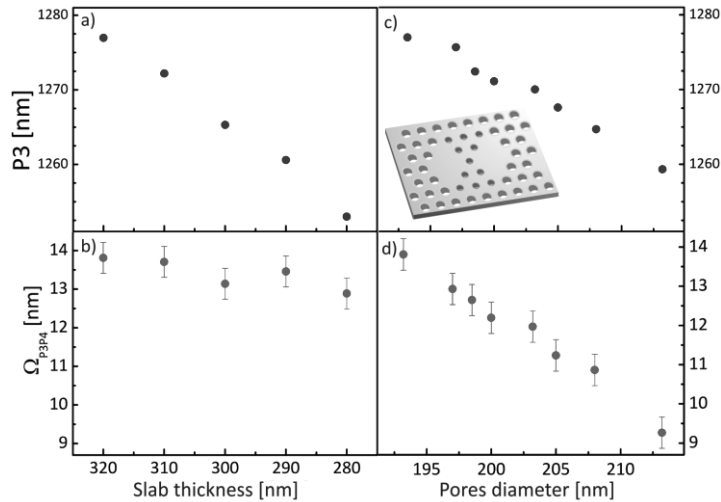


Figure 5.13: FDTD calculations performed on K-aligned photonic. a)-b) P3 mode wavelength and  $\Omega$  as a function of the GaAs membrane thickness, respectively. c)-d) P3 mode wavelength and  $\Omega$ , respectively, as a function of the diameter size of the eleven central pores of the K-aligned photonic molecule reported in the inset of c). The error bars are provided by the finite spectral resolution of the FDTD calculations.

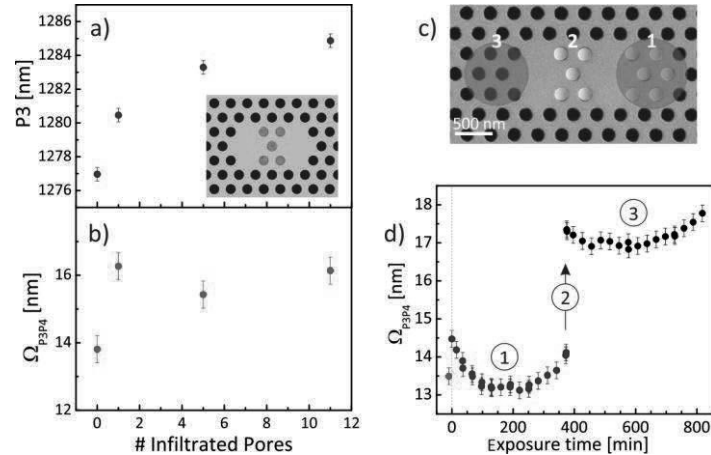


Figure 5.14: a)-b) P3 mode wavelength and  $\Omega$ , respectively, calculated by FDTD as a function of the number of infiltrated pores with  $n = 1.33$ , as schematically shown in the inset of a). c) Schematic view of the three experimental steps performed. d)  $\Omega$  is reported as a function of the exposure time of subsequent lateral micro-evaporation and micro-oxidations, as described in c). The red dot at negative time corresponds to the value before the right-side infiltration. The blue circles represent  $\Omega$  after the right-side infiltration and during the right-side laser illumination (1). The black dots represent  $\Omega$  after the central infiltration (2) and during the left-side laser exposure (3).

Imaging and engineering optical localized modes at the nanoscale

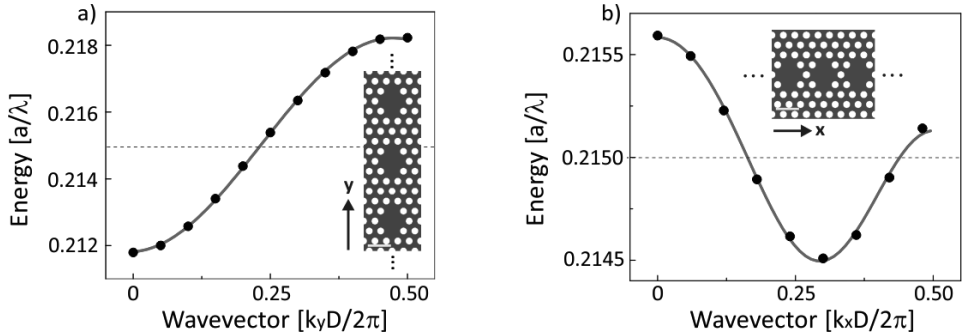


Figure 5.15: Two-dimensional calculations of the dispersion relation (black dots) of infinite array of D2 nanocavities, performed with plane wave expansion, reported in the energy range of the single cavity fundamental mode, whose energy is highlighted by horizontal dashed line. a) Calculation relative to the M-coupled infinite array (schematics in the inset) in the irreducible part of the first Brillouin zone, with  $D = 3\sqrt{3}a$ . The  $y$ -axis is parallel to the  $\Gamma M$  direction of the reciprocal lattice. The red curve provides the monotonous dispersion fit performed with Eq. (5.11). b) Calculation relative to the K-coupled infinite array, (schematics in the inset) in the irreducible part of the first Brillouin zone, with  $D = 3a$ . The  $x$ -axis is parallel to the  $\Gamma K$  direction of the reciprocal lattice. The red curve provides the non-monotonous dispersion fit performed with equation Eq. (5.11). The scale bar in both insets is 600 nm.

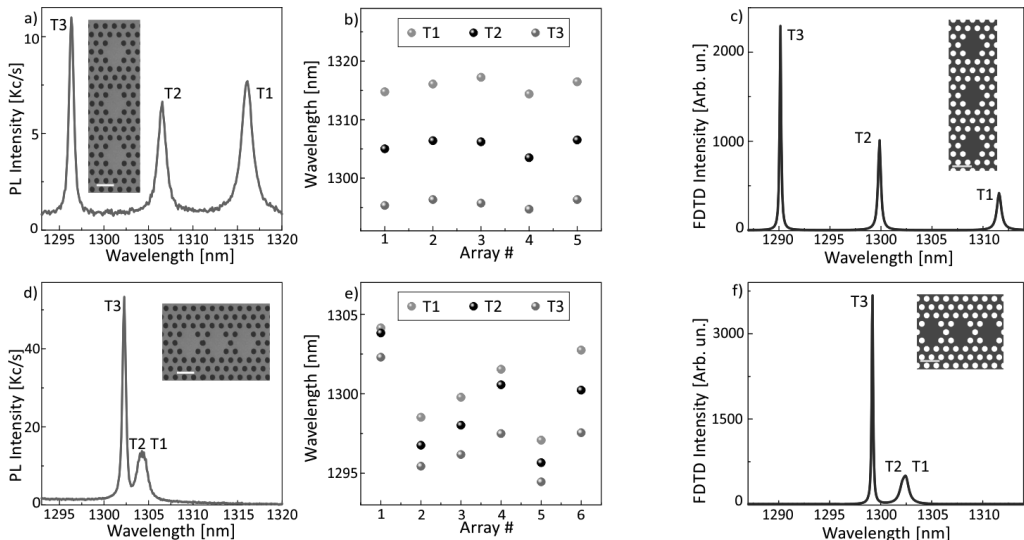


Figure 5.16: a) Experimental PL near-field spectrum averaged over the three M-coupled array nanocavities (see SEM image in the inset). Three sharp peaks (T1, T2, T3)

are observed. b) Resonant modes wavelength in nominally identical M-coupled arrays, evaluated by fitting each PL mean spectrum with a three Lorentzian peaks function. The second case in b) corresponds to the spectrum in a). c) FDTD spectrum averaged over the M-coupled array, see the inset schematics. d)-f) Same analysis of a)-c), but concerning the K-aligned array. e) Resonant modes wavelength for nominally identical K-coupled arrays. The first case corresponds to the spectrum shown in b). The scale bar is 600 nm.

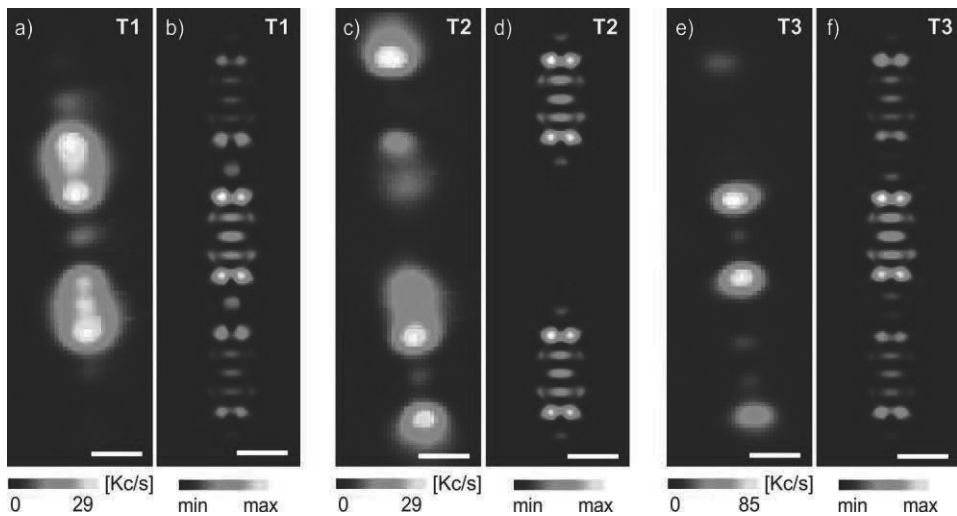


Figure 5.17: M-coupled array: PL near-field intensity map and FDTD calculated electric field intensity relative to T1 mode a)-b), T2 mode c)-d) and T3 mode e)-f). The experimental maps are relative to the array investigated in Fig. (5.16 a), while the FDTD maps correspond to the peak wavelength of modes reported in Fig. (5.16 c). The scale bar in all the maps is 600 nm.

Imaging and engineering optical localized modes at the nanoscale

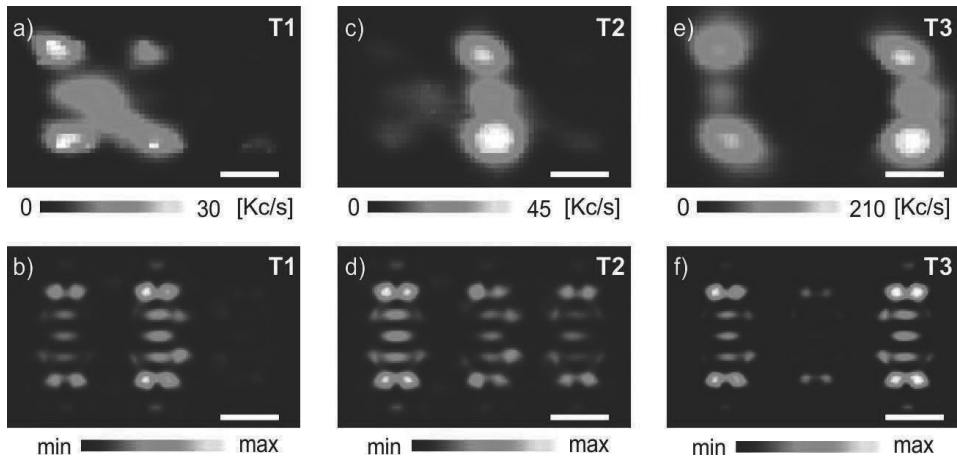


Figure 5.18: K-coupled array: PL near-field intensity map and FDTD calculated electric field intensity relative to T1 mode a)-b), T2 mode c)-d) and T3 mode e)-f). The experimental maps are relative to the array investigated in Fig. (5.16 d), while the FDTD maps correspond to the peak wavelength of modes reported in Fig. (5.16 f). The disorder induced detuning could be the responsible for the exchange of the experimental intensity distribution between T1 and T2, with respect to the FDTD calculation. The scale bar in all the maps is 600 nm.

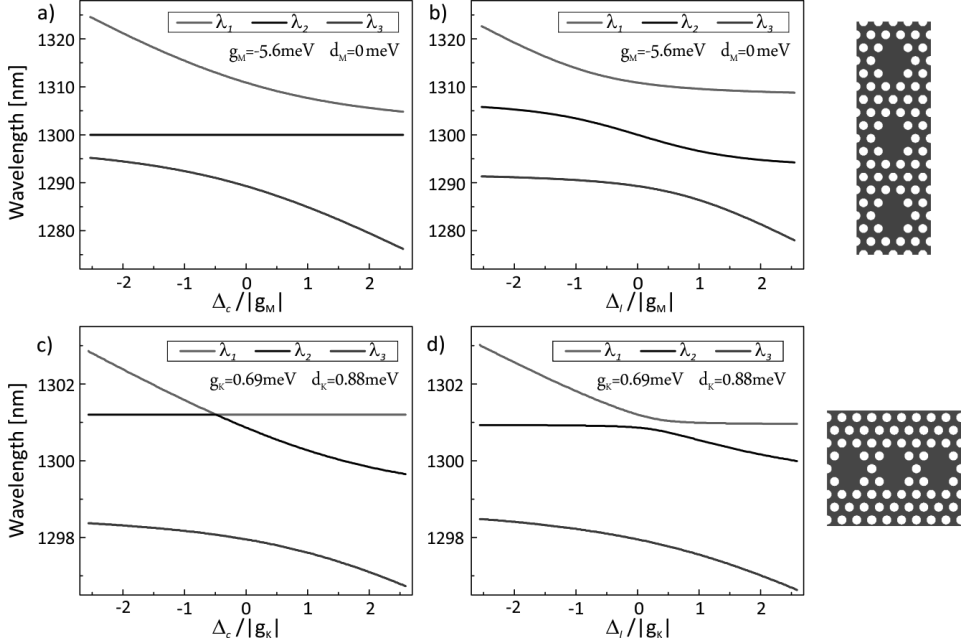


Figure 5.19: a)-b) Eigenvalues of M-matrix (5.13) as a function of central and lateral cavity detuning, normalized to  $|g_M|$ , respectively. The used parameters are:  $E_0 = 953.7 \text{ meV}$  ( $\lambda_0 = 1300 \text{ nm}$ ),  $g_M = -5.6 \text{ meV}$  and  $d_M = 0 \text{ meV}$ , reported in wavelength units. c)-d) Eigenvalues of K-matrix (5.17) as a function of central and lateral cavity detuning, normalized to  $|g_K|$ , respectively, calculated with  $E_0 = 953.7 \text{ meV}$ ,  $g_K = 0.69 \text{ meV}$  and  $d_M = 0.88 \text{ meV}$ , reported in wavelength units.

	$J_1 [a/\lambda]$	$J_2 [a/\lambda]$	$J_3 [a/\lambda]$
M-alignment	$-3.2 \cdot 10^{-3}$	$-8.3 \cdot 10^{-5}$	$-3.5 \cdot 10^{-5}$
K-alignment	$+2.9 \cdot 10^{-4}$	$+3.9 \cdot 10^{-4}$	$-0.7 \cdot 10^{-4}$

Table 5.1: Values of the coupling terms  $J_m$ , in  $a/\lambda$  units, calculated for the two-dimensional infinite array aligned along M and K-direction, respectively, and obtained by fitting with Eq. (5.11) the dispersion relations calculated in Fig. (5.15 a-b).

## References

- [1] J. Joannopoulos, S. Johnson, J. Winn, and R. Meade. Photonic Crystals: Molding the Flow of Light. Princeton University Press, 2nd edn., (2008).
- [2] S. Noda, M. Fujita, and T. Asano. “Spontaneous-emission control by photonic crystals and nanocavities” In: Nat. Photon. 1 (2007), pp. 449–458.
- [3] M. Bayer, T. Gutbrod, J. Reithmaier, A. Forchel, T. Reinecke, P. Knipp, A. Dremin, and V. Kulakovskii. “Optical Modes in Photonic Molecules” In: Phys. Rev. Lett. 81, 12 (1998), pp. 2582–2585.
- [4] S. Ishii, K. Nozaki, and T. Baba. “Photonic Molecules in Photonic Crystals” In: Jpn. J. Appl. Phys. 45, 8R (2006), p. 6108.
- [5] F. Brossard, B. Reid, C. Chan, X. Xu, J. Griffiths, D. Williams, R. Murray, and R. Taylor. “Confocal micro-photoluminescence mapping of coupled and detuned states in photonic molecules” In: Opt. Express 21, 14 (2013), pp. 16934–16945.
- [6] S. Vignolini, F. Intonti, M. Zani, F. Riboli, D. Wiersma, L. Li, L. Balet, M. Francardi, A. Gerardino, A. Fiore, and M. Gurioli. “Near-field imaging of coupled photonic-crystal microcavities” In: Appl. Phys. Lett. 94, 15 (2009), p. 1103.
- [7] C. Schmidt, A. Chipouline, T. Käsebier, E.-B. Kley, A. Tünnermann, T. Pertsch, V. Shuvayev, and L. Deych. “Observation of optical coupling in microdisk resonators” In: Phys. Rev. A 80, 4 (2009), p. 3841.
- [8] A. Nakagawa, S. Ishii, and T. Baba. “Photonic molecule laser composed of GaInAsP microdisks” In: Appl. Phys. Lett. 86, 4 (2005), p. 1112.
- [9] Y. Rakovich, J. Donegan, M. Gerlach, A. Bradley, T. Connolly, J. Boland, N. Gaponik, and A. Rogach. “Fine structure of coupled optical modes in photonic molecules”. In: Phys. Rev. A 70, 5 (2004), p. 1801.
- [10] S. Vignolini, F. Riboli, F. Intonti, D. Wiersma, L. Balet, L. Li, M. Francardi, A. Gerardino, A. Fiore, and M. Gurioli. “Mode hybridization in photonic crystal molecules” In: Appl. Phys. Lett. 97, 6 (2010), p. 3101.
- [11] D. Smith, H. Chang, K. Fuller, A. Rosenberger, and R. Boyd. “Coupled-resonatorinduced transparency” In: Phys. Rev. A 69, 6 (2004), p. 3804.
- [12] Q. Xu, S. Sandhu, M. Povinelli, J. Shakya, S. Fan, and M. Lipson. “Experimental Realization of an On-Chip All-Optical Analogue to Electromagnetically Induced Transparency” In: Phys. Rev. Lett. 96, 12 (2006), p. 3901.
- [13] S. Yanik M.F. and Fan. “Stopping Light All Optically” In: Phys. Rev. Lett. 92, 8 (2004), p. 3901.
- [14] A. Dousse, J. Suffczynski, A. Beveratos, O. Krebs, A. Lemaître, I. Sagnes, J. Bloch, P. Voisin, and P. Senellart. “Ultrabright source of entangled photon pairs” In: Nature 466 (2010), pp. 217–220.
- [15] A. Imamoglu, D. Awschalom, G. Burkard, D. DiVincenzo, D. Loss, M. Sherwin, and A. Small. “Quantum Information Processing Using Quantum Dot Spins and Cavity QED” In: Phys. Rev. Lett. 83, 20 (1999), pp. 4204–4207.
- [16] J. Vasco, P. Guimarães, and D. Gerace. “Long-distance radiative coupling between quantum dots in photonic crystal dimers” In: Phys. Rev. B 90, 15 (2014), p. 155436.

- [17] D. Angelakis, M. Santos, and S. Bose. “Photon-blockade-induced Mott transitions and XY spin models in coupled cavity arrays” In: Phys. Rev. A 76, 3 (2007), p. 1805.
- [18] D. Gerace, H. Türeci, A. Imamoglu, V. Giovannetti, and R. Fazio. “The quantumoptical Josephson interferometer” In: Nature Phys. 5 (2009), pp. 281–284.
- [19] M. Hartmann, F. Brandão, and M. Plenio. “Quantum many-body phenomena in coupled cavity arrays” In: Laser Photon. Rev 2, 6 (2008), pp. 527–556.
- [20] A. Tomadin, V. Giovannetti, R. Fazio, D. Gerace, I. Carusotto, H. Türeci, and A. Imamoglu. “Signatures of the superfluid-insulator phase transition in laser-driven dissipative nonlinear cavity arrays” In: Phys. Rev. A 81, 6 (2010), p. 061801.
- [21] F. Intonti, F. Riboli, N. Caselli, M. Abbarchi, S. Vignolini, D. Wiersma, A. Vinattieri, D. Gerace, L. Balet, L. Li, M. Francardi, A. Gerardino, A. Fiore, and M. Gurioli. “Young’s Type Interference for Probing the Mode Symmetry in Photonic Structures” In: Phys. Rev. Lett. 106, 14 (2011), p. 143901.
- [22] M. Brunstein, T. Karle, I. Sagnes, F. Raineri, J. Bloch, Y. Halioua, G. Beaudoin, L. Le Gratiet, J. Levenson, and A. Yacomotti. “Radiation patterns from coupled photonic crystal nanocavities” In: Appl. Phys. Lett. 99, 11 (2011), p. 1101.
- [23] A. Yariv, Y. Xu, R. Lee, and A. Scherer. “Coupled-resonator optical waveguide: a proposal and analysis” In: Opt. Lett. 24, 11 (1999), pp. 711–713.
- [24] F.-S. Chien, J. Tu, W.-F. Hsieh, and S.-C. Cheng. “Tight-binding theory for coupled photonic crystal waveguides” In: Phys. Rev. B 75, 12 (2007), p. 125113.
- [25] A. Chalcraft, S. Lam, B. Jones, D. Szymanski, R. Oulton, A. Thijssen, M. Skolnick, D. Whittaker, T. Krauss, and A. Fox. “Mode structure of coupled L3 photonic crystal cavities” In: Opt. Express 19, 6 (2011), pp. 5670–5675.
- [26] F. Intonti, N. Caselli, S. Vignolini, F. Riboli, S. Kumar, A. Rastelli, O. Schmidt, M. Francardi, A. Gerardino, L. Balet, L. Li, A. Fiore, and M. Gurioli. “Mode tuning of photonic crystal nanocavities by photoinduced non-thermal oxidation” In: Appl. Phys. Lett. 100, 3 (2012), p. 3116.
- [27] C.-S. Kee, H. Lim, and J. Lee. “Coupling characteristics of localized photons in two-dimensional photonic crystals” In: Phys. Rev. B 67, 7 (2003), p. 073103.
- [28] M. Doty, J. Climente, M. Korkusinski, M. Scheibner, A. Bracker, P. Hawrylak, and D. Gammon. “Antibonding Ground States in InAs Quantum-Dot Molecules” In: Phys. Rev. Lett. 102, 4 (2009), p. 7401.
- [29] B. Gallinet, J. Kupec, B. Witzigmann, and M.-A. Dupertuis. “Analysis of photonic crystal defect modes by maximal symmetrization and reduction” In: J. Opt. Soc. Am. B 27, 7 (2010), pp. 1364–1380.
- [30] K. Atlasov, K. Karlsson, A. Rudra, D. B., and E. Kapon. “Wavelength and loss splitting in directly coupled photonic-crystal defect microcavities” In: Opt. Express 20, 16 (2008), pp. 255–264.
- [31] L. Andreani and D. Gerace. “Photonic-crystal slabs with a triangular lattice of triangular holes investigated using a guided-mode expansion method” In: Phys. Rev. B 73, 23 (2006), p. 5114.
- [32] K. Hennessy, C. Högerle, E. Hu, A. Badolato, and A. Imamoglu. “Tuning photonic nanocavities by atomic force microscope nano-oxidation” In: Appl. Phys. Lett. 89, 4 (2006), p. 1118.

- [33] C. Chen, J. Zheng, T. Gu, J. McMillan, M. Yu, G.-Q. Lo, D.-L. Kwong, and C. Wong. “Selective tuning of high-Q silicon photonic crystal nanocavities via laser-assisted local oxidation” In: Opt. Express 19, 13 (2011), pp. 12480–12489.
- [34] I. Fushman, E. Waks, D. Englund, N. Stoltz, P. Petroff, and J. Vuckovic. “Ultra-fast nonlinear optical tuning of photonic crystal cavities” In: Appl. Phys. Lett. 90, 9 (2007), p. 1118.
- [35] M. Loncar, T. Yoshie, A. Scherer, P. Gogna, and Y. Qiu. “Low-threshold photonic crystal laser” In: Appl. Phys. Lett. 81, 15 (2002), pp. 2680–2682.
- [36] T. Tanabe, M. Notomi, S. Mitsugi, A. Shinya, and E. Kuramochi. “All-optical switches on a silicon chip realized using photonic crystal nanocavities” In: Appl. Phys. Lett. 87, 15 (2005), p. 1112.
- [37] K. Hennessy, A. Badolato, M. Winger, D. Gerace, M. Atatüre, S. Gulde, S. Fält, E. Hu, and A. Imamoglu. “Quantum nature of a strongly coupled single quantum dot-cavity system” In: Nature 445 (2007), pp. 896–899.
- [38] F. Intonti, S. Vignolini, F. Riboli, A. Vinattieri, D. Wiersma, M. Colocci, L. Balet, C. Monat, C. Zinoni, L. Li, R. Houdré, M. Francardi, A. Gerardino, A. Fiore, and M. Gurioli. “Spectral tuning and near-field imaging of photonic crystal microcavities” In: Phys. Rev. B 78, 4 (2008), p. 041401.
- [39] A. Faraon and J. Vuckovic. “Local temperature control of photonic crystal devices via micron-scale electrical heaters” In: Appl. Phys. Lett. 95, 4 (2009), p. 3102.
- [40] K. Hennessy, A. Badolato, A. Tamboli, P. Petroff, E. Hu, M. Atatüre, J. Dreiser, and A. Imamoglu. “Tuning photonic crystal nanocavity modes by wet chemical digital etching” In: Appl. Phys. Lett. 87, 2 (2005), p. 1108.
- [41] X. Yang, C. Chen, C. Husko, and C. Wong. “Digital resonance tuning of high- $Q/V_m$  silicon photonic crystal nanocavities by atomic layer deposition” In: Appl. Phys. Lett. 91, 16 (2007), p. 1114.
- [42] F. Intonti, S. Vignolini, F. Riboli, M. Zani, D. Wiersma, L. Balet, L. Li, M. Francardi, A. Gerardino, A. Fiore, and M. Gurioli. “Tuning of photonic crystal cavities by controlled removal of locally infiltrated water” In: Appl. Phys. Lett. 95, 17 (2009), p. 3112.
- [43] L. Midolo, P. van Veldhoven, M. Döndar, R. Nötzel, and A. Fiore. “Electromechanical wavelength tuning of double-membrane photonic crystal cavities” In: Appl. Phys. Lett. 98, 21 (2011), p. 1120.
- [44] H. Lee, S. Kiravittaya, S. Kumar, J. Plumhof, L. Balet, L. Li, M. Francardi, A. Gerardino, A. Fiore, A. Rastelli, and O. Schmidt. “Local tuning of photonic crystal nanocavity modes by laser-assisted oxidation” In: Appl. Phys. Lett. 95, 19 (2009), p. 1109.
- [45] S. Vignolini, F. Intonti, L. Balet, M. Zani, F. Riboli, A. Vinattieri, D. Wiersma, M. Colocci, L. Li, M. Francardi, A. Gerardino, A. Fiore, and M. Gurioli. “Nonlinear optical tuning of photonic crystal microcavities by near-field probe” In: Appl. Phys. Lett. 93, 2 (2008), p. 3124.
- [46] A. de Rossi, M. Lauritano, S. Combrié, Q. Tran, and C. Husko. “Interplay of plasma-induced and fast thermal nonlinearities in a GaAs-based photonic crystal nanocavity” In: Phys. Rev. A 79, 4 (2009), p. 3818.

- [47] C.-H. Tsai, S.-R. Jian, and H.-C. Wen. “Tip-induced local anodic oxidation on p-GaAs surface with non-contact atomic force microscopy” In: *Applied Surface Science* 254, 5 (2007), pp. 1357–1362.
- [48] T. Suzuki and M. Ogawa. “Degradation of photoluminescence intensity caused by excitation-enhanced oxidation of GaAs surfaces” In: *Appl.Phys. Lett.* 31, 7 (1977), pp. 473–475.
- [49] V. Bermudez. “Photoenhanced oxidation of gallium arsenide” In: *J. Appl. Phys.* 54, 11 (1983), pp. 6795–6798.
- [50] Y. Chen, J. Seo, F. Stepniak, and J. Weaver. “Visible-light-induced oxidation for O<sub>2</sub> on GaAs(110): The role of hot electrons” In: *J. Chem. Phys* 95, 11 (1991), pp. 8442–8448.
- [51] F. Intonti, V. Matarazzo, A. Nasir, O. Makarovskiy, R. Campion, A. Patanè, S. Kumar, A. Rastelli, O. Schmidt, and M. Gurioli. “Nano-sized light emitting diodes by near field laser exposure” In: *Appl.Phys. Lett.* 98, 18 (2011), p. 3102.
- [52] N. Matsuda, H. Takesue, K. Shimizu, Y. Tokura, E. Kuramochi, and M. Notomi. “Slow light enhanced correlated photon pair generation in photonic-crystal coupled-resonator optical waveguides” In: *Opt. Express* 21, 7 (2013), pp. 8596–8604.
- [53] N. Matsuda, E. Kuramochi, H. Takesue, and M. Notomi. “Dispersion and light transport characteristics of large-scale photonic-crystal coupled nanocavity arrays” In: *Opt. Lett.* 39, 8 (2014), pp. 2290–2293.
- [54] J. Ma, L. Martínez, S. Fan, and M. Povinelli. “Tight-binding calculation of radiation loss in photonic crystal CROW” In: *Opt. Express* 21, 2 (2013), pp. 2463–2473.
- [55] D. Smith and C. Mailhot. “Theory of semiconductor superlattice electronic structure” In: *Rev. Mod. Phys.* 62, 1 (1990), pp. 173–234.
- [56] N. Ashcroft and N. Mermin. *Solid State Physics*. Harcourt Inc., Orlando, FL, USA, (1976).



## **Chapter 6**

### **Engineering light confinement in disordered media**

Disordered photonic materials can diffuse and localize light through random multiple scattering, offering opportunities to study mesoscopic phenomena, control light-matter interactions, and provide new strategies for photonic applications. Light transport in such media is governed by photonic modes characterized by resonances with finite spectral width and spatial extent. Considerable steps have been made towards control over the transport using wavefront shaping techniques. The selective engineering of individual modes, however, has been addressed only theoretically. Here, we experimentally demonstrate the possibility to engineer the confinement and the mutual interaction of modes in a two-dimensional disordered photonic structure. The strong light confinement is achieved at the fabrication stage by an optimization of the structure and an accurate and local tuning of the mode resonance frequencies is achieved via post-fabrication processes. To show the versatility of our technique, we selectively control the detuning between overlapping localized modes and observe both frequency crossing and anti-crossing behaviors, thereby paving the way for the creation of open transmission channels in strongly scattering media.

#### **6.1 Disorder driven light confinement**

The ability to mold the flow of light at the wavelength scale has been largely investigated in photonic-crystal-based devices, in which the light propagation is driven by interference between multiply Bragg scattered waves giving rise to Bloch modes, which can be engineered by varying the structural parameters of the material [1]. In disordered media, both the direction and phase of the propagating waves are randomized in a complex manner, making any attempt to control light propagation particularly challenging.

Disordered media are at present investigated in several contexts, ranging from the study of collective multiple scattering phenomena to cavity random lasing and to the possibility to provide efficient solutions in renewable energy, imaging and spectroscopy-based applications [2–7]. Transport in such systems can be described in terms of photonic modes, or quasimodes, which exhibit characteristic spatial profiles and spectra [8]. In diffusive systems, these modes are spatially and spectrally overlapping whereas in the regime of Anderson localization, they become spatially and spectrally isolated [9]. Unlike Bloch modes in periodic systems, the precise formation of photonic modes in a single realization of the disorder is unpredictable. Control over light

transport can be obtained by shaping the incident wave to excite only a specific part of the modes available in a given system [7,10]. To fully exploit the potential of disordered systems, however, mode control is needed. It was shown theoretically that isolated modes could be selectively tuned and possibly coupled to each other by a local fine modification of the dielectric structure [11, 12].

We experimentally prove the ability to control the spectral properties of an individual photonic mode in a two-dimensional disordered photonic structure. The disordered pattern of air holes is fabricated on the same suspended GaAs membrane with InAs QDs embedded, already presented in Sec. (3.2) for the realization of PCNs. The difference relies on the disorder distribution of circular holes, as reported in the SEM images of Fig. (6.1 a-b). We design different disordered structures with holes filling fraction ( $f$ ) ranging from 0.13 to 0.35 and hole diameters size ( $h_d$ ) ranging from 195 nm to 270 nm. Fabrications induced deviations from the nominal structural parameters values are measured with a scanning electron microscope and are found to be within 5% for  $h_d$  and 10% for  $f$ . To avoid merging between adjacent holes during the growth process (proximity effects), we imposed a minimum distance equal to 1.3  $h_d$  between the centers of the nearest neighboring holes.

The PL of the sample is excited and detected by means of the SNOM setup in illumination-collection geometry presented in Sec. (3.1), equipped with dielectric probes. As excitation source we use a diode laser (780 nm) delivering to the near-field probe 60  $\mu$ W power. The combination of spectrometer and photodiodes array allows us to investigate during a single SNOM scan the spectral range between 1150 nm and 1380 nm with a resolution of 0.45 nm. Figure (6.2) shows typical SNOM PL maps evaluated at a fixed emission wavelength for samples with  $f = 0.35$  and  $f = 0.13$ , respectively, whose intensity values are normalized by the average intensity of the sample. Several localized modes are identified by the bright spots in the intensity distributions and by the peaks in the wavelength spectrum. For instance, two spectra corresponding to the maximum intensity observed in Fig. (6.2 a-b) are reported in Fig. (6.2 c-d). The main difference between the two spectra is the peak amplitude value. In fact, the PL spectrum of the sample with  $f = 0.35$  supports a peak more than ten times more intense than the average intensity value of the entire sample; whereas the PL spectrum of the sample with  $f = 0.13$  exhibits a peak with an intensity 3.6 times the average value. Although such intensity distributions and spectra provide useful local information about two single peaks, a statistical analysis of all the investigated wavelength and positions is required to understand the mesoscopic properties of every sample, and in particular the influence of the filling fraction and the hole diameter size on the localized modes.

Figures (6.3 a-b) shows the probability density function (P) of PL normalized intensity ( $I_{PL}/\langle I_{PL} \rangle$ ) in linear and semi-logarithmic scale, respectively. Each distribution is evaluated taking into account all the collected data during the SNOM scan. By increasing  $f$  the P distributions become more asymmetric, see Fig. (6.3 a), and heavy-tailed, see Fig. (6.3 b), with a notably higher probability to observe high-intensity peaks. For instance, peaks with a normalized intensity about 4 are roughly 100 times more probable in samples with  $f = 0.35$  than in those with  $f = 0.20$ . The onset of the occurrence of rare, yet very bright peaks can be quantified by the normalized variance  $\sigma^2/\mu^2$  of P, where  $\sigma$  and  $\mu = \langle I_{PL} \rangle$  are the variance and the mean intensity of

the distribution, respectively. Figure (6.3 c) shows that  $\sigma^2/\mu^2$  increases by at least a factor of five on increasing the filling fraction from  $f = 0.13$  to  $f = 0.35$ . The influence of  $h_d$  on the normalized variance is less evident, as shown in Fig. (6.3 d).

The PL fluctuations of the integrated quantum sources are primarily driven by LDOS fluctuations, which in turn are related to the light transport properties of the system as well as to the near-field interaction between sources and scatterers [13–16]. In our experimental configuration the interplay between the involved processes, such as the excitation efficiency of QDs, the collection efficiency of the SNOM tip and the light transport in the disordered medium, does not allow us to quantitatively relate the slope of the P distributions tails to the dimensionless conductance, which is the universal scaling parameter that quantifies the wave transport in a random medium [17]. Nevertheless, the appearance of longer tails for samples with increasing  $f$  is a signature of the enhanced confinement of the photonic quasi-modes. On the other hand, the weak dependence of the fluctuations on  $f = 0.35$  shows that the investigated disordered systems are structurally independent of possible dispersion of the scatterer size, as highlighted in Fig. (6.3 d). To retrieve the average spatial extension of the photonic modes, we exploit the quality factor decrease in proximity of the sample borders due to in-plane leakages. In fact, the more confined modes exhibit a  $Q$  reduction at shorter distances from it. The average mode decay length is then evaluated by investigating the mode spectral width dependence on the distance to the border [18]. Figures (6.4 a-b) show the FWHM of the averaged wavelength autocorrelation function of the spectra, collected in spatial strips parallel to the sample border as a function of distance to the sample border. The average wavelength autocorrelation FWHM is calculated within a vertical strip (200 nm width 9  $\mu\text{m}$  height) parallel to the sample border and contains 45 near-field spectra. The average FWHM decreases very rapidly for samples with  $f = 0.35$  ( $h_d = 200$  nm), reaching a constant value at a distance of 3.4  $\mu\text{m}$  away from the border, whereas for samples with  $f = 0.13$  ( $h_d = 200$  nm) the decay is much slower, reaching a constant value at a distance of approximately 10 – 12  $\mu\text{m}$ . The slight increase of the FWHM in the bulk of the sample with  $f = 0.35$  is probably due to a small increase in the hole diameter sizes caused by a proximity effect of the electron beam during the writing stage. Figure (6.4 c) shows the decay length, calculated from exponential fits of the FWHM decrease, as a function of the density of scatterers. The  $f = 0.35$  samples support modes with a decay length of approximately  $\xi = 0.8 \mu\text{m}$  with a ratio  $L/2\xi = 15$ , where  $L = 25 \mu\text{m}$  is the sample size; whereas for  $f = 0.13$  the decay length is approximately  $\xi = 3.5 \mu\text{m}$  with a ratio  $L/2\xi = 3.5$ .

The average FWHM of frequency autocorrelation in the middle of the samples is related to the spectral width of localized modes, which provide the average intrinsic quality factor  $Q = 440 \pm 80$  for  $f = 0.35$ . This value is bounded by the out-of-plane losses, which are roughly four times larger than the in-plane losses (inherent to the finite size of the sample), as we verified by a comparison between two- and three-dimensional FDTD calculations (not shown here).

## 6.2 Engineering disordered photonic modes

Having identified a proper set of design parameters to create disordered structures that support strongly confined photonic modes, we implement a post-processing step for achieving a fine-tuning of the resonant modes wavelength. The technique is based on the local modification of the dielectric environment in the proximity of the maximum intensity of the modes. In a sample found to be in the regime of strongest confinement, that is with  $f = 0.35$  and  $h_d = 200$  nm, we demonstrate the ability to perform a gentle and reversible spectral tuning on a single localized mode. We also engineer the spectral splittings of selected pairs of modes, which show a crossing or an anti-crossing feature, depending on the mutual spatial overlap and therefore on the mode interaction strength, as discussed for coupled PCNs in Sec. (5.1.1).

A reversible and smooth engineering is achieved by exploiting the perturbation induced by the dielectric SNOM tip, which modifies the local dielectric environment where multiple light scattering takes place, inducing a red-shift of the modes proportional to the intensity of the confined electric field, as deeply discussed in Sec. (2.5). Figure (6.5 a) shows the intensity image of an isolated mode, whereas Fig. (6.5 b) shows the normalized intensity spectra taken close to the PL maximum intensity of the mode (point A) and on the PL low intensity tail (point B). The spectral shift map is reported as three-dimensional function in the inset of Fig. (6.5 b) and as the ordinary two-dimensional distribution in Fig. (6.5 c). Therefore, the localized electric field intensity distribution clearly describes the speckle patterns typical of disorder induced localization [18–20]. Moreover, the amplitude of the observed maximum spectral shift is 0.43 nm, which represents a small fraction of the mode linewidth (about 3 nm), but demonstrates that the dielectric perturbation in the near-field is able to slightly modify the resonant frequency of a disordered resonant mode. The spectral shift maximum value also allows us to give an estimation of the modal volume  $V$  of the localized mode. The polarizability of the tip employed, and therefore a direct calibration-measurement of the spectral shift method used to retrieve  $V$ , is determined by measuring the spectral shift in a photonic crystal nanocavity with known  $V$ . This allowed us to give an accurate estimation of the modal volume,  $V = 0.2 \mu\text{m}^3$ , that is a value consistent both with the spatial extension retrieved by SNOM imaging of Fig. (6.5 c) and by statistical estimation based on the decay length reported in Fig. (6.4 c).

To control the modes over a broader spectral range, we exploit the post-fabrication technique based on laser-assisted micro-oxidation through SNOM probe presented in Sec. (5.2.2). This technique permanently and locally modifies the dielectric environment by reducing the effective GaAs membrane thickness and increasing the effective pore diameter, thus shifting the localized photonic modes towards lower wavelengths. In order to demonstrate the ability to engineer the spectral and spatial properties of disorder based modes we carefully choose a set of three modes that are spatially close but detuned spectrally. Figures (6.6 a-c) show the PL intensity distribution of the three modes (labeled A, B and C) before starting the laser assisted oxidation process. Each mode is characterized by a main intensity peak surrounded by speckles with lower intensity. The spatial regions highlighted by the white (red) dotted lines in Fig. (6.6 a-c), identify the spatial overlap between A and B modes (B and C modes). The overlaps indicate a stronger expected interaction between A and B rather

than between B and C. The laser exposition is made in correspondence to the maximum intensity of mode B (white circle). Figures (6.6 e and g) show the evolution for increasing laser exposure time of the normalized PL spectra averaged over the B-C and A-B overlap regions, respectively. The lower PL intensity in BC with respect to AB (demonstrated by the larger signal to noise ratio in the normalized spectra) reflects the smaller spatial overlap between the modes.

Figure (6.6 f) shows the evolution of the resonant wavelengths of modes A, B and C as a function of the laser exposure time. Let us first consider the variation of mode B with respect to mode C. The wavelength of mode B blue-shifts monotonically whereas that of mode C stays at the unperturbed value within the experimental uncertainty. After about 310 min of exposure, the spectral overlap between the two modes is maximized. By further oxidizing the structure, the two resonances spectrally cross until they go out of resonance at  $\Delta t = 465$  min. Therefore, the coupling strength mode B and C results much smaller than the broadening of the individual modes. The two modes are likely to be in the weak coupling regime. One possible way to get a greater interaction strength is to choose two modes with a larger spatial overlap, as for the case of mode A and B. The time evolution of the A and B wavelengths reported in Fig. (6.6 f) shows that the local oxidation undoubtedly induces a mode anti-crossing. The position of the anti-crossing occurrence is highlighted by reporting the wavelength splitting  $\Omega_{AB}$  as a function of the exposure time, as shown in Fig. (6.6 d). Initially  $\Omega_{AB}$  decreases, reaching the minimum value around  $\Delta t = 170$  min. Furthermore, the amplitudes of the two interacting modes reach the same value at the time of minimum splitting, as highlighted by the evolution of the PL spectra in Fig. (6.6 g). The black solid line in Fig. (6.6 d) is the result of the fit of the experimental splitting with the expected strong coupling behavior [21]. Following Eq. (5.10), the minimum splitting evaluated by the fit of the anticrossing experimental data directly gives the mode interaction strength. In fact, we get that  $\Omega_{AB} \text{ min} = 2g$ . We find that  $\Omega_{AB} \text{ min} = (3.55 \pm 0.15)$  nm, that is larger than the mode spectral FWHM, equal to  $(3.00 \pm 0.10)$  nm, and thus the strong coupling condition is satisfied.

The observation of both resonant wavelength crossing and anticrossing behaviors represents the first step towards the creation of chains of hybridized localized random-based modes, better known as necklace states, observed in 1D-systems and predicted also for higher dimensions [22, 23].

In conclusion, we proved how it is possible to obtain and optimize strongly confined optical modes in two-dimensional disordered structures. Moreover, the near-field imaging of the localized photonic modes allowed us to statistically evaluate the degree of light confinement. The investigated two-dimensional disordered structures are particularly suited for improving the absorption efficiency of thin-film solar cells and can provide a new approach for high-extraction-efficiency in light-emitting diodes. In fact, they sustain an efficient light trapping due to coherent optical effects along with broadband and wide-angle properties due to disorder. More strikingly, in this work we demonstrated the possibility to largely engineer the spectrum and the interaction of random modes by a fine-tuning of the disordered system in post-fabrication processes. Our achievements constitute an important step towards the control of disorder-based photonic resonators and traps. Therefore, they could be of great advantage for developing random laser devices. Furthermore, the presented findings

Imaging and engineering optical localized modes at the nanoscale

may open new routes for addressing mesoscopic transport phenomena in random media. As an example, the control of the optical confinement and the coupling between modes could be used to exploit two-dimensional necklace states in designing open transmission channels in disordered structures.

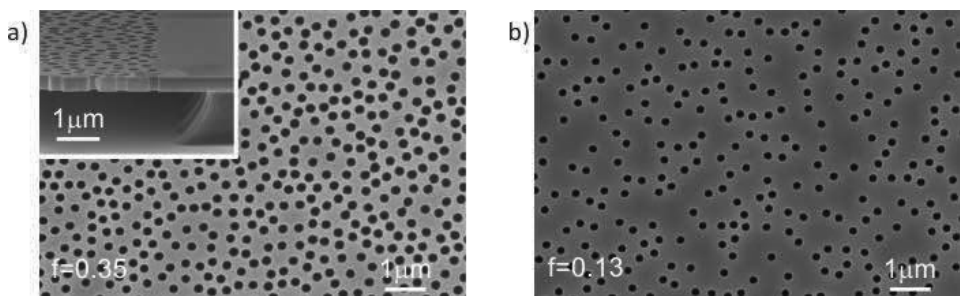


Figure 6.1: a)-b) SEM images of disordered samples with  $f = 0.35$  and  $f = 0.13$  and hole diameters  $h_d = 215 \text{ nm}$  and  $h_d = 185 \text{ nm}$ , respectively. The inset of a) shows the suspended photonic membrane clamped at its edges.

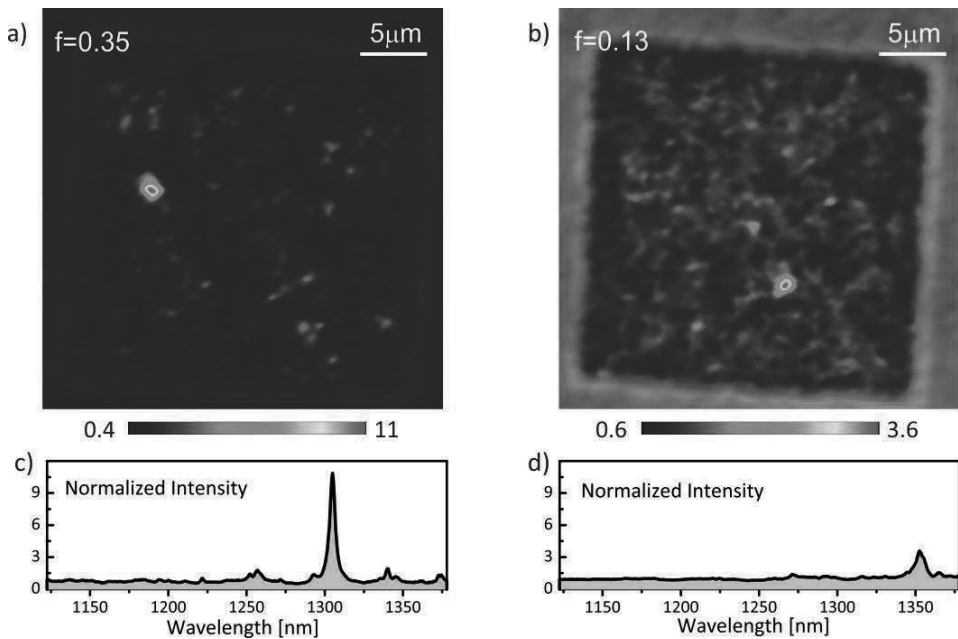


Figure 6.2: a)-b) SNOM PL intensity maps for samples with  $f = 0.35$  and  $f = 0.13$ , respectively, evaluated at the wavelength of the highest intensity peak of each scan. c)-d) Near-field spectra of  $f = 0.35$  and  $f = 0.13$  detected in the position corresponding to the maximum value of the images shown in a) and b), respectively. The reported intensities as a function of position and as a function of wavelength are normalized to the average PL of each sample.

Imaging and engineering optical localized modes at the nanoscale

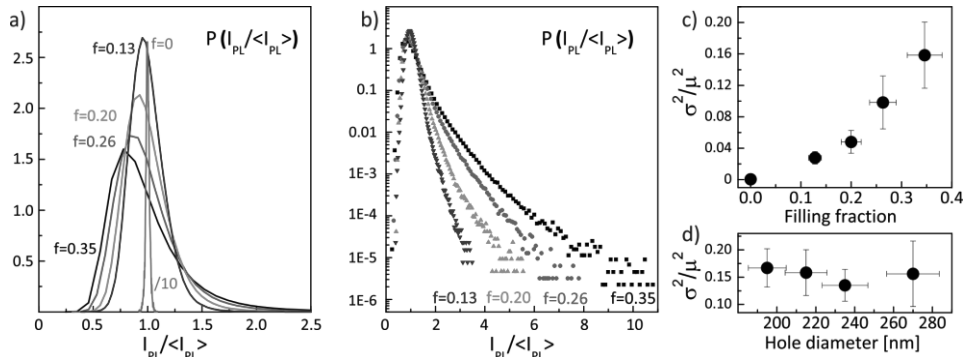


Figure 6.3: a)-b) Probability density function ( $P$ ) of the PL measured intensities for  $f = 0.00, 0.13, 0.20, 0.26, 0.35$  and  $h_d = 200$  nm, presented on linear and semi-logarithmic scales, respectively. The PL intensities  $I_{PL}$  are normalized to the PL average value of the respective sample ( $\mu = \langle I_{PL} \rangle$ ). For the linear scale a) we also show the distribution for the slab without any holes ( $f = 0$ ) divided by a factor of 10 that exhibits the minor fluctuations only due to the InGaAs quantum dots. c)-d) Normalized variance ( $\sigma^2/\mu^2$ ) of the probability density function distributions as a function of  $f$  (with  $h_d = 200$  nm) and as a function of  $h_d$  (with  $f = 0.35$ ). The error bars of  $\sigma^2/\mu^2$  have been evaluated by calculating this quantity for different wavelengths ranges, whereas for the filling fractions the uncertainty comes from the dispersion of the hole diameter sizes evaluated using SEM images.

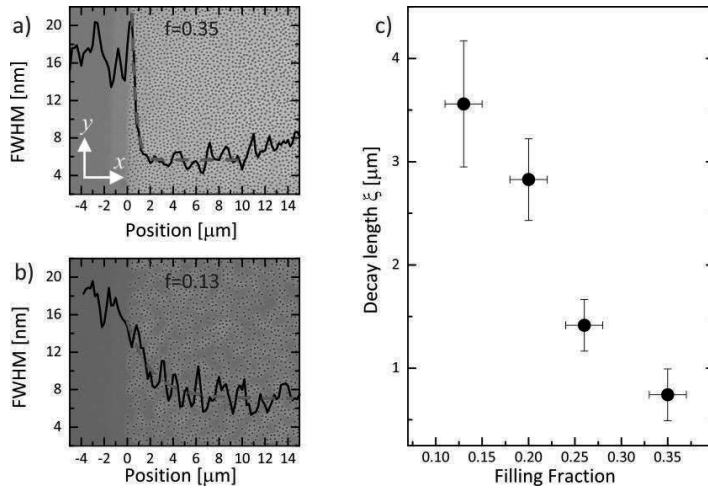


Figure 6.4: a)-b) Average spectral FWHM of the peaks as a function of the penetration depth inside the sample (black line) for filling fractions  $f = 0.35$  and  $f = 0.13$ , respectively, superimposed on a SEM image of the samples. The border of the samples is located at position  $x = 0$ . The red dotted line is an exponential fit to the data. c) Average decay lengths of the photonic modes versus filling fraction, evaluated by the exponential fits. The errors are evaluated by performing the above analysis along the four edges of each sample.

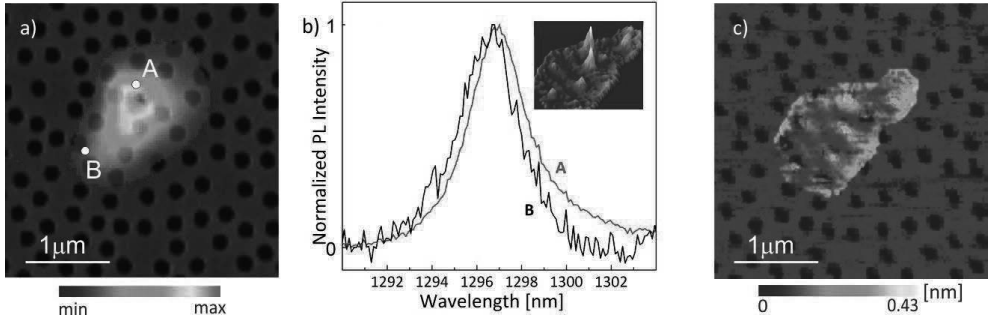


Figure 6.5: a) PL amplitude map of a localized mode in  $f = 0.35$  and  $h_d = 200$  nm disordered sample, whose SEM image is superimposed. The amplitude is obtained by a Lorentzian fit of the collected spectra. b) Normalized spectra of the mode shown in a) evaluated close to the maximum amplitude (A) and at a point showing a low PL signal (B). The mode shift is caused by the presence of the dielectric SNOM tip in the near-field of the mode and its three-dimensional distribution is reported in the inset. c) Two-dimensional spectral shift map of the mode reported in a)-b) with superimposed the topography map acquired during the SNOM scan.

## Imaging and engineering optical localized modes at the nanoscale

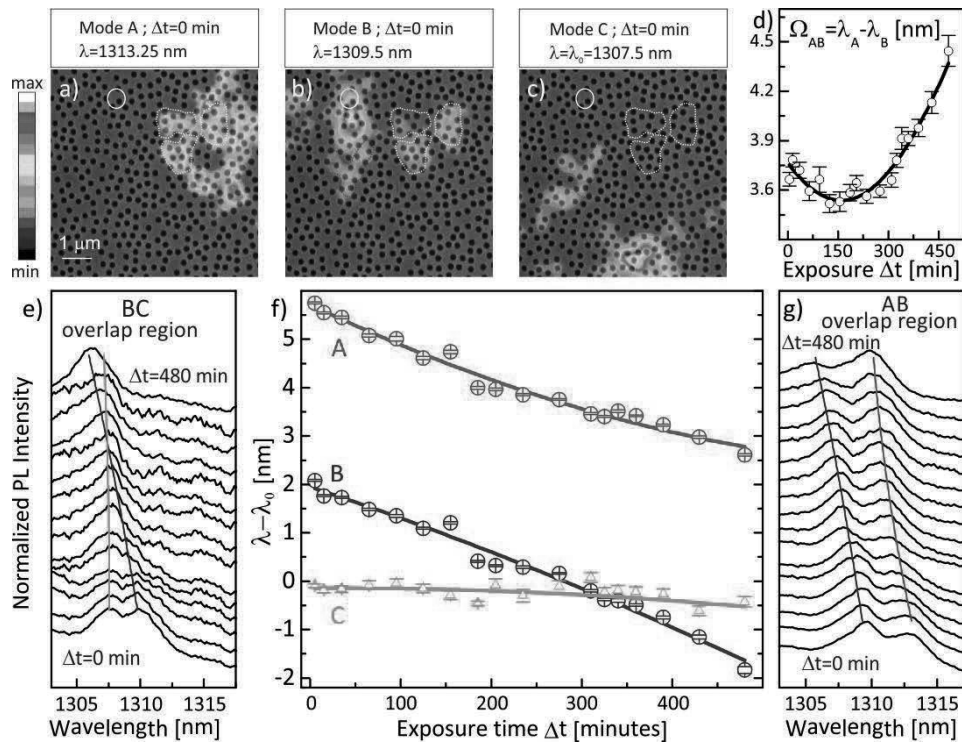


Figure 6.6: a)-c) PL intensities of modes A, B and C before starting the laser-assisted local oxidation, respectively. The white circle indicates the position of the SNOM tip performing the laser-induced oxidation. The the white (red) dotted-lines regions identify the spatial overlap between the modes A and B (B and C). The resonant wavelength of mode C is considered as the reference value defined  $\lambda_0$ . d) Separation between the resonant wavelengths of A and B (AB) as a function of the exposure time  $\Delta t$  showing an anticrossing behavior. The black solid line shows the fit of the experimental splitting with the expected trend for strong coupling. e) and g) Evolution of the normalized PL spectra mediated within the overlap regions B-C and A-B, respectively, for increasing laser exposure time. The average intensity of the modes within these regions is typically 10 – 15 times smaller than the maximum value of each mode. f) Resonant wavelength of the three modes evaluated in the overlap regions as a function of  $\Delta t$ . The error bars are provided by the two-peak Lorentzian fits of each spectrum.

## References

- [1] J. Joannopoulos, S. Johnson, J. Winn, and R. Meade. Photonic Crystals: Molding the Flow of Light. Princeton University Press, 2nd edn., (2008).
- [2] B. Payne, A. Yamilov, and S. Skipetrov. “Anderson localization as position-dependent diffusion in disordered waveguides” In: Phys. Rev. B 82, 2 (2010), p. 4205.
- [3] L. Sapienza, H. Thyrrstrup, S. Stobbe, P. Garcia, S. Smolka, and P. Lodahl. “Cavity Quantum Electrodynamics with Anderson-Localized Modes” In: Science 327, v (2010), pp. 1352–1355.
- [4] H. Noh, J.-K. Yang, S. Liew, M. Rooks, G. Solomon, and H. Cao. “Control of Lasing in Biomimetic Structures with Short-Range Order” In: Phys. Rev. Lett. 106, 18 (2011), p. 3901.
- [5] K. Vynck, M. Burresi, F. Riboli, and D. Wiersma. “Photon management in two-dimensional disordered media” In: Nat. Mater. 11 (2012), pp. 1017–1022.
- [6] J. Bertolotti, E. van Putten, C. Blum, A. Lagendijk, W. Vos, and A. Mosk. “Non-invasive imaging through opaque scattering layers” In: Nature 491 (2012), pp. 232–234.
- [7] B. Redding, S. Liew, R. Sarma, and H. Cao. “Compact spectrometer based on a disordered photonic chip” In: Nat. Photon. 7 (2013), pp. 746–751.
- [8] E. Ching, P. Leung, A. Maassen van den Brink, W. Suen, S. Tong, and K. Young. “Quasinormal-mode expansion for waves in open systems” In: Rev. Mod. Phys. 70, 4 (1998), pp. 1545–1554.
- [9] M. Noginov, G. Dewar, M. McCall, and N. Zheludev. Tutorials in complex photonic media. Chap.9; Bellingham: SPIE, (2010).
- [10] S. Popoff, G. Lerosey, R. Carminati, M. Fink, A. Boccara, and S. Gigan. “Measuring the Transmission Matrix in Optics: An Approach to the Study and Control of Light Propagation in Disordered Media” In: Phys. Rev. Lett. 104, 10 (2010), p. 0601.
- [11] L. Labonté, C. Vanneste, and P. Sebbah. “Localized mode hybridization by fine tuning of two-dimensional random media” In: Opt. Lett. 37, 11 (2012), pp. 1946–1948.
- [12] C. Vanneste and P. Sebbah. “Complexity of two-dimensional quasimodes at the transition from weak scattering to Anderson localization” In: Phys. Rev. A 79, 4 (2009), p. 1802.
- [13] B. van Tiggelen and S. Skipetrov. “Fluctuations of local density of states and  $C_0$  speckle correlations are equal”. In: Phys. Rev. E 73, 4 (2006), p. 5601.
- [14] A. Cazé, R. Pierrat, and R. Carminati. “Near-field interactions and nonuniversality in speckle patterns produced by a point source in a disordered medium” In: Phys. Rev. A 82, 4 (2010), p. 3823.
- [15] R. Sapienza, P. Bondareff, R. Pierrat, B. Habert, R. Carminati, and N. van Hulst. “Long-Tail Statistics of the Purcell Factor in Disordered Media Driven by Near-Field Interactions” In: Phys. Rev. Lett. 106, 16 (2011), p. 163902.

Imaging and engineering optical localized modes at the nanoscale

- [16] M. Birowosuto, S. Skipetrov, W. Vos, and A. Mosk. “Observation of Spatial Fluctuations of the Local Density of States in Random Photonic Media” In: Phys. Rev. Lett. 105, 1 (2010), p. 3904.
- [17] A. Chabanov, M. Stoytchev, and A. Genack. “Statistical signatures of photon localization” In: Nature 404 (2010), pp. 850–853.
- [18] D. Laurent, O. Legrand, P. Sebbah, C. Vanneste, and F. Mortessagne. “Localized Modes in a Finite-Size Open Disordered Microwave Cavity” In: Phys. Rev. Lett. 99, 25 (2007), p. 3902.
- [19] P. Sebbah, B. Hu, A. Genack, R. Pnini, and B. Shapiro. “Spatial-Field Correlation: The Building Block of Mesoscopic Fluctuations” In: Phys. Rev. Lett. 88, 12 (2002), p. 123901.
- [20] V. Emiliani, F. Intonti, M. Cazayous, D. Wiersma, M. Coloccia, F. Aliev, and A. Lagendijk. “Near-Field Short Range Correlation in Optical Waves Transmitted through Random Media” In: Phys. Rev. Lett. 90, 25 (2003), p. 0801.
- [21] S. Vignolini, F. Riboli, D. Wiersma, L. Balet, L. Li, M. Francardi, A. Gerardino, A. Fiore, M. Gurioli, and F. Intonti. “Nanofluidic control of coupled photonic crystal resonators” In: Appl. Phys. Lett. 96, 14 (2010), p. 1114.
- [22] J. Pendry. “Quasi-extended electron states in strongly disordered systems” In: J. Phys. C: Solid State Phys. 20, 5 (1987), p. 733.
- [23] J. Bertolotti, S. Gottardo, D. Wiersma, M. Ghulinyan, and L. Pavesi. “Optical Necklace States in Anderson Localized 1D Systems” In: Phys. Rev. Lett. 94, 11 (2005), p. 113903.

## Conclusions

In conclusion, in this thesis we expanded the horizons of nano-photonics by developing novel near-field probes, along with groundbreaking imaging techniques and post-fabrication methods. The presented experimental results are carefully supported by theory and numerical calculations.

The introduction of the campanile tip nanoantenna on top of an optical fibre represents a new paradigm for scanning near-field probes and, more in general, for sub-wavelength investigation. We demonstrated the strong field confinement and enhancement at the campanile tip nanogap apex, which gives a very efficient throughput and an outstanding sub-wavelength spatial resolution, by investigating light emitting InP nanowires. The novel properties of the campanile tip are exalted by the perturbation imaging technique applied to photonic crystal nanocavities. In fact, a high-fidelity simultaneous detection of the electric and the magnetic field components of the localized light states was clearly observed. By means of the campanile tip perturbation imaging we obtained a comparable strength between the observed red and the blue spectral shifts, which are the fingerprints of the electric and magnetic interaction, respectively. In addition we gained a dramatic improvement of the near-field imaging spatial resolution down to  $\lambda/30$ . The campanile near-field probe architecture could therefore allow the nanoscale investigation of light behaviour in optical metamaterials with an unprecedented resolution, thus triggering the quest for novel sensing applications and field enhancement effects.

In this work we also defined a new near-field imaging technique. The developed Fano phase-sensitive near-field investigation could revolutionize the sub-wavelength imaging research field for two reasons. Firstly, the optical imaging method is applicable to every kind of nano-resonator which exhibits sharp resonances, even realized on optically non active materials, such as silicon based as well as glass, polymer or metallic materials. Secondly, exploiting a detailed analysis of the modification of the Fano lineshapes, the technique allows the phase retrieval of the localized modes, since it is based on an integrated optical interferometer. Therefore, our developments opens up new strategies to investigate with a deep sub-wavelength spatial resolution the electric field intensity and the phase distribution of modes localized in a wealth class of nanophotonic and nanoplasmonic resonators as it does not need any special design or challenging fabrication steps and it can also image different polarization components.

## Imaging and engineering optical localized modes at the nanoscale

Concerning the topic of photonic molecules, we characterized the coupling strength and the symmetry character of the supermodes in coupled nano-resonators with different alignment. The notably systems of two and of three closely aligned photonic crystal nanocavities were investigated. We found that the effective mode interaction is not limited to the nearest-neighbour coupling.

We also developed a laser-assisted oxidation technique that enables a local post-growth modification of the underlying photonic crystal dielectric environment. Such post-fabrication technique was exploited to adjust the resonant wavelength of a given nano-resonator to a target value, and, more significantly, in combination with a local nano-infiltration procedure, was used to increase or decrease on demand the coupling strength in photonic molecules. It also allowed to probe the antibonding character of the K-aligned molecule ground state by means of an accurate minimization of the disorder induced detuning. The coupling between adjacent optical nano-resonators is a topic of vast attraction both for fundamental physics that exploits cavity quantum electrodynamics and for high density photonic integrated circuits applications. Our findings could open the way to exploit exotic configurations of coupled nanocavities to tailor the mode spatial distribution or the group velocity in CROW of any length by engineering the dielectric properties of adjacent resonators.

In the last part of the thesis we investigated disordered photonic systems by scanning near-field microscopy. The presented analysis led to an optimization of the structure parameters in order to achieve the highest degree of light localization. Moreover, we were able to fine tune the observed photonic modes and to probe the effective mode interaction between them by employing the laser-driven nano-oxidation technique. Our achievements constitute an important step towards the control of disorder-based photonic resonators and traps. Therefore, they could be of large interest for random laser applications. Furthermore, they could allow for addressing mesoscopic transport phenomena in random media. In fact, the control of the coupling between photonic modes could be used to create two-dimensional necklace states and design open transmission channels in disordered structures.

Finally, all the presented results put the basis for an unprecedented imaging investigation of light behaviour in optical nano-resonators. Therefore, they would possibly pave the way for novel interactions and devices which exploit the strong coupling regime between single light emitter and localized optical modes or even between complex interacting light states.

## Appendix: Coupling strength calculation in photonic molecule

In order to give an analytical expression of the coupling strength ( $g$ ) between two nanocavities that constitute a photonic molecule, in Sec. (5.1.1) we used the result of tight-binding theory:

$$g = \hbar\omega \frac{\int \Delta\varepsilon(\mathbf{r}) \mathbf{E}_0(\mathbf{r}) \cdot \mathbf{E}_0(\mathbf{r}+\mathbf{D}) d\mathbf{r}}{\int [\mu_0 |\mathbf{H}_0(\mathbf{r})|^2 + \varepsilon(\mathbf{r}) |\mathbf{E}_0(\mathbf{r})|^2] d\mathbf{r}} \quad (\text{A.1})$$

In this Appendix we will discuss the exact expression of the interaction between two optical resonators that results from Maxwell's equations evaluated in a photonic crystals molecule. The following analysis will also strengthen the analogy between photonic molecules and coupled harmonic oscillators employed in Sec. (5.1.1).

The usual employed hypothesis are the absence of e.m. sources, homogeneous and neutral linear dielectric media (with a magnetic permeability  $\mu_r = 1$ ) so that the dielectric constant ( $\varepsilon = n^2$ ) is a scalar depending only to the spatial coordinate. After factorizing the temporal evolution, it follows the Master equation (in c.g.s units) can be equivalently expressed both for the magnetic and for the electric field:

$$\left\{ \nabla \wedge \frac{1}{\varepsilon(\mathbf{r})} \nabla \wedge \right\} \mathbf{H}(\mathbf{r}) = \left( \frac{\omega}{c} \right)^2 \mathbf{H}(\mathbf{r}) \quad (\text{A.2})$$

$$\left\{ \nabla \wedge \nabla \wedge \right\} \mathbf{E}(\mathbf{r}) = \left( \frac{\omega}{c} \right)^2 \varepsilon(\mathbf{r}) \mathbf{E}(\mathbf{r}) \quad (\text{A.3})$$

The frequencies related to any of photonic problem for which  $\varepsilon(\mathbf{r})$  is defined, can be found by solving the eigenvalues of the hermitian operator  $\left\{ \nabla \wedge \frac{1}{\varepsilon(\mathbf{r})} \nabla \wedge \right\}$ . But this is in general a difficult task. Therefore, for the photonic molecule case, we take a different approach. We choose the Master Eq. (A.3) to exploit the linearity of the derivatives. Then, the magnetic field can be evaluated as:

$$\mathbf{H}(\mathbf{r}) = -\frac{i}{\omega\mu} \nabla \wedge \mathbf{E}(\mathbf{r}) \quad (\text{A.4})$$

while the electric field has still to satisfy the scalar Maxwell equation:

$$\nabla \cdot \varepsilon(\mathbf{r}) \mathbf{E}(\mathbf{r}) = 0 \quad (\text{A.5})$$

Then, considering for instance the K-aligned photonic molecule reported in Fig. (A.1 c), we apply Eq. (A.3) to the single nanocavities, whose dielectric environment is shown in Fig. (A.1 a-b), respectively, and to the photonic molecule as well:

$$\{\nabla \wedge \nabla \wedge\} \mathbf{E}_i(\mathbf{r}) = \left(\frac{\omega_i}{c}\right)^2 \varepsilon_i(\mathbf{r}) \mathbf{E}_i(\mathbf{r}) \quad i = 1, 2; \quad (\text{A.6})$$

$$\{\nabla \wedge \nabla \wedge\} \mathbf{E}_t(\mathbf{r}) = \left(\frac{\omega_t}{c}\right)^2 \varepsilon_t(\mathbf{r}) \mathbf{E}_t(\mathbf{r}) \quad (\text{A.7})$$

where the frequency, the electric field and the dielectric constant are  $\omega_i$ ,  $\mathbf{E}_i$  and  $\varepsilon_i$ , respectively for the single nanocavities and  $\omega_t$ ,  $\mathbf{E}_t$  and  $\varepsilon_t$  for the molecule. Therefore Eq. (A.7) holds for the molecule case.

Moreover, it is useful to express the overall dielectric constant as:

$$\varepsilon_t(\mathbf{r}) = \varepsilon_1(\mathbf{r}) + \Delta\varepsilon_1(\mathbf{r}) = \varepsilon_2(\mathbf{r}) + \Delta\varepsilon_2(\mathbf{r}) \quad (\text{A.8})$$

where  $\varepsilon_1$  and  $\varepsilon_2$  are defined in Fig. (A.1 a-b). While  $\Delta\varepsilon_i$  corresponds to the four holes that form the D2 single nanocavity with refractive index equal to  $(\varepsilon_{\text{slab}} - \varepsilon_{\text{air}})$ .

Then, in the tight-binding hypothesis the molecular modes can be expressed as a linear combination of the single nanocavity modes, considering the coupling at a weak perturbation. This assumption gives:

$$\mathbf{E}_t(\mathbf{r}) = c_1 \mathbf{E}_1(\mathbf{r}) + c_2 \mathbf{E}_2(\mathbf{r}) \quad (\text{A.9})$$

Therefore, putting together Eq. (A.6) and Eq. (A.7) thanks to the linearity of the derivatives and exploiting the relations (A.8) and (A.9), in the zero detuning approximation ( $\omega_1 = \omega_2 = \omega_0$ ) we obtain the equation:

$$\left(\frac{\omega_0}{c}\right)^2 (\varepsilon_1 c_1 \mathbf{E}_1 + \varepsilon_2 c_2 \mathbf{E}_2) = \left(\frac{\omega_t}{c}\right)^2 [(\varepsilon_1 + \Delta\varepsilon_1)c_1 \mathbf{E}_1 + (\varepsilon_2 + \Delta\varepsilon_2)c_2 \mathbf{E}_2] \quad (\text{A.10})$$

As often done in these kind of calculation we project (A.10) on the basis of the single cavity modes  $\mathbf{E}_1$  and  $\mathbf{E}_2$ , thus finding the matrix expression of the problem:

$$\begin{pmatrix} [(\omega_0^2 - \omega_t^2)a_{1,1} - \omega_t^2\Delta a_{1,1}] & [(\omega_0^2 - \omega_t^2)a_{1,2} - \omega_t^2\Delta a_{1,2}] \\ [(\omega_0^2 - \omega_t^2)a_{2,1} - \omega_t^2\Delta a_{2,1}] & [(\omega_0^2 - \omega_t^2)a_{2,2} - \omega_t^2\Delta a_{2,2}] \end{pmatrix} \begin{pmatrix} c_1 \\ c_2 \end{pmatrix} = 0 \quad (\text{A.11})$$

where the coefficient  $a$  and  $\Delta a$  for  $i, j = 1, 2$  are given by:

$$a_{i,j} = \int \mathbf{E}_i^*(\mathbf{r}) \cdot \varepsilon_j(\mathbf{r}) \mathbf{E}_j(\mathbf{r}) d\mathbf{r} \quad (\text{A.12})$$

$$\Delta a_{i,j} = \int \mathbf{E}_i^*(\mathbf{r}) \cdot \Delta\varepsilon_j(\mathbf{r}) \mathbf{E}_j(\mathbf{r}) d\mathbf{r} \quad (\text{A.13})$$

In the framework of the perturbation method we can safely neglect some terms in (A.11). Moreover, by exploiting the fact that the two considered cavities are identical we therefore assume that:

$$|\omega_0^2 - \omega_t^2| \ll \omega_0^2 \quad (\text{A.14})$$

$$a_{1,2} = a_{2,1}; \quad a_{1,1} = a_{2,2}; \quad \Delta a_{1,2} = \Delta a_{2,1}; \quad \Delta a_{1,1} = \Delta a_{2,2} \quad (\text{A.15})$$

$$a_{1,2} \approx \Delta a_{1,2} \ll a_{1,1} \quad (\text{A.16})$$

The condition (A.14) allows us to make the approximation  $\omega_t^2 \Delta a_{1,1} \approx \omega_0^2 \Delta a_{1,1}$  in the diagonal terms and  $\omega_t^2 \Delta a_{1,2} \approx \omega_0^2 \Delta a_{1,2}$  in the off-diagonal terms. The relations (A.15) are due to the two considered identical cavities. The validity of (A.16) relies on the fact that the integral  $a_{1,1}$  involves the superposition of the same field, while the other terms in (A.16) are proportional to the superposition of different fields, which we assume to give a lower contribution. Therefore, (A.11) can be written as:

$$\begin{pmatrix} [(\omega_0^2 - \omega_t^2)a_{1,1} - \omega_0^2 \Delta a_{1,1}] & [-\omega_0^2 \Delta a_{1,2}] \\ [-\omega_0^2 \Delta a_{1,2}] & [(\omega_0^2 - \omega_t^2)a_{1,1} - \omega_0^2 \Delta a_{1,1}] \end{pmatrix} \begin{pmatrix} c_1 \\ c_2 \end{pmatrix} = 0 \quad (\text{A.17})$$

The solutions for  $\omega_t$  can be determined by solving:

$$\begin{vmatrix} [(\omega_0^2 - \omega_t^2)a_{1,1} - \omega_0^2 \Delta a_{1,1}] & [-\omega_0^2 \Delta a_{1,2}] \\ [-\omega_0^2 \Delta a_{1,2}] & [(\omega_0^2 - \omega_t^2)a_{1,1} - \omega_0^2 \Delta a_{1,1}] \end{vmatrix} = 0 \quad (\text{A.18})$$

which gives:

$$\omega_t^2 = \omega_0^2 \left( 1 - \frac{\Delta a_{1,1} - \Delta a_{1,2}}{a_{1,1}} \right) \quad (\text{A.19})$$

This finding means that the molecular modes are slightly spectrally shifted from the single cavity resonances. In particular, the term  $\Delta a_{1,1}$  gives a shift due to the presence of another cavity in the dielectric environment ( $\Delta \varepsilon_i$ ) where the single cavity mode ( $\mathbf{E}_i$ ) is present. Therefore, it is as a self-sustained perturbation. On the other hand, the term  $\Delta a_{1,2}$  accounts for an effective interaction between the two cavities. In fact, as stated in the expression (A.13) it depends on the overlap integral between  $\mathbf{E}_1$  and  $\mathbf{E}_2$ .

In order to add more clarity, we can also define the parameters which allow us to write a matrix equation for the photonic molecule problem that is equivalent to that of two classical coupled harmonic oscillators:

$$\beta^2 = \omega_0^2 \left( 1 - \frac{\Delta a_{1,1}}{a_{1,1}} \right) \quad (\text{A.20})$$

$$g^2 = \omega_0^2 \frac{\Delta a_{1,2}}{a_{1,1}} \quad (\text{A.21})$$

in fact, (A.17) becomes:

$$\begin{pmatrix} \beta^2 - \omega_t^2 & -g^2 \\ -g^2 & \beta^2 - \omega_t^2 \end{pmatrix} \begin{pmatrix} c_1 \\ c_2 \end{pmatrix} = 0 \quad (\text{A.22})$$

### Coupled harmonic oscillators

The motion equations of the system of two coupled classical harmonic oscillators, as the one reported in Fig. (A.2), are:

$$\ddot{x}_1 + \omega_0^2 x_1 + g^2(x_1 - x_2) = 0 \quad (\text{A.23})$$

$$\ddot{x}_2 + \omega_0^2 x_2 + g^2(x_2 - x_1) = 0 \quad (\text{A.24})$$

where  $x_1$  and  $x_2$  are the position of the two masses,  $\omega_0^2 = k/m$  and  $g^2 = k_{1,2}/m$ . Then, by looking for wave solutions of the form  $x_i = c_i e^{-i\omega t}$  we obtain in the basis of the two single oscillators:

$$\begin{pmatrix} \omega_0^2 - \omega^2 + g^2 & -g^2 \\ -g^2 & \omega_0^2 - \omega^2 + g^2 \end{pmatrix} \begin{pmatrix} c_1 \\ c_2 \end{pmatrix} = 0 \quad (\text{A.25})$$

Finally, the Eq. (A.25) has the same structure and solutions of Eq. (A.22) if we define  $\beta = \omega_0^2 + g^2$ .

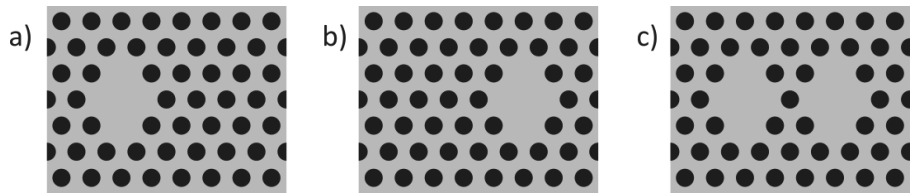


Figure A.1: a) Dielectric environment  $\varepsilon_1$  of the single left-side PCN. b) Dielectric environment  $\varepsilon_2$  of the single right-side PCN. c) Dielectric environment  $\varepsilon_t$  of the resulting photonic molecule.

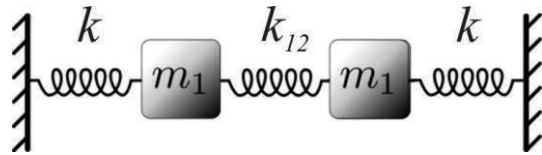


Figure A.2: Schematics of two classical coupled one-dimensional harmonic oscillators made by two equal masses and springs, which interact through a third spring  $k_{1,2}$ .



PREMIO TESI DI DOTTORATO

ANNO 2007

- Bracardi M., *La Materia e lo Spirito. Mario Ridolfi nel paesaggio umbro*  
Coppi E., *Purines as Transmitter Molecules. Electrophysiological Studies on Purinergic Signalling in Different Cell Systems*  
Mannini M., *Molecular Magnetic Materials on Solid Surfaces*  
Natali I., *The Ur-Portrait. Stephen Hero ed il processo di creazione artistica in A Portrait of the Artist as a Young Man*  
Petretto L., *Imprenditore ed Università nello start-up di impresa. Ruoli e relazioni critiche*

ANNO 2008

- Bemporad F., *Folding and Aggregation Studies in the Acylphosphatase-Like Family*  
Buono A., *Esercito, istituzioni, territorio. Alloggiamenti militari e «case Herme» nello Stato di Milano (secoli XVI e XVII)*  
Castenasi S., *La finanza di progetto tra interesse pubblico e interessi privati*  
Colica G., *Use of Microorganisms in the Removal of Pollutants from the Wastewater*  
Gabbiani C., *Proteins as Possible Targets for Antitumor Metal Complexes: Biophysical Studies of their Interactions*

ANNO 2009

- Decorosi F., *Studio di ceppi batterici per il biorisanamento di suoli contaminati da Cr(VI)*  
Di Carlo P., *I Kalasha del Hindu Kush: ricerche linguistiche e antropologiche*  
Di Patti F., *Finite-Size Effects in Stochastic Models of Population Dynamics: Applications to Biomedicine and Biology*  
Inzitari M., *Determinants of Mobility Disability in Older Adults: Evidence from Population-Based Epidemiologic Studies*  
Macri F., *Verso un nuovo diritto penale sessuale. Diritto vivente, diritto comparato e prospettive di riforma della disciplina dei reati sessuali in Italia*  
Pace R., *Identità e diritti delle donne. Per una cittadinanza di genere nella formazione*  
Vignolini S., *Sub-Wavelength Probing and Modification of Complex Photonic Structures*

ANNO 2010

- Fedi M., *«Tuo lumine». L'accademia dei Risvegliati e lo spettacolo a Pistoia tra Sei e Settecento*  
Fondi M., *Bioinformatics of genome evolution: from ancestral to modern metabolism. Phylogenomics and comparative genomics to understand microbial evolution*  
Marino E., *An Integrated Nonlinear Wind-Waves Model for Offshore Wind Turbines*  
Orsi V., *Crisi e Rigenerazione nella valle dell'Alto Khabur (Siria). La produzione ceramica nel passaggio dal Bronzo Antico al Bronzo Medio*  
Polito C., *Molecular imaging in Parkinson's disease*  
Romano R., *Smart Skin Envelope. Integrazione architettonica di tecnologie dinamiche e innovative per il risparmio energetico*

ANNO 2011

- Acciaioli S., *Il trompe-l'œil letterario, ovvero il sorriso ironico nell'opera di Wilhelm Hauff*  
Bernacchioni C., *Sfingolipidi bioattivi e loro ruolo nell'azione biologica di fattori di crescita e citochine*  
Fabbri N., *Bragg spectroscopy of quantum gases: Exploring physics in one dimension*  
Gordillo Hervás R., *La construcción religiosa de la Hélade imperial: El Panhelenion*  
Mugelli C., *Indipendenza e professionalità del giudice in Cina*  
Pollastri S., *Il ruolo di TAF12B e UVR3 nel ciclo circadiano dei vegetali*  
Salizzoni E., *Paesaggi Protetti. Laboratori di sperimentazione per il paesaggio costiero euro-mediterraneo*

ANNO 2012

- Evangelisti E., *Structural and functional aspects of membranes: the involvement of lipid rafts in Alzheimer's disease pathogenesis. The interplay between protein oligomers and plasma membrane physicochemical features in determining cytotoxicity*
- Bondi D., *Filosofia e storiografia nel dibattito anglo-americano sulla svolta linguistica*
- Petrucci F., Petri Candidi Decembri *Epistolarum iuvenilium libri octo.* A cura di Federico Petrucci
- Alberti M., *La 'scoperta' dei disoccupati. Alle origini dell'indagine statistica sulla disoccupazione nell'Italia liberale (1893-1915)*
- Gualdani R., *Using the Patch-Clamp technique to shed light on ion channels structure, function and pharmacology*
- Adessi A., *Hydrogen production using Purple Non-Sulfur Bacteria (PNSB) cultivated under natural or artificial light conditions with synthetic or fermentation derived substrates*
- Ramalli A., *Development of novel ultrasound techniques for imaging and elastography. From simulation to real-time implementation*

ANNO 2013

- Lunghi C., *Early cross-modal interactions and adult human visual cortical plasticity revealed by binocular rivalry*
- Brancasi I., *Architettura e Illuminismo. Filosofia e progetti di città nel tardo Settecento francese*
- Cucinotta E., *Produzione poetica e storia nella prassi e nella teoria greca di età classica*
- Pellegrini L., *Circostanze del reato: trasformazioni in atto e prospettive di riforma*
- Locatelli M., *Mid infrared digital holography and terahertz imaging*
- Muniz Miranda F., *Modelling of spectroscopic and structural properties using molecular dynamics*
- Bacci M., *Coarse-grained molecular dynamics and continuum models for the transport of protein molecules*
- Martelli R., *Characteristics of raw and cooked fillets in species of actual and potential interest for Italian aquaculture: rainbow trout (*Oncorhynchus mykiss*) and meagre (*Argyrosomus regius*)*

ANNO 2014

- Lana D., *A study on cholinergic signal transduction pathways involved in short term and long term memory formation in the rat hippocampus. Molecular and cellular alterations underlying memory impairments in animal models of neurodegeneration*
- Lopez Garcia A., *Los Auditoria de Roma y el Athenaeum de Adriano*
- Pastorelli G., *L'immagine del cane in Franz Kafka*
- Bussoletti A., *L'età berlusconiana. Il centro-destra dai poli alla Casa della Libertà 1994-2001*
- Malavolti L., *Single molecule magnets sublimated on conducting and magnetic substrates*
- Belingardi C., *Comunanze urbane. Autogestione e cura dei luoghi*
- Guzzo E., *Il tempio nel tempio. Il monumento ligneo a Jean-Jacques Rousseau nel Panthéon di Parigi, dalla capanna vitruviana ai Lumi francesi*

ANNO 2015

- Lombardi N., *MEREA FaPS: uno Studio di Farmacovigilanza Attiva e Farmacoepidemiologia in Pronto Soccorso*
- Baratta L., *«A Marvellous and Strange Event». Nascite mostruose nella street literature dell'Inghilterra della prima età moderna*
- Richichi I.A., *La teocrazia: crisi e trasformazione di un modello politico nell'Europa del XVIII secolo*
- Palandri L., *I giudici e l'arte. Stati Uniti ed Europa a confronto*
- Caselli N., *Imaging and engineering optical localized modes at the nano scale*
- Calabrese G., *Study and design of topologies and components for high power density dc-dc converters*
- Porzilli S., *Rilevare l'architettura in legno. Protocolli metodologici per la documentazione delle architetture tradizionali lignee: i casi studio dei villaggi careliani in Russia*



